UNIVERSITÀ DEGLI STUDI DI MILANO

DEPARTMENT OF CHEMISTRY

PH.D. COURSE IN INDUSTRIAL CHEMISTRY

XXVIII CYCLE

Novel approaches towards the optimisation of metal nanoparticle based catalysts

Tutor: Prof. Laura Prati

Cotutor: Dr. Alberto Villa

Candidate

Sebastiano Campisi (R10081)

Academic Year 2014-2015

Why heterogeneous catalysis?

Differently from real life, in heterogeneous catalysis noble metals are reactive rather than reactionary, aristocratic atoms are active sites rather than inert parasites…consequently I've positively reconsidered the nobleness and the aristocracy…even if only in the fabulous and utopic world of the chemistry.

To

Giuseppe, Maria, Chiara, Salvatore and Celestina

Part I

Introduction

Supported noble metal nanoparticles as effective heterogeneous catalysts: From design to final application

P_{art} II

R_{esults} and discussion

P_{art} III

Experimental section

Part I

Introduction

Introduction

When in 1935 Jöns J. Berzelius, a Swedish chemist, drew from ancient Greek glossary the term "catalysis" (from καταλὺειν = to dissolve)[1], describing the speeding up of chemical reactions by substances that remain unchanged after the process, he probably ignored that in the following 200 years catalysis would have occupied a central role in science and technology.

Nowadays catalysts are employed in more than 90% of industrial chemical processes. About 35% of the gross global product in 2011 can be associated to catalytic processes. The global catalyst market in 2013 was approximately $15 billion, and the corresponding added value to world economies was about $2.4 trillion. In other words, catalysts create a value that extensively overcomes the production costs of themselves. This positive trend shows no sign of decreasing in the future: world demand for catalysts is forecast to grow 4.8 percent per year to $20.6 billion in 2018, according to the Freedonia Group.[2]

The "success" of catalysis is not restricted just to industry, since in the last decades catalysis has received specific attention from academia as well. Indeed, looking at the catalysis papers published in the 10-year period from 1996 to 2005[3], an interesting trend can be revealed: the growth rate in catalysis papers (5.4%) is, by far, higher than the one of all scientific papers indexed in the Science Citation Index (SCI) over the same period (2.9%), suggesting an increasing interest devoted to catalysis research.

Beyond mere numbers, these statistics highlight the economic and social impact of catalysis. Currently catalysts are used extensively in the petroleum industry (e.g. reforming, cracking, hydrodesulphurization), in environmental technologies (e.g. catalytic converter for vehicle and industrial emission control), for energy production (e.g. fuel cells, hydrogen production) and, last but not least, in fine chemicals industry.

In particular, with regard to the latter, fine chemicals synthesis and catalysis followed different and separated lines of evolution until 1990, when after the introduction of the concept of Green Chemistry and under the consequent pressure of environmental legislation, catalysis has intersected fine chemical route. Catalysis, indeed, is explicitly embodied in the 12 principles of Green Chemistry : **9** *Catalytic rather than stoichiometric reagents*.[4]

In addition, catalysis is also indirectly involved in the realization of the other Green Chemistry principles; indeed, the use of catalysts allows to reduce waste production and lowering energy costs, just by increasing the process selectivity and resource consumption efficiency. Moreover the design of novel catalyst has opened (and will open) the way to new industrial processes (bio-refinery *in primis*), using alternative chemical feedstocks for energy and goods production.

---

[1] J.N. Armor / *Catalysis Today* **163** (2011), 3–9

[2] *World Catalysts - Industry Market Research, Market Share, Market Size, Sales, Demand Forecast, Market Leaders, Company Profiles, Industry Trends* - 12/2014 http://www.freedoniagroup.com/World-Catalysts.html

[3] *International Assessment of Research and Development in Catalysis by Nanostructured Material*, Robert Davis, World Scientific, 2011, ISBN 1848166893, 9781848166899

[4] *Green Chemistry and Catalysis*, Roger Arthur Sheldon, Isabel Arends, and Ulf Hanefeld, © 2007 WILEY-VCH Verlag GmbH & Co. KGaA, Weinheim, Germany, ISBN 978-3-527-30715-9

Despite its fundamental role, catalysis presents still many unsolved problems. In particular heterogeneous catalysis, the main topic of this thesis, is currently limited by the difficulty to understand and to describe the nature and the structure of active centres, which makes complicated an accurate design of catalysts.

A brief introduction to the huge field of heterogeneous catalysis and its main aspects is given in Chapter 1. These aspects, and in particular the identification of active sites, the role of reaction medium and support are discussed more in detail for the specific case of gold-based catalysts, whose application as catalysts in liquid phase alcohol oxidation has been the main topic of my Ph.D project.

Supported noble metal nanoparticles as effective heterogeneous catalysts: from design to final application

1 Heterogeneous catalysis: challenges and perspectives

1.1 Catalyst definition and classification[1-3]

A catalyst is a substance that enhances the rate of a thermodynamically feasible reaction without changing the position of the thermodynamic equilibrium and which remains unchanged after reaction. In the presence of a catalyst, the transformation of reactants into products thus proceeds through a lower energy activation state, following an "*uninterrupted and repeated cycle of elementary steps in which the catalyst is changed through a sequence of reactive intermediates, until the last step in the cycle regenerates the catalyst in its original form*". [1]

This definition describes an ideal catalyst; actually real catalysts, although not permanently involved in the reaction, experience structural changes after many cycles and their activity becomes lower (catalyst deactivation).[2]

Many classifications are possible for catalysts, according to various criteria. The most common refers to their physical state compared to reactant. From this point of view two main groups can be distinguished:

- *homogeneous catalysts* are in the same phase as reactants, forming only one physical phase
- *heterogeneous catalysts* are in a different phase (usually solid) with respect to reactants (liquid and/or gas).

Homogeneous catalysis is very efficient and specific, the active site is readily identified and well-characterized. However, the difficulty of catalyst removal from the reaction media imposes an additional separation operation, and therefore, together with the poor thermal stability, limits the industrial application of these systems (Figure 1.1), even some example can be recognised.

Conversely, heterogeneous catalysts, existing in a different phase from reactant, can be easily separated from products and reactants and benefit from good resistance at high temperatures. The catalytic process is dominated by interfacial phenomena and a comprehensive understanding of mechanistic aspects is complicated by the difficult to disclose the real nature of the active site. (Fig. 1.1).

In this context, nanotechnology could help in the design of specific active site thus providing a combination of both the advantages of heterogeneous (easy separation) and homogenous (high selectivity) catalysts.

Figure 1.1 Comparison of homogeneous and heterogeneous catalysts (from Ref.[3])

	Homogeneous	Heterogeneous
Effectivity		
Active centers	all metal atoms	only surface atoms
Concentration	low	high
Selectivity	high	lower
Diffusion problems	practically absent	present (mass-transfer-controlled reaction)
Reaction conditions	mild (50–200 °C)	severe (often >250 °C)
Applicability	limited	wide
Activity loss	irreversible reaction with products (cluster formation); poisoning	sintering of the metal crystallites; poisoning
Catalyst properties		
Structure/stoichiometry	defined	undefined
Modification possibilities	high	low
Thermal stability	low	high
Catalyst separation	sometimes laborious (chemical decomposition, distillation, extraction)	fixed-bed: unecessary suspension: filtration
Catalyst recycling	possible	unnecessary (fixed-bed) or easy (suspension)
Cost of catalyst losses	high	low

1.2 The Catalytic Cycle: principles and concepts [4,5]

"*A heterogeneous catalyst is a functional material that continually creates active sites with its reactants under reaction conditions. These sites change the rates of chemical reactions of the reactants localized on them without changing the thermodynamic equilibrium between the materials*." (Prof Schlögl, from Ref. [4])

In the definition reported above, it's possible to identify the essential features and, at the same time, the critical points of heterogeneous catalysts.

The catalytic cycle, the mechanism for the generation of the catalytic active site, the relation between catalytic activity and free energy associated with reactant-active site interactions represent the conceptual building blocks of any theory or model devoted to understand heterogeneous catalysis at molecular level.

A simplified schematic description of the catalytic cycle in heterogeneous catalysis is given in Figure 1.2. The first step requires the diffusion of reactants from the bulk solution to region near the surface. This step (1) is determined by diffusion and related physicochemical parameters: temperature, concentration, stirring rate, solubility (in the case of three phasic systems), affinity for the solvent. When reactants reach the catalyst surface, they are adsorbed through the formation of a chemical bond (2, chemisorption). Diffusion onto surface

brings the reactant molecules in contact with the active sites (3). Here the chemisorbed molecule can be activated, undergoes reorientation and finally reacts (4). When reaction is complete, there are three possibilities: the desorption of products, which leaves the catalyst surface and diffuse into the solution (5) or the irreversible adsorption of products through strong interactions with surface or subsurface layer (diffusion into the solid). Once products desorbed, self-repair and reorganization phenomena regenerate the catalytic site and its environment after each catalytic cycle.[6]

Figure 1.2 The catalytic cycle
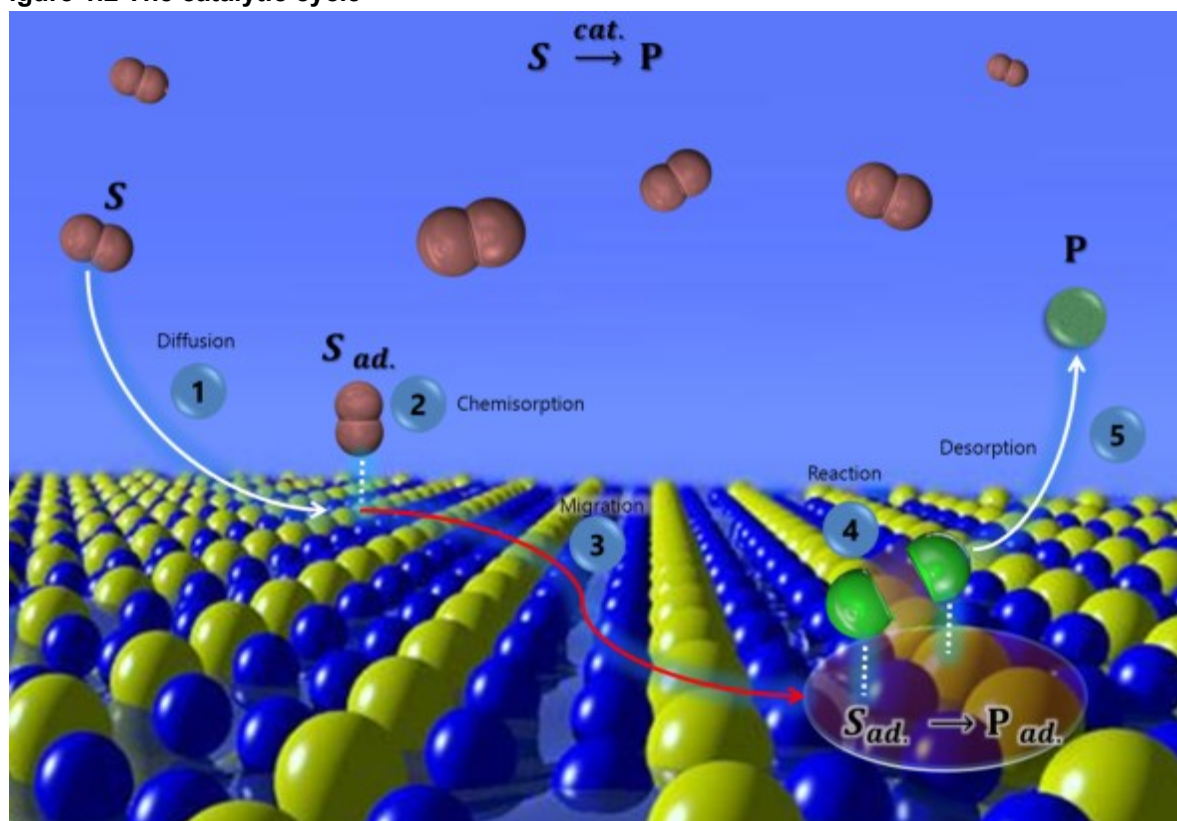
In order to maintain the activity, catalytic sites need to be regenerated after each catalytic cycle. Therefore, in an ideal catalytic process, bonds within the reactant molecule are broken whereas bonds between the substrate and the active site are created during the first steps (2-3). Analogously the bonds between chemisorbed species and the active surface are broken in the final step (4-5), when bonds within the substrate are formed resulting in the final product. This implies that the overall catalytic reaction rate is determined by competition between the kinetics for surface reaction and desorption steps, and then by the balance of the catalyst-adsorbate bond strength during the course of reaction. Catalytic reaction rate is maximized for an optimal (not too strong and not too weak) interaction between the adsorbed species and the active site, so as to activate the adsorbates, but avoid poisoning of the surface. If the interaction between substrates and catalyst is too weak, chemisorption will not happen and reactants cannot be converted into products. Conversely, also too strong bonding between catalyst and reactant can lead to a stabilization of the substrate, which won't undergo any reaction. Furthermore, when the bond between product molecules and the catalyst becomes too strong, the desorption of products becomes rate limiting. This principle was formulated by Sabatier and it is known as **Sabatier principle**.[7]

Plotting the reaction rate against reactant-interaction strength a volcano-type curve is obtained, whose maximum is called the Sabatier maximum.

The Sabatier principle provides a strategy for a rational optimization of catalyst design. For instance, by comparing for the same reaction the catalytic rates measured with different catalysts and by plotting them as a function of adsorbate-catalyst interactions, it is possible to identify the catalytic system, in correspondence of which Sabatier maximum is achieved[8]. For this purpose, the interaction strength should be evaluated; a very useful and common procedure relates changes in the enthalpy (measured or computed adsorption energies) with the interaction strength. In particular the **Brønsted–Evans–Polanyi relationship** associates enthalpic changes with changes in the activation energy for a particular elementary reaction step over a family of similar catalytic materials.[9] From an atomic point of view, it can be interesting to rationalize the free energies of adsorption in terms of catalyst structure and composition. In the 1960 's, the dependence of surface-adsorbate interactions from the electronic structure of the surface was revealed for the first time by Tanaka and Tamaru [10], who observed similar trends in the interaction energies of different molecules as a function of catalyst surfaces. Further reports evidenced that catalysis can be influenced by electronic properties such as the local density of states at the Fermi level or d-electron occupation. Recently Hammer and Norksov [11] unravelled the link between catalytic performances and the interaction with the relative positioning of the *d*-valence band centre with respect to the Fermi level at the surface, which in turn can be related to the degree of coordinative unsaturation of the surface. The limit of these theories and of the Brønsted–Evans–Polanyi relationship as well, lies in neglecting the entropic contributions thus replacing free energy, the more important thermodynamic feature to focus on, with enthalpy. The entropic contributions can be valuated using the **transition-state theory** [12], which for the sake of brevity won't be dealt with.

1.3 Active site definition in heterogeneous catalysis: pressure gap and material gap

Introduced by Sir Hugh Taylor in 1925 [13], the concept of active centre plays a crucial role in all type of catalysis. In the simplest definition, an active centre can be described as a coordination site devoted to the exchange and to the transfer of adsorbates (or their fragments) and/or electrons. As pointed by M. Boudart [14], the existence and structure of active centres in heterogeneous catalysis have been debated for a long time, contributing to give heterogeneous catalysis a "*bad reputation as a black art".* From this point of view, classical question in heterogeneous catalysis concerns with the local description of active site with either a Langmuir [15] or Taylor[13] models. According to the Langmuirian view, the catalytic surface comprises a uniform distribution of static sites considered to be similar and not interacting with one another. In this model, the selectivity of a particular reaction is determined exclusively by the number of reactive surface atoms that take part to elementary reaction events.

In the Taylor model, the catalytic surface contains a distribution of different sites, but just a small fraction of sites, Taylor called "*aristocratic atoms*" (vacancies and/or surface atoms with a peculiar topological configuration) acts as centres of reactivity. This view is supported by recent surface science discoveries, demonstrating that step edges and defects show markedly lower activation barriers than generic surface sites. The coordinative undersaturation of reactive atoms on crystal defects is a determining feature of active site, of course, however it is not the only one. The reaction environment has a great influence, as well. The constitutive elements included in the reaction environment depend on how large is

the range of the chemical interactions we consider. Beside the intrinsic chemical interactions between active sites and chemisorbed molecules, also solvent and support (strong-metal support interactions) can interact with active sites, thus affecting the activity. In addition, long-range electrostatic forces between the catalyst and the reactive complex, relaxation and reconstruction phenomena, the presence of promoters and lateral interactions between surface adsorbates can contribute significantly to the process. These considerations leads to another fundamental issue: active sites in heterogeneous catalysts cannot be described only in terms of static systems. A dynamic component has to be considered along with geometric structure (average composition, particle shape, exposed surface orientation, defect distribution), thus resulting in the introduction of the notion of dynamical active site [16]. Dynamical active sites are not part of the post-synthesis structure of a catalyst, rather they are stochastic high energy sites formed only in situ, under reaction conditions, as a consequence of restructuring, sub-surface chemistry or segregation phenomena, and induced by the interactions with the reactants, the solvent, the support and eventual promoters.

The great relevance of dynamical active site notion as unifying concept between all sorts of catalysis has been recently highlighted by Prof. Schlögl in an interesting review published in *Angewandte Chemie* in 2015, to celebrate 150 Years of **BASF** [4]. In the same review, the author examines all the critical aspects and problematics currently afflicting catalysis science. It's remarkable that most of the criticisms revealed in this review has been already presented by M. Boudart [17] in 1985. This confirms that, despite great advances have been made in synthesis, characterization and modelling techniques in the last three decades, only few steps towards the complete understanding of heterogeneous catalysis have been accomplished, partly due to the intrinsic complexity of this field. On the other hand, there is not a solid knowledge background able to deal with this complexity. In fact, nowadays research in catalysis still suffers from the existence of "*pressure gap*" and "*material gap*". The former refers to the discrepancy between the majority of surface characterization techniques working in ultra-high vacuum (P $=10^{-9}$ mbar) and the operative conditions adopted in catalytic process (P $\geq$ 1 bar); while the latter indicates the enormous difference between single crystals and ideal materials, used in many modelling simulations, and the real catalyst. Overcoming these gaps will be possible in the future only if a cooperative and multidisciplinary approach will be applied to catalyst design (see section 2), thus allowing to attain the "structure-function relation".

Figure 1.3 Bridging the gap between theory and practice in heterogeneous catalysis
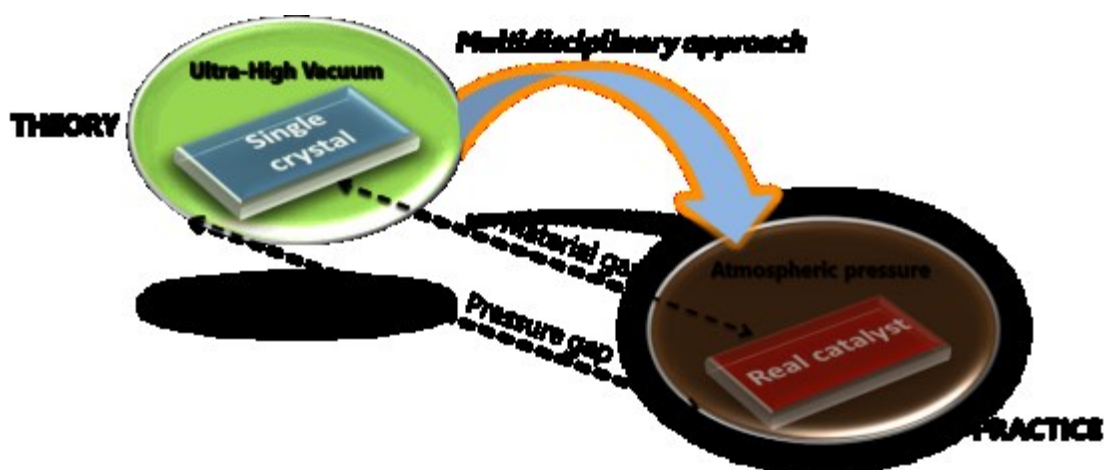
2   Catalyst design for industrial application

With the increased relevance of catalysis as primary tool for taking on the new challenges in energy, economy and environment sustainability of industrial processes, a novel term, design, is always more frequently associated to catalysis. Although in the collective wisdom this term is usually linked to fashion industry or architecture, actually the rational design of optimized catalysts in terms of composition, structure and reaction dynamics represents the new paradigm for the future achievement of catalysis as multidisciplinary and systematic science. To this day, indeed, catalyst development is based on a semi-empirical process (see section 2.2), which at length results deleterious and restrictive. By combining new advances in synthesis, characterization, and modelling is possible to unravel the structure–function relationships and to control the catalyst surfaces on a molecular level, thus overcoming the current limitations of catalysis, evidenced in par. 1.3.

2.1 Properties and characteristics of the ideal industrial catalysts

The main goal of catalyst design is the development of a catalytic structure that will meet the demands of an industrial user. The success of the process is then the result of a delicate balance between a series of requirements, often conflicting. Some of these requirements (activity, selectivity and stability) originate from the definition of catalyst, others (morphology, mechanical strength, thermal behaviour, regenerability, reproducibility, originality, costs) are connected to the final industrial scale-up.[18-20]

 Looking at the definition of catalyst reported in par. 1.1 we deduce that a small quantity of an ideal catalyst should be able to convert a large amount of reactants, preferentially under milder operating conditions than the ones required by the stoichiometric pathway. This property is referred as **activity**. An elegant definition of activity is reported in ref. [4], where catalysts are defined active if they "*are able to carry out their interactions with the reactants several times and can, thus, achieve a super-stoichiometric conversion*". Such a general concept requires an unambiguous way of estimating and quantifying it in order to compare and reproduce experiments. In a vast number of publications activity is expressed as **Turn Over Frequency** (TOF).

$$TOF = \frac{reaction\ rate}{\textbf{number of active centers}} = \frac{converted\ mols}{unit\ time \cdot \textbf{number of active centers}}$$

However this concept, borrowed from enzymatic catalysis[5], in heterogeneous catalysis is affected by an high degree of approximation deriving from undeniable difficulties in counting and determining active sites. An approximation that is often used is to identify the active site number with the number of surface atoms (TSA for total surface area)[4]. In the case of supported metal nanostructures the number of surface atoms is estimated as the area measured by chemisorption or electroxidation (ASA for active surface area) of a probe molecule (N_2, H_2 or CO)[4]. In an ideal situation the active site count should be performed close to reaction conditions, using the reactants themselves as probes. This is possible in the case of RSA (reactive surface area) characterization, even if, at the moment, this kind determination is applicable to few cases[21]. In any case, although these values are commonly reported in the literature, they suffer from strong limitations, deriving from the uncertainty associated to the number and the nature of active sites under reaction conditions, as evidenced also by M. Boudart [22], who first introduced the concept of TOF.

---

[5] The **turnover number** in enzymatic catalysis denotes the maximum value of the rate per active site, at saturation of the enzyme by the reacting substrate, as defined by Michaelis-Menten kinetics.

An active catalyst produces an acceleration of the reaction rate, though this benign effect is often followed by an undesired broad distribution of products. Indeed, due to their complex pathway, rarely chemical reactions proceed with the formation of a single product, but then usually industry is interested to one specific product. Therefore **selectivity** is the most attractive function of catalysts: an ideal catalyst should to promote the generation of the desired product, without accelerating, rather suppressing or slowing competitive and/or consecutive reactions leading to undesired products.

Two possible strategies are possible to achieve high selectivity: *substrate specificity* (typical of enzymes) and *reaction* or *product specificity* (typical of adaptive catalyst).

Another characteristic implicit in catalyst definition is its **durability** or **stability**, deriving from the statement that a catalyst should to maintain unaltered its structure and performances. Of course, the latter affirmation reflects an idealistic concept, since active sites unavoidably modify their structure during the catalytic cycle because of interactions with reactants and products, therefore over time catalysts undergo deactivation. For this reason, proper regeneration treatments become necessary. Various strategies (*e.g.* burning off, rejuvenation, etc.) are suitable for catalyst regeneration, in any case, catalysts have to preserve their structures and properties after many regeneration cycles, and namely they must possess a good **regenerability**.

Even when a catalytic formula seems to satisfy all previous requirements, the subsequent scale-up to industrial plant imposes additional criteria to be verified, with reference to the reactor design and the operating conditions of the process. First of all the catalytic material has to be malleable in order to be easily shaped. The final **external morphology** will be selected among various possibilities showed in fig., taking into account resistance to attrition and to abrasion and reaction-diffusion problems. [23-24]
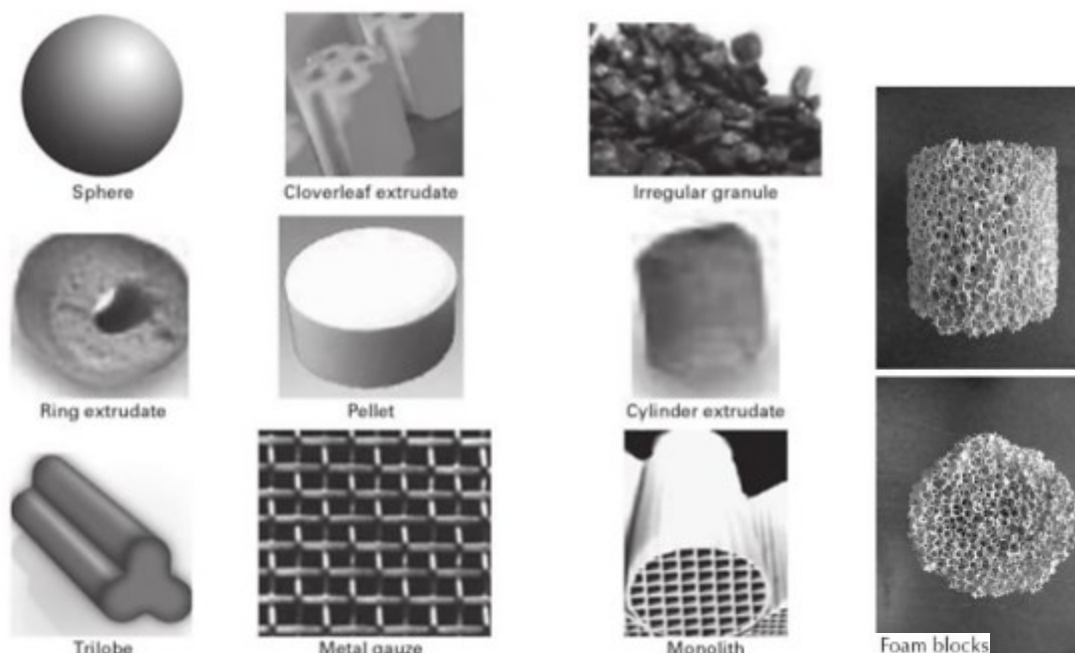
Fig. 1.4 Examples of catalyst shapes (From Ref.[23])

In many cases, catalysts in industrial reactors work in severe conditions (high temperature, high pressure, and mechanical stress), therefore **mechanical strength** and **thermal resistance** are essential characteristics.

Once a catalyst successfully passed all tests in pilot plant, it can be produced on large scale for industrial application. For this purpose, the catalyst manufacturing should be simple and economical to be expanded to industrial scale. **Reproducibility** and **costs** are not the only aspects to be considered. From a legal point of view, it is important to protect the catalyst with fundamental patents, for which **originality** is an inescapable prerequisite.

2.2 Catalyst development: from empirical to knowledge-based approach

Currently in R&D laboratories as well as in university the development of a catalyst is carried out by following a trial-and-error approach, consisting in a three-step process: *formulation → testing → modification* [25]. This sequence can be repeated until the attainment of an optimum; indeed the above-mentioned properties are not independent (rather they are often opposing), thus making impossible to obtain the ideal catalyst.

However obvious it may seem, the first step is selecting the optimal combination of catalytic active species (*i.e.* metal) and support. The material choice can be achieved on the basis of fundamentals of inorganic chemistry and chemistry of the solid by applying the knowledge gleaned from the literature. Once active species and its supports has been chosen, a family of initial catalysts is prepared and characterized. The catalysts are then submitted to experiments, thus starting the so-called *catalyst screening* in order to assess the eventual conformity to all of the above requirements. Results from preliminary catalyst screening are used to perform an initial selection of the most promising systems, worthy of being studied more thoroughly. Further catalytic tests are then carried out in order to optimize experimental conditions to improve catalytic performances[6]. In this context, catalytic performances are also related to the physicochemical properties of the materials obtained from characterization. This experimental procedure advances step-by-step to reach the desired commercial target.

The success of this empirical approach derives from the practicality of the method, which assures in any case useful results. Moreover, due to experimental and theoretical complexity, the desirable goal of the "design" of a catalytic system supported by the combination of theoretical description and experimental evidence of its atomic details, still lies far in the future. Nevertheless, whereas on one hand this observation justify the reticence of industrial and academic researchers to change approach, on the other hand it should be an incentive to increase the cooperation between different scientific fields so as to create "an unified concept of catalysis"[4] in a collaborative and multidisciplinary way.
Borrowing the immediate scheme adopted by R.A. van Santen [18], the transition between the two approaches can be effectively illustrated by using geometrical elements. If the current empirical approach could be represented by a triangle, whose apices are the three key aspects (synthesis, reaction and characterization), the new approach would be visualized by translating the triangle in the three dimensions so as to obtain a prism, where three different level (microscopic, mesoscopic and macroscopic) are related in a continuous dialogue mediated by different disciplines (Fig.1.5).

---

[6] If possible, for reaction already working in industrial plant, it is preferable to operate under conditions similar or even milder than the current industrial ones.

Figure 1.5 A knowledge-based approach to heterogeneous catalyst design (Adapted from Ref.[18])
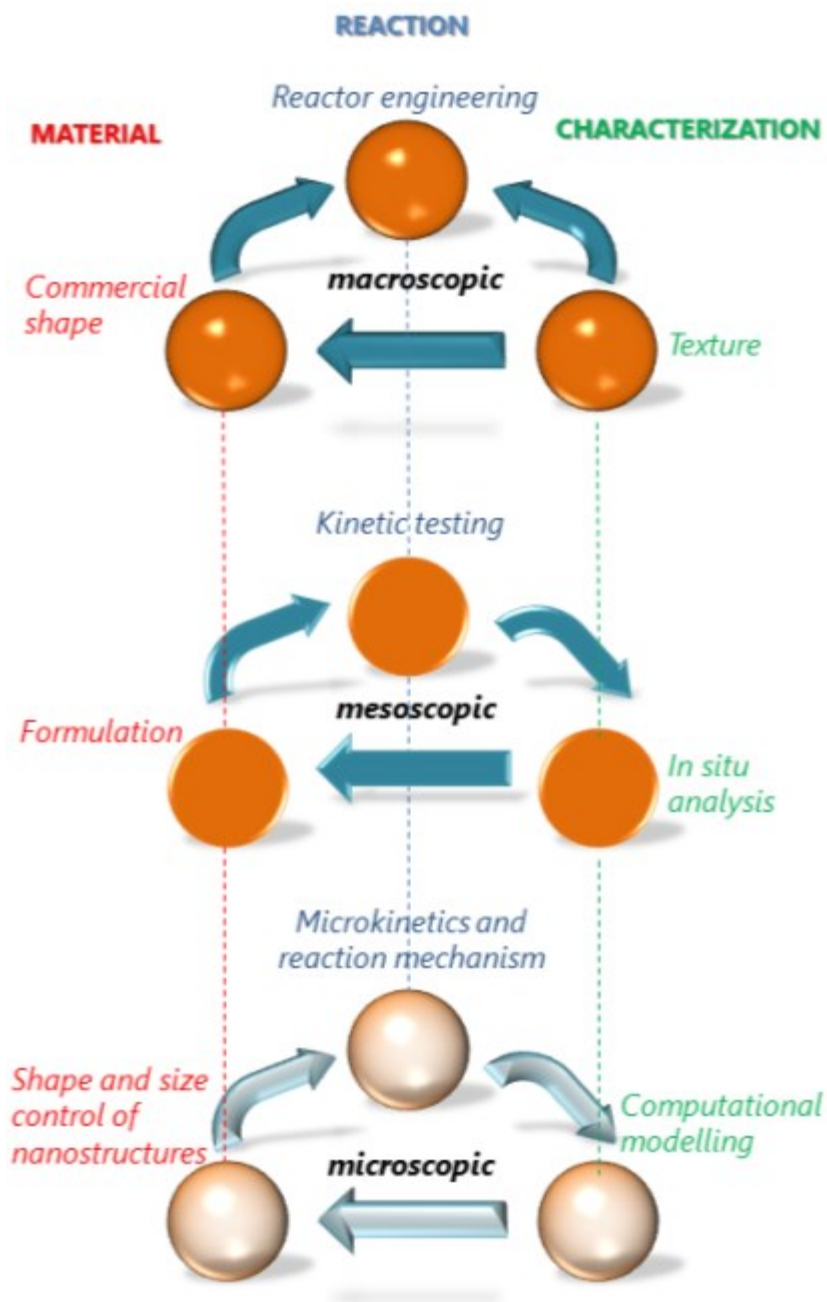
In such a multidisciplinary knowledge-based approach, the design of catalytic materials will proceed by combining and integrating the evaluation of the catalytic performances in reactor studies with the information deriving from:

1. Size, shape and composition control by proper synthesis route
2. Fundamental surface science studies under ultrahigh vacuum (UHV) conditions and *in situ* or *operando* characterization of catalytic material under reaction conditions.
3. Molecular modelling by computational chemistry

In the last three sections, we will deal with each of the above aspects separately, after having introduced the specific example of supported noble metal nanoparticles.

3. Surface science and catalysis

"*God made the bulk; the surface was invented by the devil*" - Wolfgang Pauli

The above citation of the famous scientist W. Pauli, Nobel Prize in Physics 1945, often recurs in scientific papers or books introducing the concept of surface and its intrinsic complexity. In any case, far away from taking the side of devil either of God, no doubt surface is one of the best inventions whoever could do.

A surface or interphase is formed whenever two different regions of matter (phases) are putted into direct contact; it represents the phase boundary, and atoms in it experience an *asymmetric environment* and therefore they undergo inevitably an alteration of their properties compared to the ones in the bulk. For this reason, property gradients are present at surface, and these gradients are driving forces for many processes. Some of these processes are at the basis of the heterogeneous catalysis. Indeed, in heterogeneous catalysis the main events take place in the interface between two phases: catalyst (usually a solid) and the reaction medium (liquid or gas). Therefore, the catalytic reactions are strongly affected by the surface properties of crystalline catalytic materials.

In any surface an abrupt change in crystal structure and orientation (as well as in chemical and physical properties) is experienced, therefore surface represents the most extended defect in solid (two-dimensional defect).

3.1 Morphology and defects in solids

Chemical reactivity and surface properties of materials are firstly determined by their morphology. The term morphology generally refers to the three-dimensional structure of materials, however, the concept of structure includes several basic features and therefore it is much more general than we might think.

Indeed, looking at material structure, first of all it is fundamental to define the length of scale we are considering. From this point of view it is possible to distinguish between: macro-, micro- and nanostructure.

Macrostructure of a solid material is the three-dimensional structure because of atom positions in the space. For crystalline materials the unit cell, its dimensions and the fractional coordinates of the atoms constituting the cell give the crystal structure. A full characterization of macrostructure is usually performed through X-ray diffraction (XRD).

For polycrystalline materials physical (mechanical, electrical, optical) properties are often induced by their structure at the micron level (**microstructure**), as a consequence of the presence of crystallites (or crystalline grains), namely small domain with crystalline order at microscopic level. The sizes, shape, orientation and distribution of the crystallites, as well as the bounding between them, strongly affect the physical and chemical properties of materials.

With the increasing climb of nanotechnology, the design, the synthesis, the control and the investigation on the structure at the nanometer level (**nanostructure**) are becoming even more appealing. The challenge of nanomaterials has encouraged the development of more sophisticated characterization techniques (e.g. Scanning probe Microscopy, Neutron Scattering, Atom Probe Tomography) and the improvement of previously established techniques, such as Scanning Tunnelling Microscopy (STM), Atomic Force Microscopy (AFM) Electron Microscopy (SEM, TEM, HR-TEM) and X-ray Diffraction. [26]

With the introduction of these techniques, the differences between long-range and short-range ordering and the impact of the latter on physical and chemical properties have become even more evident. Indeed the average structure, as determined by classical crystallography, often fails in explaining electronic and physical properties, since it neglects the presence of defects, impurities and structural issues inside nanoscale domains, which is the so-called local structure.

Indeed, in practice ideal crystals do not exist, the presence of defects or impurities being unavoidable in non-molecular materials, because of thermodynamic constraints, and energy-minimization requirements, and crystal growth kinetic (native defects) or external stresses (induced defects).

Although in their simplest definition defects can be described as imperfections or mistakes in the regular crystal structure, they are far from having a detrimental effect. Actually, defects in catalysis play a crucial role and usually represent preferential sites for anchoring and adsorption, as well as active centres.

Therefore, a full morphological characterization of a catalytic material implies also the determination of the number, the nature and the distribution of defects.

Defects can be classified by following a dimensional hierarchy.[27]

Figure 1.6 Defects in solid
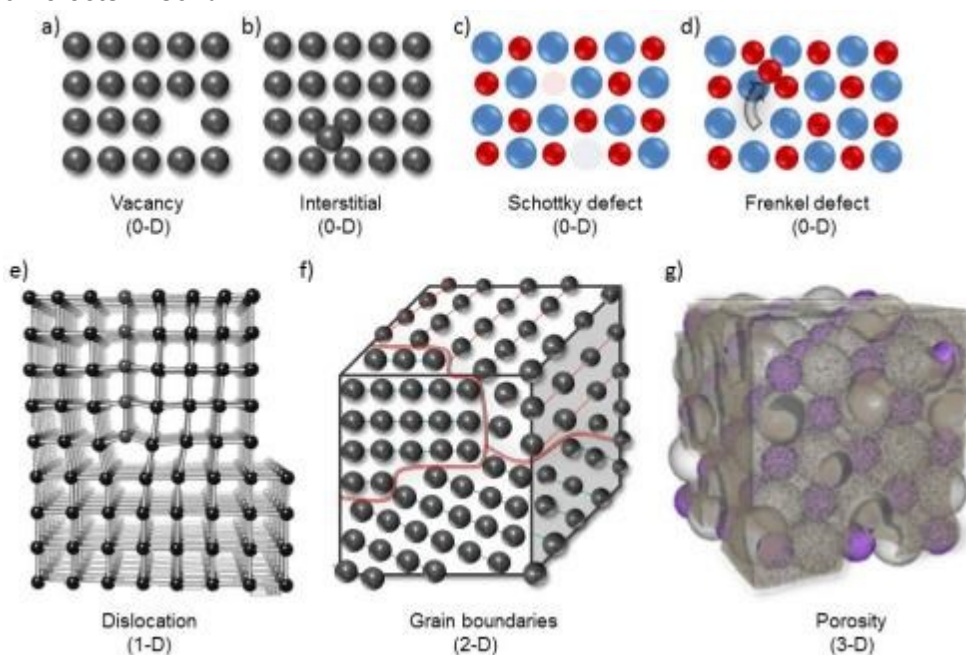
Zero-dimensional defects or point defects are the most common and simplest defects in a solid. Typically, this type of defect is localized at single atom site generating two possible situations: the absence of an atom from a normal occupied position (*vacancy*, Fig 1.6, a) or of the incorporation of an extra atom, forced to be placed in an interstitial site (*interstitial atom*, Fig. 1.6, b). In addition, some foreign atoms are invariably included in the structure during the crystal growth, constituting the so-called impurities. In ionic crystal, the numbers of vacancies, interstitials and impurities are strictly connected to restore the electronic neutrality (ionic or structural compensation). **Schottky defects** (opposite charged ions leaving their lattice site and creating vacancies) and **Frenkel defects** (displacement of an atom or ion from its lattice position to an interstitial site, creating a vacancy at the original site and an interstitial defect) are common defects in ionic crystals (Fig 1.6, c and d).

Solid deformation mechanism is strictly related to the presence of lines of irregularity in the structure, the so-called *dislocations*. Dislocations are **one-dimensional defects** similar to the humps in bumps in a creased blanket (Fig 1.6, e).

Internal (grain boundaries, shown in Fig. 1.6 f, dislocation loops, stacking faults, shear planes) and external surfaces are the most attractive defects (**two-dimensional defects**) from a catalytic point view. For this reason, surface morphology will be thoroughly discussed separately in the next paragraph along with porosity. In fact also pores can be described as **three-dimensional (or volume) defects**, they being a portion of void space in the bulk structure (Fig 1.6, g).

3.2 Surface crystallography[28-30]

The surface geometry determines possible adsorption sites and the type and density of active centres, therefore describing surface crystallography is extremely useful in heterogenous catalysis. The generation of a surface can be figured as the result of cutting a perfect crystal along an arbitrary angle. The most important crystallographic structures in inorganic solids are the face-centred cubic (fcc), body-centred cubic (bcc) and hexagonal close-packed (hcp) structures. Directions in lattices are uniquely identified by the *Miller indices*, a set of three *h,k,l* (in the case of fcc, bcc structures) or four (hcp) rational numbers, reported inside square brackets, and indirectly related to the positions of the atoms in the lattice. The same set of number can be used to indicate a plane of atoms: planes, indeed, are uniquely defined by the direction normal to the plane, hence planes are labelled with the Miller indices of the normal direction, by enclosing these numbers in parentheses.

Crystal planes are characterized by the corresponding packing-density. *Low index planes* are the simplest and flattest of the fundamental planes and they are characterized by an high packing-density; conversely, high index planes (*h,k* or *l* > 1) present lower packing-density and often possess open structures that can expose second and even third layer atoms. A lower packing-density results in a higher surface roughness. Low-index planes, possessing lower surface energy, are more stable compared to high-index planes. Consequently, if possible, a solid prefers to expose low-index planes. The stability of low-index planes can be understand by introducing the concept of *coordination*.

Generally, physical and chemical properties of materials depend on the connectivity (number, strength, direction of bonds) between atoms and at nanometric level on local geometry. The coordination describes the number and arrangement of nearest-neighbour atoms with respect to a reference atom. The creation of a surface leads to the exposition of atoms (or ions) with a lower coordination number than that in the bulk. Due to the lower number of neighbours, atoms at surface present unsaturated bonds, called *dangling bonds*, which are responsible of the higher energy of surface atoms compared to bulk atoms. A high packing-density implies a higher coordination and then a lower number of dangling bonds, and this justifies the higher stability of low-index planes.

A well-established principle of thermodynamics states that physical systems evolve to a state of minimum total energy. Surface atoms abide by thermodynamic rules, and then they react to the imbalance of bonding forces acting on the surface. The simplest (and most energetically favourable) way for minimizing the total surface excess energy consists in decreasing the bond length between atoms of the first and second layer, without modifying the atomic arrangement ("*surface relaxation*"). Alternatively, in multicomponent systems surface energy can be reduced by varying the composition at surface, with an enrichment of the component with the lower heat of sublimation ("*surface segregation*"). In many cases,

however, surfaces undergo dramatic change in the structure of the first atomic layer in order to reduce the total number of dangling bonds ("***surface reconstruction***").

Surface reconstruction phenomena are often associated to *vicinal surfaces*. Vicinal surface are "*close to but not flat low index planes*"[29], formed by cutting a single crystal with a small deviation (miscut angle) from the exact [hkl] direction. In order to get closer to a low index structure, vicinal surfaces reconstruct forming **terraces** of low index planes and **steps** (vicinal surfaces are also called stepped surfaces). The introduction of step-like discontinuities leads also to the presence of defects, such as **kinks** (figure 1.7). Atoms at **edges**, **steps** and **kinks** experience a lower coordination compared to atoms in terraces and therefore they are more prone to react and adsorb external species. In fact, the formation of a new bond, typical of adsorption, and in particular of chemisorption, leads to a lowering of the surface excess energy. For this reason, these defects play a crucial role in heterogeneous catalysis.

Figure 1.7 Kink, step and terraces in solid surfaces
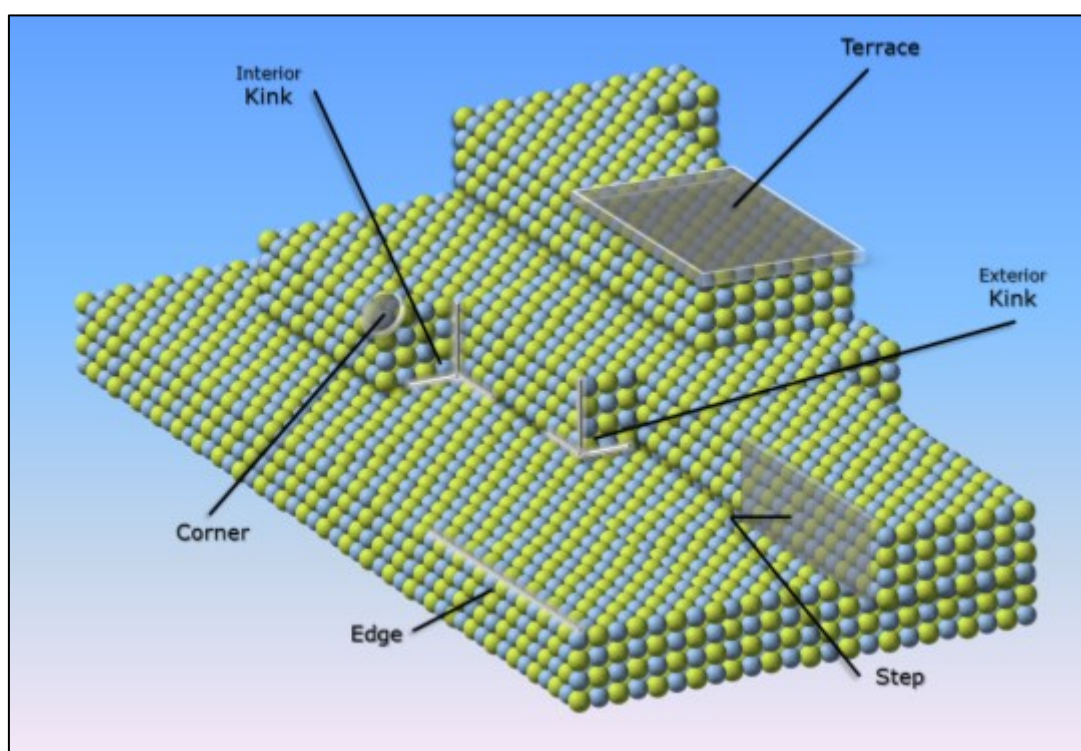
3.3 Surface area and porosity[31,32]

Thus, surface has been described just from a qualitative point of view. However the knowledge of surface geometry is preliminary to the quantitative treatment of surface in terms of its area. Roughly, the external surface area is determined by the particle size and shape. Actually, although the measure of geometrical area is a well-established mathematical concept, some additional critical features have to be taken into account, as often happens when mathematics bumps into chemistry. Indeed, because of the presence of voids, steps and other imperfections on the surface, the real surface area never coincides with the ideal geometric surface.

In material science, the specific surface area (defined as surface area per unit volume or mass) is commonly used. Depending upon the nature of the active component, a maximum active surface area per unit weight otherwise a maximum active surface area per unit volume

is more suitable. With highly expensive active components (noble metals) a maximum active surface area per unit weight of active component is the most attractive, whereas, when less costly active components are employed, a maximum active surface area per unit volume is desired, so as to reduce catalytic reactor volume.

Many solids used as supports are porous, then the total surface area is the sum of external and internal surfaces, the latter including the contribution of pore walls. Porous solids present specific surface area values much higher than non-porous ones (1-1000 m^2/g vs. 0.01-10 m^2/g, respectively).

In dealing with porous material two different features have to be taken into account: porosity and pore texture. Porosity indicates the fraction of the total void volume with respect to the volume of the catalyst. The pore texture includes pore sizes, pore size distribution and pore shape. Both porosity and pore texture are influenced by the preparation method. The presence of pores, indeed, either originates from the generation of intracrystalline cavities during the precipitation, or from the presence of template, then removed through selective dissolution, or from the elimination of volatile materials during post-synthesis thermal treatments. According to their sizes, pores can be classified in four different groups (Fig 1.8):

- ultramicropores (size<0.7 nm),
- micropores (size <2 nm),
- mesopores (2 nm <size<50 nm),
- macropores (size >50 nm).

Pores can be closed (not accessible from the external), blind (open at only one end), or through (open at both extremities). In addition, pores can be isolated or, more frequently, connected to other pores in a porous network (Fig 1.8).

Figure 1.8 Pore texture: sizes, shapes and connectivity
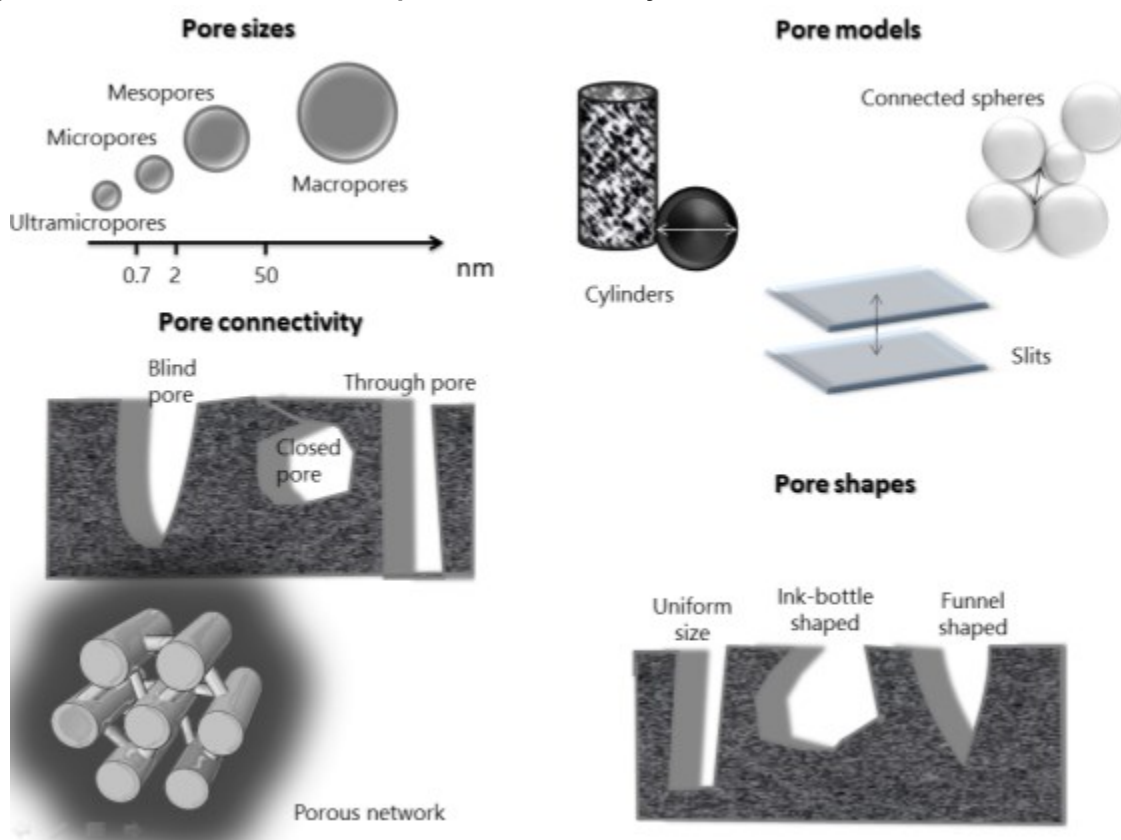
Pores can present regular or irregular shape, in any case some specific geometrical forms are usually employed as models for describing pore shape (Fig 1.8):

- cylinders (alumina and magnesia), the size coincide with the diameter
- slits (activated carbons and clays), the size is the distance between walls
- voids between connected solid spheres (in silica and solids obtained from gels),

An uniform size along the length is assumed in these models, however ink-bottle shaped (pore body larger than pore mouth) or funnel shaped (*viceversa*) are common (Fig 1.8).

The knowledge and estimation of total surface area and pore shape, size and connectivity is fundamental in understanding catalytic phenomena in the reaction medium. On one hand, the number and accessibility of active sites (and consequently the catalytic activity) depend on total surface area. On the other hand, pore sizes and texture are crucial criteria, since transport phenomena and transfer processes (bulk diffusion, Knudsen diffusion) are controlled by pore architecture and tortuosity factor (i.e. the ratio between distance covered by a molecule and granule size). Several techniques can be employed for surface area measurements and pore texture determination.

Specific surface area can be calculated from particle size distribution obtained by dynamic light scattering, assuming spherical particles, or by microscopy, combined with shape analysis. The analysis of the profile of the Small angle X-ray scattering (SAXS) curve provides important morphological parameters, such as mean size, size distribution and specific surface area. However, all these methods consist in indirect measurements and are, therefore, affected by approximations, deriving from assumptions on the shape of particles. Gas adsorption based techniques are more often used.

Nitrogen adsorption at boiling temperature (77 K) and the corresponding isotherm curves (relating the amount of adsorbed gas to the relative vapour pressure at a certain temperature) are widely used for the determination of surface area and porous texture. According to IUPAC classification, six types of adsorption isotherm and four hysteresis shapes (adsorption-desorption cycles) can be identified. The most diffuse isotherms (I, II, IV, VI) and hysteresis shapes (H1, H2, H3, H4) in catalyst characterization and the corresponding physical significance are reported in Figure 1.9.

Surface area, pore size distribution and pore volume can be extrapolated from these curves. The classical BET method, proposed by Brunauer, Emmet and Teller in 1940s, is nowadays the most used tool for surface area determination. In this model, surface area (A_s) is related to the monolayer volume (V_m) and the area σ, covered by one nitrogen molecule (0.162 nm^2), according to the equation:

$$A_s = (V_m/22414)N_a\sigma$$

<div align="right">E.1</div>

Monolayer volume (V_m) is the critical parameter in BET theory and it is determined by the equation E.2, valid in the assumption of infinite number of adsorbed layer (***two parameters BET equation***):

i = intercept
s = slope

$$\frac{P}{V_a(P_o-P)} = \underbrace{\frac{1}{V_mC}}_{i} + \underbrace{\frac{C-1}{V_mC}}_{s}\left(\frac{P}{P_o}\right)$$

<div align="right">E.2</div>

P = partial vapour pressure of adsorbate gas in equilibrium with the surface at 77.4 K (b.p. of liquid N_2), in Pa,

P_o = saturated pressure of adsorbate gas, in pascals,

V_a = volume of gas adsorbed at standard temperature and pressure (STP) [273.15 K and atmospheric pressure (1.013 × 10^5 Pa)], in millilitres,

V_m = volume of gas adsorbed at STP to produce an apparent monolayer on the sample surface, in millilitres,

C = dimensionless constant that is related to the enthalpy of adsorption of the adsorbate gas on the powder sample.

Figure 1.9 Isotherms and hysteresis cycles

(a) Isotherms

(b) Hysteresis
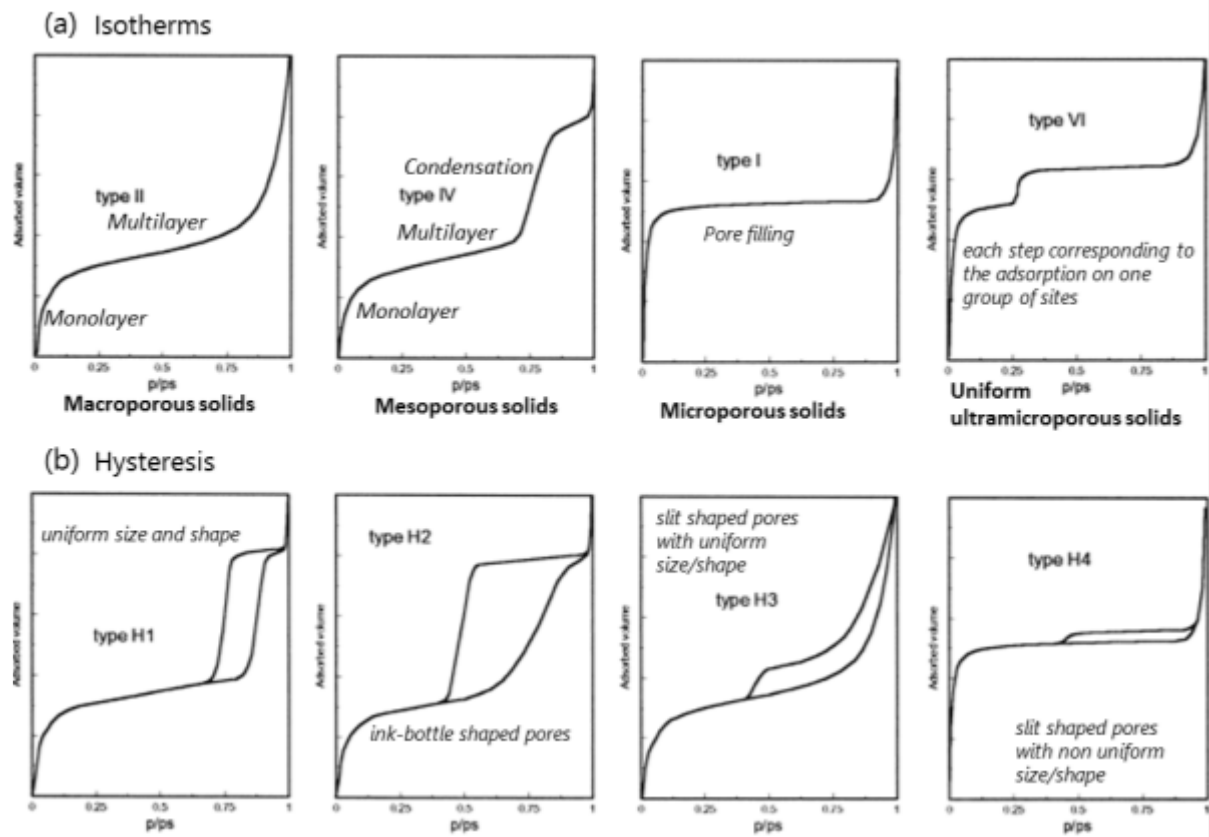
In multi-point measurements, BET equation requires a linear plot of $P/[V_a(P_0 - P)]$ against P/P_0, from which V_m is calculated, by combining slope and intercept:

$$V_m = \frac{1}{s + i}$$

A minimum of three data points is required for this method. Alternatively, single point method can be applied, using only one point in the isotherm, and valid only in the case of materials possessing a material constant C much greater than unity, so that E.2 can be replaced by:

$$V_m = V_a \left(1 - \frac{P}{P_0} \right)$$

E.3

Beside surface area, total pore volume can be derived from adsorption isotherms, by inserting the amount of vapour adsorbed at a relative pressure close to unity in the equation E.4, valid in the hypothesis that pores are filled with liquid adsorbate.

$$V_{liq} = \frac{P_a\ V_{ads}\ V_m}{R\,T}$$

E.4

Average pore size is estimated from the pore volume (E.5), assumung cylindrical pore geometry:

$$r_p = \frac{2 V_{liq}}{S}$$

E.5

Despite its wide use, BET method suffers from some criticism due to assumptions of the model (uniform adsorption sites, constant heat of adsorption, negligible lateral interactions of adsorbed molecules) and to the lack of applicability to microporous systems.

As an alternative, surface area, micropore and mesopore volume can be extrapolated from *t-plot* or from *αs-plot*. Both methods are based on the comparison of adsorption isotherm data

of a porous sample and of a nonporous material of identical chemical composition and surface texture. The former is based on the plot of V_{ads} versus the statistical thickness t (adsorbed volume per unit of surface), while the latter has been proposed by Sing in 1969 and resorts in normalizing V_{ads} compared to the V_{ads} at a given value of p/p$_0$ (usually 0.4).

Pore size distributions can be obtained by means of Horvath-Kavazoe (HK) method (micropores) and Barrer, Joiyner and Halenda (BJH) method (based on Kelvin equation and valid for mesopores), even if many methods have been developed in the last years.

Mercury porosimetry represents the best alternative to gas adsorption for the measure of meso- and macropore volume and size distribution.

3.4 Surface acid-base properties [33,34]

Once surface has been described from a quantitative and qualitative point of view, all we can do is to focus the attention on the most interesting feature from a catalytic point of view, which is the surface reactivity. The reactivity of surfaces can be essentially ascribed to redox and acid-base properties. The latter have been extensively studied and applied in industrial chemistry, since the use of solid acids and solid bases assures many advantages over liquid Brønsted and Lewis counterparts. The acidic character of a solid surface was revealed and then reported for the first time by Kobayashi for a clay named Kambara (he recalled *acid earth*), in 1902 and 1912 respectively [35], and even if the first solid acid catalyst was developed by Houdry in 1933 for petroleum cracking process [36]. However, no systematic studies about the solid acid catalysis were accomplished until 1960's. With the establishment of the concept of solid acid or base catalysts and the characterization of surfaces, the progress of solid acid-base catalysts experienced a sensible improvement attested by the increased number of industrial processes using this kind of catalysts. As reported by Tanabe [37], in 1999 the number of solid acid-base catalysed processes was 127, however to date this number is surely raised, due to the increasing application of solid acid-base catalysts in fine chemical production.

Solid acid-base catalysts include a large number of materials, several examples are reported in fig.1.10.

Figure 1.10 Types of solid acids and solid based used as catalysts in industrial processes

| Solid acids	Solid bases
1. Natural clay minerals: kaolinite, bentonite, attapulgite, montmorillonite, clarit, fuller's earth, zeolites	1. Mounted bases: NaOH, KOH mounted on silica or alumina; alkali metal and alkaline earth metal dispersed on silica, alumina, carbon, K_2CO_3 or in oil; NR_3, NH_3, KNH_2 on alumina; Li_2CO_3 on silica
2. Mounted acids: H_2SO_4, H_3PO_4, H_3BO_3, $CH_2(COOH)_2$ mounted on silica, quartz sand, alumina or diatomaceous earth	2. Anion exchange resins
3. Cation exchange resins	3. Mixtures of oxides: $SiO_2 \cdot Al_2O_3$, $SiO_2 \cdot MgO$, $SiO_2 \cdot CaO$, $SiO_2 \cdot SrO$, $SiO_2 \cdot BaO$
4. Mixtures of oxides: $SiO_2 \cdot Al_2O_3$, $B_2O_3 \cdot Al_2O_3$, $Cr_2O_3 \cdot Al_2O_3$, $MoO_3 \cdot Al_2O_3$, $ZrO_2 \cdot SiO_2$, $Ga_2O_3 \cdot SiO_2$, $BeO \cdot SiO_2$, $MgO \cdot SiO_2$, $CaO \cdot SiO_2$, $SrO \cdot SiO_2$, $Y_2O_3 \cdot SiO_2$, $La_2O_3 \cdot SiO_2$, $SnO \cdot SiO_2$, $PbO \cdot SiO_2$, $MoO_3 \cdot Fe_2 (MoO_4)_3$, $MgO \cdot B_2O_3$, $TiO_2 \cdot ZnO$	4. Inorganic chemicals: BeO, MgO, CaO, SrO, BaO, SiO_2, Al_2O_3, ZnO, Na_2CO_3, K_2CO_3, $KHCO_3$, $(NH_4)_2CO_3$, $CaCO_3$, $SrCO_3$, $BaCO_3$, $KNaCO_3$, $Na_2WO_4 \cdot 2H_2O$, KCN
5. Inorganic chemicals: ZnO, Al_2O_3, TiO_2, CeO_2, As_2O_3, V_2O_5, SiO_2, Cr_2O_3, MoO_3, ZnS, CaS, $CaSO_4$, $MnSO_4$, $NiSO_4$, $CuSO_4$, $CoSO_4$, $CdSO_4$, $SrSO_4$, $ZnSO_4$, $MgSO_4$, $FeSO_4$, $BaSO_4$, $KHSO_4$, K_2SO_4, $(NH_4)_2SO_4$, $Al_2(SO_4)_3$, $Fe_2(SO_4)_3$, $Cr_2(SO_4)_3$, $Ca(NO_3)_2$, $Bi(NO_3)_3$, $Zn(NO_3)_2$, $Fe(NO_3)_3$, $CaCO_3$, BPO_4, $FePO_4$, $CrPO_4$, $Ti_3(PO_4)_4$, $Zr_3(PO_4)_4$, $Cu_3(PO_4)_2$, $Ni_3(PO_4)_2$, $AlPO_4$, $Zn_3(PO_4)_2$, $Mg_3(PO_4)_2$, $AlCl_3$, $TiCl_4$, $CaCl_2$, AgCl, CuCl, $SnCl_2$, CaF_2, BaF_2, $AgClO_4$, $Mg(ClO_4)_2$	5. Charcoal heat-treated at 900°C or activated with N_2O, NH_3 or $ZnCl_2$-NH_4Cl-CO_2
6. Charcoal heat-treated at 300°C	From Ref. [38]

The Brønsted-Lowry acid-base theory and the Lewis acid-base theory can be applied also to solid acids and bases. A surface site (specifically an hydrogen-containing species) able to release a proton is called Brønsted acid site, whereas a surface site with property of proton acceptor is called Brønsted basic site.

In Lewis view, an acidic site is any species at the surface that, because of the intrinsic coordinative unsaturation, can accept an electron pair to form a dative or coordination bond. Conversely, a Lewis basic site is a site that possesses a non-bonding electron pair that can be donated to generate a coordination bond. In almost all cases both Brønsted and Lewis acidic/basic sites are a direct (Lewis sites) or indirect (Brønsted sites) consequence of the presence of coordinatively unsaturated centers and defects at the exposed surfaces. Coordinatively unsaturated metal cations at the surface act as Lewis acid sites. Metal cations can be also incorporated in the structure of zeolites or mesoporous silica materials during synthesis. Analogously, unsaturated metal anions serve as Lewis bases: except for non-oxide catalysts, the basic sites are believed to be surface oxygen atoms. In any case, the number of coordinatively unsaturated centers is often reduced by reaction with molecules from the environment (H_2O, CO_2, CO) resulting in the formation of new surface species, such as hydroxy groups and surface carbonates. Consequently, Lewis acidity is not usually observed for the covalent oxides of non-metal elements, due to the extreme polarizing power of cationic species (related to the high charge/ionic radius ratio) which makes difficult breaking the M – (OH) bonds.

The hydroxyl groups on surfaces (arising either from water dissociative adsorption in the case of oxides or from functionalization in the case of carbon based materials) potentially act as Brønsted acid sites or, alternatively, as basic sites. The surface hydroxy groups of ionic metal oxides (oxides of low-valency metals, with cations in oxidation number ≤ 4) have predominantly a basic character, due to the strong polarization of the metal-oxygen bond and to its tendency to be dissociated by water. Covalent low-valency non-metal oxides (such as silica, germania and boria) show quite weak Brønsted acidic properties, due to the lack of delocalization of the negative charge arising from OH groups dissociation. Contrariwise, the possibility to delocalize the anionic charge through M=O double bonds confers a strong Brønsted acidity to oxides of elements with valency five or higher (tungsta, molybdena, vanadia, phosphoric anhydride niobia). In any case the simplest type of Brønsted acid is the acid in the solid form, such as heteropolyacids $H_3PW_{12}O_{40}$. Alternatively, also phosphate and sulfate-containing surfaces (functionalized oxides, polymeric resins or carbons) exhibit a significant Brønsted acidity.

The discrimination between Brønsted and Lewis acidic sites can be performed by monitoring the adsorption of basic molecules, such as ammonia and amines, in the gas-phase by Infrared Spectroscopy[39,40]. The interactions of the probe molecules with Brønsted-type and Lewis sites (Fig.1.11) perturbate vibrational modes of the molecules, thus resulting in the appearance of specific bands in the corresponding IR spectra and in changes in the position and shape of the stretching mode bands of surface hydroxy groups, in the case of Brønsted sites.

Figure 1.11 Adsorption modes of a base (e.g. pyridine) on the Lewis (a) and weak (b,c) and strong (d) Brønsted sites on a solid oxide surface
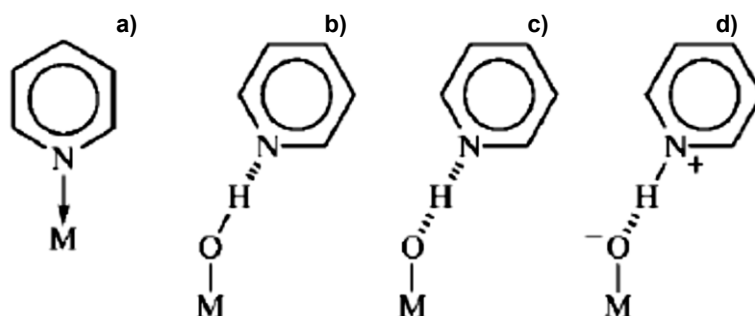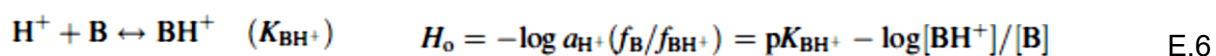
Other techniques for distinguishing Brønsted and Lewis acid sites are ^{31}P MAS NMR and CP/MAS NMR, when trialkylphosphines and trialkylphosphine oxides are used as probe molecules. These species form different adducts with Brønsted and Lewis sites, identifiable by their chemical shifts.

In order to relate surface acid/base properties with the catalytic activity, beyond the identification of acidic or basic sites, other two important terms have to be considered and quantified: the number of acidic (or basic) sites and the acid strength.
The amount of chemisorbed basic molecules is a measure of the number of acid sites, althoug it does not allow to separate the contribution of Brønsted-type or Lewis-type acid sites.
The acid strength of acidic sites of solid surfaces can be estimated by the H_0 acidity function (E.6), proposed by Hammett and Deyrup[41] in 1932 for measuring the acidity of solutions, and based on the determination of the extent of protonation of neutral[7] basic indicators (B).

$$\mathrm{H^+ + B \leftrightarrow BH^+} \quad (K_{\mathrm{BH^+}}) \qquad H_o = -\log a_{\mathrm{H^+}}(f_{\mathrm{B}}/f_{\mathrm{BH^+}}) = pK_{\mathrm{BH^+}} - \log[\mathrm{BH^+}]/[\mathrm{B}] \qquad \text{E.6}$$

Upon adsorption of an indicator B from the solution, the solid surface exhibits the colour of $\mathrm{BH^+}$ when $[\mathrm{BH^+}]_s/[\mathrm{B}]_s \gg 1$, whereas it shows the colour of B when $[\mathrm{BH^+}]_s/[\mathrm{B}]_s \ll 1$.
$[\mathrm{BH^+}]_s$ and $[\mathrm{B}]_s$ can be determined by spectrophotometric techniques, however, in practice, it is difficult to appreciate these concentration values. For this reason, more often the H_0 function is indicated as included in the range between the lowest $pK_{\mathrm{BH^+}}$ values of the indicators, which respectively exhibits and does not exhibit the colour of the conjugate acid $\mathrm{BH^+}$ on the surface.
The value of H_0 is independent of any particular indicator, but it depends on the solvent. This method neglects the reciprocal influence between vicinal acidic sites and the heterogeneity of the acidic sites. Moreover it suffers from many limitations: the lack of applicability to the measure of Lewis site strength, the $pK_{\mathrm{BH^+}}$ values of colour indicators are determined in aqueous phase, while organic solvent are usually employed in titration.

Alternatively the number and strength of acid sites can be measured by following adsorption–desorption phenomena by thermal techniques, such as temperature-programmed desorption (TPD) techniques or microcalorimetry. In the former case, the desorption of the basic probe is monitored under heating by a temperature ramp: the integral area of the desorption peak provides the total acid site density and the position of the peak maximum gives the activation energy of desorption (indirect measure of the acid strength). Differently, microcalorimetry provides a direct and accurate measure of the adsorption heat, which can be considered a good assessment of the acid strength. Shifts in the frequencies of OH signals and of characteristic band in IR spectra upon adsorption allow to estimate the acid strength, if probe molecules are properly selected (ammonia, pyridine and CO are the most used).

All characterization techniques based on adsorption, usually use probe molecules in gas-phase. However, solid acids or bases are often used in liquid-solid heterogeneous conditions and therefore the investigation and measurement of adsorption properties should be carried out under the operative catalytic conditions (*effective adsorption*). Indeed the surface

---

[7] In the original paper a whole series of acidity functions is proposed, each one distinguished by a subscript representing the sign of the base in the conjugate acid-base system used for their determination (H_, H_+, H_++).

properties of catalyst are strongly affected by the reaction medium and then differ from the intrinsic properties, measured *ex situ* before the use. Solvent can quench or mask specific sites, thus modifying their reactivity. Recently the investigation of adsorption properties in the presence of liquid of various characteristics (apolar, polar, aprotic, protic) has been successfully performed with dynamic (pulse liquid chromatographic method)[42] or equilibrium (liquid recirculation chromatographic method)[43] methods.

3.5 Surface modification: strategies and applications

As mentioned above, surface structure and composition determine and limit, to some degree, the number and the nature of the active sites and, as a consequence, the range of reactions that a catalyst can affect. Therefore, in many cases the modification of catalyst surfaces is an agreeable strategy to tune their properties and to introduce additional active sites. The surface modification will change the composition, the geometric ad electronic structure, the acidity and the reactivity of surfaces. From this point of view it's possible to distinguish between functionalization and doping.[44] The former consists of the addition of new functionalities, namely chemically reactive groups, and it involves the formation of localized covalent bonds, thus modifying the surface morphology. The latter refers to the physisorption or chemisorption of foreign species with the aim to modify just the electronic structure thus preserving the crystal lattice. However, in many cases the difference between doping and functionalization is too subtle to be effectively appreciated[8]. For this reason a more practical classification is used, discerning between chemical functionalization and physical functionalization, according to the strategy adopted for the surface modification.

Physical functionalization involves the formation of non-covalent interactions between molecules and surface. These methods include the wrapping of macromolecules around nanostructures or the encapsulation of chemical species inside cavities or pores. The weak character of these interactions leads just to a mild modification of surface properties.

In chemical functionalization, the introduction of functional groups occurs by chemical reactions. The spectrum of possible reactions that can be exploited is large and actually depends on the nature and structure of the surface. In the case of inorganic oxides, chemical functionalization implies a condensation reaction or an oxidative addition between the functionality-containing molecule and hydroxyl groups on the surface (grafting).[45] Alternatively nucleophilic or electrophilic addition to coordinatively unsaturated centres (e.g. defects) can be used, even if these methods result in an inhomogeneous functionalization, due to the random distribution of defects on the surface. All these methods act on preformed surface and therefore they are defined post-synthesis functionalizations. However, rarely surface properties can be functionalized by introducing the modifiers directly during the synthesis. Examples are mercaptoalkyl groups introduced by co-condensation method in the structure of mesoporous silica and then converted in sulfo groups (Brønsted acidic sites)[46], or Zr or Sn ions (Lewis acidic sites) incorporated into zeolite or silica structure by the direct hydrothermal method[47].
A greater number of possibilities is available in the case of carbon-based materials. Oxygen- and nitrogen-containing surface groups can be formed on the surface of activated carbon by

---

[8] In fact, on the one hand the morphology modification, induced by functionalization, strongly affects the electronic structure of the material, thus obtaining a similar effect than doping; on the other hand the doping in some cases can result in the formation of covalent bonds in the same manner as functionalization.

treatment with strong inorganic acid (nitric acid and hypochlorous acid) or ammonia and amines[48]. The surface modification of carbon nanotubes (CNTs) can be carried out either by sidewall functionalization (fluorination and derivate reactions, hydrogenation, cycloaddition, and radical attachment) or defect functionalization (amidation, esterification, thiolation, silanization, and polymer grafting). [49]

The modification of surface in catalysis aims at the introduction of reactive sites (typically acid or base), at tuning the hydrophilic or hydrophobic behaviour of the material, and, in the case of supported noble metal nanoparticles at improving catalytic performance, by increasing the stabilization and the dispersion of nanoparticles, by affecting support-metal interactions and by controlling the selectivity. [50]

4. Supported noble metal nanoparticles

Supported catalysts play a significant role in many industrial processes, representing the largest group of heterogeneous catalysts. The majority of supported catalysts consists of nanometer[9]-sized metal particles (0.1-20 weight %) dispersed over the surface of a support, which is typically a high-surface-area material. The efficacy of these materials as catalysts can be specifically attributed to the fact that the active metallic phase is present as extremely small particles.

Noble metal nanoparticles (NPs) were employed in catalysis since the 19th century, when silver nanoparticles were used in photography. Several pioneering applications of NPs in catalysis have been proposed. However, only in the last decades, advances in nanoscience and nanotechnology have contributed to the development of nanocatalysis as a science, due to a fine control of particle composition, size, and shape during the synthesis and a detailed understanding of their effects on catalytic performance. For this reason, nanocatalysts represent actually the ideal bridge between classical heterogeneous catalysts and molecular catalysts, and the preferential target of a rational catalyst design as described in section 1.2.

4.1 Chemical bonding at transition metal surface: the *d*-band model

Among metal catalysts, noble metals are most relevant. In the largest classification, noble metals include ruthenium, rhodium, palladium, silver, osmium, iridium, platinum, gold, mercury and rhenium, all having in common a remarkable resistance to oxidation and corrosion in moist air.[10] In any case, from a catalytic point of view the group VIII and IB metals, show an unequalled activity. Indeed according to Sabatier principle for a good working catalyst (see section 1.1.2), the interaction between adsorbates and transition metal surface is strong enough to bind and activate molecules upon chemisorption, but not so strong for the product molecules to desorb. A first explanation for these evidences was proposed by Dowden with its **electronic theory of catalysis**[51]. In Dowden's view, chemisorption is the result of an electron transfer: molecules adsorb on metal surfaces by either accepting or releasing an electron. The electron transfer results easiest when metal atoms at surface possess:

- Unoccupied levels (i.e. holes) in the d-band; or
- High density of states at the Fermi surface

From this point of view, metals at the end of the Transition Series satisfy both requirements.

Dowden's model failed after 1960's, when it became evident that a covalent bond instead of an electron transfer is involved in chemisorption. The catalytic behaviour of transition metal surface was, therefore, described in terms of **d-band Model**, developed by Hammer and Nørskov. [52] According to this model, the chemisorption is the result of an interaction between molecular orbitals of the adsorbate and electronic bands (continuous range of available electronic states) of metal (Figure 1.12).

In the case of transition metals, the chemisorption is assumed to occur in two steps. In the first one, molecular orbitals of adsorbate interact with broad *s*-band of metal, resulting in a broadening and downshift of the adsorbate states. The latter interact with narrow transition metal band of localized *d*-electrons, thus splitting into bonding and anti-bonding states. Electrons from transition metal will fill up all states located below the Fermi level. If anti-

---

[9] 1 nm = 10^{-9} m

[10] Physics definition is more restrictive, it including in noble metals only ones which possess filled electronic d-bands. According to this definition, only gold, silver and copper are noble metals.

bonding states are located above the Fermi level they remain empty without weakening the chemisorption bond.

Conversely, the more anti-bonding states are below the Fermi level, the weaker the resulting interaction between adsorbate and metal surface.

Figure 1.12 Schematic density of states (DOS) illustration of the d-band model
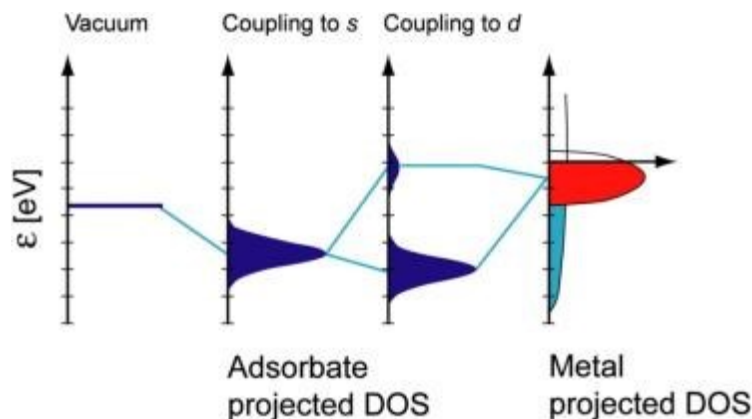
As a general rule, the strength of the bond is given by the filling of the antibonding states and consequently by the position of d-band respect to Fermi level (the contribution of *s*-band to the bond energy being similar for all transition metals to a first approximation). Indeed, the higher the d states are in energy relative to the Fermi level, the higher in energy the antibonding states are, therefore transition metals with higher-lying *d*-bands show stronger chemisorption properties. The position of *d*-band, however, is not the only criterion. In many cases, back-donation (e.g. the case of CO) or re-hybridization (e.g. the case of ethylene) phenomena are involved in chemisorption interaction.

4.2 The effect of particle size: electronic effects, equilibrium shape and structure sensitivity

The *d*-band model allows predicting with sufficient accuracy the reactivity of bulk or infinite transition metal surfaces, but it dramatically fails in describing the adsorption properties of small clusters and nanoparticles. As an instance, the exceptional catalytic activity showed by nanosized Au systems[53] cannot be explained in terms of interactions between adsorbates and *d*-electrons of gold (see par. 1.4.3). Indeed, going from infinite surface to semi-infinite crystals and metal clusters, size and shape effects become particularly prominent.[54]

According to Boudart[17], transition metal particles can be classified as a function of their dimensions, distinguishing three different characteristic regions:

i. **Metal Clusters (d < 1 nm)**
    Below 1 nm, specific molecular structures, constituted of less than 40 atoms, are formed. Due to the high number of surface atoms, small metal clusters are extremely reactive.

ii. **Nanoparticles (1 nm < d < 5 nm)**
    Particle in the size range between 1 nm and 5 nm show peculiar physical and chemical properties, intermediates between those for the molecular structures and those for bulk crystal.

iii. **Crystallites of bulk lattice structures (d > 5 nm)**
    Metal particles larger than 5 nm have structure with faceted morphologies, similar to those of metal bulk.

Supported metal particles practically used in industrial catalysis fall in the range of nanoparticles (1 nm < d < 5 nm). The unusual and extreme reactivity of these systems can be ascribed essentially to three features:

a. Geometrical effects: equilibrium shape
b. Electronic effects: quantum size effect
c. Metal – support interactions: the smaller the particle the more its physical properties can be affected by these interactions (as discussed separately in section 1.5.2)

Geometrical effects

The first consequence of the decrease in particle size is the increasing amount of surface atoms and coordinatively unsaturated sites (atoms on edges and corners), which are expected to be more reactive and then to represent the active centres in heterogeneous catalysis. The number of surface atoms, edge atoms and corner atoms depends on the size and on the shape of nanoparticles. Metal nanoparticles can be described as "close packing " (fcc or hcp) of metal atoms with magic numbers (N) corresponding to the filling of this close packed structure. Usually the shape of metal nanoparticles can be assimilated to three basic types of structure [5]: cuboctahedron, decahedron and icosahedron. (Figure 1.13)

Interconversion between these structures can occur as a function of particle sizes. For free-standing nanoparticles the equilibrium shape can be predicted using the Wulff construction: starting from the knowledge of particle volume and of the surface energies of the single crystal surface (γ_{hkl}), surface facets are arranged in the three-dimensional space so as to minimize the total surface free energy. However, in the case of supported nanoparticles support surface contribution has to be included in the construction, as it will be described in section 1.5.2.

The effect of particle size and shape on catalytic performances is more evident in the case of structure sensitive reactions, i.e. reactions whose rate varies as a function of particle size, surface morphology and composition (in the case of bimetallic systems). A possible explanation for structure sensitivity refers to the number of metal atoms directly involved in the chemisorption and activation of molecule. Structure sensitivity is observed when surface active sites consist of more than one atom. From this point of view, structure insensitivity, revealed, for example, in the case of Pt-catalysed hydrogenation of cyclopropane, can be ascribed to surface reconstruction, extractive chemisorption and formation of a catalytic metal-alkyl overlayer. [17] This view, however, has been replaced with the introduction of dynamic active site (section 1.1.3).

Figure 1.13 Structures of 309 atom clusters (Adapted from Ref.[5])

a) Cubaoctahedron   b) Decahedron   c) Icosahedron
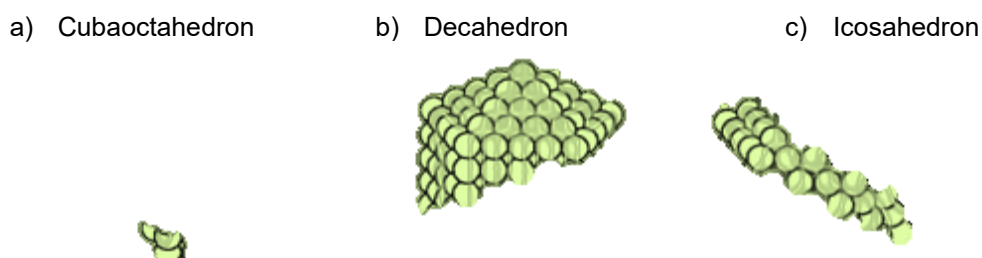
Electronic effects

Particle size does not affect only particle shape; electronic structure is influenced by particle size, as well. Decreasing the size of particles to the nanometer size scale, the band structure of metals evolve into a molecular-like structure with discrete energy differences between electronic states. The electronic properties undergo, therefore, a transition from metallic to insulator, because of the larger energy gap between the highest occupied and lowest unoccupied states. This effect, known as quantum size effect, seems to affect also catalytic performances.[55]

4.3 Monometallic gold catalyst [56,57]

Among transition metals, gold is the most interesting example of unexpected catalytic activity, which can be attributed to nanoscale effects, and in particular to:
- a) Quantum size effects
- b) Low-coordination sites presence
- c) Charge transfer between gold and support
- d) Perimeter interface between gold and support

Actually, the chemical inertness of bulk gold is a well-established evidence, justified also by *d*-band model, which predicts the presence of low energy *d*-bands, thus a high occupation of antibonding levels.

For this reason, the discovery by Haruta and colleagues in 1987 that nanometer-sized Au particles highly dispersed on reducible transition metal oxide (TiO_2, α-Fe_2O_3, Co_3O_4 and NiO) were very active for low temperature CO oxidation[58] has provided a real breakthrough in the field of catalysis. Just a few years before, in 1985 Hutchings [59], based on standard electrode potentials, predicted that Au^{3+} would be the most active species for acetylene hydrochlorination, which was subsequently confirmed experimentally. [60]

Since then, catalysis by gold became a trend topic in academic and industrial research. Extensive efforts were devoted to understand the high reactivity of supported small gold clusters. Experimental and theoretical investigation of CO chemisorption [61] allowed the identification of different adsorption sites on supported gold catalysts, CO being a probe molecule sensitive to the chemical state of the atom to which is bonded. The possible adsorption sites are depicted in Figure 1.14. Specifically CO can adsorb on:

1. Low coordination number gold atoms (corner, edges, defects)
2. Gold atom on perimeter interface
3. Gold atom on perimeter interface in proximity to support hydroxyl group (hydrogen bond formation)
4. Gold atom close to chemisorbed oxygen atom
5. Gold partially oxidized ($Au^{\delta+}$) or cationic species (Au^+, Au^{3+})
6. Support cation
7. Support cation in proximity to support hydroxyl group (hydrogen bond formation and carbonates evolution)

Figure 1.14 Sites for the adsorption of CO on a supported gold catalyst (Adapted from Ref. [62])
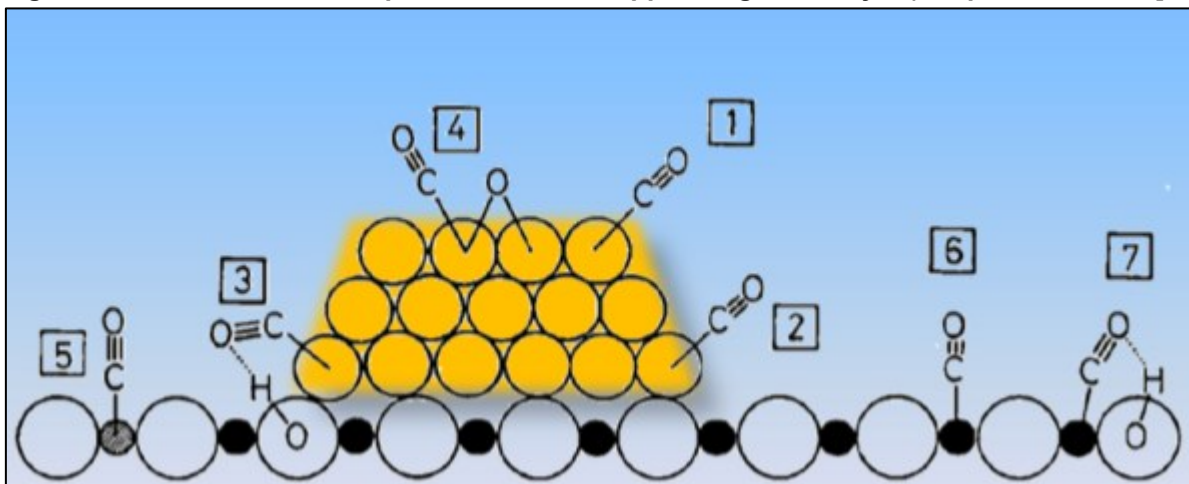
Recently, low –temperature CO oxidation experiments [63] carried out on model "single crystal" catalysts and real powder catalysts allowed to elucidate reaction mechanism and to better understand particle size and support dependence, often observed for this reaction.
In particular, the peculiar catalytic activity of supported gold can be explained by assuming that the gold-support perimeter interface acts as a site for activating at least one of the reactants.

Gold based catalysts have been extensively explored for many gas phase reactions, such as the water-gas shift[64], selective oxidation of CO in H_2 atmosphere (**PR***eferential* **OX***idation* – **PROX**)[65] and propylene epoxidation [66].

Research interest on gold received a new input in 1998, when Prati and Rossi reported the liquid phase oxidation of polyalcohols to the corresponding carboxylic acids with molecular oxygen in aqueous alkali solutions [67]. Since then, the application of gold-based catalysts to liquid-phase reactions has been enormously expanded, due to the increasing relevance of these reactions in fine chemical production and biomass valorisation. [68]

Gold offered several advantages over Pd and Pt counterparts when used as catalyst with liquid phase reactants, showing higher selectivity and better resistance to oxygen-induced deactivation. The use of gold catalysis on industrial scale, however, is nowadays limited by some not negligible drawbacks, such as the strong dependence of catalytic performances on the catalyst preparation method and on the support properties.

Furthermore, in some cases, such as liquid phase alcohol oxidation, an alkaline environment is required. For these reasons, a lot of attention has been paid in producing gold-based catalysts active also in base-free conditions and from this point of view the development of bimetallic systems (Au-Pd and Au-Pt) represent a promising alternative (see next section).

4.4 Bimetallic systems [69, 70]

The mixing of two metal components within a single catalyst has been for a long time investigated. Platinum-based alloys have been successfully used as catalysts in petrochemical industry (Pt-Ir and Pt-Ru for reforming, Pt-Sn in alkane dehydrogenation) [71]. Bimetallic systems have been of interest also for academic research. In particular the attention was focused on catalysts containing an element of Groups 8-10 (Group VIII) plus one of Group 11 (Group IB).

Pioneering studies of Schwab [72] and Sinfelt [73] unravelled the so-called "electronic factor", deriving from the interaction between the incompletely filled d band of a group VIII metal and the filled d band of a group IB metal, when they are alloyed. By tuning the alloy composition, the degree of filling of the resulting d-band can be altered thus affecting the catalytic activity.

With the discovery of gold catalyst activity (see 1.4.3), bimetallic catalysts containing gold received great attention.

In particular, it has been shown that the addition of gold as modifier has a beneficial effect on the performances of other metals such as Ag, Cu, Pd, Pt and Ru. [74]

The principal parameter to be evaluated in designing a bimetallic system is the reciprocal miscibility of the two components.[75] Gold and palladium form a continuous series of solid solutions over a wide range of compositions and the standard free energy of single-phase alloy formation is negative over a large range of temperature. [76] Platinum and gold form a continuous series of solid solutions only above 1150°C. Below this temperature, the reciprocal solubility of the two components decreases resulting in a miscibility gap, in correspondence of which a gold-rich phase coexists with a platinum-rich phase. [77]

In any case the reciprocal solubility depends on the size [78,79]

The type of mixing that occurs between two metals and the final structure are determined by several factors, including:

a) the relative strength of the bond between the two components in the alloy contrasted with the two pure metals: a greater alloy bond strength favours intimate mixing, otherwise segregation of the two metals occurs

b) the surface energy of the two metals: the metal with lower surface energy migrates to the surface of the alloy (surface segregation);

c) relative atomic sizes

d) charge transfer

e) stabilizer or ligand: the metal, that interacts more strongly with a ligand, will prefer to move to the surface in order to maximize interactions with ligand.

f) specific electronic/magnetic effects

g) the preparation method

The combination of all these factors results in the final structure of the bimetallic systems. In particular, four possible types of mixing patterns (Figure 1.15) can be identified [80]:

a) Core–shell structures: a core of metal atoms are surrounded by a shell of metal atoms of a different type

b) Sub-cluster segregated nanoalloys: two metals form separated phases separated by a pseudo-planar interface

c) Homogeneously mixed alloys: intimate mixing of the two metals in either an ordered or a statistically random manner

d) Multi-shell alloys: concentric core-shell systems in an ''onionlike' structure.

Figure 1.15 Schematic representation of some possible mixing patterns in bimetallic systems: (a) core–shell alloys, (b) sub-cluster segregated alloys, (c) random homogeneous alloys, and (d) multishell alloys.

(a) core–shell

(b) subcluster segregated

(c) random alloy

(d) three shell
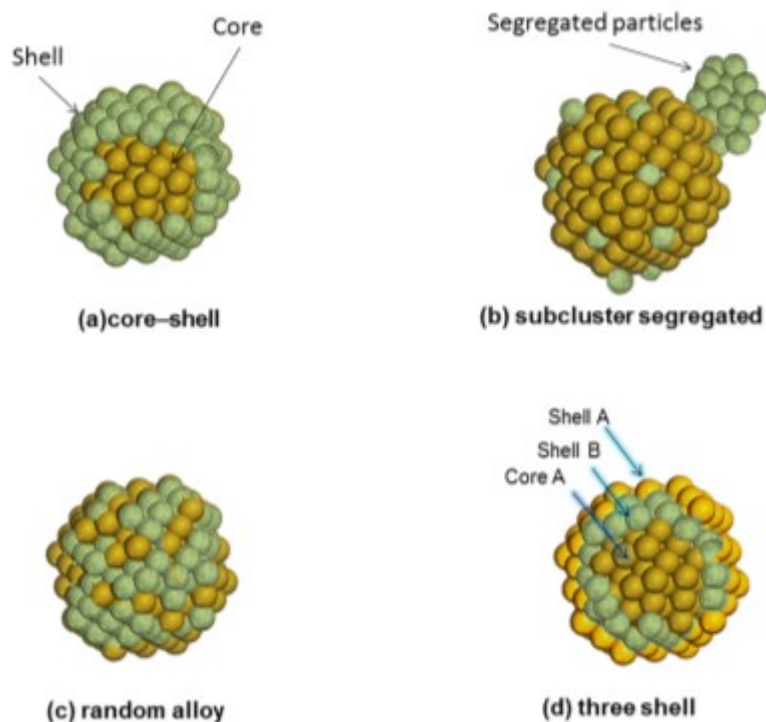
The enhanced catalytic activity and the improved selectivity often observed with nanoalloys is usually ascribed to a synergistic effect. The latter is a general term, including several events, which can be devided in two categories:

- Geometric or ensemble effects: the coordination on active sites is modified by the replacement of metal atom A with a metal atom B, which acts as diluent
- Electronic or ligand effects: electronic modification of the active metal atoms due to the altered local environment and the vicinity of the atoms of second component.

However, the origin of synergistic effect is not clear and is still debated.

Bimetallic catalysts containing gold showed activity that is superior to that of monometallic counterparts in different chemical reactions, including CO oxidation [81], the direct synthesis of hydrogen peroxide from H_2 and O_2 [82], the oxidation of primary C–H bonds [83], the selective oxidation of alcohols to aldehydes [84], and the transformation of biomass to fuel and chemicals [85]. The extent of the effect strictly depends on the real structure of the bimetallic nanoparticles.

4.5 The effect of promoters

The catalytic performances of industrial catalysts can be improved by adding external substances (additives). Additives can act as promoters, when they enhance the catalyst activity, or as modifier, if they are able to control the reaction selectivity. Alternatively, the presence of additives can negatively affect the catalytic behaviour of system and in this case, they are called catalyst poisons. However, the distinction between promoter, modifier and poison is not so straightforward. A promoter beyond improving activity can also address the reaction pathway towards the formation of the desired product, thus increasing the selectivity. Otherwise, a selectivity modifier could be a substance acting as poison for an undesirable side reaction.

The action of promoters can involve a modification either of the electronic properties or of the geometric properties. In the first case, the promoter influences the adsorption and activation process, by affecting the binding energy of adsorbates on active sites (electronic promotion). In the latter case, the additive acts as geometric promoter, by alloying an active metal with an inactive metal or by diluting metal particles to prevent rapid sintering. A typical example of industrial catalyst containing both types of promoters is the iron-based ammonia synthesis catalyst, in which alumina is present as geometric promoter preventing pure iron sintering, whereas potassium oxide is added in order to improve the adsorption and dissociation kinetics of nitrogen on adjacent iron sites.

The coadsorption of organic molecules (polymers, dendrimers, ligands) can induce a steric control of the reaction selectivity, by guiding specific reactants to specific products.
By choosing the optimal size and shape, these molecules can create a three-dimensional structure or a channel in proximity of the active site thus causing reactants to adopt a preferential adsorption geometry in order to fit in it.
The use of enantiomeric molecules can also confer enantiomeric selectivity, as in the case of cinchona-modified Pt/Al_2O_3 catalyst, which showed enantioselectivity higher than 90% for the hydrogenation of α-keto-esters, as a consequence of N–H–O interaction between Cinchonidine and ketone resulting in important selectivity preferences.[86]
Another mechanism to control catalytic selectivity by organic molecule adsorption exploits the site-isolation concept first formulated by Callahan and Grasselli [87].
Site isolation consists in the physical separation of active sites from each other on the surface of a heterogeneous catalyst. As an instance, the isolation of surface lattice oxygen in 2-5 atoms grouping allows propene to be selectively oxidized to acrolein (since more than 5 oxygen atoms promote total oxidation product formation).
Finally, as mentioned above, selectivity can be controlled by adding poisons, which block specific sites promoting undesired side reactions.
Recently it has been revealed that selectivity can be also tuned by directing the orientation of substrate toward the active site.
In conclusion, the careful selection of additives (promoters or modifiers) represents a suitable strategy in the design of catalyst with high activity and selectivity.

5 The key role of support in heterogeneous catalysts

5.1 Definition and classification of supports

The noun "support" derives from the verb *to support*. By consulting a generic dictionary, several meanings are reported for this entry. In a more scientific definition, the IUPAC Compendium of Chemical Terminology [88] reports the following outline:

"*In multiphase catalysts, the active catalytic material is often present as the minor component dispersed upon a support sometimes called a carrier. The support may be catalytically inert but it may contribute to the overall catalytic activity.*"

Actually, metals (the typical active centres in heterogeneous catalysis) present a high surface energy and tend to agglomerate, so as reducing their surface area. Therefore, the primary function of the support in a heterogeneous catalyst is acting as a mere carrier, sustaining and stabilizing the dispersion of the active component, thus preventing particle growth. However, in many cases it could play also a crucial role in the catalytic process, by contributing directly (e.g. by providing acidic/base sites) or indirectly (e.g. through strong metal-support interactions) to the catalytic cycle. The phenomena and the properties through which supports usually exert their own function will be dealt with separately hereinafter, in proper paragraphs.

In theory, any bulk material can be used as support, however in practice some important requirements in terms of physical properties (e.g. mechanical resistance, thermal stability) and chemical stability have to be taken into account in selecting a suitable material for catalytic applications. Furthermore, high-surface-area materials are preferred, playing the surface a leading role in catalysis.

The range of solid materials currently used as supports is wide, as well as the range of corresponding surface areas, porosities, shapes and sizes: a schematic classification, based on chemical composition, is reported in Table 1.1.

Herein, the attention will be focused just on the materials used in the thesis work, namely:

- Inorganic binary oxides: including binary metal oxides (MgO, TiO_2, NiO, ZrO_2), aluminas and silicas.
- Complex multicomponent oxides: including zeolites and hydroxylapatite.
- Carbon based materials: including activated carbons and graphitic materials.

Table 1.1 Support classification

Group	Examples
INORGANIC BINARY OXIDES	
IIa group metal oxides	CaO, MgO, BaO
Transition metal oxides	TiO_2, NiO, ZrO_2
Silicas	Amorphous silica, SiO_2, Mesoporous Silica
Aluminas	Al_2O_3 of different phases (e.g. γ, δ, θ, etc.)
COMPLEX MULTICOMPONENT OXIDES	Aluminum silicates, Zeolites, Aluminum phosphates, Hydrotalcites, Clays, Vanadium phosphates, Bismuth molybdates, Antimonites, Scheelites, Perovskite, Hydroxylapatites, Heteropolyanions, etc.
CARBIDES	SiC
CARBON BASED MATERIALS	
Carbon	Charcoal, Activated Carbon (AC)
Graphitized Materials	Graphite
Carbon nanostructures	Carbon nanotubes (CNTs), Carbon nanofibers (CNFs), Graphene.
POLYMER AND RESINS	Ion Exchangers, Sulfonic resins, Nafion

In the following section a brief introduction to these materials and to their use in catalysis will be provided. Morphological and surface properties will be discussed in section 5.2 and section 5.3, respectively.

5.1.A Inorganic binary and multicomponent oxides[89]

Oxides are compounds of oxygen in which the O atom is the more strongly electronegative component. Oxides of metals are usually solids.

A key aspect of inorganic oxides is their multi-functionality. Possessing multiple functional properties (acid-base, electron transfer and transport, hydrocarbon chemisorption by σ and π-bonding, H-abstraction, O-insertion, etc.), inorganic oxides represent a widely employed classes of catalytic materials, frequently used also as supports. Specifically the application of these materials in catalysis is strictly related to three key features:

a) The composition and the bonding character
b) The surface coordination environment, which is mainly determined by the exposed crystallographic faces and by the presence of impurities of defects deriving from synthesis procedure.
c) The redox and acid-base properties, governed by the electronic structure and the possible oxidation states of the elements bound to oxygen.

The bulk structures of most inorganic oxides are known and full-characterized.

Oxides commonly employed as catalytic supports belong to the structural classes of corundum, rocksalt, wurtzite, fluorite, spinel, perovskite, rutile and layer structure.

In general, due to their higher ionic radium, in close packing description O^{2-} anions are usually close-packed while the smaller metal ions are located in the octahedral or tetrahedral holes. The most important crystallographic structures are the face-centred cubic (fcc), body-centred cubic (bcc) and hexagonal close-packed (hcp) structures.

When inorganic oxides are used as supports for liquid phase processes, also the dissolution behaviour in contact with aqueous solutions plays a crucial role. These properties must be considered also in catalyst preparation, when oxides are impregnated from aqueous solutions of the active phase precursor. In general the dissolution behaviour depends on surface acid – base properties. The acidic oxides (e.g., SiO_2 and zeolites) as well as transition metal oxides in their highest oxidation state (e.g., V_2O_5, CrO_3) dissolve with formation of acids or anions, whereas amphoteric oxides (e.g., Al_2O_3, ZnO) form cations in acidic and anions in basic medium, basic oxides (e.g., MgO, lanthanide oxides) form hydroxides or dissolve by forming bases or cations.

5.1.B Carbon based materials[90-91]

Depending on the level of atomic orbital hybridization, carbon is able to combine its atoms in several geometries, thus forming a great number of allotropes (or polymorphs), with identical composition, but different physical structure. Graphite, diamond and lonsdaleite are three allotropic forms of carbon in the solid phase. Starting from 1980's with fullerene discovery, carbon science experienced a new season of great success, culminated in the isolation of graphene in 2004. In this context a new class of synthetic carbon allotropes was gradually discovered, the so-called low-dimensional carbon allotropes, characterised by regular nanostructures with dimensionality ranging from zero-dimensional (0-D, for fullerenes) to one-dimensional (1-D, for carbon nanotubes) and two-dimensional (2-D, for graphene) depending on their nanoscale range (< 100 nm) in different spatial directions.

However, in its broadest sense the term carbon usually refers also to all natural and synthetic substances containing carbon as main constituent. Therefore carbon based materials include a variety of substances.

As perfect crystal (Highly oriented pyrolytic graphite, HOPG), graphite is rare applicable in the field of catalytic supports, principally because of its low surface area (10–50 m^2/g) and the relatively low reactivity towards the activation agents (steam, oxygen, carbon dioxide). A moderate increase in surface area (100–300 m^2/g) can be achieved by chemical and electrochemical expansion of intercalated graphite[11] with sulphuric and nitric acids. From a catalytic point of view greater interest has been attracted by high surface area graphite (HSAG, SA 600 m^2/g) obtained by high-energy ball-milling and consisting of small particles with crystalline graphite structures connected to form mesopores. High surface area graphite can be also obtained by recrystallization of carbon black particles at 2500-3000°C.

The unique physical and chemical properties of carbon materials (Table 1.2) make them suitable for application in heterogeneous catalysis as supports in many industrial relevant processes[12], activated carbon (AC) and carbon black (CB) being the most commonly used. Indeed large surface area and high porosity of the latter facilitate the anchoring, the dispersion and the stabilization of the active phase, reducing sintering occurrence even at high metal loadings.

Furthermore, the surface chemistry and the pore size distribution can be properly tuned to satisfy the requirements of several reactions or to improve active phase dispersion (e.g. increasing the surface hydrophilicity just by oxidation treatment).

Carbon black (CB) is an aggregate of small spherical crystallites connected via polycyclic aromatic hydrocarbon in a random branching structure; due to its key properties (fineness, structure, aggregate size/shape, porosity, and surface chemistry) is the carbon material of choice for most carbon-supported catalysts, second only to activated carbons.

The term activated carbon[13] (AC) includes a group of amorphous carbonaceous materials (carbon being the major constituent, 85-95%) with extended internal (namely inter-particulate) surface area (800-1500 m^2/g) and high degree of porosity (pore volume between 0.2 and 1 cm^3/g), resulting in an unique capacity for adsorbing substances from gases and liquids.

Despite a misleading confusion between carbon black and activated carbon is often observed in the literature, these two materials have very different macrostructures: activated carbons possess more intricate porosity and mean particle size at least three order of magnitude larger than that of carbon black (0.01-1 mm vs. 0.01-1 μm).

The adsorption properties are strongly affected by the precursor nature and the experimental conditions adopted during the AC synthesis. The production of AC consists of two main stages: the carbonization by thermal treatment (400-800°C) of the starting material (usually coal, wastes from agriculture, wood, petroleum based residues and in general any material possessing a high fixed carbon content) and the further activation. Depending on the raw materials and on the desired final texture, physical or chemical method can be pursued for the activation.

---

[11] Graphite intercalated compounds can increase their volume by hundreds of times after a high temperature treatment, with a significant expansion of the material along the crystallographic c-axis.
[12] The Catalytic Reaction Guide published by Johnson Matthey, reported that 50 of 69 reactions of industrial interest catalyzed by noble metals used carbon materials as catalyst support (e.g. fatty acid hydrogenation, selective nitrobenzene hydrogenations, reductive alkylation, hydrogenation of dinitrotoluene, butanediol synthesis, purified terephthalic acid, etc.).
[13] Alternatively known as activated charcoal

During the carbonization (pyrolysis) the heteroatoms (namely O, N, H, and S) present in the precursor are released as volatile gaseous compounds, while the residual elementary carbon atoms form a disordered structure, consisting of an irregular arrangement of aromatic sheets and ribbons (BSUs, basic structural units)[14], crosslinked in a random manner and separated by variable interstices of molecular dimensions (Fig.1.16). These interstices are occluded by disorganized carbon, deriving from tars and other decomposition products, which quickly reacts with the gases in the activation process, generating the porosity (see section 1.3.3). Pore texture and dimensions are then influenced by the activation conditions.

Table 1.2 Advantages and disadvantages of activated carbons as supports

Advantages	Disadvantages
Large surface area and tunable surface chemistry	Easy gasification inhibit their use in high temperature hydrogenation and oxidation processes
Easy reduction and recovery of supported metals	
High resistance to acids and bases	
High thermal stability (even above 750°C under inert atmosphere)	Poor reproducibility in synthesis: different batches of the same material can contain varying ash amounts
Plasticity, allowing to prepare porous carbon in different physical forms (granules, cloth, fibers, pellets)	
Lower cost compared to metal oxides	

Not only porosity is conditioned by the activation treatment, the sizes of the aromatic sheets, as well, decrease with the extent of the activation. A meticulous control of the activation process conditions is then fundamental for the application of activated carbons as catalyst supports, since the activation process determines the adsorptive properties of activated carbon. Indeed the adsorption on the surface is the result of Van der Waals or London dispersion forces. Therefore it is essentially determined by the surface morphology and the chemical composition.

High adsorption takes place on graphitic basal structural units and it is favoured by a large amount of "π-sites". Atoms at the edge of basal planes (where the termination causes the formation of dangling bonds) and defects are preferential adsorption sites, because of the presence of incompletely saturated valences and unpaired electrons. Unlike crystalline graphite, where the edge area is small compared to that of the basal plane, activated carbons due to their disordered structure possess a large edge area and then are likely to adsorb molecules. In addition, the unavoidable presence of heteroatoms strongly affects the adsorption properties.

Although AC are currently used as supports for catalysts for various reactions (fuel cells, NO_x reduction, wet air oxidation, hydrodechlorination, hydrogenations of fatty acids or nitroaromatics and decomposition of NH_3), the lack of reproducibility represents the greatest obstacle to a successful and wide application of these materials upon industrial scale. Moreover the microporosity which characterizes AC appears to limit often the reaction rate due to diffusional limitation and/or clogging of the pores.

---

[14] The presence of graphitic domains depends on the ability of the precursor to form polycyclic aromatic structures.

Figure 1.16 Schematic representation of activated carbon (a) and ordered mesoporous carbon (b) structures

a)   b)
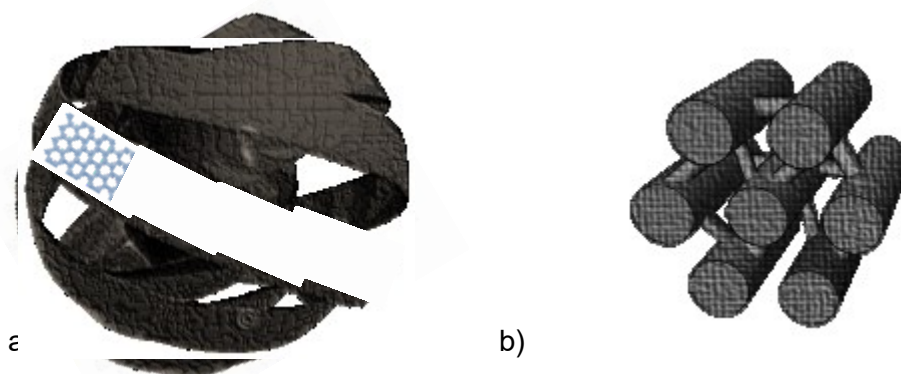
From this point of view, the recent development of template-assisted synthesis approach allowed to control the porosity thus obtaining mesoporous carbons with monodisperse pores of well-defined size and shape. This new generation of carbon based materials, called ordered mesoporous carbons (OMCs), is promising for future industrial applications.

Also low-dimensional graphitized allotropes, namely carbon nanofibers (CNFs), carbon nanotubes (CNTs) and graphene, revealed to be attractive and competitive catalyst supports presenting high surface area, high resistance to abrasion, dimensional and thermal stability and specific adsorption properties.

From a theoretical point of view, graphene, the two-dimensional carbon allotrope (one-atom-thick layer of graphite), is the ideal candidate for application as catalytic support, possessing the highest possible surface area (3000 m^2/g), and a combination of unique physical, electronic, chemical and mechanical properties. However, to date the application of a single graphene sheet (SG) as a catalytic support is far to be achieved, due to the difficult synthesis and the unavoidable tendency to agglomerate in reaction medium. Anyway, interesting preliminary results have been obtained using few-layer graphene (FLG) as support.

Differently, CNTs and CNFs represent a valid alternative, since they exhibit a well-defined structure and controlled porosity, without suffering the same drawbacks as AC and carbon black. In these cases a controlled functionalization can be performed.

Carbon nanotubes are usually referred as the 1-D carbon allotrope, due to the restricted dimensions of diameter compared to the length. In their simplest structure as single wall carbon nanotubes (SWCNTs), they can be envisioned by rolling or wrapping a graphene sheet into a seamless cylinder such that all carbon atoms align. Depending on the angle the graphene sheet is wrapped a (chiral) roll-up vector R can be defined. The R vector is described by a pair of indices (n,m): the value of n and m determines the type of SWCNT (armchair or zig-zag) and the electronic behaviour (metallic or semiconductor).
Many concentric single wall tubes originate multi-wall carbon nanotubes (MWCNTs). The distance between rolled layers in MWCNTs is close to the interlayer distance in graphite, approximately 3.4 Å.

CNTs represent a valid alternative to conventional supports, presenting several advantages [92] including:

a) High purity that reduces the risk of self-poisoning;
b) Unique mechanical properties, high electrical conductivity and thermal stability;
c) High accessibility of the supported active phase and the absence of any microporosity, thus eliminating diffusion and intraparticle mass transfer.
d) Aptitude to be easily processed for macroscopic shaping;
e) Specific metal–support interactions, deriving from the different curvature of the surfaces where the metal nanoparticles are deposited (curvature effects)
f) Confinement effects in their inner cavity, influencing diffusion and adsorption.[93]

Carbon nanotubes (CNTs) and carbon nanofibers (CNFs) show many similarities, concerning the synthesis procedure and the nanometric sizes. They, however, strongly differ from a morphological and strict dimensional point of view. [94]

The main structural difference between nanotubes and nanofibers is the growth direction that in the case of nanofibers results in the absence of the hollow cavity. Three different types of CNFs can be distinguished, according to the disposition of the graphene layers respect to the growth axis: ribbon-like CNFs (CNF-R) display graphene layers parallel to the growth axis, in the platelet CNFs (CNF-P) display graphene layers are perpendicular to the growth axis whereas herringbone nanofibers have layers stacked obliquely in respect to the growth axis. The diameters of CNFs are generally higher than the ones presented by nanotubes, being comprised between 50-200 nm.

5.2 Support-Metal Interactions

The traditional view of support as an inert carrier started fading away since 1950 [95], when the influence of acidic properties of silica-alumina support in petroleum reforming process was revealed. In the following decades, several studies and many fragmentary observations [96] corroborated the idea that maintenance of metal dispersion under severe processing conditions was not the only function of supports, rather interactions to some degree between metal nanoparticles and the underlying surface might influence the catalytic behaviour. In 1978 S.J. Tauster [97] introduced the term "**strong metal-support interactions**" (**SMSI**) in order to justify the deviation from ordinary adsorptive properties showed by group VIII (8-10) metal nanoparticles, when supported on titanium oxide. Many studies discussing metal-support interactions between noble metals (Pt, Pd, Rh, Au etc.) and various metal oxides (TiO_2, MgO, CeO_2, ZrO_2, Fe_2O_3) appeared. However the first systematic dissertation about metal-support interactions was proposed in 1982 by G.C. Bond [95-a], who distinguished between weak, medium and strong interactions. According to Bond classification, noble metals establish *weak metal-support interactions* (WMSI) with irreducible oxides (SiO_2, Al_2O_3, MgO, etc.) and carbon based supports (activated carbon, graphite); *medium metal-support interactions* (MMSI) are typical of zeolite supported noble metal nanoparticles, while noble metal nanoparticles dispersed on transition metal oxides exhibit *strong metal-support interactions*.

The catalytic performance modification induced by strong interactions between the support and metal nanoparticles can be attributed to various effects, which can be split in three different categories: geometric, energetic and electronic effects. The combination of these effects results in various phenomena, the most common being:

- The encapsulation of metal nanoparticles under a thin metal oxide film
- The formation of a hetero-interface at the periphery of metal particles, where the cooperation between adjacent metal and support sites play a crucial role.
- The migration or spillover of active species from metal to support [98] and vice versa [99]

As a general concept, when two different phases are put in contact, they rearrange in order to minimize the total surface energy; the equilibrium structure is a function of surface free energies of the two components and of the interfacial free energy between the two components. Four extreme situations can be distinguished (see Figure 1.17) depending on species mobility and on whether predominant forces are adhesive or cohesive. Most of the times, however, we encounter intermediated situations. In the case of strong metal support interactions, metal nanoparticles tend to wet the support in order to maximize the interfacial contact.

Figure 1.17 Schematic representation of metal-support interactions (From Ref.[95-b])
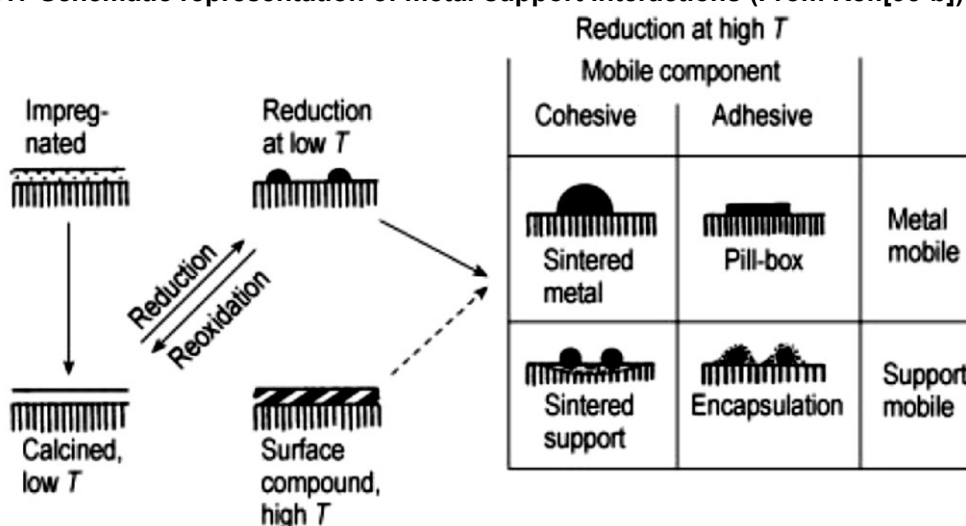
The final equilibrium shape of nanoparticles can be predicted through Wulff construction, by including the contribution of metal-support interfaces. Usually the resulting shape is a truncated polyhedral. In addition, the stronger the metal-support interaction, the higher the adhesion energy is and the more flattened the supported particle is, consequently the length of the perimeter region also increases. The adhesion energy values are not the only factors determining particle shape. As an example, the most stable structure predicted by DFT calculations for Au NPs supported on MgO(100) is not the one constructed according to Wulff rule [100]. Indeed, on decreasing particle sizes, the contribution of the formation energy of the edge and the corner atoms has to be taken into account.

Experimental evidences obtained by High Resolution Transmission Electron Microscopy (HRTEM) investigation on the morphology of Au/MgO, Au/ZrO$_2$ and Au/TiO$_2$ showed that nanoparticle shape is strongly affected by the nature of the support, the surface morphology, the preparation method and the thermal treatment.

Even when high adhesion energy is observed, the presence of a mismatch between crystal structure of metal nanoparticle and support crystal lattice is unavoidable. The misalignment of the metal lattice to the registry of the support leads to a strain of the metal–metal bonds, resulting in remarkable alterations of cohesive forces and of electronic structure.

As demonstrated by Mavrikakis et al.[101], the metal-metal bond strain results in a shift in the centre of the *d*-band, which induces foreseeable changes in chemisorption properties and catalytic activity. The modification of band structure alone is not able to justify the great influence of support on catalytic performances. In many cases, an additional electron transfer from support to metal or *viceversa* has been hypothesized. The role of positively or negatively charged gold clusters has been extensively investigated. Flytzani-Stephanopoulos and co-workers [102] evidenced the unique activity of cationic Au^{3+} clusters supported on ceria or La-doped ceria in catalyzing the water gas shift (WGS) reaction, whereas Gusman and Gates[103] attributed the activity of Au/MgO and Au/zeolite ethylene hydrogenation to the presence Au^{3+} revealed by in-situ X-ray absorption spectroscopy. On the other hand Ab-initio calculations showed that electron transfer from the support (typically MgO) to gold NPs results in the formation of negatively charged gold cluster, which could be active in CO oxidation. [104]

Despite the huge amount of experimental observations, an atomic level understanding of the strong metal support interactions is not still possible, due to many experimental challenges. First, it is difficult to separate the effect of particle sizes from the effect of metal support interactions. Reproducible synthesis procedures for free standing and supported metal nanoparticles are required in order to compare the corresponding properties. In the same manner, the comparison between metal nanoparticles deposited on different supports is complicated by different metal dispersions and size distributions. Finally, the unavoidable presence of external substances deriving from the synthesis and potentially acting as promoters or poisons get more difficult a systematic investigation of these interactions.

Recently, the introduction of advanced characterization techniques opened up new opportunities for complementary and exhaustive studies of these phenomena, thus making more feasible the goal of predicting and exploiting SMSI in catalysis. [105]

6 Catalyst preparation: an overview[19, 106,107]

The preparation is one, if not the most, crucial step in the course of catalyst design. The uncertainty associated to the nature and structure of active sites (the actual task of catalyst design) makes the choice of a suitable preparation route complicated and delicate. In addition, the eventual application on industrial scale requires reproducibility, scalability and economic and environmental feasibility. For these reasons, catalyst preparation can be considered an art, or as affirmed by Richardson [108]: "*catalyst preparation is the secret to achieving the desired activity, selectivity and life time*".

At the moment, the production of supported catalysts can be performed by three different procedures (figure 1.18):

- Selective removal of one or more components
- Application of the active component (or its precursor) onto a separately prepared support
- Simultaneous formation of active phase (or its precursor) dispersed onto the support

The first procedure is usually employed for achieving high metal loading (the preparation of Raney metals is a typical example of selective removal) and therefore it is not indicated for the preparation of supported noble metal nanoparticles [19], for which low metal loadings are preferable in terms of activity and costs. Hence, in the following sections the attention will be focused only on the last two procedures.

Figure 1.18 Synthetic strategies for supported catalyst preparation
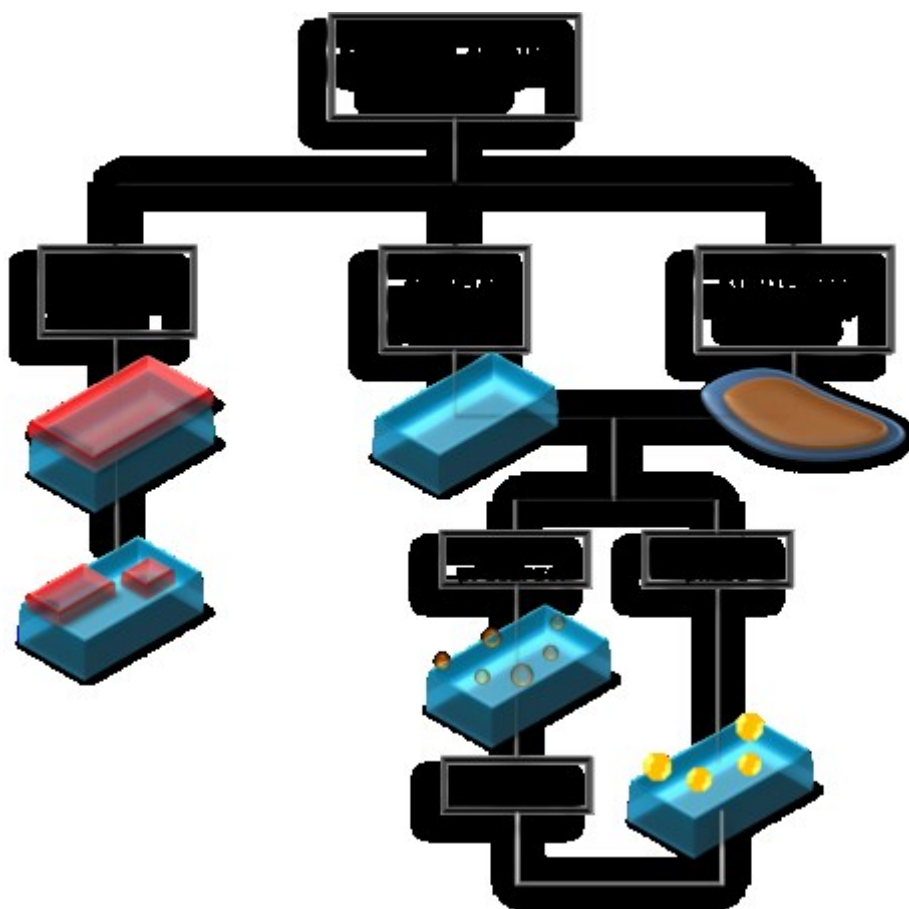
6.1 Addition of the active component (or its precursor) onto a support

The most rapid procedure to prepare supported catalysts consists in applying the active component or its precursor uniformly and finely divided onto a commercially available support of the desired size, shape, porous structure, and mechanical properties.

No matter which form (active phase or precursor) is added to the support, all preparation routes ascribable to this procedure are essentially governed by three important variables:

- o Nucleation and growth
- o Interactions at interfaces
- o Diffusive phenomena

The extent, the occurrence and the control of these phenomena are reasons behind the distinction between the different preparation methods.

6.1.   A) Impregnation

In impregnation method a solution of precursor is mixed with the support and thus introduced into the pore space. In principle, the precursor (usually a metal salt) does not strongly interact with the support thus remaining in the dissolved state in the solution. Actually, the only interactions between the support and the precursor are dipole-dipole forces, hydrogen-bonding forces, London dispersion forces and van der Waals forces, which don't affect the coordination chemistry of the surface. In any case, the support is expected to retain the whole precursor, although the latter is not fixed on the surface.

Two types of impregnation can be distinguished. In **dry impregnation** (also called capillary impregnation) a volume V of precursor solution is put in contact with the previously dried support, whose pores are then initially filled with air. The process is ruled by the replacement of the solid-gas interface by a solid-liquid interface, and by the capillarity. Usually the volume of precursor solution is equal to the pore volume ($V = V_p$). In **pore-volume impregnation** the precursor solution volume coincides with the pore volume of the support, as determined by physicochemical characterization. This technique has the advantage of no excess solution remaining outside of the pore space at the end of the operation, but the downside is that the filling and the redistribution into the pore space is usually slow (as a consequence of the presence of trapped air). Similar to pore-volume, **incipient-wetness impregnation** differs from the previous method in the procedure for the determination of the volume of precursor solution to be added. Indeed, in incipient-wetness impregnation the solution volume is "empirically determined to correspond to that beyond which the catalyst begins to look wet". [106] Dry impregnation is not suitable in the case of relatively high metal loading. Indeed, if the solubility of the precursor is not high enough to allow the dissolution of the required amount of the precursor in a small volume of liquid (a volume equal to the pore volume of the support), it is necessary the use of multiple impregnations, often resulting in an unfavourable distribution of precursor onto the external support surface (the so-called crust of precursor).
A more homogeneous dispersion can be obtained by diffusional impregnation. In **diffusional or wet impregnation** pore space of the support is pre-filled with pure solvent (the same as the impregnation solution, of course), so as $V > V_p$. Once solvent-saturated support is immersed into the precursor solution, the precursor migrates gradually from the solution into the pore under the concentration gradient. The process is very slow but a control of species distribution and high dispersions can be realised.

6.1. B) Ion exchange

Ion exchange method can be described as a particular case of wet impregnation, in which the precursor is an ionic species fixed onto the support surface by means of electrostatic interactions. When an excess volume (compared to the pore volume) of a solution containing precursor ions is contacted with the support, a competitive equilibrium is established between the precursor ions and the ions previously incorporated in the support. If the support is a natural ion exchanger (e.g. zeolites, clays, polymeric resins), precursor ions replace the compensating ions originally present in the support to neutralize the electric charges of opposite sign, naturally occurring in the framework. In this case the equilibrium is not pH dependent. On the contrary, in the case of metal oxides the pH plays a fundamental role, since the precursor ions replace the so-called potential-determining ions, H+ or OH-, deriving from the ionization of surface hydroxide groups of metal oxide in contact with water. Consequently the adsorption properties and ion exchange ability of metal oxide depends on operative pH and on the pristine point of zero charge (PPZC or simply ZPC) of the oxide (i.e. the value of pH for which the oxide surface is not charged): if pH < ZPC oxide surface tends to be positively charged and to adsorb anions. Conversely, at pH > ZPC, cation adsorption is favoured.

6.1. C) Anchoring and grafting

In the same way as ion exchange, also anchoring and grafting can be included as exceptions in impregnation methods. In these cases a condensation reaction between the precursor or active species and the surface groups of the support takes place with the formation of a strong covalent bond. A very slight difference distinguishes grafting from anchoring. In anchoring the initial species bound to the solid surface is already active, whereas in grafting a chemical reaction occurs between functional groups of the support and a species, which requires at a later stage to be properly treated (decomposition or metal-ligand bond hydrolysis) in order to modify its structure and to become active. In all cases the metal oxidation state does not change after the binding. Grafting and anchoring are the most appropriate methods for the synthesis of heterogenized homogenous catalysts, namely coordination metal complexes (metal halides and oxyhalides; metal alkoxides; organometallics, and especially metal allyls and metal carbonyls) immobilized on solid support, to sum up the advantages of homogenous (versatility and selectivity) and heterogeneous (easy recovery) catalysis.

6.1. D) Deposition-precipitation [109]

In classical precipitation method, the deposition of the metal precursor is the consequence of a chemical reaction, leading to the formation of a metal compound with low solubility. With the usual addition of a precipitant to a solution, the concentration of soluble precursor reaches locally and temporarily values above the supersolubility curve (the curve, in solubility plot, above which nucleation and subsequent precipitation occur), leading to a rapid nucleation and growth in the solution. Consequently, large crystallites of precursor are formed and deposited on the support. Due to their size, these clusters cannot enter into the pores; moreover soluble precursor molecules migrate, under the effect of a capillary flow, from the wide pores of the support to the more narrow interstices between the deposited crystallites, thus contributing to the growth of these pre-formed crystallites. This brings about an undesired heterogeneous distribution of large nanoparticles on the external surface of supports. In deposition-precipitation, a modification of the classical precipitation method,

good crystallite distributions are achieved by controlling the concentration of the soluble precursor and by exploiting large interactions between the nuclei of the insoluble active precursor and the surface of support in order to obtain the precipitation of the precursor exclusively at the surface of the support. Specifically, the precursor concentration is controlled (by adjusting the pH level, or the valence state, or the concentration of a complexing agent) so that it does not exceed locally the limit of supersolubility and no precipitation occurs in the bulk solution. The same concentration value, however, is above the supersolubility curve at the support-solution interface, because of strong support-precursor interactions decreasing the nucleation barrier (Figure 1.19). Hence, in these conditions nucleation starts exclusively on the support surface.

Figure 1.19 Deposition-precipitation principles
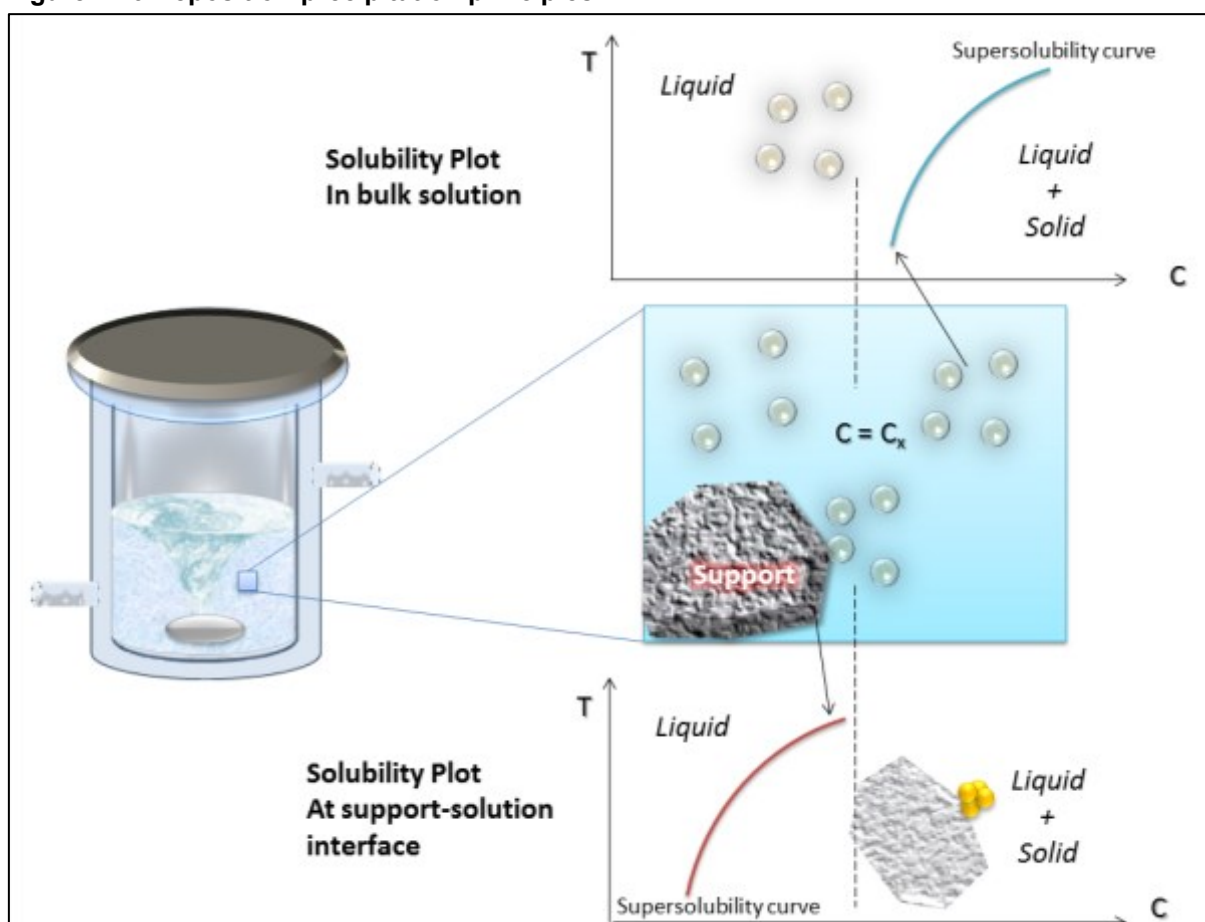
This method offers the advantage of producing a very narrow particle size distribution. However, the efficiency of the process strongly depends on the nature of the support.

6.1. E) Deposition-reduction

Redox properties of metals can be used for the deposition either on the support or on another metal centres (in the case of bimetallic catalyst preparation).

In **electrodeposition** metal precursor is reduced by applying a potential to an electrode in the presence of an electrolyte (e.g. KCl). Alternatively metal ions can be reduced by electrons provided by another metal. This electroless deposition is called **galvanic displacement**.

6.1. F) Chemical vapour deposition and its modifications

In chemical vapour deposition (CVD) metal precursors are vaporized in a vacuum system by heating and then deposited from gas phase onto a solid support. The immobilization of precursor onto the support surface and the subsequent transformation in active phase can involve various chemical reactions, such as thermal decomposition (pyrolysis), hydrolysis, disproportionation, reduction, oxidation, carburization, and nitridization. For this reason, CVD is a versatile procedure, applicable to any kind of support. However, it requires the use of metal precursors with sufficient volatility at low temperature, which in almost all cases are also toxic and expensive. Recently many alternatives have been proposed, overcoming the limitations of CVD. In **Pulsed Laser Ablation (PLA)-assisted electrodeposition**, metal nanoparticles from a solid precursor are generated in liquid environment by incident laser radiation and simultaneously deposited onto a support. The main advantage of this synthesis route is the use of solid precursor, cheaper and less toxic than metal-organic precursors. [110]. In **magnetron sputtering** [111] (a particular type of Physical Vapor Deposition, PVD) solid precursor acts simultaneously as cathode and as magnetron source, and is located inside a vacuum chamber filled with an inert gas (Ar). The application of a high voltage or radiofrequencies leads to the ionization of the inert gas and to the acceleration of the positive ions to the target (negatively charged). The ions reach the target surface with an high energy and numerous events can occur as a consequence of this ionic bombardment. First of all, neutral metal atoms are expulsed (sputtered) from the surface and deposited on the support (placed in a rotating stainless steel cup), where it nucleates and grows in correspondence of functional groups and/or defect sites to form nanoparticles. The application of a magnetic field, generated by permanent magnet arranged behind the target, produces a confinement of emitted secondary electrons near the target, thereby increasing the ionization efficiency. PLA-assisted electrodeposition and magnetron sputtering are line-of-sight techniques, resulting in metal deposition just onto surface fraction directly exposed to the metal flux.

6.1. G) Sol immobilisation [112]

Sol immobilisation can be described as a particular type of impregnation, in which active phases instead of precursors are deposited on the support. This procedure consists in the preparation of a metal sol (colloidal solution) and the subsequent deposition (immobilisation) of the preformed metal nanoparticles on the support. Metal nanoparticles can be prepared either by reduction of metal salts, or by photochemical or thermal decomposition of metal precursor, or by reduction of organometallic complexes. The colloidal solution is stabilized using a "protecting agent" in order to prevent coagulation (consequence of reciprocal attraction between nanoparticles at short distances, through van der Waals interactions). Stabilization is the result of three effects, which can work either separately or simultaneously:

- Electrostatic stabilization: the adsorption of surfactant molecules (long-chain ionic species) leads to a higher charge density at the surface, resulting in increased repulsive Coulomb forces between nanoparticles.
- Reduction of van der Waals forces: rigid hydrophilic macromolecules (i.e., dextrin, starch), adsorbed on the surface, act as "isolating layer", reducing reciprocal van der Waals interactions.
- Steric stabilization: polymer molecules attached to the particle surface form a coating, which creates repulsive forces.

The introduction of pre-formed nanoparticles (NPs) on the support entails numerous advantages. First, the deposited material is already in the active phase (metallic state), thus avoiding further step of activation. Particle sizes (and distribution) and shapes can be properly tuned and controlled during the NP synthesis, and the method can be applied with almost all supports. Indeed the immobilization step depends on sol stabilizer and on the IEP of the support. Metal NPs with narrow size distribution can be deposited on whatever support with an high dispersion degree by selecting accurately the proper protecting agent and the operative pH in the immobilization step.

6.2 Simultaneous formation of active phase (or its precursor) and support

6.2. A) Coprecipitation

Supported catalysts can be prepared by coprecipitation, consisting in the simultaneous precipitation of more than one component. This method results in a homogeneous dispersion of the active components. However the main drawback is the intrinsic difficulty of controlling the process. Indeed characteristics of the final catalyst are strongly affected by several parameters: the order and rate of addition of the components, the precipitating agent and the addition procedure (e.g. drop-wise, continuous supply), the initial pH and variation of pH during the process, the mixing procedure, the temperature, the solvent and the maturation process.

6.2. B) Sol-gel synthesis

 The sol-gel preparation is a two-step procedure. In the first step a liquid suspension of solid particles ranging in size from 1 nm to 1µm (sol) is formed by the hydrolysis and partial condensation of a precursor (inorganic salt or metal alkoxide). In the second step sol particles condense, forming a solid three-dimensional network (gel), encapsulating in its pores the solvent, which is subsequently (after aging) removed by either evaporative drying (xerogel) or drying with supercritical extraction (aerogel).
The process is governed by the relative rates of hydrolysis and condensation, which are both nucleophilic displacement and are therefore influenced by pH, by the positive partial charge of the metal atom and its coordination number and by the amount of water. Also phenomena occurring during the aging (further cross-linking) and the drying (capillary pressure) can influence the structure of the final material. However, an easy control of all these variables is feasible, thus making sol-gel synthesis a suitable strategy for the preparation of supported catalysts. In fact sol-gel procedure shows the convenience of saving a step, by introducing the active phase during, instead of after, the formation of the support, even if the incorporation of the precursor within the support structure can make more difficult the subsequent activation.

6.3 Active phase production

Most often the active phase (metal) is produced during a second step called "activation". This crucial operation consists in a thermal treatment (calcination) or in a chemical reaction (reduction or sulfidation). Two critical factors determine the outcome of the activation process: the dispersion degree of the precursor and the interaction of the precursor with the support. The former influences the rate of reduction and the competition between nucleation and growth during the formation of active phase; the latter governs the reactions occurring at the interface between supported phase and support and consequently the nature of the interface active phase-support and the extent of metal-support interactions in the final catalyst.

7 Catalyst characterization an overview [113]

The characterization is not just one step in catalyst design, rather it can be considered the main validation tool, allowing a continuous monitoring and feedback on the overall process of catalyst development. Numerous techniques are employed for the characterization of both model and real solid catalysts at different levels (nanoscopic, microscopic and macroscopic) and at different stages of their design (i.e., during preparation, after functionalization, after chemical or thermal activation, during catalytic tests in order to probe surface reactivity and after catalytic tests). The main task of characterization is not merely to draw the "identity card" of a catalyst, by providing precious information concerning its structure, morphology, porosity, and chemical composition. An accurate characterization should be able to investigate also the surface reactivity so as to predict its catalytic behaviour and to identify the characteristics of the surface responsible for its reactivity.

According to a general scheme often proposed in the literature [113-a], almost all characterization techniques are based on the same approach: a probe system (photons, electrons, ions, neutrals, or magnetic, electric, acoustic, or thermal fields) hits the sample and interacts with it, giving rise to an emitted signal (photons, electrons, ions, neutrals, or magnetic, electric, acoustic, or thermal fields) which is then detected and elaborated. Various classification are possible depending on the nature of the probe system and the types of information gained, although it's worth specifying that these two aspects are strictly connected, since the nature of the probe determines the catalyst characteristic to be investigated.

Herein a rapid overview of most common characterization techniques will be presented, distinguishing between physical and chemical characterization.

7.1 Physical characterization

The physical characterization includes the determination of:

- *Morphology, particle size and dispersion*
  X-ray powder diffraction is a routine technique for the identification of crystalline phase by comparison with database. Using Sherrer equation it is also possible to estimate average crystallite size. Information on phase transitions, changes in compositions of bulk catalyst materials, on crystallinity and on the nature
  of surface functional groups can also be acquired through **vibrational spectroscopy** (including Transmission Infrared Spectroscopy FT-IRS, Diffuse Reflectance Infrared Fourier Transform Spectroscopy DRIFTS, Attenuated total reflection Infrared Spectroscopy ATR-FTIR and Raman Spectroscopy). Complementary structural information to XRD can be obtained by **Neutron Scattering**, a technique particularly sensitive to light elements (*e.g.* H or D) and very useful in defect determination.
  Using **electron microscopies** (SEM, TEM, HR-TEM, STEM) particle shapes and sizes of the support and active phase, their size distributions and lattice spacing can be determined.
- *Porosity and surface area*
- *Texture: pore structure of the particles* (pore size, pore size distribution, pore shape)

  Physisorption of probe gas molecules allows to measure indirectly the specific surface area, according to the Brunauer– Emmett – Teller (BET) method; the specific pore volume, pore widths, and pore-size distributions in the range of mesopores by

Kelvin equation (in the assumption of cylindrical shaped pores) and in the range of micropores, by theoretical (Dubinin – Radushkevich and the Dubinin – Stoeckli theories) and empirical (t-method and α_s-method) methods. Alternatively, **mercury pressure porosimetry** can be used to obtain pore size distribution in the case of meso- and macropores.

Temperature programmed desorption (TPD) is used to investigate the behaviour of the catalyst during calcination with an inert carrier gas and, in the case of metal oxides, the interaction of probe molecules (ammonia, pyridines) with acidic sites.

7.2 Chemical characterization

The chemical characterization concerns the characterization of a material in terms of its:

- *Bulk composition*

The distribution of elements in the catalyst can be obtained by elemental analysis and inductively coupled plasma atomic emission spectroscopy (**ICP-AES**). As an alternative, the determination of the elemental composition (for elements with atomic numbers Z > 11) of a solid catalyst at the microscopic level can be provided by energy dispersive detection of the electron-induced X-ray emission (**EDX spectroscopy**), often coupled to TEM analysis. For lighter elements (Z < 11), **electron energy loss spectroscopy (EELS)** is applied.

- *Surface analysis*
- <u>Surface crystallography</u>

  Electrons with low kinetic energies (in the range 2–200 eV) interact with the electrons of the solids, thus penetrating to a depth of only a few atomic layers. In the **Low-Energy Electron Diffraction (LEED)** diffraction effects observed when low-energy electrons with high cross sections hit solid surface, provide information about the spatial arrangement of the atoms in the surface region, and hence the periodic structure of the catalyst surface.

- <u>Surface composition and valence states</u>

  Ion Scattering Spectroscopy (ISS) the composition and structure of outer layers are investigated by ion bombardment: the elements present on the surface are identified by their mass, calculated from mechanical energy and impulse equations, by comparing the energy of the bombarding ions before and after the impact. Ion bombardment is used also in **Secondary Ion Mass Spectrometry (SIMS)**, where charged fragments (both positive and negative ions or clusters) are analysed and identified by mass spectrometry.

  In **Electron Spectroscopy for Chemical Analysis (ESCA)** or **X-ray Photoelectron Spectroscopy (XPS)** photoelectrons emitted by a sample exposed to X-ray radiation are collected and analysed according to their kinetic energy to determine the value of the binding energy. The latter varies as a function of the electron configuration, hence it allows to identify the element and its valence state. A similar principle is applied in **Auger Electron Spectroscopy (AES)**: surface is bombarded with high-energy (1–5 keV) electrons, causing the emission of photoelectrons from surface atoms and the subsequent relaxation by X-ray fluorescence or Auger electrons (electrons from valence shell). Measuring the kinetic energy of Auger electrons is possible to determine their binding energy. The advantage of Auger

spectroscopy is the possibility to obtain concentration profile, by moving electron beam across the surface.

- o Surface acidity/basicity

  Vibrational spectroscopic investigations are frequently applied technique for monitoring the adsorption of selected probe molecule. If the probe is a basic molecule, the detection and discrimination between Brønsted and Lewis acid sites is possible.

  The measure of differential heats of adsorption of probe molecules by **microcalorimetry** provide information on the acidic (or base) site strength and their distribution. Site densities and acid strength distributions can be determined also by **titration method**.

- o Redox Properties

  In Temperature-programmed reaction methods (**temperature-programmed reduction TPR** and **temperature-programmed oxidation TPO**) chemical reaction is monitored while the temperature is increased linearly in time. These experiments and their cyclic application are used to investigate redox behaviour of catalytic materials.

- o Surface coordination

  Extended X-ray absorption fine structure (EXAFS) is a particular type of X-ray Absorption Spectroscopy. In XAS the absorption of an X-ray photon results in the ejection of a photoelectron by a central atom. The outgoing photoelectron wave can be backscattered by neighbouring atoms. In EXAFS the analysis of the interference between a primary photoelectron wave and a backscattered one provides information on the nature and coordination of the central atom.

7.3 Characterization of catalyst under working conditions [114]

The characterization of a catalyst under working conditions represents together a challenge and a precious tool in the catalyst design. The study of a catalyst in the real conditions of its application involves the investigation of gas–solid and/or liquid–solid interfaces. The main hurdles derive from the fact that the characterization and reaction are performed in the same cell and then they experience the same environment (reactants, flow, temperature, pressure, concentration). Engineering an appropriate reactor-cell is important, but, above all, it's necessary to select a characterization technique or a combination of techniques as informative as possible and able to work effectively under reaction conditions and without perturbing the system at a molecular level.

This is in part possible using *in situ* and *operando* investigations, combining the analysis of geometric or electric structure of species at interface (adsorbates and active sites) with the simultaneous evaluation of the catalytic performances (determination of conversion and selectivity by online quantification of reactants and products). Although the terms *in situ* and *operando* are employed indiscriminately in the literature, there is a differentiation between these concepts, as pointed by Schoegl, who proposed the following definition: "*operando investigations identify the geometric or electronic structure of a catalyst under simultaneously documented production of the desired reaction product*".[4]

8 Computational chemistry in catalysis [115]

Atomistic modelling and simulation technologies aim to comprehend and to control the chemical and physical processes. Recently the optimization of pre-existing and the development of new computational methods, the increase of computer power and the enormous processing capacity offered by cluster machines make the calculations more reliable and then applicable in the field of heterogeneous catalysis.

As affirmed above, catalysis is a multiscale problem, therefore we need predictive modelling approaches able to describe real chemistry, valid over a broad range of conditions, and covering several orders of length and time scales.

The spectrum of information that can be explored by simulations is broad, ranging from the identification of the most likely reaction pathway to the calculation of the elementary kinetics, from the estimation of the influence of the local reaction environment to the prediction of changes in the particle size, shape, morphology, chemical composition and atomic configurations of active sites, and their effect on catalytic performances and lifetime.

From this point of view, the different approaches can be arranged in a hierarchy of models, reflecting the different levels of complexity, which they are applied to. A rough classification categorizes models into:

- Quantum-mechanical methods describe the electronic structure, thus allowing to calculate the intrinsic catalytic reactivity of bond-breaking and bond-making events
- Molecular simulations explore catalyst structure and morphology or reaction kinetics, by tracking the atomic structure

In **Density Functional Theory (DFT)**, based on the Hohenberg – Kohn theorem [116], all the properties of a system are determined by the electron density. Dynamics of reactions, activation barriers, adsorbed structures and frequencies can be investigated by DFT simulations, using three different approaches to mimic the actual reaction system studied.

The cluster algorithm (used by GAUSSIAN and TURBOMOLE softwares) is focused only on the local region about the active site, described by a discrete number of atoms. The small number of atoms (few hundred) that can be studied is not just a characteristic of this approach, but it is a limit as well. In the embedded cluster approach also the external structural and electronic environment around the primary cluster are simulated using much simpler quantum-mechanical treatment or an empirical force field. Longer range electrostatic interactions and the Madelung potential can be modelled, as well.
The "planar waves" or "periodic boundaries" algorithm is the base of periodic slab method (used in CASTEP, DACAPO, and VASP). In this approach a unit cell, which comprises a large enough surface, is initially defined and subsequently expanded by applying periodic boundary conditions. Calculations are then performed on structures periodic in three dimensions (supercell approach). The success of this approach strongly depends on the chosen functionals, the size of the cell and the convergence criteria.

Ab initio, quantum-chemical methods allow to explore only system with quite small size compared to the actual system. Larger system sizes can be examined by **Structural Monte Carlo (MC)** simulations, which treat just interatomic interactions without taking into the account the electronic structure. Potential parameters that are necessary for structural

simulations can be deduced either from experiment or from rigorous QM methods. Structure, adsorption/desorption, and, in some cases, even diffusion phenomena can be simulated by Statistical mechanical Monte Carlo. **Kinetic Monte Carlo (kMC)** simulations, on the other hand, follow elementary kinetic surface processes, by proceeding event by event, to describe the temporal changes in the atomic structure occurring over time or as a function of processing conditions. However, the computational effort and time required for this kind of studies are enormous.

Microkinetic modeling of catalytic reactions in technical systems can be performed using the **mean-field (MF) approximation**, a computationally efficient method based on a uniform distribution of adsorbates and catalyst sites. The local state of the catalytic surface is described by mean values by assuming randomly distributed adsorbates on an uniform surface. However, mean field is a poor approximation for inherently heterogeneous phenomena, where the configuration of the adsorbate structure and lateral interactions (neglected in MF approximation) play a crucial role.

The combination of DFT and microkinetic model allows for the rapid screening of materials based on computational tools.

References

[1]   M. Boudart in G. Ertl, H. Knözinger, J. Weitkamp (eds.): *Handbook of Heterogeneous Catalysis*, Wiley-VCH, Weinheim 1997, p. 1.

[2]   O. Deutschmann, H. Knözinger, K. Kochloefl, and T. Turek, *Heterogeneous Catalysis and Solid Catalysts, 1. Fundamentals. Ullmann's Encyclopedia of Industrial Chemistry*., 2011, Wiley-VCH Verlag GmbH & Co. KGaA, DOI: 10.1002/14356007.a05_313.pub3

[3]   J. Hagen, *Industrial Catalysis: A Practical Approach*, 2006 WILEY-VCH Verlag GmbH & Co. KGaA, ISBN-13: 978-3-527-31144-6

[4]   R. Schlögl, *Angew. Chem. Int. Ed.* 2015, 54, 3465 – 3520

[5]   R. A. van Santen, M. Neurock, *Molecular Heterogeneous Catalysis: A Conceptual and Computational Approach*, 2006 WILEY-VCH Verlag GmbH & Co. KGaA

[6]   a) G. Ertl, Adv. Catal. 37, 213 (1990); b) R. Imbihl, G. Ertl, Chem. Rev. 95, 697 (1995) 4.

[7]   P. Sabatier, J. B. Senderens, *C. R. Acad. Sci.* 134 (1902) 51

[8]   A. Ozaki and K. Aika, in J. Anderson and M. Boudart (eds.) *Catalysis* Vol. 1 (1981), Springer-Verlag, Berlin, p. 87

[9]   (a) J.N. Bronsted, *Chem. Rev.* 5, 231 (1928); (b) M.G. Evans, N. Polanyi, *Trans. Faraday Soc.* 32, 1333 (1936)

[10]   K.-I. Tanaka, K. Tamaru, *J. Catal.* 2, 366 (1963)

[11]   B. Hammer, J.K. Norskov, *Adv. Catal.* 45, 71 (2000)

[12]   D. G. Truhlar,; B. C Garrett,.; S. J. Klippenstein, *J. Phys. Chem*., 100, 31, (1996), 12771–12800. doi:10.1021/jp953748q

[13]   H.S. Taylor, *Proc. R. Soc. London* A 108 (1925) 105.

[14]   M. Boudart, *Journal of Molecular Catalysis A: Chemical* 120 (1997) 271-280

[15]   I. Langmuir, *Trans. Faraday Soc.* 17, 62 (1921)

[16]   A. Haghofer, K. Fottinger, F. Girgsdies, D. Teschner, A. Knop-Gericke, R. Schlçgl, G. Rupprechter, *J. Catal*. 2012, 286, 13 – 21

[17]   M. Boudart, *Journal of Molecular Catalysis*, 30 (1985) 27 - 38

[18]   R. A. van Santen, *Theoretical Heterogeneous Catalysis (World Scientific Lecture and Course Notes in Chemistry)*, World Scientific Pub Co Inc (1991), ISBN-13: 978-9810203849

[19]   J. F. Lepage, in G. Ertl, H. Knözinger, J. Weitkamp (eds.), *Preparation of Solid Catalysts*, WILEY-VCH Verlag GmbH (1999), 3-10, DOI: 10.1002/9783527619528.ch2

[20]   U. S. Ozkan, *Design of Heterogeneous Catalysts: New Approaches based on Synthesis, Characterization and Modeling*, 2009 WILEY-VCH Verlag GmbH & Co. KGaA, Weinheim

[21]   M. Hävecker, S. Wrabetz, J. Kröhnert, R. Naumann d'Alnoncourt, Y. V. Kolen'ko, F. Girgsdies, R. Schlögl, A. Trunschke, *J. Catal*. 2012, 285, 48 – 60.

[22]   M. Boudart, *Chem. Rev*. 1995, 95, 661-666

[23]   D. Murzin, *Engineering Catalysis*, De Gruyter. (2013), from http://www.degruyter.com/view/product/182241

[24]   J. Gascon, J. R. van Ommen, J. A. Moulijn and F. Kapteijn, Catal. Sci. Technol., 2015, 5, 807

[25]   S. P. S. Andrew, Chemical Engineering Science, Vol. 36. No. 9. pp. 1431-1445. 1981

[26]   Richard Haight, Frances M. Ross, James B. Hannon (eds.), *Handbook of Instrumentation and Techniques for Semiconductor Nanostructure Characterization*, World Scientific Pub Co Inc, 2012

[27]   R. J. D. Tilley, Defects in Solids, 2008 John Wiley & Sons, Inc., Print ISBN: 9780470077948, Online ISBN: 9780470380758, DOI: 10.1002/9780470380758

[28]   G. A. Somorjai, Y. Li, *Introduction to Surface Chemistry and Catalysis*, 2010, John Wiley & Sons, ISBN: 978-0-470-50823-7

[29]   K. W. Kolasinski, *Surface Science: Foundations of Catalysis and Nanoscience*, Third Edition, 2012 John Wiley & Sons, Ltd, Print ISBN: 9781119990352, Online ISBN: 9781119941798, DOI: 10.1002/9781119941798

[30]   K. Hermann, *Crystallography and Surface Structure: An Introduction for Surface Scientists and Nanoscientists,* 2011 Wiley-VCH Verlag GmbH & Co. KGaA, Print ISBN: 9783527410125, Online ISBN: 9783527633296, DOI: 10.1002/9783527633296

[31]   S. Storck, H. Bretinger, W. F. Maier, *Applied Catalysis A: General* 174 (1998) 137-146

[32]   G. Leofanti, M. Padovan, G. Tozzola, B. Venturelli, Catalysis Today 41 (1998) 207-219

[33]   H. Hattori, Chem. Rev. 1995, 95. 537-550

[34]   H. Hattori, Y. Ono, Solid Acid Catalysis: From Fundamentals to Applications, 2015, by Taylor & Francis Group, LLC, ISBN 978-981-4463-28-7 (Hardcover), 978-981-4463-29-4 (eBook)

[35]   K. Kobayashi, J.Ind.Eng.Chem., 4 891 (1912)

[36]   A. G. Oblad, in B.H. Davis, W. P. Hettinger, Jr. (eds.) Heterogeneous Catalysis, ACS Symp. Ser. 222, 61 (1983), ISBN13: 9780841207783, eISBN: 9780841210479, DOI: 10.1021/bk-1983-0222

[37]   K. Tanabe, W.F. Hölderich, *Applied Catalysis A: General* 181 (1999) 399-434

[38]   K.Tanabe, *Solid Acids and Bases: Their Catalytic Properties*, 2012, Elsevier, ISBN 0323160581

[39]   A. Zecchina, C. Lamberti, S. Bordiga, Catalysis Today, 41 (1998) 169-177

[40]   G. Busca, Phys. Chem. Chem. Phys., 1999, 1, 723-736

[41]   L. P. Hammett, A. J. Deyrup J. Am. Chem. Soc. vol. 54, nº 7, 1932, pp. 2721–2739, DOI:10.1021/ja01346a015

[42] P. Carniti, A. Gervasini, S. Biella, Ads. Sci. Technol. 23, 739 (2005)

[43] P. Carniti, A. Gervasini, M. Marzo, Catal. Today 152, 42 (2010)

[44] M. Schulz, V. Shanov, Z. Yin (eds*.), Nanotube Superfiber Materials: Changing Engineering Design - Micro and Nano Technologies series*, 2013, Elsevier Inc. (William Andrew Editor), ISBN   1455778648, 9781455778645

[45] X. Sheng, J. Gao, L. Han, Y. Jia, W. Sheng, *Micropor. Mesopor. Mater.*, 143, 73 (2011).

[46] A, Taguchi, F. Schüth, *Micropor. Mesopor. Mater.*, 77, 1 (2005).

[47] A. Corma, M. T. Navarro, L. Nemeth, M. Renz, *Chem. Commun.*, 2190 (2001).

[48] C. Moreno-Castilla, M. A. Ferro-Garcia, J. P. Joly, I. Bautista-Toledo, F. Carrasco-Marin, J. Rivera-Utrilla, *Langmuir* 1996,11, 4386-4392

[49] A. Hirsch, *Angew. Chem. Int. Ed*. 2002, 41, No. 11

[50] C. E. Chan-Thaw, A. Villa, G. M. Veith, L. Prati, *ChemCatChem* 2015, 7, 1338 – 1346

[51] a) D.A.Dowden, J.Chem.Soc. (1950) 242; b) D.A.Dowden, Ind.Eng.Chem. 44 (1952) 977; c) D.A.Dowden, P.W.Reynolds, Disc.Faraday Soc. 8 (1950) 184

[52] a) J. K. Nørskov, F. Abild-Pedersen, F. Studt F and T. Bligaard, Proc. Natl. Acad. Sci. USA, 2011, 108, 937–943; b) B. Hammer and J. K. Nørskov, Adv. Catal., 2000, 45, 71–129. c) B. Hammer and J. K. Nørskov, Surf. Sci., 1995, 343, 211–220.

[53] M. Chen, D. W. Goodman, *Acc. Chem. Res*., 2006, 39, 739-746

[54] E. Roduner, *Chem. Soc. Rev*., 2006, 35, 583–592

[55] M. Valden, X. Lai, D.W. Goodman, *Science* 281, 1647 (1998)

[56] G.C Bond, C. Louis, D.T. Thompson, Catalysis by Gold, Imperial College Press, London, 2006

[57] T. Takei, T. Akita, I. Nakamura, T. Fujitani, M. Okumura, K. Okazaki, J. Huang, T. Ishida, M. Haruta Advances in Catalysis, 55, B.C. Gates, F.C. Jentoft ed., Elsevier, Chapter 1, 1-124 (2012)

[58] M. Haruta, T. Kobayashi, H. Sano and N. Yamada, Chem. Lett., 4 (1987) 405

[59] G.J. Hutchings, J. Catal., 96 (1985) 292.

[60] B. Nkosi, N.J. Coville, G.J. Hutchings, Appl. Catal. 43 (1988), 33-39

[61] a) G.C. Bond, D.T. Thompson, Catal. Rev. Sci. Eng., 41, 1999, 319; b) M. Boronat, P. Concepcion, A. Corma, J. Phys. Chem. , 113, 2009, 16772; c) R. Coquet, K.L. Howard, D.J. Willock, Chem. Soc. Rev., 37, 2008, 2046; d) C. Louis, in D. Astruc (ed.), Nanoparticles and Catalysis, Wiley-VCH, Weinheim, 2007, p. 475

[62] G.C. Bond in C. Louis, O. Pluchery (eds.) Gold Nanoparticles for Physics, Chemistry and Biology, Imperial College Press, London, 2012, Chapter 7, p. 175

[63] [63] a) M. Chen, D.W. Goodman, Chem. Soc. Rev., 37, 2008, 1860; b) A.A. Herzing, C.J. Kiely, A.F. Carley, P. Landon, G.J. Hutchings, J. Mater. Chem., 19, 2009, 1; c) G. C. Bond, Gold Bull., 43, 2010, 88; d) G. C. Bond, Faraday Discuss., 152, 2011, 277

[64] D. Andreeva, Gold Bull., 35 (3), 2002, pp 82-88

[65] O.H. Laguna, F. Romero Sarria, M.A. Centeno, J.A. Odriozola, J. Catal, 276 (2), 2010,360-370

[66] T. Hayashi, K. Tanaka, M. Haruta, J. Catal. 1998, 178, 566 – 575.

[67] L. Prati, M. Rossi, J. Catal. 1998, 176, 552 – 560.

[68] a) A. Corma, S. Iborra , and A. Velty, Chem. Rev., 2007, 107 (6), pp 2411–2502; b) E. Taarning, I. S. Nielsen, K. Egeblad, R. Madsen, C. H. Christensen, ChemSusChem, 1 (1-2), 2008, p. 75–78; c) D. M. Alonso,   J. Q. Bonda, J. A. Dumesic, Green Chem., 2010,12, 1493-1513; d) P. Gallezot, Chem. Soc. Rev., 2012,41, 1538-1558; e) A. Villa, N. Dimitratos, C.E. Chan-Thaw, C.Hammond, L. Prati, G.J. Hutchings, Acc Chem Res. 2015; 48(5), 1403-12

[69] M. Sankar, N. Dimitratos, P. J. Miedziak, P. P. Wells, C. J. Kielye, G. J. Hutchings, Chem. Soc. Rev., 2012, 41, 8099–8139

[70] A. Villa, D. Wang, D. Sheng Su, L. Prati, Catal. Sci. Technol., 2015, 5, 55

[71] J. H. Sinfelt, Bimetallic Catalysts: Discoveries, Concepts and Applications, Wiley-Interscience, 1st edn, 1983.

[72] a) G. M. Schwah, Discuss. Faraday Soc., 8, 166 (1950); b) D. A. Dowden, J. Chem. Soc., 242 (1950); c) D. A. Dowden and P. Reynolds, Discuss. Faraday SOC.8, ,184 (1950); d) W. K. Hall and P. H. Emmett, J. Phys. Chem., 62, 816 (1958); e) W. K. Hall and P. H. Emmett, J. Phys. Chem., 63, 1102 (1959).

[73] a) J. H. Sinfelt, J. L. Carter and D. J. C. Yates, J. Catal., 1972, 24, 283–296; b) J. H. Sinfelt, J. Catal., 1973, 29, 308–315; c) J. L. Carter, G. B. McVinker, W. Weissman, M. S. Kmak, J. H. Sinfelt, Appl. Catal., 1982, 3, 327–346.

[74] (a) N. Dimitratos, J. A. Lopez-Sanchez and G. J. Hutchings, Chem. Sci., 2012, 3, 20; (b) S. E. Davis, M. S. Ide and R. J. Davis, Green Chem., 2013, 15, 17.

[75] J. Schwank, Gold Bull, 1985, 18, (1)

[76] J.B. Darby, Acta Met., 1966, 14, 265

[77] a) R.E Vines, 'The Platinum Metals and their Alloys', The International Nickel Company, Inc., New York, 1941 b) M. Hanen and K. Anderko, 'Constitution of Binary Alloys , 2nded., McGraw Hill, New York, 1958

[78] A.A. Rudnitskii and O.A. Novikova, Russ. J. Inorg. Chem., 1959, 4, 722

[79] a) J. Schwank, G. Parravano, H.L. Gruber,J Catal., 1980, 61, 19-28, b) S. Galvagno, J. Schwank and G. Parravano,J. Catal., 1980, 61, 223-231; c) W. Bassi, E Garbassi, G. Vlaic, A. Marzi, G.R. Tauszik, G. Cocco, S. Galvagno, G. Parravano,J. Catal., 1980, 64, 405-416; d) G.R. Tauszik, E Garbassi and A. Marzi, Gazz. Chim. Ital., 1980,110, 443.448

[80] R. Ferrando, J. Jellinek and R. L. Johnston, Chem. Rev., 2008, 108, 845–910.

[81] (a) C. George, A. Genovese, A. Casu, M. Prato, M. Povia, L. Manna and T. Montanari, Nano Lett., 2013, 13, 752; (b) J. Xu, T. White, P. Li, C. He, J. Yu, W. Yuan and Y.-F. Han, J. Am. Chem. Soc., 2010, 132, 10398.

[82] J. K. Edwards, S. J. Freakley, A. F. Carley, C. J. Kiely, G. J. Hutchings, Acc. Chem. Res., 2014, 47, 845.

[83] L. Kesavan, R. Tiruvalam, M. H. A. Rahim, M. I. bin Saiman, D. I. Enache, R. L. Jenkins, N. Dimitratos, J. A. Lopez-Sanchez, S. H. Taylor, D. W. Knight, C. J. Kiely and G. J. Hutchings, Science, 2011, 331, 195.

[84] (a) N. Dimitratos, A. Villa, D. Wang, F. Porta, D. Su, L. Prati, J. Catal., 2006, 244, 113; (b) D. I. Enache, J. K. Edwards, P. Landon, B. Solsona-Espriu, A. F. Carley, A. A. Herzing, M. Watanabe, C. J. Kiely, D. W. Knight, G. J. Hutchings, Science, 2006, 311, 362.

[85] (a) D. Martin Alonso, S. G. Wettsteina and J. A. Dumesic, Chem. Soc. Rev., 2012, 41, 8075; (b) H. Zhanga, N. Toshima, Catal. Sci. Technol., 2013, 3, 268.

[86] N. Maeda, K. Hungerbühler, A. Baiker, J. Am. Chem. Soc., 2011, 133 (49), pp 19567–19569, DOI: 10.1021/ja2054918

[87] J. L. Callahan, R. K. Grasselli, AIChE J. 9 (1963) 755

[88] IUPAC. Compendium of Chemical Terminology, 2nd ed. (the "Gold Book"). Compiled by A. D. McNaught and A. Wilkinson. Blackwell Scientific Publications, Oxford (1997). XML on-line corrected version: http://goldbook.iupac.org (2006-) created by M. Nic, J. Jirat, B. Kosata; updates compiled by A. Jenkins. ISBN 0-9678550-9-8. doi:10.1351/goldbook.

[89] A.R. West, Solid State Chemistry and Its Applications: Student Edition, 2nd Edition, 2014, Wiley.

[90] a) F.Rodriguez-Reinoso, Carbon Vol. 36, No. 3, pp. 159-175,1998; b) P. Serp, B. Machado, Nanostructured Carbon Materials for Catalysis, RSC Catalysis Series (Book 23), 2015

[91] P. Serp, J. L. Figueiredo, Carbon Materials for Catalysis, John Wiley & Sons, 2009

[92] P. Serp, E. Castillejos, ChemCatChem 2010, 2, 41–47

[93] X. Pan, X. Bao, Accounts Of Chemical Research Vol. 44, No. 8, 2011, 553–562

[94] K. P. De Jong, J. W. Geus, "Carbon nanofibers: catalytic synthesis and applications." Catalysis Reviews 42.4 (2000): 481-510.

[95] a) G.C. Bond in B. Imelik et al. (Eds), Metal-Support and Metal-Additive Effects in Catalysis,1982, Elsevier Scientific Publishing Company, Amsterdam; b) J. H. Sinfelt in G. Ertl, H.Knøzinger, J.Weitkamp (eds.): Handbook of Heterogeneous Catalysis, Vol. 4, Wiley-VCH, Weinheim 1997, p. 1939.

[96] a) G.C. Bond and J. Turkevich, Trans. Faraday SOC., 49 (1953) 281; b) D. Briggs, J. Dewing, A.G. Burden, R.B. Moyes and P.B. Wells, J. Catal., 65 (1980) 31. c) J .H. Sinfelt , Catal. Reviews, 3 (1970) 175. d) G.-M. Schwab, Adv. Catal., 27 (1978) 1; e) F. Solymosi, Catal. Reviews, 1 (1967) 233.

[97] S. J.Tauster, S.C. Fung., R.L. Garten, J. Am. Chem. SOC. 1978, 100, 170.

[98] D.A. Dowden, Specialist Periodical Reports, Catalysis , 3 (1980) 136.

[99] G.C. Bond and P.A. Sermon, J. Chem. SOC. Farad. Trans. I, 76 (1980) 889.

[100] L.M. Molina, B. Hammer, Phys. Rev. Lett. 90, 206102 (2003)

[101] M. Mavrikakis, P. Stoltze, J.K. Nørskov Catal. Lett. 64, 101 (2000)

[102] Q. Fu, H. Saltsburg, M. Flytrani-Stephanopoulos, Science 301, 935 (2003)

[103] B.C. Gates and J. Guzmann, Angew. Chem. Int. Ed., 42 (2003) 690.

[104] a)H. Hakkinen, S. Abbet, A. Sanchez, U. Heiz, U. Landman, Angew. Chem. Int. Ed., 42, 1297 (2003) 74. b) I.D. Socaciu, J. Hagen, T.M. Bernhardt,L. Woste, U. Heiz, H. Hakkinen, U. Landman, J. Am. Chem. Soc. 125, 10437 (2003), 75. c) A. Sanchez, S. Abbel, U. Heiz, W.D. Schneider, H. H¨akinnen, R.N. Barnett, U. Landman, J. Phys. Chem. A, 103, 9573 (1999); d) G. Pacchioni, L.Giordano, M. Baistrocchi, Phys. Rev. Lett. 94, 226104 (2005)

[105] a) A. Bruix, J. A. Rodriguez, P. J. Ramírez, S. D. Senanayake, J. Evans, J. B. Park, D. Stacchiola, P. Liu, J. Hrbek, F. Illas, J. Am. Chem. Soc. 2012, 134, 8968−8974; b) M. G. Willinger, W. Zhang, O. Bondarchuk, S. Shaikhutdinov, H-J. Freund, R. Schlögl, Angew. Chem. Int. Ed. 2014, 53, 5998 –6001; c) J. Carrasco, D. López-Durán, Z. Liu, T. Duchoň, J. Evans, S. D. Senanayake, E. J. Crumlin, V. Matolìn, J. A. Rodrìguez, M. V. Ganduglia-Pirovano, Angew. Chem. Int. Ed. 2015, 54, 3917 –3921, d) L. Liu, C. Ge, W. Zou, X. Gu, F. Gao, L. Dong, Phys.Chem.Chem.Phys., 2015, 17, 5133

[106] J. Haber, J. H. Block, B. Delmon, Pure & Appl. Chem., Vol. 67, Nos 8/9, pp. 1257-1306, 1995.

[107] J. Regalbuto, *Catalyst Preparation: Science and Engineering*, CRC Press, 2006.

[108] J. T. Richardson, Principles of Catalyst Development, Plenum Press, New York, 1989, p. 134.

[109] a) L.A. Hermans and J.W. Geus, Stud. Surf. Sci. Catal., 4, 1979, 113; b) K. P. de Jong, J. W. Geus, Appl. Catal. , 4, 1982 , 41; c) S.Tsubota, D.A.H. Cunningham, Y. Bando and M.Haruta, Stud. Surf. Sci. Catal. 91, 1995, 227; d) R.Zanella, S. Giorgio, C.R. Henry and C. Louis, J. Phys. Chem. B, 106, 2002, 7634.

[110] S. Barcikowski, G. Compagnini, Phys.Chem.Chem.Phys., 2013, 15, 3022—3026

[111] H. Nalwa, Handbook of Thin Films, Five-Volume Set, Vol. 1 Deposition and Processing, 2001, Academic Press, pp. 417-420

[112] a) L. Prati, G. Martra, Gold Bull. 1999, 32, 96–101; b) D.G Duff, A. Baiker, P.P. Edwards, J. Chem. Soc. Chem. Commun. 1993, 96–98; c) L. Prati, A. Villa, Catalysts 2012, 2, 24-37.

[113] a) M. Che, J. C. Védrine, Characterization of Solid Materials and Heterogeneous Catalysts From Structure to Surface Reactivity, Volume I, 2012 Wiley-VCH Verlag & Co. KGaA, ePub ISBN: 978-3-527-64533-6; b)

[114] Rodríguez, J. A., Hanson, J. C., & Chupas, P. J. (Eds.). (2013). In-situ characterization of heterogeneous catalysts. John Wiley & Sons.

[115] a) Nørskov, Jens Kehlet, et al. "Towards the computational design of solid catalysts." Nature chemistry 1.1 (2009): 37-46; b) Senkan, Selim. "Combinatorial heterogeneous catalysis—a new path in an old field." Angewandte Chemie International Edition 40.2 (2001): 312-329; c) Thiel, Walter. "Computational Catalysis—Past, Present, and Future." Angewandte Chemie International Edition 53.33 (2014): 8605-8613.

Part II

Results and Discussion

1 *Aim of the work*

The main goal of my Ph.D. project has been the development of novel approaches for the optimisation of supported noble metal nanoparticles, which are well-established catalysts for liquid phase oxidation reactions.

The partial oxidation of oxygen-containing compounds (alcohols, aldehydes, carbohydrates) is a profitable process, the corresponding products (aldehydes, ketones, epoxides, carboxylic acids, esters and lactones) being key intermediates in the synthesis of fine chemicals and commodity. In the perspective of biomass valorisation these processes are recently assuming an increasing relevance. Indeed, many biomass-derived platform molecules contain oxidizable functional groups and therefore can be easily converted in value-added compounds by oxidation.

The oxidation of organic compounds can be carried out in the gas phase through continuous-flow reactors using air or oxygen as oxidant. Nevertheless, these processes require high temperatures and their application is restricted to volatile and thermally stable reactants and products. From this point of view working in the liquid phase seems to be more suitable for energy saving, since milder conditions can be adopted, compared to gas phase. The main drawback of the current industrial technologies for liquid phase oxidation processes is the use of stoichiometric inorganic oxidants, such as dichromate and permanganate, which are toxic and corrosive. The employment of these reactants therefore entails environmental issues (production of high volumes of toxic wastes), handling difficulties and reactor maintenance problems (corrosion, plating out on reactor walls). According to green chemistry principles, the replacement of toxic stoichiometric processes with catalytic and environmentally benign routes is then heartily recommended.[15]

Noble metal unsupported and supported nanoparticles have been extensively explored as heterogeneous catalysts for the liquid phase oxidation of oxygen-containing organic compounds in the presence of molecular oxygen, air or hydrogen peroxide as sole oxidants.

In particular platinum group metals (Pt, Pd, Ru, Rh) have shown to be able to oxidize alcohols to the corresponding carbonyl or carboxylic compounds under mild conditions (close to ambient conditions)[16]. However, these systems rapidly undergo deactivation by over-oxidation or metal dissolution into solution (leaching). Otherwise, nano-sized gold exhibits a remarkable activity and it possesses unexpected advantages over platinum group metals in terms of selectivity control and resistance to deactivation. The strongest limitation in using gold NPs as catalysts is the compulsory use of a basic environment[17]. Recent studies showed that alloying gold with a second metal (platinum or palladium) is possible to obtain

[15] R. A. Sheldon, I. Arends, U. Hanefeld, *Green Chemistry and Catalysis*, Ch. 4, John Wiley & Sons, 2007 ISBN 352730715X.

[16] a) M. Besson, P. Gallezot, *Catal. Today* 2000, 57, 127– 141; b) T. Mallat, A. Baiker*, Chem. Rev*. 2004, 104, 3037– 3058; c) N. Dimitratos, J. A. Lopez-Sanchez, G. J. Hutchings, *Chem. Sci.* 2012, 3, 20–44; d) S. E. Davis, M. S. Ide, R. J. Davis, *Green Chem.* 2013, 15, 17–45.

[17] T. Takei, T. Akita, I. Nakamura, T. Fujitani, M. Okumura, K. Okazaki, J. Huang, T. Ishida, M. Haruta *Advances in Catalysis*, 55, B.C. Gates, F.C. Jentoft ed., Elsevier, Chapter 1, 1-124 (2012)

effective catalytic systems in terms of activity, durability and selectivity even in the absence of a base.[18] Besides the use of bi- or multimetallic systems (e.g. AuPt or AuPd), the catalytic performances are strongly affected by many factors, including the addition of promoters (e.g. Bi), the influence of support and the preparation route. A simultaneous fine tuning of all these parameters is not a straightforward task, therefore the design of catalysts is a still challenging research target. A multidisciplinary approach seems to be the better strategy for facing this challenge. In this view, the development of a catalyst should be the result of the combination of three main aspects (preparation, characterization, testing), which can be investigated on different levels (from atomic to macroscopic level) and with several tools (from *in situ* characterization to computational modelling).

During my Ph.D. project a similar approach has been adopted. In the first section (Chapter 2) my research focused on the possible strategies for tuning the selectivity in base-free glycerol oxidation, a reaction of industrial interest, which has attracted significant attention in the last decades, due to the need for the valorisation of this bio-platform molecule. The reaction pathway of glycerol oxidation is complex and leads to a large number of valuable organic compounds (glyceric acid, tartronic acid, dihydroxyacetone, lactic acid, etc.). Therefore directing the reaction to the desired target product represents a key-point. Two main features were investigated in the detail: the role of support and the addition of promoters.

It has been observed that the support greatly affected the selectivity of AuPt based catalysts in base-free glycerol oxidation. In particular, using an acidic support, H-Mordenite, an enhancement in the selectivity to C3 products (glyceric and tartronic acid) has been obtained.[4a] Also basic supports such as hydroxyapatite and MgO have been shown to be useful supports.[4b] In order to investigate more in the detail the effect of support acidity, I extended these studies to a series of supports with different acid-base properties, namely H-Mordenite, SiO_2, MCM-41, sulfated ZrO_2, Activated Carbon (AC X40S) as representative of acidic supports, and MgO and NiO as references for basic supports. Acidic surface properties of these materials have been full characterised by means of Infrared Spectroscopy and microcalorimetry, and their influence on the catalytic behaviour of alloyed AuPt nanoparticles was highlighted. An high selectivity to C3 compounds was observed, using acidic supports, glyceric acid and glyceraldehyde being the main products. Both these compounds are obtained by the oxidation of the primary hydroxyl function, on the other hand the main product of secondary hydroxyl group oxidation, dihydroxyacetone (DHA), is economically the most interesting oxidation product due to its use as tanning agent in cosmetic industries. In the literature it has been reported that the addition of Bi as promoter for Pt catalysts enhances the yield of DHA.[19] On the other hand Bi-Pt catalysts suffer from heavy deactivation during reaction, due to the leaching of metals.

On the basis of these considerations, we decided to modify AuPt and AuPd alloyed catalysts with Bi to investigate the effect of the addiction of this promoter, not only in terms of selectivity to DHA, but also for the durability of the catalyst.

In the second part (Chapter 3) Operando Attenuated Total Reflectance Infrared (ATR-IR) spectroscopy[20] and catalytic batch reactor experiments were performed in parallel to elucidate the different catalytic performance of Au, Pd, and AuPd supported on TiO_2 and Al_2O_3 in the liquid-phase oxidation of benzyl alcohol. In particular the development of

[18] a) A. Villa, G.M. Veith and L. Prati, *Angew. Chem. Int. Ed*. 49 (2010) 4499-4502; (b) G. L. Brett, Q. He, C. Hammond, P. J. Miedziak, N. Dimitratos, M. Sankar, A. A. Herzing, M. Conte, J. A. Lopez-Sanchez, C. J. Kiely, D. W. Knight, S. H. Taylor, and G. J. Hutchings, *Angew. Chem. Int. Ed*. 50 (2010) 10136

[19] H. Kimura and K. Tsuto, *Appl. Catal. A: General* 96 (1993) 217

[20] B. M. Weckhuysen, Phys. Chem. Chem. Phys., 2003,5, 4351-4360

different surface species and the role of the protective agent (polyvinyl alcohol, PVA) in catalysts prepared by a sol immobilization route were examined.

Finally, in the last part of the thesis (Chapter 4) a periodic Density Functional Theory (DFT) study of the adsorption and activation of ethanol on different surfaces (13 atom Au cluster, oxygenated 13 atom Au cluster, TiO_2 rutile surface and Au ribbon on TiO_2 surface) is proposed, in order to unravel the presence of preferential sites for the adsorption of alcohol on catalyst surfaces. Simulations were carried out using the plane wave basis set code VASP and the Perdew, Burke and Ernzerhof (PBE) functional.[21]

---

[21] A.R. Leach, *Molecular Modeling: Principles and Applications*, Pearson Education, Harlow (1996)

2 *Tuning the selectivity in glycerol oxidation*

2.1 Industrial relevance of glycerol

To date, transportation fuels and bulk chemicals have been manufactured principally from finite fossil resources. The gradual depletion of the latter and the global environmental problems associated to petrochemical industries have given strong impetus to academic and industrial research for developing alternative energy carriers. Renewable raw materials, like biomass or biomass-derived compounds, represent an attractive alternative. Consequently, the bio-refinery concept experienced a dramatic growth in the last decades and substances, such as bioethanol, bio-diesel (Fatty Acid Methyl Esters, FAMEs), hydrotreated vegetable oils (HVO), renewable diesel fuels, and biogas have become ever more widespread as possible substitutes for gasoline, diesel and natural gas, respectively. Starch, triglycerides, and lignocellulose represent the main families of biomass-derived feedstock. Specifically, triglycerides from waste frying oils, waste animal fats and from non-edible vegetable oils are renewable raw materials non-competitive with the agri-food production and find application in many industrial processes for the production of soaps, fuel additives and biofuels. In all these processes glycerol is generated as an unavoidable co-product.[1] The biodiesel manufacturing is experiencing a gradual decrease (-10% in Europe in 2011 compared to 2011)[2], but it is still nowadays the first source of glycerol. Fat hydrolysis, now the second, is forecast to increase.

The overall economy of a process reaches an optimum, when secondary products are valorised and fruitfully exploited. In the specific case of triglycerides, an unused surplus of the crude glycerol fraction would result in serious problems of storage and, above all, in a dramatic rise of the cost.

Currently a broad spectrum of traditional uses of glycerol (more than 1500) is known, as reported in many reviews on this topic.[3] Glycerol finds application in the production of food additives, sweeteners, humectant, pharmaceuticals, cosmetics and other various industrial applications, such as the synthesis of polyethers, polyols and alkyl resins, or the production of antifreezes, plasticizers, explosives, solvents, detergents, cellophane, triacetin, tobacco.[4] However, the increasing supply of glycerol exceeds the demand for it in this traditional market. For this reason, the valorisation of cheap glycerol represents a relevant research target. Fortunately, the presence of three hydroxyl groups makes glycerol a highly versatile molecule and a potential starting material that can be easily transformed in numerous value-added products.

Figure 2.1 Market shares for glycerol demand in traditional industrial applications (From Ref. [4-e])
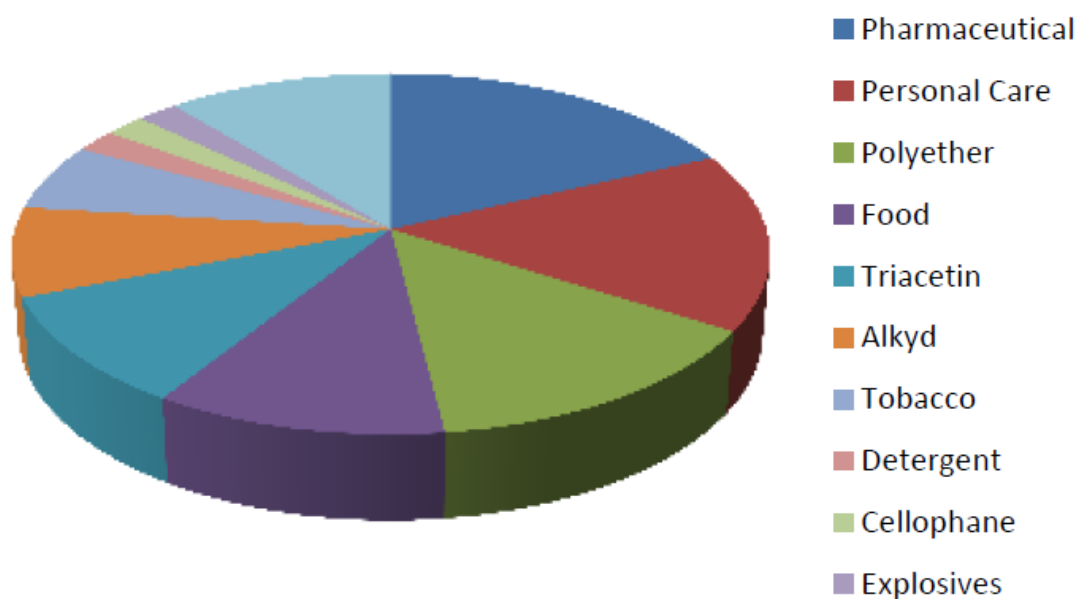
2.1.1 Glycerol valorisation: challenges and possibilities in the perspective of integrated bio-refineries [4]

Due to its highly functionalized nature, glycerol can undergo several transformations. A large amount of valuable derivatives, such as fuels, fuel additives, fine chemicals, and polymers, can be obtained from the catalytic conversion of glycerol. Indeed, in the last decades new catalytic routes have been proposed for the chemo-catalytic conversion of glycerol to fuels and chemicals, using a wide range of reactions. The main processes are summarized below.

Figure 2.2 Possible routes for glycerol valorization (From Ref. [4-c])
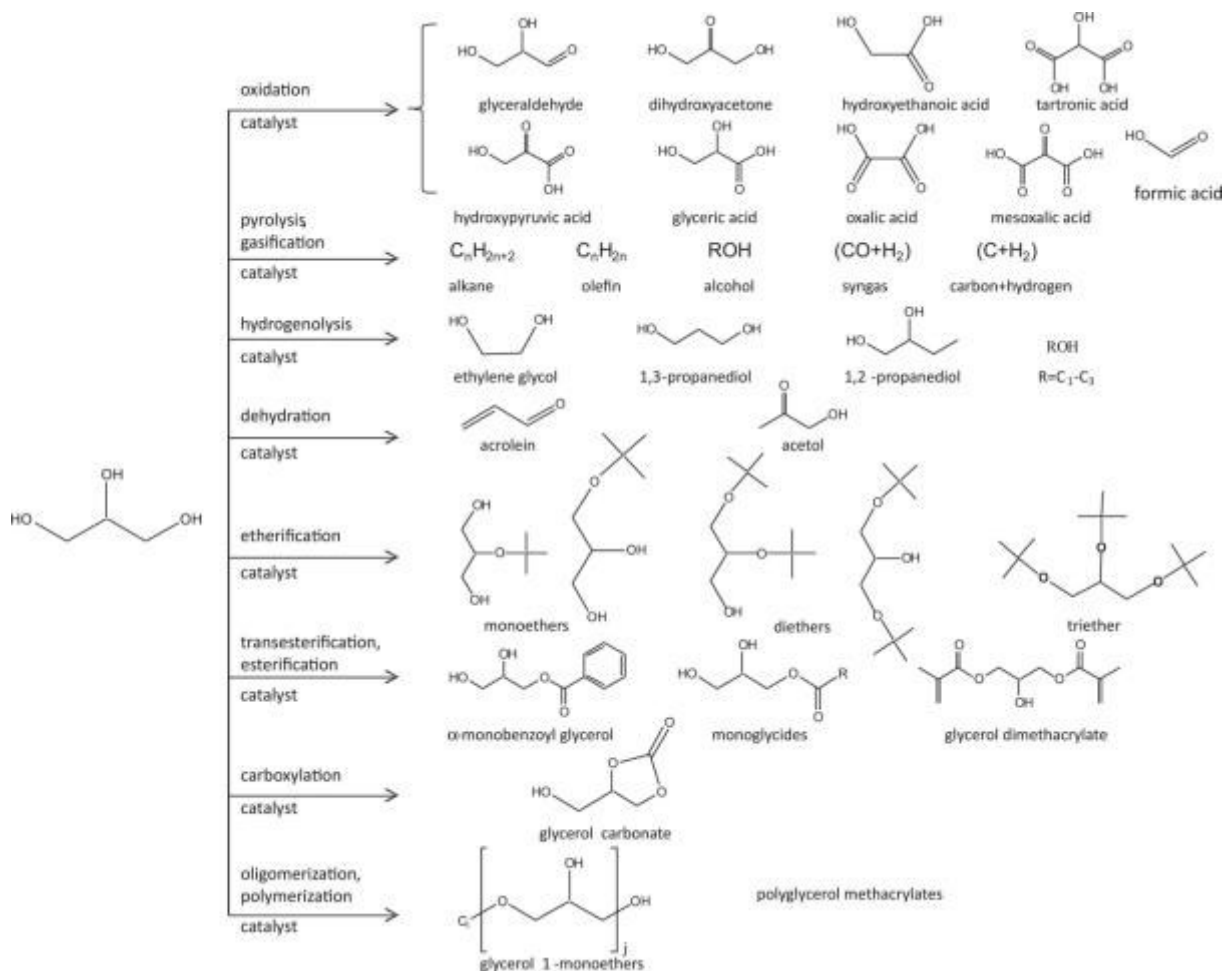
- <u>Catalytic reforming</u>: the production of **hydrogen** or **syngas** from glycerol can be achieved by reforming with water in gas (steam reforming) or liquid (aqueous phase reforming, APR) phase. In both cases supported Pt, Rh, Ru, Ir, Ni and Co are active catalysts [5], although in aqueous phase the catalytic behaviour is quite different and the hydrothermal stability of metal species plays a key role. Pt-based catalysts are the most stable systems in these conditions. Anyhow, due to the huge amount of by-products and to the lower number of hydrogen atoms in glycerol molecule, at the current state reforming of glycerol is not economically competitive with hydrocarbon reforming.
- <u>Catalytic hydrogenolysis</u>: the term hydrogenolysis refers to the selective cleavage of C – O single bond by hydrogen. Depending on which alcohol function (primary or secondary) is involved, either **1,2-propanediol** or **1,3-propanediol** can be obtained by glycerol hydrogenolysis. According to the literature, hydrogenolysis occurs following a

dehydration-hydrogenation mechanism, catalysed either by acid or alkaline or bifunctional catalysts. Supported Pt, Ru, Rh, Ni and Cu catalysts are selective to 1,2-propanediol, whereas $Pt/WO_3/TiO_2/SiO_2$, Pt-Re/C, $Ir-ReO_x/SiO_2$, $Cu/H_4SiW_{12}O_{40}/SiO_2$, and $Cu/ZnO/TiO_2$, showed a remarkable selectivity to 1,3-propanediol.[6]

- Catalytic dehydration: **acrolein**, an important intermediate in pharmaceutical, food and polymer industries, is currently produced by the gas-phase catalytic oxidation of propylene with atmospheric oxygen. As an alternative route, acrolein can be obtained by glycerol dehydration.[7] Compared to liquid phase processes, carried out in the presence of liquid acids and under supercritical conditions, the gas-phase glycerol dehydration catalysed by solid acids presents great advantages in terms of catalyst separation and reuse. Acidic oxides, zeolites, heteropolyacids, mixed metal oxides and (oxo)-pyrophosphates have shown to be promising catalysts for glycerol dehydration, even if they suffer from quick deactivation due to carbon deposit.[7] The introduction of water or molecular oxygen in the reactor has been proposed as solution. In particular the addition of oxygen in the dehydration system opened the way to the production of **acrylic acid** by the oxydehydration reaction of glycerol. Interesting results have been obtained using vanadium phosphate oxide catalysts, pyrophosphate oxides catalysts, molybdenum vanadium-based catalysts and tungsten vanadium based catalyst.[8]

- Catalytic ammoxidation: another widely employed monomer, **acrylonitrile**, can also be obtained from glycerol by one-pot ammoxidation, a two-step process, involving a dehydration reaction of glycerol followed by a sequential cyanation reaction. Significant results have been gained, using $V-Sb-O/Al_2O_3$ or $V-Sb-Nb/Al_2O_3$ as catalysts.[9]

- Catalytic oxidation: the selective oxidation of glycerol proceeds with a complex reaction pathway yielding different C3 products. Catalytic oxidation of glycerol will be discussed more in the detail in the next section.

- Catalytic esterification: solid materials with basic (MgO, CeO_2, La_2O_3, ZnO, Al-Mg hydrotalcites, Cs-exchanged sepiolite, and base-modified mesoporous MCM-41) or acidic (acid exchange resin Amberlyst-15®, K-10 montmorillonite, niobic acid, HZSM-5, and HUSY) character have been successfully tested as catalysts for glycerol esterification in order to produce to produce raw materials for biodegradable polyesters and fuel additives (e.g. esters of glycerol with acetic acid).[10]

- Catalytic etherification: several valuable compounds can be obtained by catalytic etherification of glycerol. Oligomerisation of glycerol is an etherification reaction leading to the formation of polyglycerols, in particular di- and triglycerols, employed in the cosmetic industries. For this reaction both homogenous ($CsHCO_3$) and heterogeneous (MgO, CaO, SrO, BaO and alkaline species supported on porous solids) alkaline catalysts have been used with good results. [11] The main challenge for this process is to achieve an high yield of a specific isomer (size- and shape selectivity of porous systems can be a solution).

  Unlike polyglycerols, alkylglycerols are produced in the presence of acidic catalysts (Amberlyst resin, p-toluenesulfonic acid, zeolites H-Y and H-Beta, silicotungstic acid, cesium salt of silicotungstic acid, ionic liquid containing sulfonic acid groups, sulfonic-acid-functionalized mesostructured silicas, and carbon-based solid acid catalysts).[12] Alkylglycerols with a short-chain alkylic groups (C1-C6), such as t-butylglycerols or ethylglycerols, are useful fuel additives. Long chain monoalkylglycerols, because of their hydrophilic-lipophylic balance, are used in formulations for cosmetic and in pharmaceuticals and biomaterials.

- <u>Catalytic acetalization</u>: the nucleophilic addition of glycerol to an aldehyde (benzaldehyde, formaldehyde, furfural) or a ketone (acetone) yields acetals and ketals, which are extensively used as fuel additives to improve the antifreeze properties and the viscosity. Supported metal oxides, zeolite and organometallic complex have been investigated as catalysts for this kind of reactions. [13]
- <u>Catalytic carboxylation</u>: glycerol carbonate is the common name for 4-hydroxymethyl-2-oxo-1,3-dioxolane, an important platform molecule for surfactants, pharmaceuticals, and polymers, such as polycarbonates, polyglycerol esters, hyper-branched polyols, and non-isocyanate polyurethanes. Due to the industrial relevance of glycerol carbonate, glycerol carboxylation is one of the most attractive glycerol transformation. Glycerol carbonate can be produced starting from glycerol by different routes:

  (A) the reaction of glycerol with phosgene: the less suitable route, due to the toxicity of phosgene; [14]

  (B) the transesterification of dialkyl carbonates: in particular the transesterification of dimethyl carbonate with glycerol, catalysed by CaO, Mg/Al/Zr mixed oxide or KF modified hydroxyapatite catalysts; [15]

  (C) the transesterification of ethylene carbonate: the most suitable route to produce glycerol carbonate at an industrial scale, it is catalysed by alkaline catalysts (e.g. CaO).[16]

  (D) the glycerolysis of urea: a relatively green route to glycerol carbonate, due to the availability and safety of both reactants. Many salts ($ZnSO_4$, $ZnCl_2$), rare earth oxides (La_2O_3, Nd_2O_3, and Co_3O_4/ZnO) and also MgO-supported Au catalysts.[16] The main drawback is the simultaneous formation of ammonia from the urea decomposition

  (E) the direct carboxylation with CO_2: it is the most attractive but also the most challenging route, due to some unavoidable thermodynamic constraints. [14]

  (F) the catalytic oxidative carbonylation of glycerol with CO and O_2: $PdCl_2$(1,10 phenanthroline) is a promising catalyst when KI is employed as additive.[17]
- <u>Catalytic chlorination</u>: epichlorohydrin is widely used for manufacturing of bisphenol A diglycidyl ether, that is a monomer in the production of polyester, epoxy resins and elastomers. In the past epichlorohydrin was also used for glycerol manufacturing. Nowadays the situation is reversed and a new green process for production of epichlorohydrin from glycerol has been proposed. This process, called GTE (glycerine to epichlorohydrin) process and catalysed by heteropolyacids, consumes less water and produces a lower amount of chlorinated residues than the petrochemical process used up to now. [18]

According to the recent review of Kimura et al.[19-a], only three processes for the valorisation of glycerol have already been scaled-up to industrial plants:

1. The chlorination of glycerol to epichlorohydrin: proposed in 2007 by both Dow and Solvay, a production plant is nowadays operating in France, where the EPICEROL® reaction is performed with a capacity of 10 kt/y. [20]
2. The esterification of glycerol to monoacyl and diacyl esters: ECONA® and ENOVA® are the commercial names of cooking oils produced from glycerol and commercialized by Archer Daniels Midland in cooperation with Kao Corp.
3. The reforming of glycerol to yield syngas: since 2006 the Dutch company BioMethanol Netherland Chemie produces syngas for the Fischer–Tropsch reaction (to methanol) by glycerol steam reforming, with a production capacity of 800 kt/y. The whole process is called glycerol-to-methanol (GTM) process.

2.1.2 Glycerol oxidation: state of the art [4-a, 19]

Many products from catalytic glycerol oxidation are attractive high-value fine chemicals. Dihydroxyacetone (DHA) is widely employed as active ingredient in formulations for sunless tanners; mesoxalic acid (MA or ketomalonic acid) is the most oxidized C3 compound can be obtained from glycerol and it finds large application, in its hydrated form (dihydroxymalonic acid), as complexing agent, diabetes therapeutic and precursor in fine chemical synthesis; tartronic acid (TAR, or hydroxymalonic acid) is used as anti-corrosive protective agent in boilers, as packaging additive for preventing oxidative decomposition and in medicines in the therapies for osteoporosis and obesity.

Nowadays these chemicals are produced by expensive biotechnological routes (as in the case of DHA) or by highly polluting oxidation processes with stoichiometric inorganic oxidants (as in the case of TAR). There is, therefore, a significant interest in replacing these processes with environmentally friendly alternatives, such as the catalytic oxidation with dioxygen or air in the presence of heterogeneous catalysts.

Because of the high functionality of glycerol molecule, an additional challenge in the catalytic glycerol oxidation is the intrinsic complexity of the reaction pathway, as depicted in Scheme 2.1. Consequently a meticulous design of catalysts is required to orientate the reaction towards the formation of the target product.

Scheme 2.1 Glycerol oxidation pathway (From Ref. [19-b])
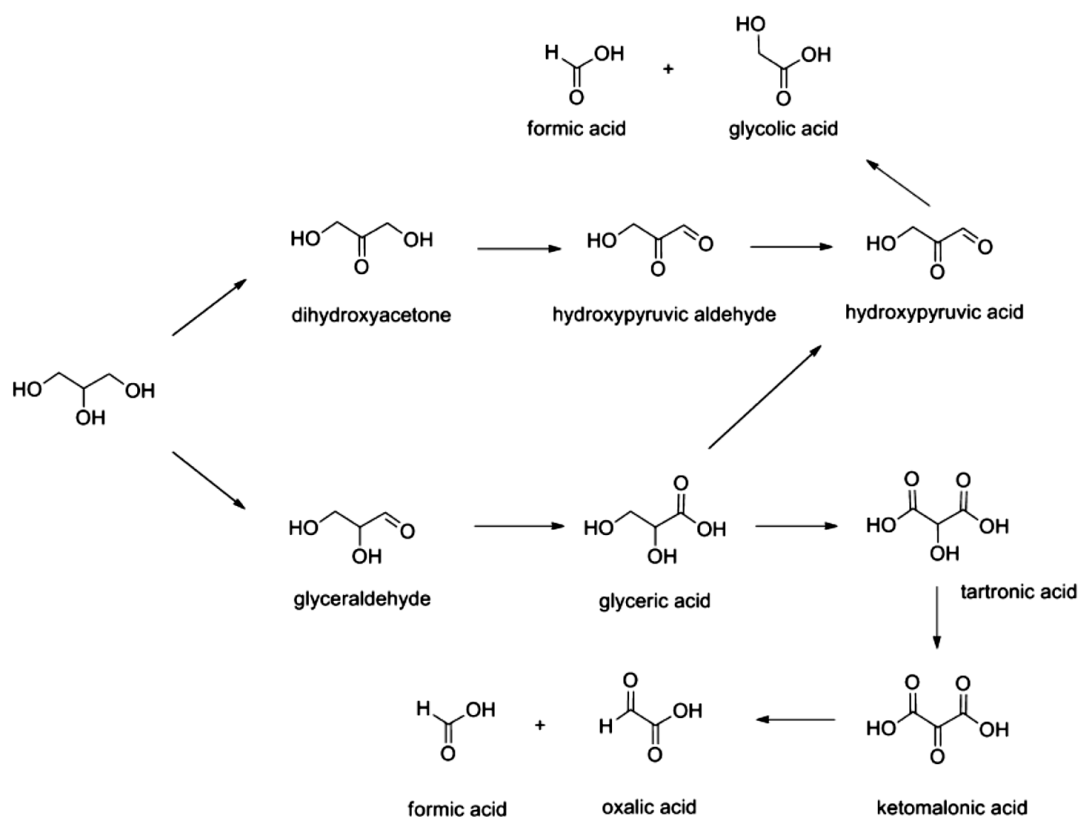
Due to their well-established ability to oxidize alcohols, supported noble metal nanoparticles have been investigated as catalysts also for polyol oxidation. Pt and Pd based catalysts for the oxidation of glycerol in aqueous solution were patented for the first time in 1977 by Miya and Matsuda [21] and in 1993 by Imanaka et al. [22]: in both cases the main product was glyceric acid; a few years later, Kimura et al.[23] and Gallezot et al. [24] reported on the

chemoselective glycerol oxidation with air in the presence of Pd/C, Pt/C and BiPt/C. A higher selectivity to glyceric acid was observed in the case of Pd/C compared to Pt/C, whereas the modification of the latter with bismuth resulted in a significant increase in the selectivity to DHA. The main drawback of both Pt and Pd based catalysts is the deactivation by leaching, overoxidation and poisoning.[23,24]

Starting from the pioneering studies of Prati and Rossi on the use of supported gold nanoparticles as effective catalysts in liquid phase alcohol oxidation [25], in 2002 Hutchings and co-workers [26] have successfully proposed Au-based catalysts for the selective glycerol oxidation to glycerate, under alkaline conditions. Although Au appears to be more resistant to oxygen-induced deactivation compared to Pt and Pd, as a key feature, aerobic alcohol oxidation on gold catalysts requires the use of a base, which might be involved in the deprotonation of the alcohol. Supporting this feature is the evidence that aldehyde can be oxidized to carboxylic acid without the presence of a base. In fact the more accepted reaction network of gold catalysed oxidation[27] consists of three major steps (Scheme 2.2). The first step is the adsorption and deprotonation of the alcohol. The as-generated adsorbed alkoxide then undergoes the elimination of the hydride in the beta position to form carbonyl compounds. The hydride removed from the alkoxide is chemisorbed on the gold surface, as revealed by electron paramagnetic resonance spectroscopy (EPRS). This second step of the oxidation, called β-elimination, is considered the rate determining step. The last step is represented by the re-oxidation of gold nanoparticle surface by O_2 to produce H_2O or H_2O_2. Such a mechanism has been supported by a considerable number of experimental evidences. The presence of Au-H species originated from β-elimination has been detected during alcohol oxidation on Au/CeO$_2$ by electron paramagnetic resonance spectroscopy (EPRS) and isotope labeling by Conte et al.[28]. The formation of Au-H species could occur via transfer of either a hydrogen atom or hydride; the latter seems to be more probable, according to recent studies evaluating Hammet plots for the alcohol oxidation over Au/CeO$_2$.[29] In addition the support plays a crucial role in stabilizing and promoting the formation of Au-H. Particularly Corma and coworkers demonstrated that Au NPs supported on nanocrystalline cerium oxide and reducible oxides are active for the oxidation of alcohols even in the absence of solvent and base.[30]

Scheme 2.2 Alcohol oxidation proposed mechanism on gold-based catalysts (Adapted from Ref.[27])
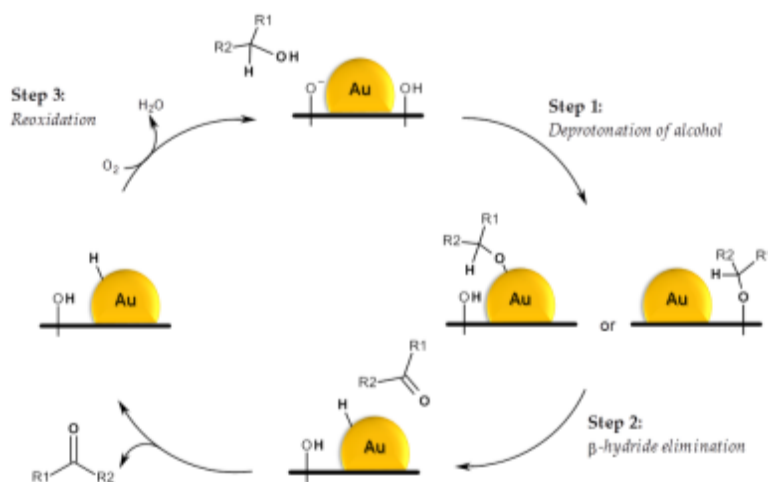
In non-reducible support the role of oxygen is more controversial, in particular the mechanism for the dioxygen reduction on gold surface in the re-oxidation step is still elusive. Previous reports generally showed that O_2 adsorption and dissociation is kinetically difficult on pure Au under ambient conditions,[31] which is disproved by the experimental observations endorsing the facile O_2 reduction over supported Au nanoparticles. A possible explanation for this apparent dichotomy refers to the presence of extremely low coordinated sites in nanosized gold, acting as preferential sites for the oxygen reduction. However these sites are present in low concentration after all, and therefore in this hypothesis the reoxidation (involving O_2 reduction) would be the rate-determining step. The O_2 reduction on Au therefore seems to be related to the peculiar reaction conditions of alcohol oxidation, including the presence of the interface, metal-support interactions, the cooperation of the base, and the possible presence of negatively charged Au particles. These aspects have been investigated by computational modelling. From a mechanistic point of view, base is supposed to promote the H-abstraction from the hydroxyl groups, the first step of the dehydrogenation pathway.[32] The role of the base has been recently investigated in the detail by Davis and co-workers [33], by combining labelling experiments with $^{18}O_2$ and $H_2^{18}O$ and density functional theory (DFT) simulations. They observed that during the Au catalysed oxidation the oxygen atoms incorporated in the final oxidized molecules derive from hydroxide ions rather than from molecular oxygen. Therefore the latter contributes to the catalytic cycle not by dissociating to atomic oxygen, but by producing *in situ* hydroxide ions through the catalytic decomposition of peroxide intermediate.

The impact of the pH on the activity and the selectivity has been explored also for Pt and Pd based catalysts. In particular Garcia et al.[24,a] proposed a systematic study of the influence of pH on the catalytic performances of carbon supported Pt and Pd nanoparticles. They concluded that the pH strongly affects the initial rates and the activity of Pd and Pt catalyst. The highest reaction rates for Pd catalysts have been obtained at pH 11, whereas Pt catalysts showed a remarkable activity also under neutral conditions. The selectivity is not pH dependent in the case of Pd/C, while product distribution changes as a function of the pH with Pt/C.

In any case, the pH of the reaction medium is not the only parameter affecting the performances of supported noble metal nanoparticles.

As a general rule, the catalytic behaviour is determined principally by the choice of the metal species and of the support.

Recently it has been shown that supported bimetallic nanoparticles can be successfully employed as catalysts for glycerol oxidation under aerobic and mild conditions [34]. In particular an enhanced activity was revealed for Au−Pd and Au−Pt nanoparticles supported on activated carbon compared to the corresponding monometallic counterparts. Also selectivity (to glycerate and tartronate with AuPd/AC and to glycolate with AuPt/AC) and durability were improved. Enhanced catalytic performances of bimetallic catalysts have been ascribed to the synergistic effect.

Also the nature, the texture and the surface properties of supports play a crucial role in modifying catalytic performances. Carbon based materials and oxides are the most used supports for glycerol oxidation catalysts [35]. Claus and co-workers [36] have demonstrated that, reaction conditions and particle size being equal, gold nanoparticles supported on carbon were more active than those supported on inorganic oxides (ceria and titania).

When activated carbon and carbon nanotubes are selected as supports, the catalytic activity has been shown to be independent on the specific surface area, but dependent on the microporosity and textural properties (e.g. graphitization degree, surface functionalities). [37]

No correlation between support surface area and catalytic activity has been revealed neither for ceria-supported gold catalysts.[36,a]

Basic and acidic properties of supports can influence the catalytic performances. The effect of pre-treatment of active carbon with nitric acid or hydrogen peroxide on the catalytic performances of supported Pt nanoparticles has been then investigated by Liang et al.[38], revealing that optimal textural properties were obtained after oxidative treatment with hydrogen peroxide. The modification of surface properties of carbon nanotubes and carbon nanofibers either by oxidative treatment with HNO_3 or by chemical treatment with ammonia and the impact on the catalytic performances of supported gold nanoparticles were studied by Prati et al. [39]. The use of functionalised materials as supports resulted in an improved activity and an enhanced selectivity to C3 compounds, as a consequence of the introduction of basic (N-containing groups) and acidic (carboxylic groups) functionalities and of the control of support's hydrophobicity/hydrophilicity.

Sobczak et al.[40] compared the catalytic performances of Au nanoparticles supported on TiO_2, Nb_2O_5, V_2O_5, Ta_2O_5 and Al_2O_3 and they concluded that supports with highly acidic character promote the C-C cleavage and the consequent high selectivity to C1 and C2 products. In some cases the acid-base properties of supports can be tuned by modifying surface composition. Al/Mg surface ratio significantly alters the selectivity of Au nanoparticles immobilized on $MgAl_2O_4$ spinels, as demonstrated by Villa et al.[41]. Specifically Al-rich surfaces promoted C-C bond cleavage, whereas higher selectivity to C3 products (glycerate and tartronate) was obtained with Mg-rich support materials. Another typical basic oxide, NiO, was studied as the support for Au nanoparticles in glycerol oxidation by Prati and co-workers[42]. The catalytic performances of Au/NiO and Au/NiO/TiO_2 catalysts were compared and the electronic effect of NiO on Au has been systematically studied. It was demonstrated that by optimising the ratio between NiO and TiO_2 ($[NiO]_{10}$-$[TiO_2]_{90}$), the selectivity towards glycerate increased to 75% at 90% conversion. The improvement in activity and selectivity by using NiO as support, was addressed to the interaction between NiO and Au nanoparticles, as confirmed by FTIR, HRTEM and XPS analysis.

Last but not least, particle sizes, as well, play a crucial role in determining the catalytic behaviour of Pt, Pd and Au nanoparticles. Liang et al.[38] tuned the particle sizes of Pt/AC catalysts from 1.2 to 26.5 nm and identified in 6 nm a critical value: below this value the activity increased, whereas above 6 nm the catalytic activity dramatically decreased, probably as a consequence of the lower exposed metallic surface area. A similar trend was observed also for supported palladium nanoparticles by Prati et al.[43], who prepared a series of 1wt.%Pd/AC catalysts by sol immobilisation method, with particle sizes ranging from 2 to 16 nm. In this case by increasing the particle size the activity dropped, while the selectivity to glyceric acid rose. Prati and co-workers investigated the effect of particle sizes also on carbon supported Au nanoparticles in the range of 6 to 20 nm synthesized by different preparation methods[44]. The catalytic activity resulted to be directly proportional to surface exposition of metal sites and, therefore, inversely dependent on particle size. Particle sizes influenced also the selectivity, an optimum selectivity to glycerate being observed for particle size of 15 nm. Authors ascribed this behaviour to a competition between size effect and shape effect, connected to a different exposed facet distribution. In fact it has been demonstrated that C – C cleavage is associated to a high frequency of (111) facets, which have shown to result in an enhanced accumulation of H_2O_2 [45]. Similar results were obtained by Ketchie et al. [46] and by Demirel et al.[47]. The latter firstly proposed the notion of structure sensitivity for gold catalysed glycerol oxidation.

2.2 Tailoring the selectivity by tuning the acid-base properties of supports

In the previous sections, it has been affirmed that the use of gold catalysts presents undeniable advantages in terms of stability and selectivity compared to Pd and Pt-based ones. It has been shown that the activities of all the catalysts are pH dependent as shown in Table 2.1. It clearly appears that basic environment is always beneficial in terms of both activity and selectivity.

Table 2.1 Catalytic performances of Au, Pd and Pt based catalysts under basic and neutral conditions

Catalyst	Conv. (%)	Selectivity (%)		
		Glyceric acid	Tartronic acid	C1 products [c]
1% Au/AC[a]	3	39	-	51
1% Au/AC (NaOH)[b]	**99**	**67**	**9**	**17**
1% Pd/AC[a]	5	43	5	47
1% Pd/AC (NaOH)[b]	**22**	**76**	**6**	**0**
1% Pt/AC[a]	78	45	7	46
1% Pt/AC (NaOH)[b]	**76**	**54**	**10**	**31**
1%Au/MgAl$_2$O$_4$[a]	6	35	6	41
1%Au/TiO$_2$[a]	8	38	7	32
1%Au/H-Mordenite	5	70	9	5
1%Pt/H-Mordenite	48	65	2	24

[a]   Glycerol 0.3M, pO$_2$=3atm, 1250rpm, 100°C, glycerol/metal=500 mol/mol ;conversion after 2 hrs
[b]   Glycerol 0.3M, pO2=3atm, 1250rpm, 50°C, glycerol/metal=500 mol/mol ;conversion after 2 hrs, 4 eq NaOH
[c]   products include CO$_2$, HCOOH.

However, from an industrial point of view, this represents the main limitation, since the use of a base results in the formation of salts and a further step is then required in order to neutralize the carboxylates and obtain free carboxylic acids, entailing additional costs and the generation of a large amount of inorganic salts as a waste. Thus the development of catalysts able to oxidize glycerol under base-free conditions to obtain free carboxylic acids has recently become a hot research topic. For that purpose, the role of the support and the nanoparticle composition has been investigated. Basic supports, such as NiO [48] and hydrotalcite [49] have been shown to speed up the reaction in base-free conditions. However they promote the formation of C−C bond cleavage products (glycolic acid, oxalic acid, formic acid, CO$_2$). In particular, by comparing the behaviour of Au, Pd and Pt catalysts (Table 2.1), it has been revealed that only Pt catalysts are effective in the base-free glycerol oxidation [37].

However Pt catalysts suffer from rapid deactivation due to overoxidation and leaching of Pt in the reaction solution. Recently it was found that by alloying Au with Pt, it is possible to combine the main advantages of the two metal components thus obtaining an active and selective catalyst also in the absence of a base and with an increased lifetime. However, these studies clearly showed that the support greatly influenced the activity and the selectivity .In particular using a zeolite, H-mordenite, as the support results in an enhanced activity compared to activated carbon (99% and 62% after 6 h for 1%AuPt/H-mordenite and 1%AuPt/AC, respectively).[50] Moreover, AuPt/H-mordenite demonstrated a high selectivity (83%) to glyceric acid, thus suppressing C−C cleavage and consequently the formation of C1 and C2 products. Also basic supports have been investigated, specifically AuPt nanoparticles supported on MgO and hydrotalcite showed a high selectivity to C3 products (85%) by properly selecting and controlling the reaction conditions.[51] These evidences opened the way to a new generation of gold-based catalysts, where the acid/base properties of the support play a crucial role, affecting both activity and selectivity of the reaction.

Starting from these considerations, we decided to investigate more in the detail the effect of the surface acidity of supports, by relating the acid site nature (Lewis, Brønsted, H-bond), the strength and the acid site density with the activity and selectivity of Au–Pt nanoparticles supported on these materials, when used as catalysts in base-free glycerol oxidation.

Six oxides with different acid/base and textural properties, i.e. H-mordenite, SiO_2, mesoporous silica (MCM-41-type), sulfated ZrO_2 (S-ZrO_2), NiO and MgO have been selected as supports. Surface area and generated pH of these materials are summarized in Fig. 2.3.

Figure 2.3 Surface area and generated pH of supports
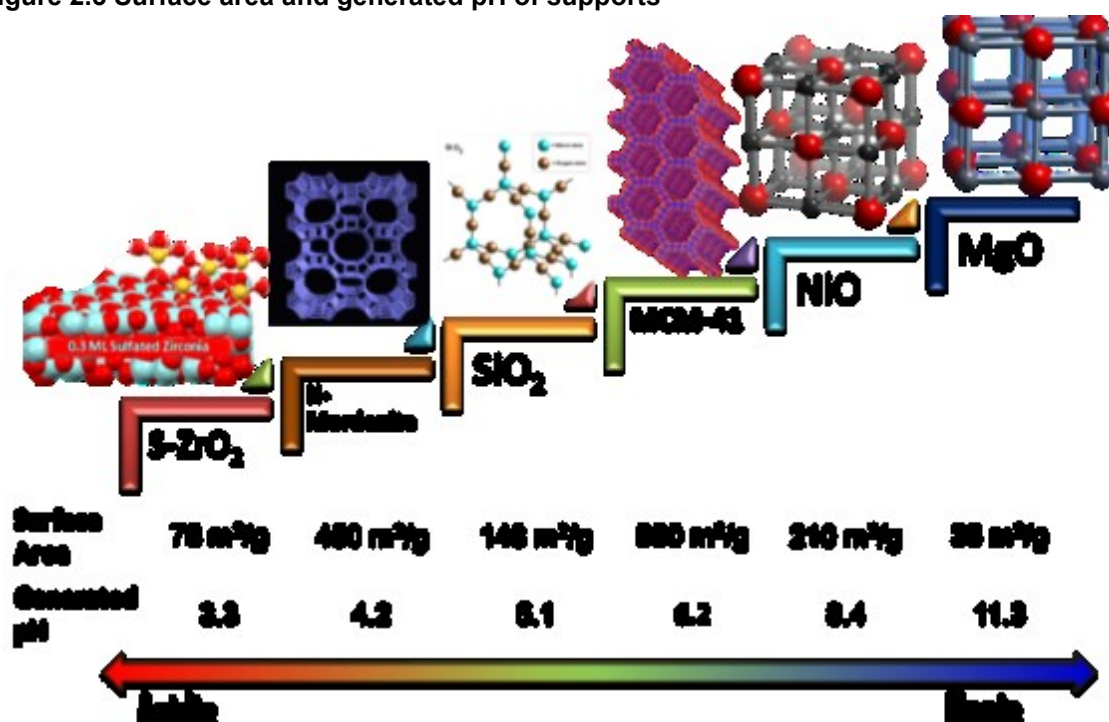
Bimetallic AuPt catalysts were prepared by the sol immobilization technique through a two-step procedure [52], illustrated in Fig. 2.4.

In the first step a preformed gold sol, generated using $NaBH_4$ as reducing agent and polyvinyl alcohol (PVA) as protective agent, is immobilised on the support; subsequently the sol of platinum was generated in the presence of Au/support using H_2 as a second reducing agent. According to the literature, the use of H_2 instead of $NaBH_4$ allows to slow down the

reduction rate of Pt ions, thus increasing the time of the diffusion and the growth of Pt on pre-existing Au nanoparticles and avoiding any metal segregation. Therefore this strategy usually ensured the generation of alloyed bimetallic nanoparticles of single composition with multiply twinned structure and controlled particle size, and highly dispersed on the support.

Figure 2.4 Two-step procedure for the preparation of a supported uniform AuPd alloy.
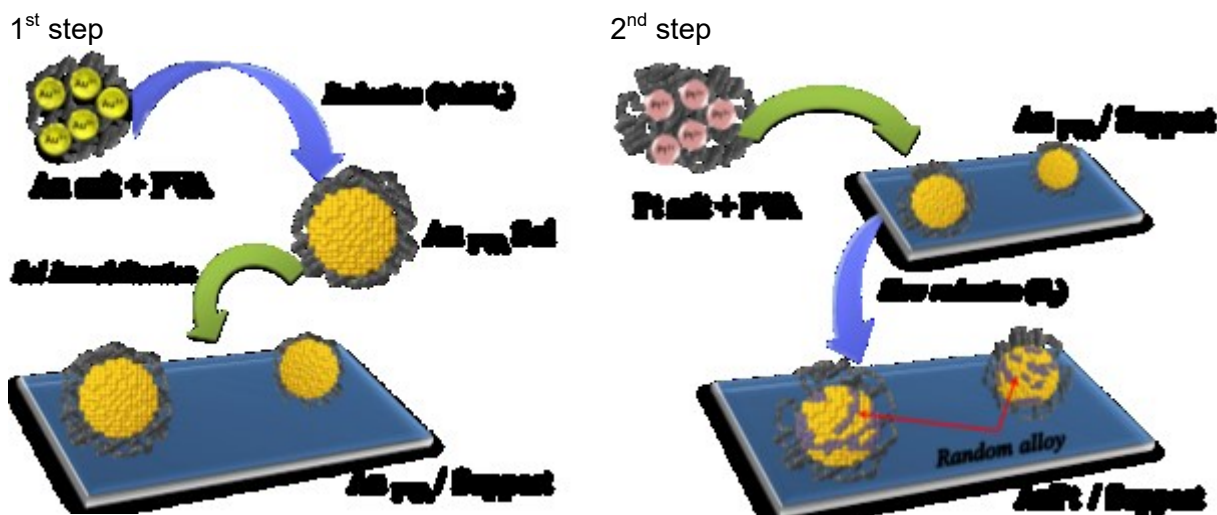
Catalysts with a total metal loading of 1% wt. and a molar internal ratio Au:Pt of 6:4 were produced. The total metal loading was assessed, by performing inductively coupled plasma atomic emission spectroscopy (ICP-AES). A detailed characterization of the morphology of as-prepared catalysts was performed in order to exclude eventual particle size effect on catalytic performances.

Transmission Electron Microscopy (TEM) data collected from the samples revealed good AuPt dispersion on all the catalysts (Fig. 2.5). Moreover, the size of the AuPt particles is not significantly affected by the support, with a mean diameter of 6.2–7.5 nm and similar distribution. (Table 2.2)

Table 2.2 Statistical median and standard deviation of particle size analysis for AuPt based catalysts

Catalyst	Statistical median (nm)	Deviation standard (σ)
AuPt/S-ZrO2	6.9	3.3
AuPt/H-Mordenite	6.2	3.2
AuPt/SiO$_2$	7.5	3.4
AuPt/MCM41	6.7	3.2

The structure and composition of metal nanoparticles were investigated by Energy Dispersive X-ray Spectroscopy (EDS) analysis. EDS spectra were acquired from single particles by converging the electron beam to the size of nanometres and detecting the X-ray photons emitted from a very local area. The single particle EDS acquisition was repeated on over fifty particles of different sizes and compared with the overall spectrum (a representative spectrum for individual single particles are shown in Fig. 2.5). The molar Au to Pt ratio obtained from the representative spectrum is 6.6 : 3.4. The ratios of Pt to Au are almost unchanged for all the examined single particles, regardless of the particle size, and are also similar to that of the overall measurement.

Figure 2.5 TEM and EDS analysis performed on the AuPt/MCM-41 catalyst. Instrumental magnification: 50000X; Inset: 200000X.
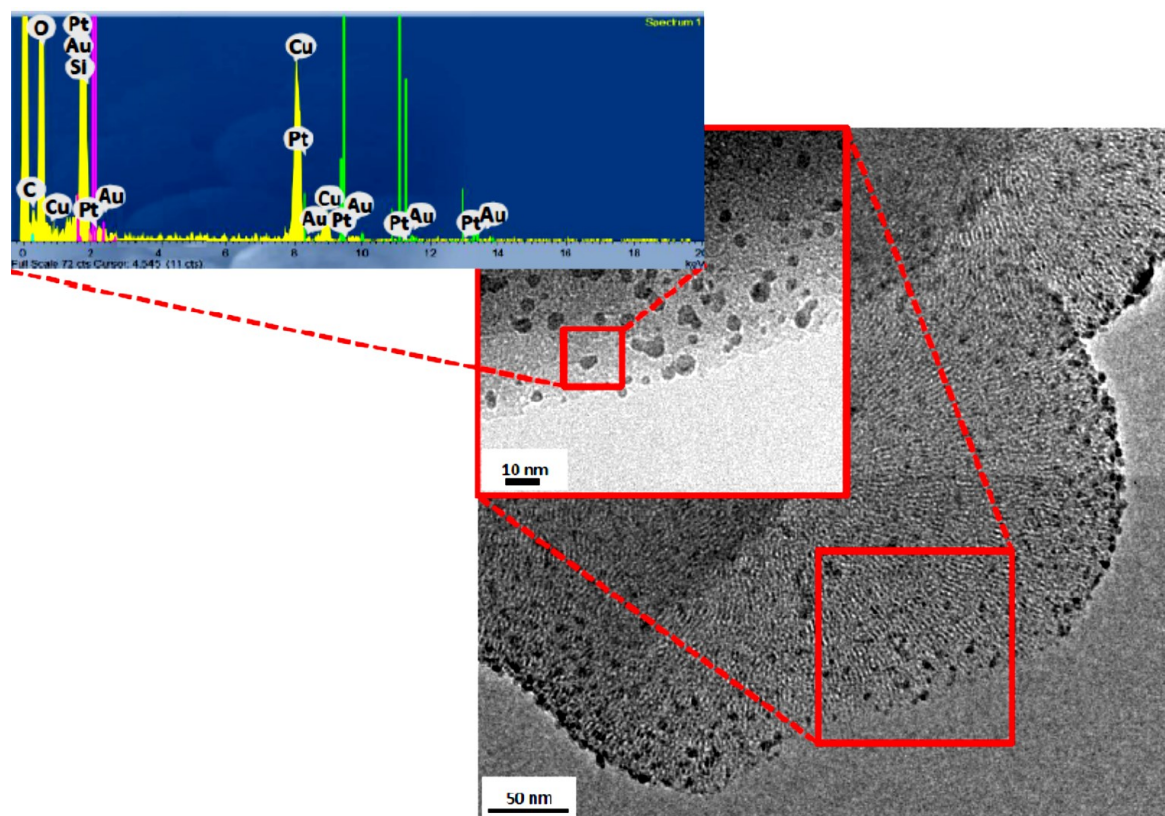
The catalysts were then tested in the base-free glycerol oxidation. The catalytic tests were carried out in a glass batch reactor at 80 °C starting from a 0.3 M aqueous glycerol solution and a definite amount of catalysts corresponding to a glycerol/metal ratio of 500 mol mol^{-1}. The reactor was pressurized with 3 atm of O_2 and an intimate contact between solid catalyst and reactant solution was assured by a magnetic stirring (1250 rpm). The initial activity and the selectivity of the catalysts are reported in Table 2.3. Considering the similar average particle size values, we can conclude that the impact of the particle size is negligible on the catalytic results shown below.

Table 2.3 Base free glycerol oxidation at 80 °C

Catalyst	Initial Activity[a]	Selectivity [b] (%)									Adsorbed amount of NH_3 [c] ($\mu mol/m^2$)
		GLYALD	GLYA	TA	DHA	C3	GLYCA	OXA	FA	C2 + C1	
1%Au$_6$Pt$_4$/MgO	657	7	21	1	12	**41**	8	6	43	**59**	-
1%Au$_6$Pt$_4$/NiO	283	10	51	8	16	**85**	7	2	8	**17**	-
1%Au$_6$Pt$_4$/MCM41	228	46	35	1	16	**98**	1	1	-	**2**	0.34
1%Au$_6$Pt$_4$/SiO$_2$	156	16	61	1	18	**96**	2	1	-	**3**	0.72
1%Au$_6$Pt$_4$/H-mord.	105	19	53	-	23	**95**	1	2	1	**4**	2.68
1%Au$_6$Pt$_4$/S-ZrO$_2$	113	19	57	3	17	**96**	1	1	1	**3**	2.96

Reaction conditions: 0.3 M glycerol, glycerol/metal = 500 mol mol^{-1}, 3 atm O_2, T = 80 °C.
[a] Moles of glycerol converted per hour per mole of the metal calculated after 15 min of reaction.
[b] Selectivity calculated at 30% conversion. GLYA = glyceric acid; GLYALD = glyceraldehyde; TA = tartronic acid; DHA = dihydroxyacetone; GLYCA = glycolic acid; OXA = oxalic acid; FA = formic acid; C2 = oxalic acid and glycolic acid; C1 = formic acid.
[c] The amount of NH3 adsorbed under an equilibrium pressure of 5 Torr. The amount of NH_3 obtained after subtracting the contribution of Lewis sites.

First of all, the higher activity of the basic supports compared to the acidic ones is not unexpected. In particular AuPt/MgO is a very active catalyst, exhibiting an initial activity (657 converted mol of glycerol $(\text{mol}_{AuPt})^{-1}$ h^{-1}) greater than those observed when the same AuPt NPs are deposited on NiO (283 converted mol of glycerol $(\text{mol}_{AuPt})^{-1}$ h^{-1}) and on the acidic supports (113, 105, 156, and 228 converted mol of glycerol $(\text{mol}_{AuPt})^{-1}$ h^{-1} for S-ZrO$_2$, H-mordenite, SiO$_2$ and MCM41, respectively). The peculiar behaviour of MgO-supported AuPt NPs can be explained considering that in terms of activity the presence of strong basic sites (as in the case of MgO, which has an isoelectric point of 10.4) enhances the β-hydride abstraction, which is the limiting step according to the mechanism of glycerol oxidation via oxidative dehydrogenation pathway[32]. This hypothesis has been confirmed by ICP analysis performed on the reaction media, which revealed the presence of Mg in solution. Mg could act as a sacrificial base, promoting both H-abstraction and the successive desorption of the Mg-glycerate, thus limiting the deactivation phenomena due to strongly adsorbed (by)products. Concerning the acidic supports, slight differences in the initial activity can be envisaged, anyhow more interesting indications can be obtained from the reaction profiles, shown in Figure 2.6.

Figure 2.6 Reaction profile for AuPt based catalysts
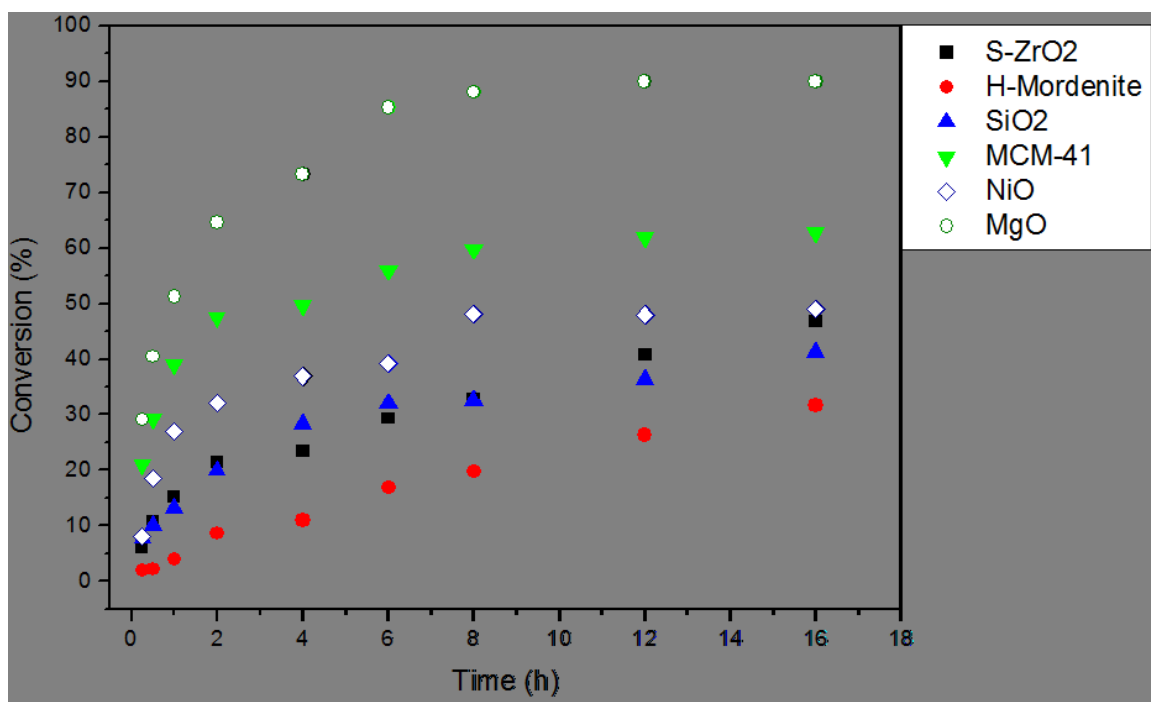
Considering trends presented in the graph of Figure 2.6, it is evident that AuPt NPs on MCM41 strongly differ from the other acidic supports, showing limited deactivation phenomena compared to AuPt NPs supported on S-ZrO$_2$, SiO$_2$ and H-mordenite amd higher activity than NiO, a basic support. In fact AuPt/MCM-41 reaction profile is similar to that of AuPt/MgO. This suggests that MCM41 represents a sort of breakout line between acid and basic supports. Moreover, the good stability of AuPt/MCM41 was supported by recycling experiments carried out by recovering the catalyst through filtration and adding fresh solution of glycerol. In the stability tests, the catalyst maintained almost the same activity and also selectivity after six runs (Figure 2.7).

Figure 2.7 Recycling tests using AuPt/MCM41(Glycerol 0.3M in water; metal/alcohol = 1/500 mol/mol; 300kPa O; T=80°C/353 K).
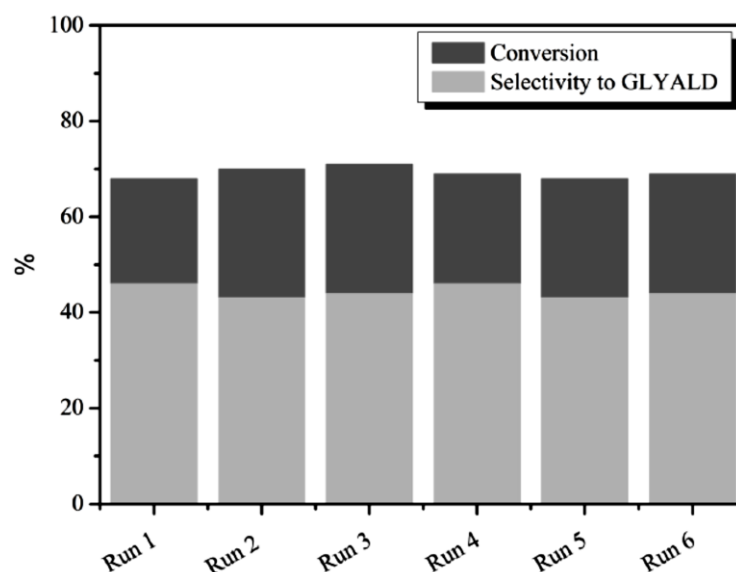
In addition, SAXRD analyses revealed that the mesostructure of MCM-41 was maintained after the recycling tests (Figure 2.8).

Figure 2.8 Small angle XRD of AuPt/MCM-41 a) before and b) after reaction

a) **b)**
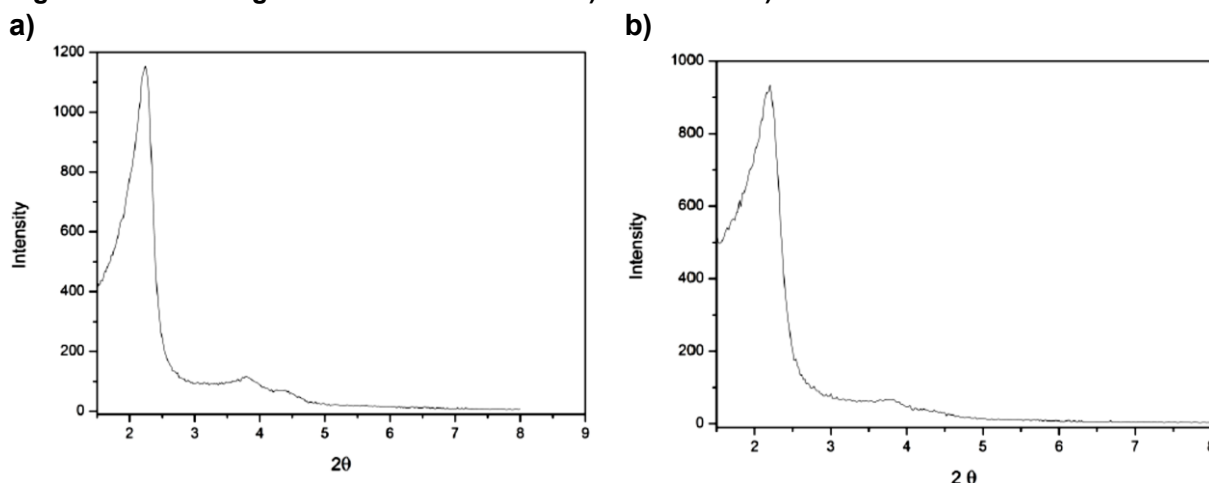
From a selectivity point of view, AuPt NPs on acidic supports seem to be more promising. Indeed, as shown in Table 1, by using acidic supports a higher selectivity to C3 compounds (GLYA + GLYALD + TA + DHA) (~95%) was obtained whereas basic supports, in particular MgO, promoted C–C bond cleavage and the consequent formation of C2 and C1 products in high amounts (59%). However, it has been reported in the literature that a high selectivity toward glyceric acid can be maintained with AuPt/MgO even at high conversion if the temperature is below 25 °C.[51]

In addition, considering the internal product distribution for C3 compounds, the formation of glyceraldehyde, a labile compound, in significant yield was observed in the presence of acidic supports. Particularly the highest selectivity to glyceraldehyde was achieved with AuPt/MCM-41 (46% at 30% conversion). To the best of our knowledge this is the first time that glyceraldehyde has been detected in such a great amount. The presence of glyceraldehyde was also proved by ^{13}C-NMR analysis of the reaction mixtures (Figure 2.9).

Figure 2.9 ^{13}C-NMR analysis of the reaction mixtures (at 30% conversion) and comparison with standard references of glyceraldehyde and glycerol.
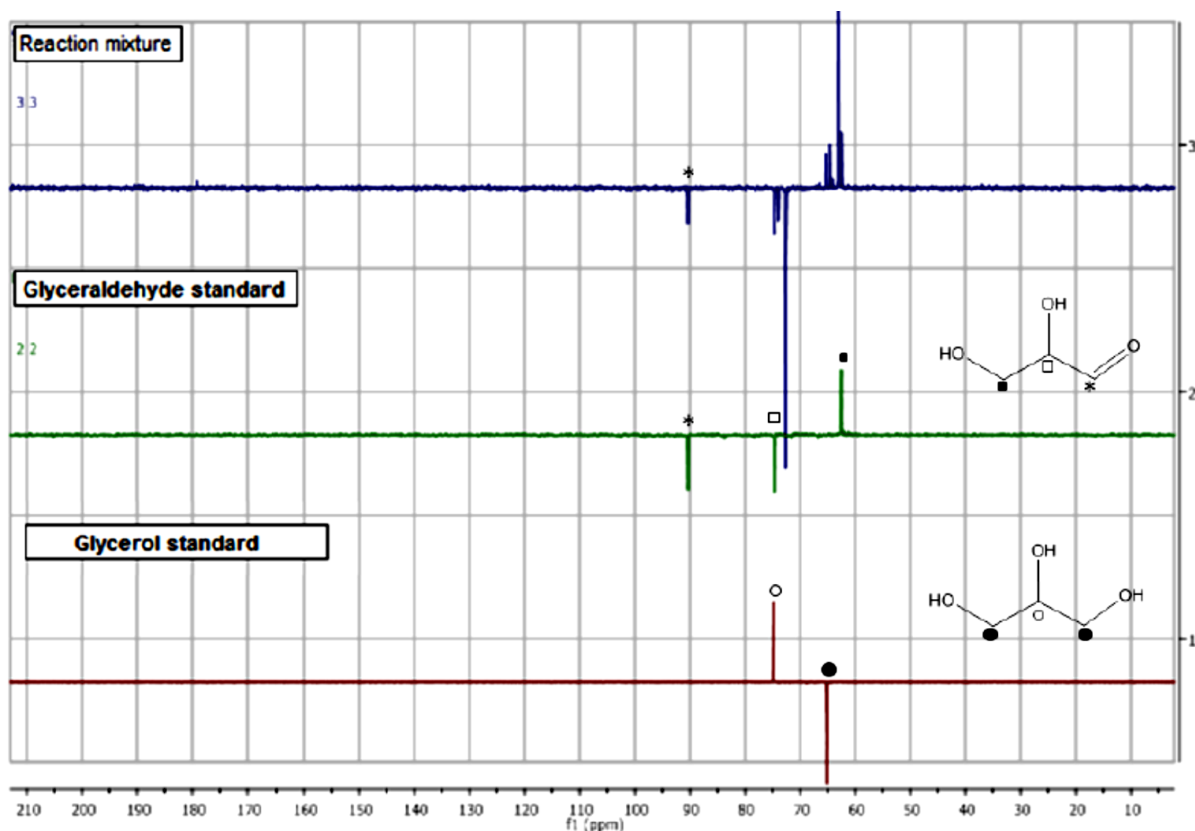
It can be noted that the higher selectivity to glyceraldehyde showed by MCM-41 is related to a lower production of glyceric acid compared to the other acidic supports. Actually glyceraldehyde is considered to be a precursor of glyceric acid.

In order to explain this catalytic behaviour, we decided to focus on the acidic supports to find any relation between the surface properties of the supports and the catalytic activity and the peculiar selectivity of AuPt NPs supported on them.

Lewis and Brønsted acidic sites were differentiated by monitoring the adsorption of 2,6-Dimethylpyridine (2,6-DMP or 2,6-lutidine) on the solid surfaces through Infrared Spectroscopy (FT-IRS). The use of 2,6-dimethylpyridine (2,6-DMP) as probe molecule presents several advantages. Indeed, even if the formation of coordinative chemisorption bonds is expected to be sterically hindered due to the presence of substituent groups in the 2- and 6-position in the pyridine ring, it has been recently demonstrated that if the 2,6-DMP adsorption is carried out at room temperature and under a reasonably high pressure, all types of coordinated and/or H-bonded species can be differentiated, distinguishing also acidic sites of different strength.[53]

The interaction with Brønsted or Lewis acid sites or H-bond with surface hydroxyl groups result in a perturbation of the aromatic ring vibrations (ν_{CCN}) and in the consequent appearance of characteristic features in the corresponding infrared spectra. In this way it is possible to discriminate between different adsorption sites. In particular, the selection rule for the di-substituted aromatic ring allows four C–C stretching modes: 8a, 8b, 19a, 19b, following the numeration proposed by Wilson (Figure 2.10). [54] These ring vibration modes, especially modes 8a and 19b according to the assignment of Kline and Turkhevich[55], are

the most sensitive vibrations with regard to the nature of intermolecular interactions via the nitrogen lone pair electrons.

Figure 2.10 Graphical schematization of 8a, 8b, 19a, 19b vibrational modes in 2,6-DMP
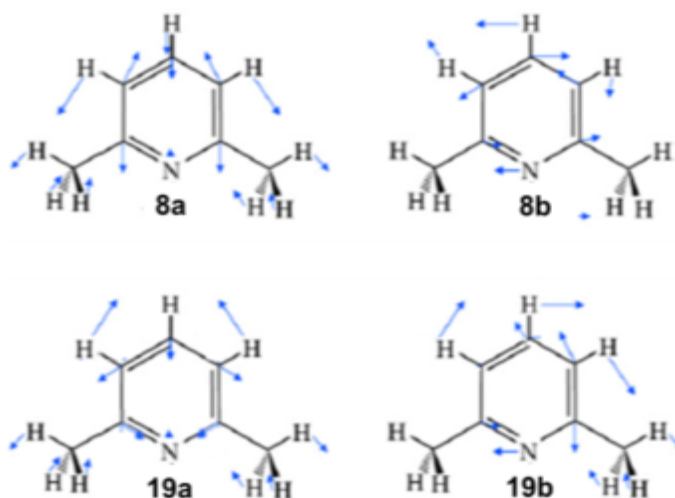
2,6-DMP is a strong base and proton transfer is possible, resulting in the formation of lutidinium ions when the molecules interact with strong Brønsted acid sites. In fact the base adsorbed at Brønsted sites in its 2,6-dimethylpyridinium form (2,6-DMPH$^+$) yields two strong and well-recognizable 8a-8b bands centered at ~1640-1655 cm^{-1} and ~1630cm^{-1}, respectively, whereas a typical three-band envelope in the 1620-1580 cm^{-1} interval can be attributed to Lewis-bound and H-bonded species (Figure 2.11).

Figure 2.11 Spectral Location of Mid-IR Vibrational Modes of Free and Adsorbed 2,6-DMP
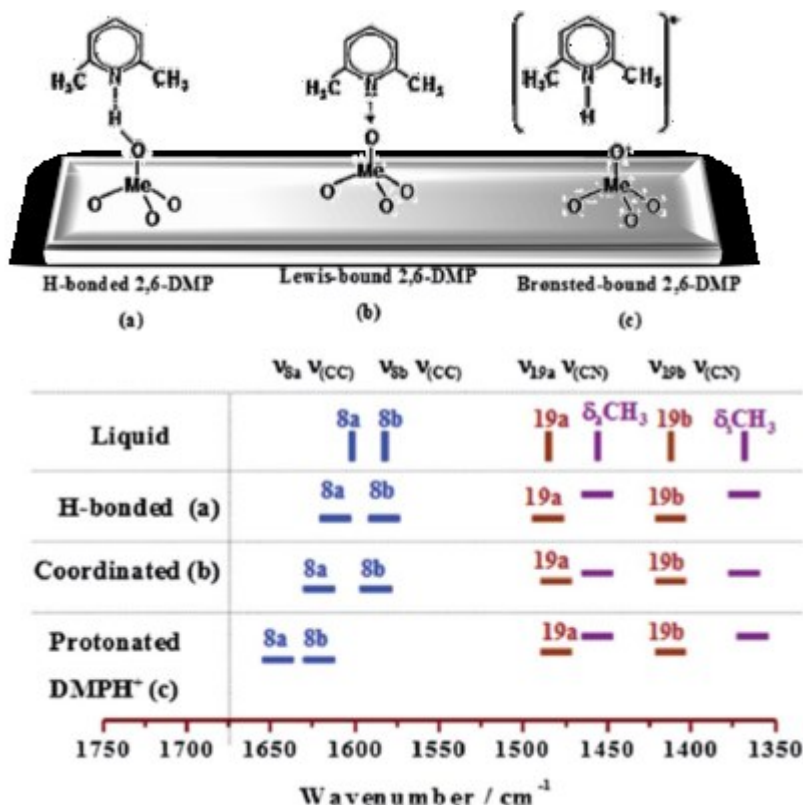
Therefore, to study the adsorption/desorption of 2,6-DMP, we monitored the bands in the 1650–1550 cm^{-1} spectral range. The FTIR spectra, normalized with respect to the surface area and collected after interaction with 2 mbar of 2,6-DMP at room temperature (r.t.) and during the outgassing, are shown in Fig. 2.12.

Figure 2.12 The IR spectral region of the 8a–8b ring modes of 2,6-DMP. FTIR absorbance spectra after interaction with 2 mbar of 2,6-DMP at r.t. (red curve) and during outgassing (black and blue curves) with AuPt NPs on a) SiO$_2$, b) MCM-41, c) S-ZrO$_2$, and d) H-mordenite.
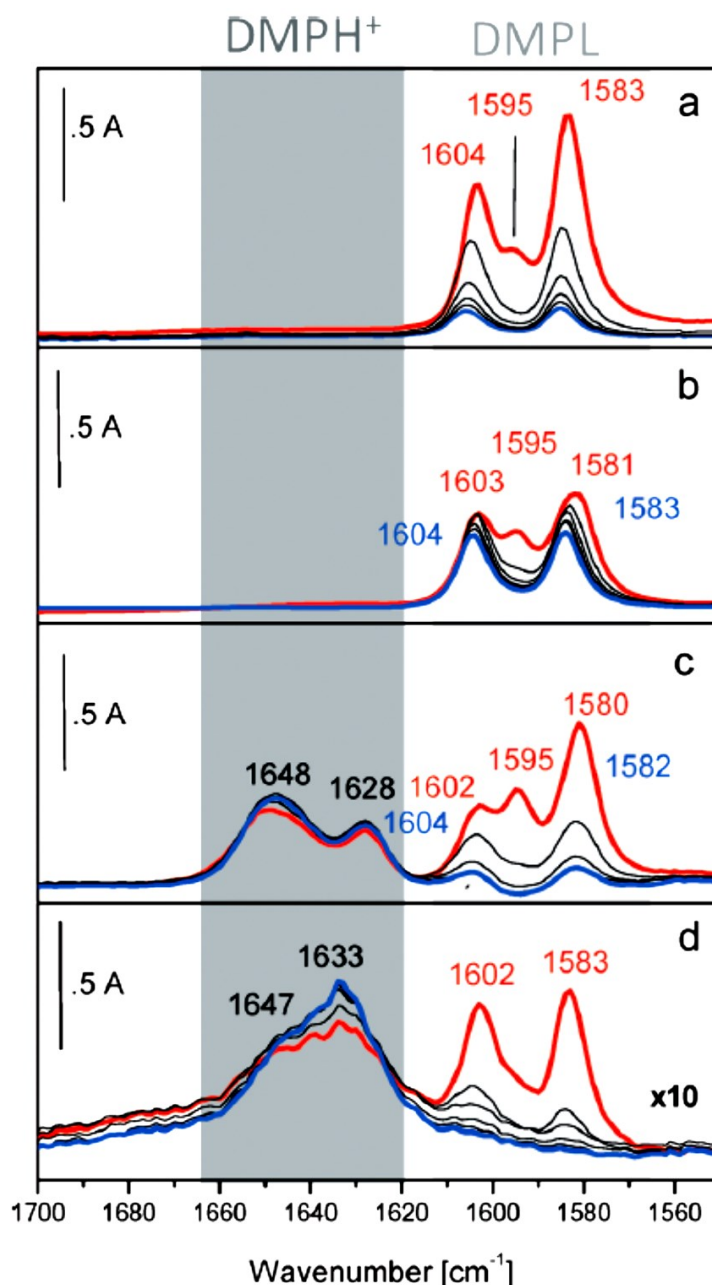
Upon adsorption of 2 mbar of 2,6-DMP at r.t. (red curves), complex bands in the 1605–1580 cm^{-1} range due to ν_{8a} and ν_{8b} of liquid-like and H-bonded 2,6-DMP are formed on all catalysts. As expected, no Lewis and Brønsted acidity was observed for AuPt/MCM-41 and AuPt/SiO$_2$. Actually, besides the liquid like form, the 2,6-DMP probe interacts with these

systems exclusively through H-bonding with silanol groups present on the surface. Moreover, a significant blue shift at 1605 cm^{-1} is observed for the ν_{8a} mode. This position is typical of the interactions between the probe and Lewis sites, thus confirming the acid character of silanols. The observed bands gradually decreased in intensity after outgassing for 30 min with increasing time at the same temperature (blue curves). However, the effect of outgassing is less pronounced in the case of AuPt/MCM-41. The higher stability of the bands related to AuPt/MCM-41, compared with those detected on AuPt/SiO$_2$ can be ascribed to a stronger interaction with silanols in the former case.

On the other hand, in the AuPt/S-ZrO$_2$ catalyst both Lewis (1602 cm^{-1}) and Brønsted acidic sites (1628 and 1648 cm^{-1}) were revealed, whereas for AuPt/H-mordenite we observed almost exclusively Brønsted acidity (bands at 1633 and 1647 cm^{-1}). It is well-recognized that the presence of extra-framework aluminium species is responsible for the appearance of Lewis acidity in H-Mordenite. In our case the apparent absence of Lewis sites on H-mordenite can be addressed to residual water still adsorbed on the surface due to the mild pre-treatment of the samples (drying at 353 K/80 °C). In any case it should be pointed that catalytic tests have been carried out in water which probably masks the Lewis sites.

The adsorption/desorption of 2,6-DMP allowed to discriminate and identify the different acidic centres present on the surface of the catalysts, however there is no clear correlation between the nature of the sites and the trend observed for the catalytic activity and selectivity. Recently, Stošić et al.[56] investigated the influence of the acid–base properties of zirconia and titania based materials on the dehydration of glycerol. In particular, authors demonstrated that the catalytic activity was dependent not only on the nature of the acid sites but also on the total acidity of the catalysts. Based on these observations, the number of acid sites present on the different samples has been quantified. Adsorption microcalorimetry of gas-phase NH$_3$ molecules was performed to study the strength and the total amount of acid sites. Among the basic molecules, ammonia is a very convenient probe to study the acid character since it can interact with acidic hydroxyls forming ammonium ions. However, when ammonia is employed for quantitative determination of acid sites, some precautions should to be taken. Indeed, when all acidic sites have been neutralized, the excess of ammonia molecules can react with the ammonium ions (which in turn act as Brønsted acid sites too), forming NH$_4^+$ × NH$_3$ dimers, and thus resulting in an overestimation of the amount of Brønsted acid sites.[57] Infrared spectroscopic studies on dimer formation and decomposition within the pores of a TON zeolite established that the optimal temperature for ammonia adsorption is 400 K because at this temperature no dimers formation was observed and only ammonium ions are generated.[58] Further, FTIR experiments on NH$_3$ adsorption at 343 K on AuPt/H-mordenite confirmed the absence of bands associated to NH$_4^+$ × NH$_3$ dimers, therefore the microcalorimetric experiments were performed at 373 K. In microcalorimetric analysis quantitative data can be extrapolated from calorimetric isotherm curves (Figure 2.13, section a) and volumetric isotherm curves (Figure 2.13, section b).

The volumetric isotherms provide information on the total amount of acid sites probed by ammonia, and the quantity of sites follows the order:

AuPt/S-ZrO$_2$ **>** AuPt/H-mordenite **>** AuPt/SiO$_2$ **>** AuPt/MCM-41

However, it should be considered that the total amount of acid sites present on the surface of AuPt/S-ZrO$_2$ includes both Lewis and Brønsted sites. Therefore, in order to define the role of the different kinds of acid sites in the glycerol oxidation reaction, it's suitable to discriminate

between Lewis and Brønsted sites and to subtract from the total amount of acid sites the contribution deriving from Lewis sites.

Figure 2.13 Section a: surface area-normalized calorimetric isotherms (integral heats vs. equilibrium pressure). Section b: surface area-normalized volumetric isotherms (mmol NH3 adsorbed vs. equilibrium pressure). (-■-) AuPt/MCM-41; (-▲-) AuPt/SiO2; (-●-) AuPt/H-mordenite; (-◆-) AuPt/S-ZrO₂.
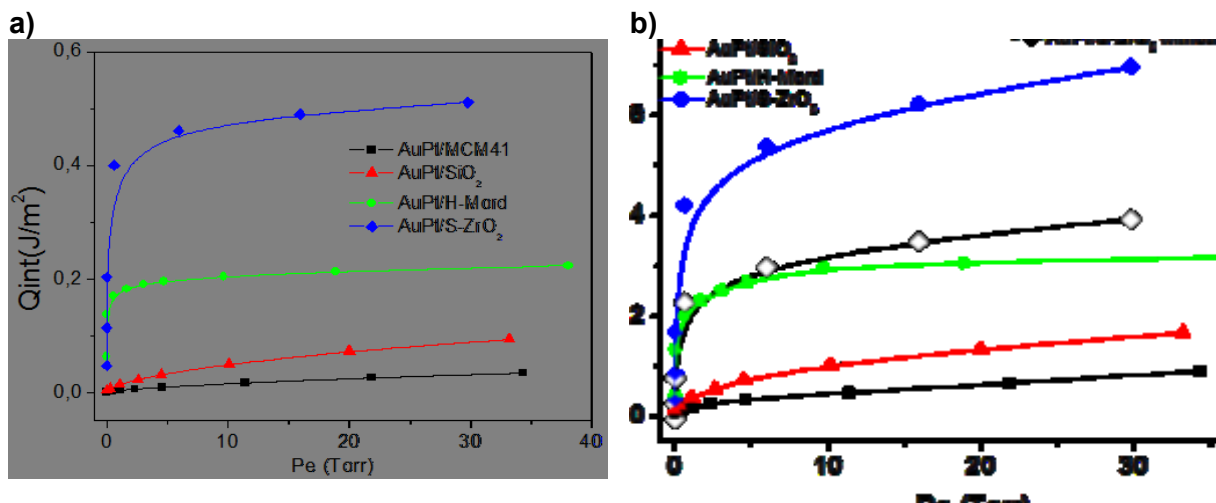
The relative abundance of the Lewis/Brønsted sites can be determined by a quantitative analysis of the IR bands of adsorbed 2,6-DMP on AuPt/S-ZrO₂ (red curve in panel c of Fig. 2.12). The amount of acid sites was calculated by applying the Lambert–Beer Law to the deconvolved bands, using the following integrated molar absorption coefficients:

$$\varepsilon(Brønsted) = 6.5 \text{ cm mmol}^{-1} \qquad \varepsilon(Lewis) = 3.4 \text{ cm mmol}^{-1}$$

It was found that the overall amount of sites exposed at the S-ZrO₂ surface encompasses 55% of Brønsted sites and 45% of Lewis sites. A new volumetric isotherm was created by subtracting the contribution of Lewis sites (Fig. 2.13, section b, (-◇-)). This new curve reveals that AuPt/S-ZrO₂ and AuPt/H-mordenite catalysts show a similar abundance of Brønsted sites. In the calorimetric isotherm the heat developed upon NH₃ adsorption, Q_{int} (J m^{-2}), is reported as a function of the equilibrium pressure, P_e (Torr), providing information on the strength of the interaction between the molecule and the sites on the catalyst. In particular, it has been frequently observed that the higher the developed heat, the higher the acidic strength of the site. For equilibrium pressures up to 0.2 Torr, the developed heats follow the trend:

AuPt/S-ZrO₂ ≈ AuPt/H-mordenite **>** AuPt/SiO₂ ≈ AuPt/MCM-41.

This relation clearly indicates that acid sites exposed on AuPt/S-ZrO₂ and AuPt/H-mordenite are stronger than those present on AuPt/SiO₂ and AuPt/MCM41, in agreement with the conclusions from FTIR spectra, revealing the presence of Brønsted acid sites on both catalysts supported on S-ZrO₂ and H-mordenite, while only silanol groups on the silica based systems.

Conversely, for P_e > 0.5 Torr, the Q_{int} follows the sequence:

AuPt/S-ZrO₂ **>** AuPt/H-mordenite **>** AuPt/SiO₂ **>** AuPt/MCM-41.

Even if, as a general rule, a greater Q_{int} implies a higher acidic strength, in this case, the calorimetric isotherms (section a of Fig. 2.13) display a quite similar trend if compared to that revealed by the volumetric ones (reported in section b of Fig. 2.13), and therefore we can conclude that the differences observed in the heat developed are directly correlated with the different amounts of adsorbed NH_3 (which in the case of AuPt/S-ZrO$_2$ include also the contribute deriving from interactions with Lewis sites), rather to a stronger interaction. This is even more evident by plotting the Q_{int} as a function of the adsorbed NH_3 (mmol) (Figure 2.14).

Figure 2.14 Q_{int} as function of the µmol of adsorbed NH₃: (-■-) AuPt/MCM-41; (-▲-) AuPt/SiO2; (-●-) AuPt/H-mordenite; (-◆-) AuPt/S-ZrO$_2$.
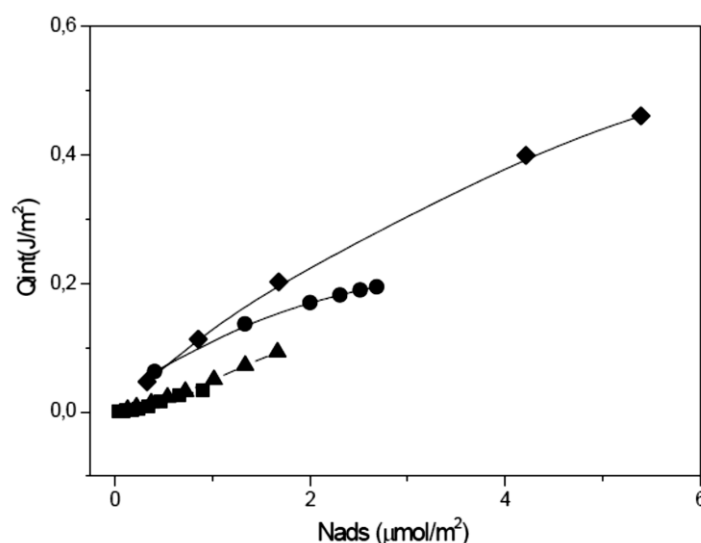
The characterization studies on the acidic surface properties allowed us to examine more critically the catalytic results shown in Table 2.3. The lower initial activity and more evident deactivation phenomena observed with AuPt/H-mordenite and AuPt/ZrO$_2$ can be attributed to the higher number of acidic sites. Indeed if we compare the trend in the catalytic activity,

AuPt/H-mordenite ≈ AuPt/ZrO$_2$ <AuPt/SiO$_2$ < AuPt/MCM-41

with that in the total amount of acid sites:

AuPt/S-ZrO$_2$ > AuPt/H-mordenite > AuPt/SiO$_2$ > AuPt/MCM-41

it is evident that the higher the total amount of acid sites, the lower the catalytic activity. The similar activity shown by AuPt/H-mordenite and AuPt/S-ZrO$_2$ catalysts can be justified by the comparable abundance of exposed Brønsted sites. This is reasonable, if we consider that Lewis acid sites are screened by water in the reaction medium and therefore they are not involved in the catalytic process.

In addition, surface properties affect also the selectivity of AuPt NPs supported on acidic oxides. Indeed, although, in general the use of acid supports leads to catalysts which are more efficient in terms of selectivity to C3 products, actually among acidic oxide supported catalyst a different trend in C3 product distribution was observed. In order to verify the presence of an eventual relation between the amount of glyceraldehyde or glyceric acid detected and the amount of acid sites or their nature, we reported in a graph the number of mols of glyceraldehyde as a function of the number of acidic sites, as determined by microcalorimetric analysis (Figure 2.15).

89

Figure 2.15 Relation between glyceraldehyde selectivity and number of acidic sites.
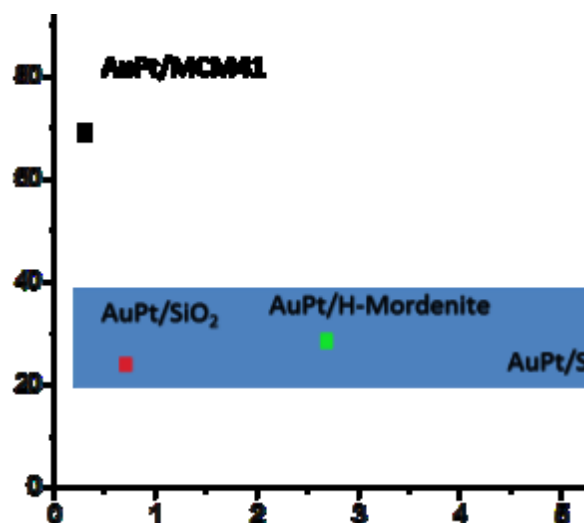
For AuPt/S-ZrO$_2$, AuPt/H-mordenite and AuPt/SiO$_2$ the main product is glyceric acid (53–61%) with a low amount of aldehyde (16–19%).Therefore AuPt on SiO$_2$, H-Mordenite and S-ZrO$_2$ show very similar activity and selectivity, despite the present different tipology and number of acidic site. In contrast, AuPt/MCM-41, which shows the lowest amount of acid sites, is able to stabilize glyceraldehyde, thus depressing its successive transformation to glyceric acid, suggesting that the latter probably contain specific acid sites accelerating the transformation of glyceraldehyde to glyceric acid. Nevertheless, we have to consider that the graph reported above is actually affected by the presence of some artefacts. Indeed the number of acidic sites has been determined by monitoring the adsorption of ammonia in the gas phase, whereas the catalytic tests have been carried out in water, which probably adsorbs on and screens Lewis sites. In addition also Brønsted sites might to be excluded, because of the rapid decrease of pH observed under reaction conditions. Therefore catalytic performances are definitively determined by H-bonding. However the critical parameter it is not the number of H-bonding sites, rather the strength of these interaction. Indeed AuPt/MCM-41 and AuPt/SiO$_2$ showed a different catalytic behaviour, despite the similar number of acid sites.

In order to support this hypothesis, AuPt/MCM41 and AuPt/H-mordenite, as representatives of the other acidic catalysts, were tested in the transformation of glyceraldehyde to glyceric acid under the same reaction conditions used for glycerol oxidation (0.3 M glyceraldehyde, glyceraldehyde/metal = 500 mol mol^{-1}, 3 atm O$_2$, T = 80 °C). After 6 h of reaction in the case of AuPt/H-mordenite glyceraldehyde was completely oxidized to glyceric acid whereas AuPt/MCM-41 converted only 25% of glyceraldehyde.

These data are in agreement with the well accepted mechanism of aldehyde conversion to a carboxylic acid via acid catalysed diol formation and the subsequent rapid dehydrogenation to the acid (Scheme 2.3).

Scheme 2.3 Mechanism for glyceraldehyde transformation to glyceric acid

(a)

(b)
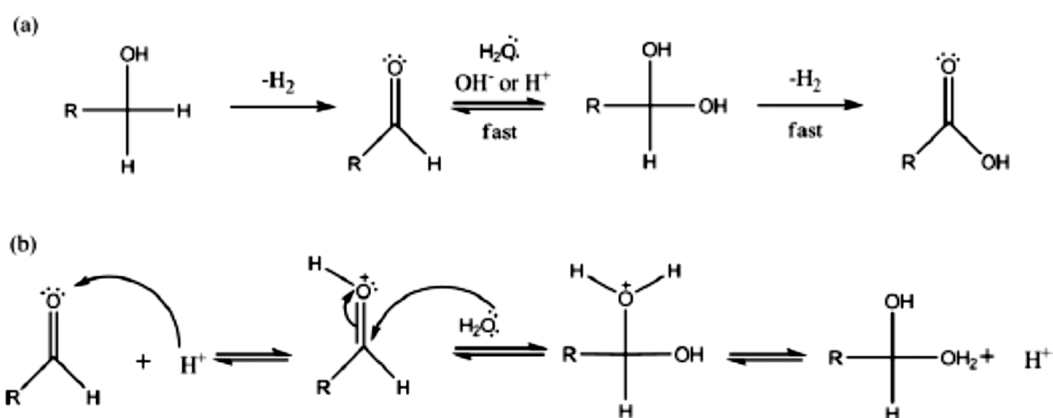
Finally, the effect of temperature was investigated for AuPt/MCM41 (Table 2.4) . By decreasing the reaction temperature from 80 °C to 60 °C and then to 40 °C the activity of the catalyst decreased as expected with an initial activity of 228, 173 and 112 (converted mol of glycerol $(mol_{AuPt})^{-1}$ h^{-1}), respectively. However decreasing the reaction temperature has a beneficial effect on the selectivity to glyceraldehyde, which increased, giving the best result at 40 °C (55% at 30% conversion).

Table 2.4 Effect of temperature on catalytic performances of 1%AuPt/MCM-41

1%Au6Pt4/MCM41	Activity[a]	Selectivity [b] (%)				
Reaction temperature	$\left(\frac{conv.\,mol}{mol_{AuPt}\,\cdot\,h}\right)$	GLYALD	GLYA	TA	DHA	C2 + C1
40°C (313 K)	112	55	31	-	14	-
60 °C (333 K)	173	50	37	1	12	-
80°C (353 K)	228	46	35	1	16	-

Reaction conditions: 0.3 M glycerol, glycerol/metal = 500 mol mol^{-1}, 3 atm O$_2$,.
[a] Moles of glycerol converted per hour per mole of the metal calculated after 15 min of reaction.
[b] Selectivity calculated at 30% conversion. GLYA = glyceric acid; GLYALD = glyceraldehyde; TA = tartronic acid; DHA = dihydroxyacetone; C2 = oxalic acid and glycolic acid; C1 = formic acid.

2.3 Bismuth modified Au-Pt bimetallic catalysts for the selective oxidation of glycerol to *1,3-Dihydroxyacetone*

Among all the oxidation products from partial glycerol oxidation, dihydroxyacetone (DHA), the product of selective secondary alcohol group oxidation, mainly attracts the interest of industrial and academic research, due to its very high value (ca. 150 US$/kg) in comparison to the current price of crude and purified glycerol (<0.3 US$/kg and ca. 0.6 US$/kg, respectively).[19-a] The commercial relevance of this compound is related to its application in cosmetic industries as active ingredient of sunless tanners (Food and Drug Administration, FDA, approved DHA for application in tanning formulations in 1977). Dihydroxyacetone has a dimeric structure, but this dimer easily dissociates in water (Scheme 2.4) and it carries out the function of tanning agent by reacting with the amino groups of skin and hair according to Maillard reaction, thus leading to the production of melanoidins, which are responsible for the appearance of tan.

Scheme 2.4 Equilibrium of dimerization of DHA in aqueous media.

Monomeric form   Dimeric form

Currently, the commercial synthesis of DHA is predominantly performed via industrial fermentation. A variety of microorganisms and derived enzymes have been studied and successfully used for the bioconversion of glycerol to DHA. Specifically, batch microbial fermentation processes frequently employ *Gluconobacter oxydans* and *Acetobacter suboxydans*. [3-a] Although a high selectivity to DHA has been obtained with these processes, they present some notable disadvantages such as low productivity and high production costs. Moreover, glycerol and DHA have an inhibitory effect on microorganism growth. Therefore, many studies were devoted in the last years to develop environmentally friendly and highly efficient chemical catalytic methods for DHA synthesis, as alternatives to biochemical technologies.

As reported in the literature, the pH value of the media intensely influences the mechanism of formation of DHA and its stability. In the presence of an alkaline environment (pH > 8), DHA quickly interconverts to glyceraldehyde (Figure 2.16), which can be rapidly oxidized to glyceric acid. Indeed, when basic conditions are used the main product is always glyceric acid (Table 2.1). Therefore the design of a catalyst for selective glycerol oxidation to DHA cannot disregard that it has to operate under neutral or acidic conditions. Moreover DHA is not stable under pH > 7.5 undergoing retro-Claisen type reaction leading to its decarboxylation.

Although several studies focused on organometallic (soluble or heterogenized) catalysts or on TEMPO-mediated electrocatalysis, most of reports concerned principally supported noble metal nanoparticles. [4-a]

Figure 1.16 Interconversion scheme of the first oxidation products of glycerol (from Ref [19-a])
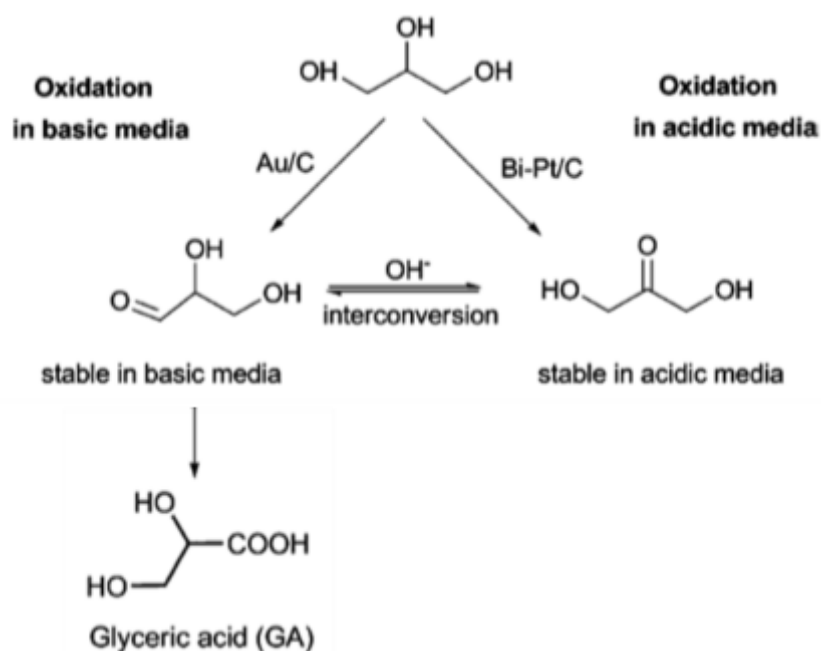
Since early 1990s, the use of platinum-based catalysts for oxidation of glycerol in acidic or neutral media has been reported to result in high selectivity to DHA.[23-24] Furthermore, in order to maximize the yield of dihydroxyacetone, the effect of different promoter (Bi, Pb, Ce) was investigated by Kimura et al. The introduction of promoters in platinum based catalysts resulted in a remarkable increase of the catalytic activity and a significant enhancement of the selectivity to DHA. In particular, according to the literature,[23] the best catalytic performances, in terms of activity and DHA yield, are exhibited by Pt-Bi system. The role of bismuth in activity and selectivity enhancement can be attributed to:

- Activation of oxygen to react directly with glycerol or intermediate;
- Formation of more active sites in alloy;
- Partial geometric blocking of some active sites, thus inhibiting the overoxidation;
- Complex formation between polyols and the promoter, that enhances the chemo- and regioselectivity (Figure 2.17);

Figure 2.17 Schematization of complex formation on catalyst surface in the presence of metal promoter in selective glycerol oxidation.
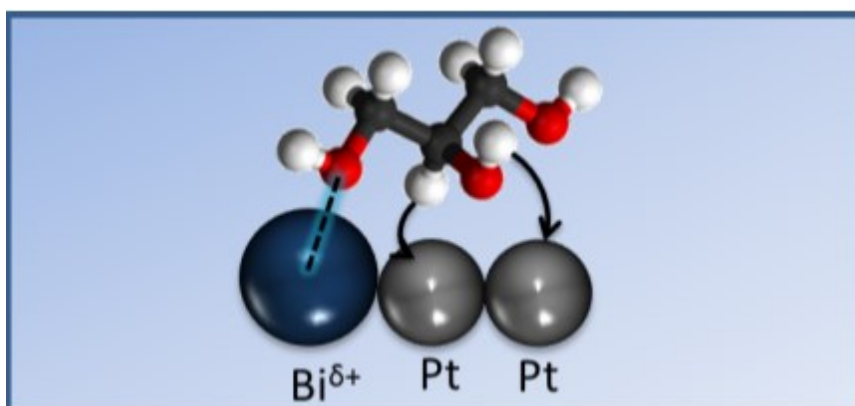
Although platinum-based catalysts favour the direct oxidation of the secondary hydroxyl group of glycerol, they suffer from deactivation phenomena as well as from drop of selectivity to DHA at high conversion. As extensively described in the previous sections, gold-based catalysts are more resistant to deactivation, but they require the presence of a base. It has been observed that the use of Au nanoparticles supported on activated carbon or multi-walled carbon nanotubes [59] in neutral conditions resulted in the preferential oxidation of glycerol secondary alcohol function, even if a low conversion was reached.

More promising results in terms of activity and stability have been obtained with bimetallic PdAg, AuPd and AuPt catalytic systems [60], as a consequence of synergistic effect.

On the basis of these considerations, the main goal we focused on, was the design of an effective and durable catalyst able to catalyse glycerol oxidation to DHA, trying to combine the knowledge acquired from the literature and the experience on the base-free glycerol oxidation previously gained (see Section 2.2).

In particular we investigated the effect of Bismuth addition to $1\%Au_6Pt_4/AC$, a stable and durable catalyst developed for the base-free liquid phase glycerol oxidation. Beside valuating the influence of the modification with bismuth on the selectivity, at the same time we would to prove the beneficial effect of AuPt alloy on the stability of Bi-AuPt/AC system compared to the classical Bi-Pt/AC catalyst extensively studied and used for this reaction.

Catalysts were prepared by sol immobilisation method, using a procedure reported in previous studies. Firstly bimetallic 1 wt.% Au_6Pt_4/AC catalyst was prepared by the two step procedure. As described in section 2.2 for AuPt nanoparticles supported on metal oxides, this procedure produces highly dispersed nanoparticles with alloyed structure of single composition, without any metal segregation and with a multiply twinned structure. Dimitratos et al. have demonstrated that similar results are obtained for AuM (M = Pd or Pt), when carbon is used as support.

The subsequent deposition of controlled amount of bismuth (0,1 wt. % or 1 wt.%) was made using preformed Bi nanoparticles with PEG-BDE as the protective agent. This procedure has been reported in the literature to enable a selective deposition of Bi on carbon supported AuPd nanoparticles without changing the morphology of alloy and without segregation on the support.[61]

The actual bismuth loading was verified by Inductively Coupled Plasma Atomic Emission Spectroscopy (ICP-AES) analysis, carried out by burning off the carbon, and it resulted to be consistent with the nominal values.

In order to investigate the effect of the modification with bismuth on the catalyst morphology, TEM images of unmodified AuPt/AC and Bi-AuPt/AC were collected (Figure 2.18).

Figure 2.18 TEM overview of AuPt/AC (a) and Bi$_x$-AuPt/AC (b) catalysts
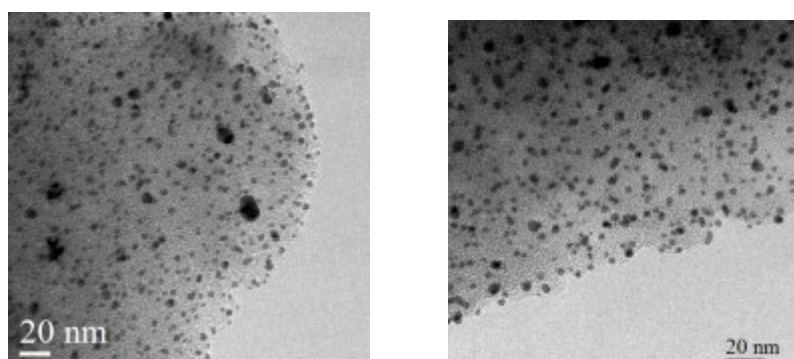
TEM analysis revealed that the deposition of preformed bismuth nanoparticles doesn't alter the alloy morphology, particle sizes and dispersion of AuPt/AC. In both cases, metal NPs are homogenously dispersed on the support and the mean size of pristine AuPt NPs (3,2 nm, see table 2.5) seems to remain similar also after the deposition of Bi (3.3-3,5 nm, Table 2.5).

Table 2.5 Statistical median and standard deviation of particle size analysis for AuPt and Bi-AuPt catalysts

Catalyst	Statistical median (nm)	Deviation standard (σ)
1 wt. % Au_6-Pt_4/AC	3.2	1.1
0,1 wt. % Bi - 1 wt. % Au_6-Pt_4/AC	3.3	1.1
1 wt. % Bi - 1 wt. % Au_6-Pt_4/AC	3.5	1.3

The composition of metal nanoparticles was investigated by EDS analysis. In the case of 0,1%Bi-AuPt/AC, the amount of bismuth was lower than the detection limit of the technique, in any case bismuth was quantified by ICP analysis and its content resulted in agreement with the nominal value, as reported above.

Conversely, in the case of 1 wt.%Bi-1 wt.%AuPt/AC, bismuth was present in higher amount and it was then detectable by EDS analysis. Figure 2.19 (a) shows a STEM overview image of 1%Bi-AuPt/AC. The STEM-EDX spectrum imaging of a considerable number of particles confirmed the presence of trimetallic particles, consisting of all the three metals (Figure 2.19, b). The quantification of Bi resulting from the integrated EDX spectrum of the whole mapping area revealed a lower bismuth concentration than the nominal value, although ICP analysis have proved the correctness of the nominal value. This discrepancy between the actual bismuth loading, as determined by ICP analysis, and the amount revealed by EDS can be explained by assuming that Bi is not homogeneously dispersed on the previously deposited nanoparticles.

The catalytic performances of AuPt/AC and Bi-AuPt/AC catalysts have been evaluated in the oxidation of glycerol in water under neutral conditions (0.3 M Glycerol solution, glycerol/metal = 500 mol/mol, 80°C, batch reactor) and compared with 5 wt.%Pt/AC (particle size 3.2 nm ± 1nm) and 1wt.%Bi-5%Pt/AC (particle size 3.6 nm ± 1.1 nm) commercial catalysts from Johnson Matthey, used as references. The similar particle distributions of commercial and homemade catalysts allow to exclude a possible influence of this parameter on the catalytic performances, as often happens in the case of structure-sensitive reactions.

Results of the batch reactions are reported in Table 2.6.

Table 2.6 Batch condition catalytic test results

Catalyst	Initial Activity [a] $\left(\frac{conv.\,mol}{mol_{AuPt}\cdot h}\right)$	Selectivity at 30% of conv. (S30)					Selectivity at 80% of conv. (S80)				
		GLYALD + GLYA	DHA	TA	HPA	C2 + C1	GLYALD + GLYA	DHA	TA	HPA	C2 + C1
5 wt. %Pt/AC	586	79	7	-	1	8	69	1	2	2	23
1 wt.% Bi-5 wt.%Pt /AC	914	32	53	1	10	4	31	35	3	7	23
1 wt. %AuPt/AC	541	79	8	2	1	6	80	4	2	1	8
0,1wt.%Bi-1%AuPt /AC	773	25	65	2	4	7	23	63	3	5	8
1wt.%Bi-1%AuPt /AC	585	22	58	1	4	16	20	56	3	5	18

Reaction conditions: 0.3 M glycerol, glycerol/metal = 500 mol mol^{-1}, 3 atm O_2, T = 80 °C.
[a] Moles of glycerol converted per hour per mole of the metal calculated after 15 min of reaction.
[b] Selectivity calculated at 30% conversion. GLYA = glyceric acid; GLYALD = glyceraldehyde; TA = tartronic acid; DHA = dihydroxyacetone; HPA = hydroxipyruvic acid; C2 = oxalic acid and glycolic acid; C1 = formic acid.

Figure 2.19 The overview STEM image of a) 1wt.%Bi-AuPt/AC, the red box represent the areas where the EDX spectrum was registered; b) EDX spectra from the selected area in a (top) and from the mapping area (bottom) c) element mapping on 1wt.%Bi-AuPt/AC with the integrated EDX spectrum from the mapping area.
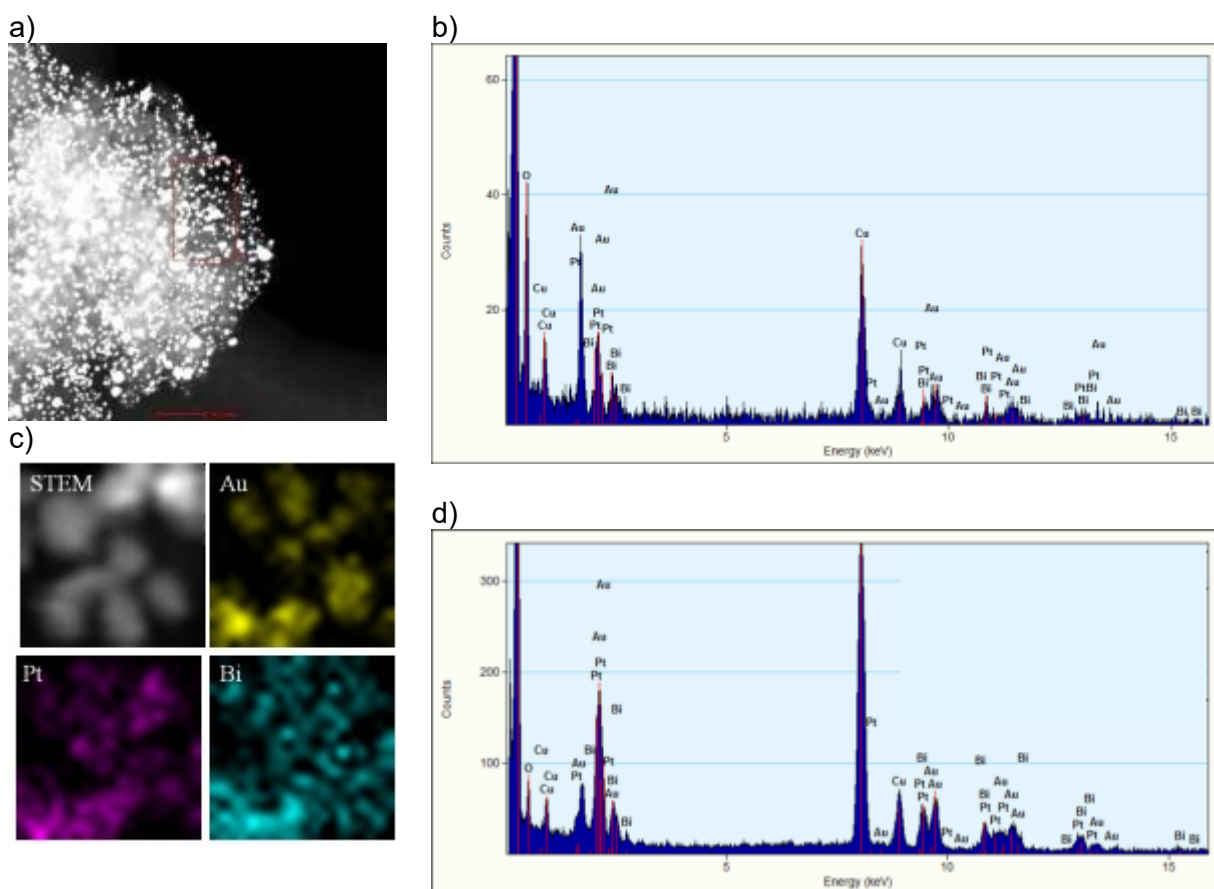
Looking at the activity values for commercial catalysts, the modification of bismuth results in a significant enhancement of the catalytic activity (586 h^{-1} versus 914 h^{-1} for Pt/AC and Bi-Pt/AC, respectively), confirming the promoting action of bismuth reported in the literature. The beneficial effect of bismuth on the selectivity to DHA is evident, as well. Indeed, considering the selectivity at 30% of conversion, the presence of bismuth is able to orientate the reaction pathway towards the oxidation of the secondary alcoholic function, thus resulting in an higher DHA production (S$^{30}_{DHA}$ = 53%) compared to Pt/AC catalyst (S$^{30}_{DHA}$ = 7%), which in turn selectively oxidise glycerol to glyceric acid and glyceraldehyde (S$^{30}_{GLYAC+GLYA}$ = 79%). Increasing the conversion (from 30% to 80%) a detrimental effect on the selectivity was observed. In both cases, at higher conversion (80%) the selectivity to C3 compounds dramatically dropped (for Pt/AC the selectivity to glyceric acid and glyceraldehyde decreases from 79% to 69%, whereas in the case of Bi-Pt/AC the selectivity to DHA drops from 53% to 35%), with the evident formation of a large amount of oxalic, glycolic and formic acids (C2 and C1). This drop is due to further oxidation and decomposition of DHA and glyceric acid

Interesting considerations can be made, by comparing these results with the ones obtained from the tests of bimetallic and trimetallic catalysts synthesized by sol immobilization. AuPt/AC showed similar activity (541 h^{-1}) and product distribution (with glyceric acid and glyceraldehyde as main products, S$^{30}_{GLYAC+GLYA}$ = 79%) as commercial Pt/AC (Table 2.6). However, the addition of gold positively affects the selectivity to C3 at higher conversion,

since no C1+ C2 products are formed with AuPt/AC, in contrast to Pt/AC; indeed, the selectivity to C3 compounds was maintained unaltered also at 80% of conversion (see Table 2.6). Such a behaviour might be ascribed to the presence of Au as modifier of Pt based catalysts. Indeed the beneficial effect of Au addition to Pt has been already reported for bimetallic systems in the literature, and it can be attributed to a selective blocking or a modification of specific active Pt sites by gold, as in the case of AuPd system [61].

Concerning the effect of Bi modification on AuPt based catalyst, the amount of bismuth seems to be a critical parameter. Indeed, surprisingly, by adding 1 wt% Bi to AuPt/AC the activity resulted almost unchanged (585 h^{-1}), on the contrary, by reducing to 0.1 wt% the content of Bi, an enhanced activity was observed (773 h^{-1}, see Table 2.6). A similar trend has been already reported for Bi-AuPd where a high amount of Bi (1–3 wt%) blocked a portion of AuPd active sites thus limiting the promotional action of added bismuth [61].

From a selectivity point of view, analogously to Pt/AC, the addition of Bi to AuPt/AC leads to an increased production of DHA. However, also in this case the amount of Bi plays a central role, influencing the selectivity to DHA: increasing the amount of Bi from 0.1wt.% to 1wt.%, the selectivity to DHA diminished from 65 to 58% at 30% of conversion (Table 2.6). These results are in good agreement with the ones of Kimura [23] reporting that a low Bi/Pt ratio is more suitable to maximize the DHA production. It is remarkable that trimetallic BiAuPt systems, independently of the amount of Bi, are able to maintain the good DHA selectivity also at high conversion (S^{80}_{DHA} is practically the same as S^{30}_{DHA}). Furthermore, XPS analyses on AuPt and BiAuPt systems evidenced that the addition of bismuth doesn't modify the electronic structure of Au or Pt. These observations seem to support the hypothesis that the effect of bismuth in switching the selectivity and promoting the DHA formation is just a consequence of a geometric rather than an electronic effect. [23-24]

The comparison of the reaction profiles of bimetallic Bi-Pt/AC (Fig. 2.20, a) and trimetallic 0.1wt.%Bi-1 wt.% AuPt/AC (Fig. 2.20, b) highlights the different behaviour of the two catalysts and the beneficial effect of gold modification on DHA production.

Figure 2.20 Reaction profiles of (a) 1wt.%Bi-5wt.%Pt/AC and (b) 0,1wt.%Bi-1wt.%AuPt/AC.
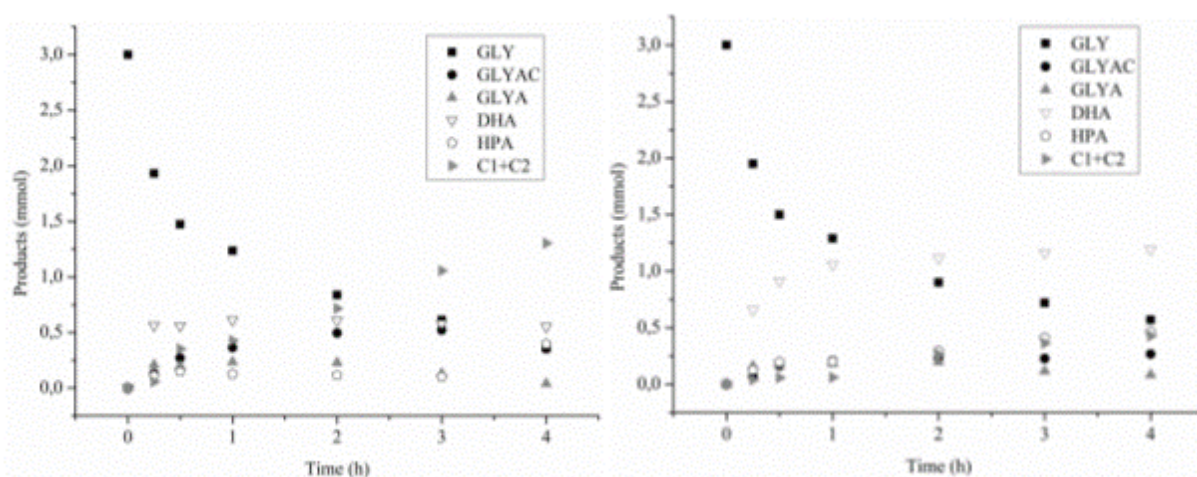
In the case of Bi-Pt, produced DHA moles initially increase, but after 30 min a plateau-like trend is assumed. On the contrary, in the case of trimetallic Bi-AuPt/AC the amount of DHA continuously increases with the conversion and the formation of C1 and C2 products was minimized. Considering the promising results obtained with 0.1wt.% Bi-AuPt/AC catalysts in terms of activity and stability, we decided to investigate also the stability of this catalytic system, in perspective of an eventual future industrial scale-up. Recycling test was

performed on 0.1wt.% Bi-AuPt/AC, by recovering the catalyst through filtration after each run (4 h reaction) and reusing it in the next run without any further treatment by adding a fresh glycerol solution. The stability of 0.1wt.% Bi-AuPt/AC was compared with the one of the commercial 1wt.%Bi-5wt.%Pt/AC under the same reaction conditions (Figure 2.21, a and b respectively).

Figure 2.21 Results of stability test for a)1wt.%Bi-5wt.%Pt/AC and b)0,1wt.%Bi-1wt.%AuPt/AC
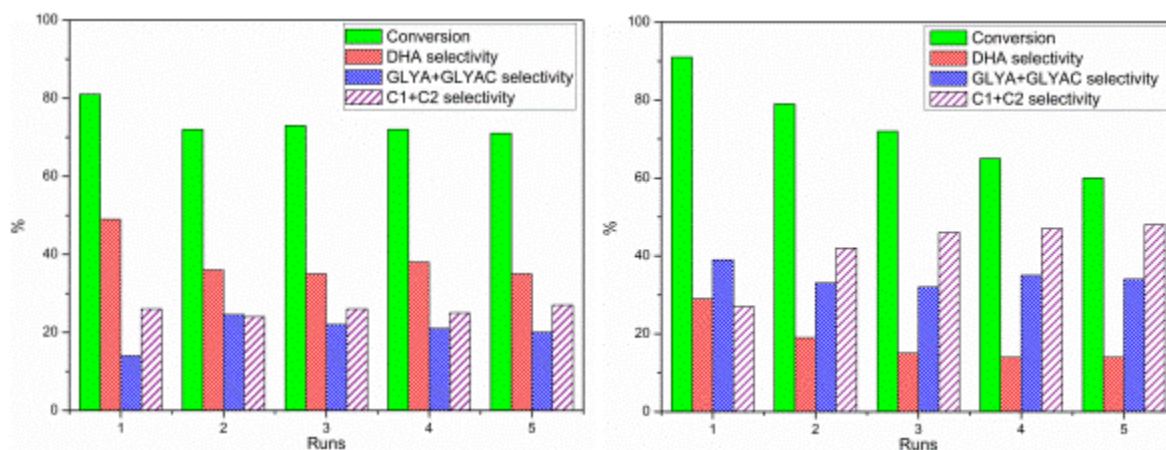
In the case of 0.1wt.%Bi-AuPt a drop of both activity and selectivity to DHA was revealed only from the first to the second run, while catalytic performance remained constant in the successive cycles (Fig. 2.21, a). On the contrary, using Bi-Pt/AC the activity and the selectivity to DHA of continuously decrease in the course of the stability test. The better resistance to deactivation detected for 0.1wt.% Bi-AuPt/AC compared to Bi-Pt/AC can be justified, by quantifying the eventual leached metal into the solution. ICP measurements were then performed on the filtered reaction media after each run, revealing for Bi-Pt/AC a continuous leaching of bismuth into the solution (−30% of the total Bi loaded after 5 cycles). Moreover, traces of platinum were also detected. In the case of 0.1wt.% Bi-AuPt/AC, the leaching of Bi occurred only after the first run (−10% of total Bi loaded), thus explaining the slight decline in the activity and selectivity, while it was almost undetectable in the successive runs. Neither Au nor Pt was found into the solution.

Finally we investigated the effect of bismuth as modifier in AuPd/AC catalysts. Indeed it has been reported in the literature that adding Bi to AuPd/AC catalysts leads to an improvement of the activity in glycerol oxidation in the presence of NaOH. Also the selectivity was influenced by the bismuth modification, since the further oxidation of glyceric acid to tartronic acid was favoured.[61] Therefore we decided to test AuPd/AC catalyst and Bi-modified AuPd/AC catalyst in base-free glycerol oxidation. The catalysts were prepared with the same procedure as Pt based ones and supported nanoparticles with particles size distribution similar to AuPt and BiAuPt were obtained (Table 2.7).

Table 2.7 Statistical median and standard deviation of particle size analysis for AuPd and Bi-AuPd catalysts

Catalyst	Statistical median (nm)	Deviation standard (σ)
1 wt. % Au_6-Pt_4/AC	3.2	1.1
0,1 wt. % Bi - 1 wt. % Au_6-Pt_4/AC	3.3	1.1
1 wt. % Bi - 1 wt. % Au_6-Pt_4/AC	3.5	1.3
1 wt. % Au_6-Pd_4/AC	3.4	1.4
0,1 wt. % Bi - 1 wt. % Au_6-Pd_4/AC	3.4	1.5

However, AuPd based catalysts appeared less active than the Pt ones (Table 2.8), probably due to a rapid deactivation. Moreover, the addition of 0.1 wt% of Bi did not provide the expected enhancement of activity previously observed, when the same amount of bismuth was added to AuPt catalyst (Table 2.6). In any case, also in this case the addition of Bi promoted the formation of DHA, by directing the reaction toward the preferential oxidation of the secondary alcoholic group.

Table 2.8 Batch condition catalytic test results

Catalyst	Activity[a] $\left(\frac{conv.\,mol}{mol_{AuPt}\cdot h}\right)$	Selectivity at 10% of conv. (S10)					Selectivity at 80% of conv. (S80)				
		GLYALD + GLYA	DHA	TA	HPA	C2 + C1	GLYALD + GLYA	DHA	TA	HPA	C2 + C1
1wt.% AuPd/AC	37	75	2	3	n.d.	17	n.d.	n.d.	n.d.	n.d.	n.d.
0,1wt.%Bi-1wt.%AuPd/AC	39	34	52	1	1	11	n.d.	n.d.	n.d.	n.d.	n.d.
1%AuPt/AC	541	79	8	2	1	6	80	4	2	1	8
0,1%Bi-1%AuPt /AC	773	25	65	2	4	7	23	63	3	5	8
1%Bi-1%AuPt /AC	585	22	58	1	4	16	20	56	3	5	18

Reaction conditions: 0.3 M glycerol, glycerol/metal = 500 mol mol^{-1}, 3 atm O_2, T = 80 °C.
[a] Moles of glycerol converted per hour per mole of the metal calculated after 15 min of reaction.
[b] GLYA = glyceric acid; GLYALD = glyceraldehyde; TA = tartronic acid; DHA = dihydroxyacetone; HPA = hydroxipyruvic acid; C2 = oxalic acid and glycolic acid; C1 = formic acid.

2.4 Selective Oxidation of Raw Glycerol Using Supported AuPd Nanoparticles

The transesterification of triglycerides with methanol for FAMEs production, using sodium (Na) or potassium (K) hydroxide as catalysts, or simply hydrolysis base/acid catalysed of triglycerides for fatty acid preparation produces a typical mixture that consists of glycerol (80%) and other contaminants, such as water, organic compounds (esters, alcohols, traces of free fatty acids) and inorganic salts.[1-3] During the subsequent catalytic transformations of glycerol these impurities could deposit on the active sites of the catalyst surface or alter the reaction pathway. For this reason, almost all catalytic processes for glycerol valorisation described in Section 2.1 require the use of pure glycerol as the reactant. Then crude glycerol has to undergo upgrading and refining steps, in order to remove residual organic compounds, water, salt and eventually alcohol. Many steps are involved in the purification process: industrial-grade glycerol with purity about 90% is firstly obtained by filtration, extraction, and distillation; subsequently, trace impurities and odors are separated by bleaching, deodorizing, and ion exchange treatments reaching a high purity up to 99.9%. As a consequence the purification of glycerol is a cost-intensive process and therefore it further burdens on the overall economy of biofuel manufacturing. Two different approaches can be followed: the one involving an heterogeneous catalyst for hydrolysis/transesterification of lipids; the second that focuses on the use of crude instead of pure glycerol. The first has been proposed by Institut Français du Pétrole (IFP)[3] and uses a Zn-Al mixed oxide.

In the second approach Skrzyńska et al. recently investigated the influence of crude glycerol impurities at various pH in liquid phase glycerol oxidation [62]. Konaka et al. [63] studied the effect of alkali metal ions in the crude glycerol conversion into allyl alcohol, by supporting different alkali metals, (Na, K, Rb, and Cs) on ZrO_2–FeO_X. The best catalytic results were obtained in the presence of K/ZrO_2–FeO_X where the amount of potassium appeared to be a crucial parameter: allyl alcohol is produced when 5 mol% K is supported on ZrO_2–FeO_X, whereas a higher amount has a detrimental effect on the catalytic performances.

Starting from these considerations, we decided to investigate and compare the catalytic performances of supported AuPd catalysts in the selective oxidation when either commercial glycerol or crude glycerol from the rapeseed oil transesterification are used as the substrate. The support effect was also investigated, by using as supports various carbonaceous materials with different textural and surface properties (such as activated carbon, carbon nanotubes (CNTs), carbon nanofibers (CNFs) and N-doped carbon nanofibers (N-CNFs)) and TiO_2 as representative of oxide materials.

AuPd catalysts were prepared by sol-immobilisation, using the two step-procedure for bimetallic nanoparticles, described in the previous sections. A nominal 1 wt. % total metal loading and an internal Au:Pd 6: 4 molar ratio were selected.

The morphology and particle size distribution of as-prepared catalysts were investigated by TEM (Table 2.9). AuPd nanoparticles on AC, CNTs and N-CNFs presented similar mean sizes (3.4, 3.5 and 3.7 nm for Au-Pd/AC, Au-Pd/CNTs and Au-Pd/N-CNFs, respectively), while bigger AuPd particles have been obtained with CNFs and TiO_2 as supports (4.5 and 4.1 nm for CNFs and TiO2, respectively).

Table 2.9 Statistical median and standard deviation of 1wt.% Au$_6$Pd$_4$ catalysts.

Catalyst	Statistical median (nm)	Deviation standard (σ)
1 wt. % Au$_6$-Pd$_4$/CNFs	4.5	1.5
1 wt. % Au$_6$-Pd$_4$/N − CNFs	3.7	0.9
1 wt. % Au$_6$-Pd$_4$/CNTs	3.5	1.3
1 wt. % Au$_6$-Pd$_4$/TiO$_2$	4.1	1.2
1 wt. % Au$_6$-Pd$_4$/AC	3.4	0.7

The composition and the structure of metal nanoparticles were studied by EDX analysis. AuPd nanoparticles supported on activated carbon showed an alloyed structure with an uniform composition. In the cases of TiO$_2$, N-CNFs and CNTs most of the nanoparticles were alloyed, even if the Au/Pd ratio was not homogeneous from cluster to cluster. Finally in 1wt.% Au$_6$Pd$_4$/CNF a partial segregation of Au and Pd was observed, as highlighted by the elemental mapping (Figure 2.22).

Figure 2.22 STEM image and element mapping on 1wt.% Au$_6$Pd$_4$/CNF.
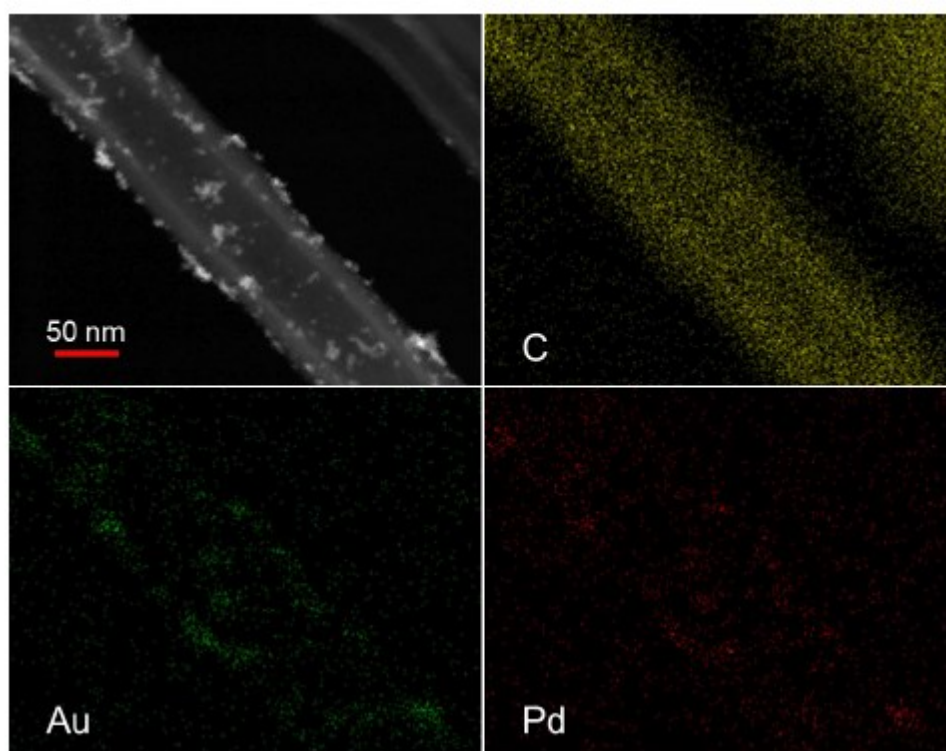
The catalysts were then tested in the aqueous phase oxidation of glycerol. In order to unravel the influence of glycerol purity on the catalytic performance, a commercial grade glycerol and raw glycerol without any pre-treatment were used as the reactant under the same reaction conditions. Raw glycerol was produced by the transesterification of rapeseed vegetable oil, carried out at 40 °C for 2h using KOH as the base. The composition of rapeseed vegetable oil was analysed by gas chromatography (GC); the chromatographic analysis revealed the presence of mono- and poly-unsaturated fatty acids: oleic acid (9-octadecenoic, C18:1), linoleic acid (9,12-octadecandienoic, C18:2), and the conjugated isomers thereof, and linolenic acid (9,12,15-octadecantrienoic, C18:3). Saturated fatty acids, namely palmitic acid (hexadecanoic acid, C16:0) and stearic acid (octadecanoic acid, C18:0), are present in less amount. (Table 2.10)

Table 2.10 Typical fatty acid composition of rapeseed oil

Oil	Fatty acids composition % by weight				
	Palmitic acid C16:0	*Stearic acid* C18:0	*Oleic acid* C18:1	*Linoleic acid* C18:2	*Linolenic acid* C18:3
Rapeseed	4.39	1.94	63.93	20.67	9.07

Catalytic tests were carried out in a batch reactor (glycerol 0.3 M, 50 °C, 3 atm O_2, glycerol/total metal 1000 mol/mol, NaOH/glycerol 4 mol/mol).

The initial activity, expressed as mol of converted glycerol per mol of metal per hour, calculated after 15 min of reaction, and the selectivity at 90% conversion are listed in Table 2. 11.

Table 2.11 Glycerol oxidation over 1wt.% Au6Pd4 NPs supported on carbon materials and oxides

Origin of glycerol	Catalyst	Activity[a] $\left(\frac{conv.\,mol}{mol_{AuPt} \cdot h}\right)$	Selectivity at 90% of conversion		
			Glyceric acid	**Tartronic acid**	**C2 +C1 products**
Pure glycerol	1 wt.% Au_6Pd_4/ AC	3205	77	5	14
	1 wt.% Au_6Pd_4/N - CNFs	1076	66	22	8
	1 wt.% Au_6Pd_4/CNTs	815	70	8	10
	1 wt.% Au_6Pd_4/ CNFs	675	78	11	9
	1 wt.% Au_6Pd_4/ TiO_2	628	79	8	12
Raw glycerol	1 wt.% Au_6Pd_4/ AC	1672	72	15	11
	1 wt.% Au_6Pd_4/N - CNFs	736	71	17	10
	1 wt.% Au_6Pd_4/CNTs	651	72	15	12
	1 wt.% Au_6Pd_4/ CNFs	269	81	8	10
	1 wt.% Au_6Pd_4/ TiO_2	230	78	10	10
Purified Raw glycerol	1 wt.% Au_6Pd_4/ AC	3150	75	7	15
	1 wt.% Au_6Pd_4/ TiO_2	598	79	3	14
Pure glycerol +fatty acids	1 wt.% Au_6Pd_4/ AC	1523	73	14	13
	1 wt.% Au_6Pd_4/ TiO_2	185	79	5	16

Reaction conditions: glycerol, 0.3 M; substrate/total metal = 1000 mol/mol; total volume, 10 mL; 4 eq NaOH; 50 °C; 3 atm O_2.
[a] Glycerol converted moles per hour per mole of metal, calculated after 15 min of reaction;

Considering the initial activity, the same trend was observed both with pure and raw glycerol, 1wt.%AuPd/AC being the most active catalysts (3205 mol/mol h and 1672 mol/mol h with pure and raw glycerol, respectively):

AC > N-CNFs > CNTs > CNFs > TiO_2.

The higher activity revealed for activated carbon supported nanoparticles confirm the findings that homogeneous alloys are more active than inhomogeneous ones in the alcohol oxidation as a consequence of a synergistic effect [34,39]. Indeed, despite a similar particle size (3.4–3.7 nm), 1 wt.%AuPd/AC is at least two-times more active than 1wt.% AuPd/N-CNFs (1076 mol/mol h and 736 mol/mol h with pure and raw glycerol, respectively) and 1wt.% AuPd/CNTs (815 mol/mol h and 651 mol/mol h). The lower activity values shown by CNFs and TiO_2 supported bimetallic catalysts can be ascribed to the larger particle sizes (4.5 and 4.1 nm) (Table 2). Particle sizes influenced also the selectivity: a higher selectivity to glyceric acid was observed for 1wt.% AuPd/CNFs and 1wt.% AuPd/TiO_2, in agreement with data from the literature reporting higher selectivity towards glyceric acid with larger particles [43-47]. However, as an exception, 1wt.% AuPd/AC gave a comparable selectivity as 1wt.% AuPd/CNFs and 1wt.% AuPd/TiO_2 despite smaller AuPd particle sizes (3.5, 4.1 and 4.5 nm for AuPd on AC, TiO_2 and CNFs, respectively). In this case the better selectivity to glyceric can be related to the homogeneous nature of the pure AuPd alloy [61].

Even if the same activity order was observed with pure and raw glycerol, in the latter case the activity was lower, probably due to the presence of impurities adsorbed onto the catalyst surface and partially blocking the active sites. In order to support this hypothesis, impurities deriving from the transesterification process were removed from raw glycerol. The purification process included the acidification with sulphuric acid in order to convert the soap into free fatty acids, the subsequent extraction of free fatty acids by hexane, and then, the methanol evaporation. The glycerol solution was then treated with activated carbon in order to remove free ions and finally filtered in order to separate the activated carbon.

As-purified glycerol was then used as the substrate in selective oxidation; the most active 1wt.% AuPd/AC and the less active 1wt.% AuPd/TiO_2 were selected as catalysts for the tests. Interestingly, similar results as the ones obtained with commercial pure glycerol were observed with both catalysts. In order to further prove the detrimental effect of impurities on catalytic performances, AuPd/AC and AuPd/TiO_2 have been tested using pure glycerol as substrate with the addition of rapeseed oil (10 wt.% with respect to glycerol). As expected, the results (Figure 2.23) confirmed the negative influence of fatty acids on the activity, the initial activity being even lower than the one obtained using raw glycerol. Looking at the reaction profiles for 1wt.% Au_6Pd_4/AC and 1wt.% Au_6Pd_4/TiO_2, reported as conversion/time curves, it appears clear that the reaction profile is strongly influenced by the purity of glycerol. Indeed, when the substrate is pure or purified glycerol, full conversion was obtained after 1 h, whereas in the presence of fatty acids, a lower activity was observed.

Figure 2.23 Reaction profile for pure glycerol, pure glycerol + 10% fatty acid, raw glycerol and purified glycerol using (a) 1% Au_6Pd_4/AC and (b) 1% Au_6Pd_4/TiO_2.

(a)　　　　　　　　　　　　　　　(b)
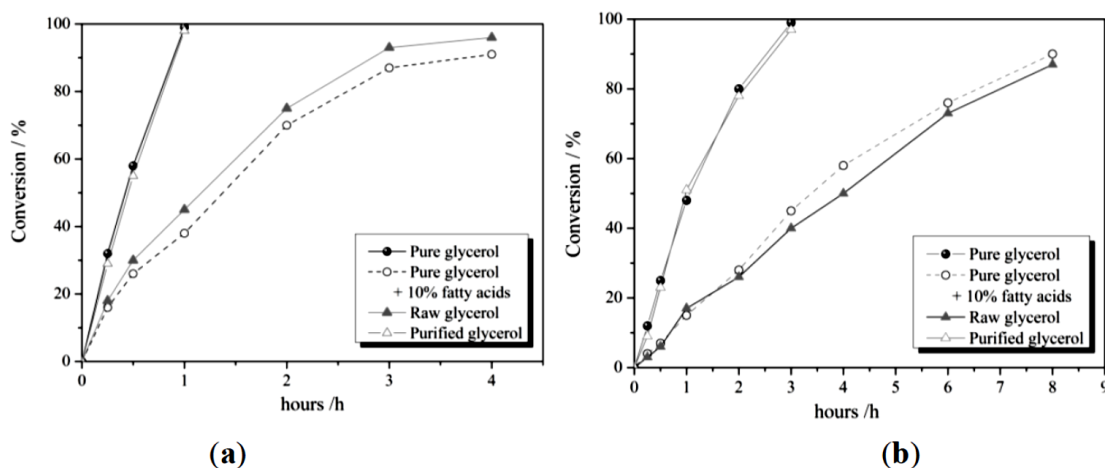
In order to clarify the role of impurities, Fourier transform infrared (FT-IR) spectra were registered for 1wt.% Au_6Pd_4/TiO_2 after reaction using both raw and pure glycerol. The choice of the catalyst is imposed by the optical properties of the carbon-based support making investigations through infrared spectroscopy more difficult. In any case the information provided by IR studies on 1wt.% Au_6Pd_4/TiO_2 can be extended also to the carbon-supported catalysts. The IR spectra collected on the used catalysts after reaction with pure and raw glycerol are shown in Figure 2.24.

Figure 2.24 FT-IR spectra of the used 1wt.% Au_6Pd_4/TiO_2 after glycerol oxidation.
Reaction conditions: glycerol, 0.3 M; substrate/total metal = 1000 mol/mol; total volume, 10 mL; 4 eq NaOH; 50 °C; 3 atm O_2. The catalyst was recovered after 6h reaction by filtration
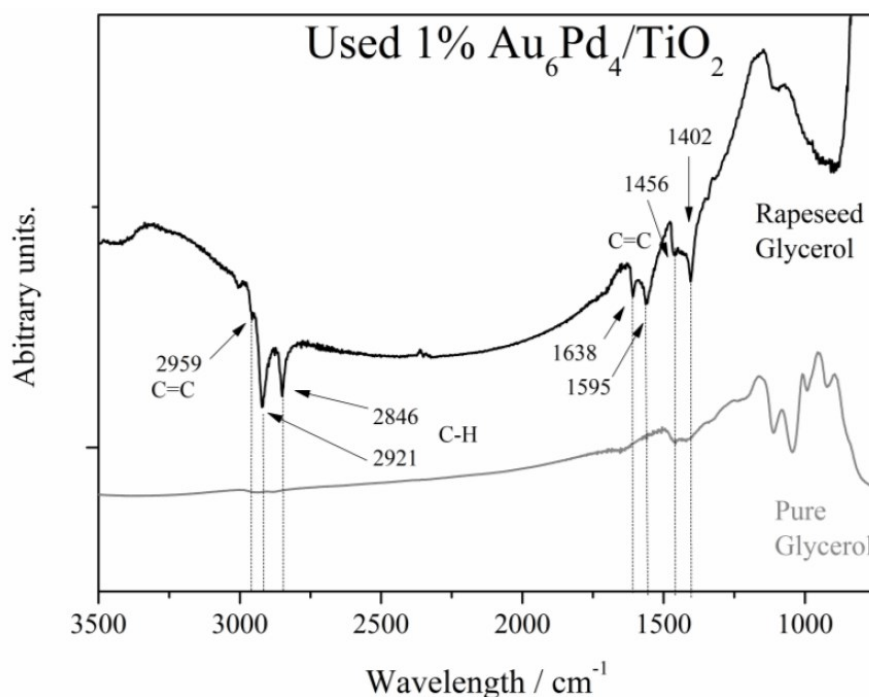
By comparing the IR spectra, some bands in common between the pure and the raw glycerol can be identified at 1456 and 1402 cm^{-1} and were assigned to O-H in plane stretching [64] and to C-O-H bending vibration [65], respectively. However, in the case of raw glycerol some additional signals are present. In particular, the bands at 2921 and 2846 cm^{-1} were attributed to the sp^3 asymmetric CH_2 stretch and the symmetric CH_2 stretch, respectively. According to Wu et al. [64], the band at 2959 cm^{-1} are associated to the sp^2 C-H stretch in C=C-H, thus revealing the presence of C=C. Moreover, a conjugated ν(C=C) stretch is highlighted by the bands at 1638 and 1595 cm^{-1}. The presence of these signals could be explained by the presence of some traces of unsaturated compounds, such as oleic, linoleic and linolenic acids in the raw glycerol. These species are not present in the IR spectrum of the catalyst used for the selective pure glycerol oxidation and therefore we can conclude that long unsaturated chains were adsorbed on the catalyst during the raw glycerol oxidation, blocking the access to the active sites, as already reported by Gil et al. [66].

The presence of impurities in the glycerol could also affect the durability of the catalyst. Recycling tests were therefore carried out using the most active catalyst, 1wt.% AuPd/AC, just by filtering the catalyst and adding a fresh solution of glycerol using purified and non-purified raw glycerol (Figure 2.25).

Figure 2.25 Evolution of the glycerol conversion over 1wt.% Au$_6$Pd$_4$/AC and over the eight runs using (a) the purified glycerol and (b) the non-purified glycerol directly obtained from transesterification of rapeseed oil.

Reaction conditions: glycerol, 0.3 M; substrate/total metal = 1000 mol/mol; total volume, 10 mL; 4 eq NaOH; 50 °C; 3 atm O$_2$; reaction time 6h.
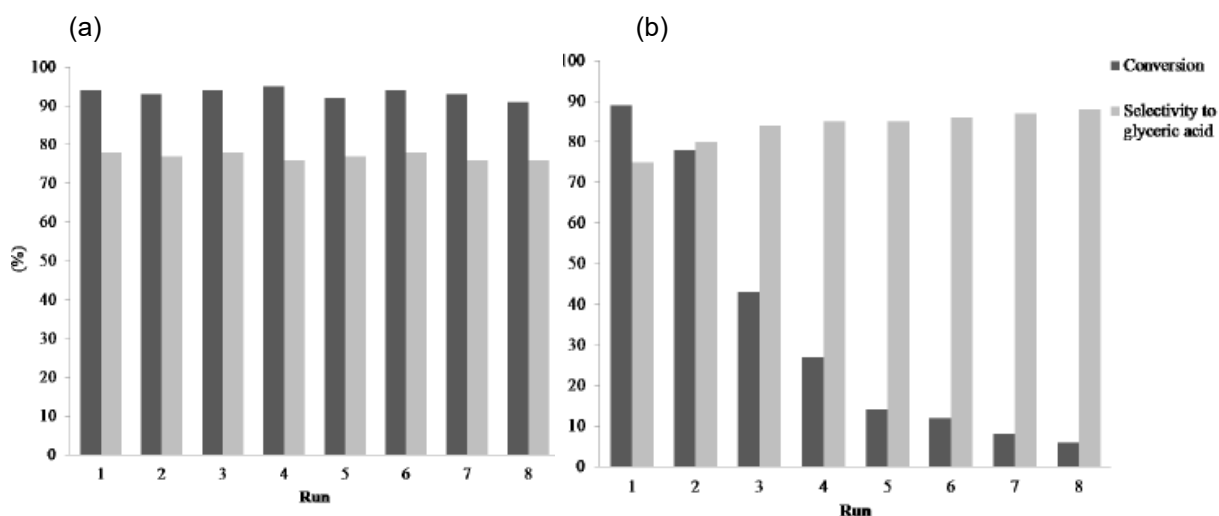
Figure 2.25 shows that, using purified glycerol the conversion (about 94%), as well as the selectivity to glyceric acid (around 77%) remained constant over the eight runs. Conversely, when the glycerol was not formerly purified, the activity of the catalyst rapidly drops from Run 1 to Run 8 (from 89% to 6%, respectively), probably due to the leaching of metal, as highlighted by ICP analyses of the final solution after the eight runs, revealing a loss of 15 wt% of total metal in the case of non-purified glycerol against only 1% in the case of the purified one. Surprisingly the selectivity to glyceric acid is constantly increasing (from 77% to 87%) along the eight successive reactions, the selectivity to glyceric acid. This evidence could be justified by an increase of the bimetallic AuPd particle sizes, as confirmed by TEM measurements (the mean particle size of the AuPd on the used catalysts increased from 3.4 to 4.7 nm), revealing the presence of aggregated AuPd particles in some regions (Figure 2.26). On the contrary, in the case of purified glycerol the morphology and sizes of the AuPd nanoparticles was unmodified during the stability test, (with AuPd mean sizes of 3.4 and 3.5 nm before and after the reaction, respectively).

Figure 2.26 TEM images of AuPd/AC (a) before and (b) after the recycling tests using raw glycerol.
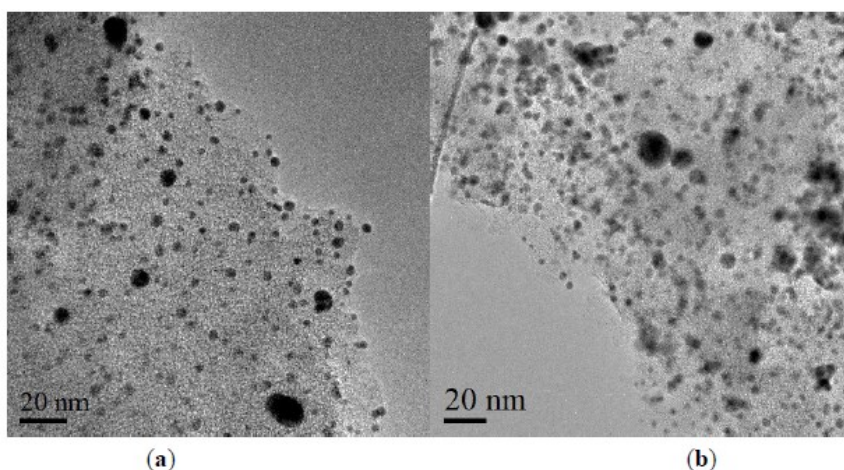
2.5 Conclusions

Tuning the selectivity in the catalytic oxidation of glycerol, an important bio-derived feedstock is an attractive challenge. Supported bimetallic AuPt nanoparticles are very effective catalysts for this transformation. Their catalytic behaviour is drastically influenced by the nature of the support in respect to both activity and selectivity. Basic supports (MgO and NiO) promoted the activity but also increased the C–C bond cleavage reactions, thus decreasing the selectivity to the desired products. In contrast, acidic supports showed a higher selectivity to C3 oxidation products. Spectroscopic and microcalorimetric measurements provided evidence that the catalytic activity and selectivity are not influenced by the nature of the acid sites but by their strength. In particular, a higher H-bonding strength enhances the catalytic activity and also stabilized labile intermediate like glyceraldehyde.

Alternatively, the addition of promoters can be used for tuning the selectivity in base-free glycerol oxidation. The modification with Bismuth is recognized to enhance the activity of monometallic Pt catalysts and to increase the selectivity to DHA, probably by selectively blocking on specific sites. We observed that a similar effect can be obtained in AuPt catalyst. Bi was successfully deposited in different amount (0.1%wt and 1%wt) on the AuPt nanoparticles without any evident segregation, producing Bi-AuPt trimetallic particles even the Bi distribution was not homogeneous. These catalysts were compared with the corresponding AuPd and Pt catalysts in the base-free oxidation of glycerol. In all cases the addition of Bi influenced the selectivity, promoting the DHA production. In particular, as already noted for Pd based catalysts, the best performance was obtained using a low Bi loading (0.1wt.%). In this latter case, an enhanced activity and an improved DHA selectivity were observed, thus suggesting that a low amount of bismuth is necessary for blocking the specific sites responsible for selectivity modification. In addition the presence of gold confers a good stability, preventing the leaching of bismuth. Indeed a stable selectivity with conversion was obtained (63-65% to DHA), whereas in the case of the most active commercial Bi-Pt/AC catalyst a drastic drop of selectivity to DHA was observed (S30=53% vst S80=35%), due to the leaching of bismuth. The improved durability of trimetallic catalysts was confirmed also in the recycling tests, where Bi-AuPt/AC resulted more stable in terms of activity and selectivity compared to a commercial Bi-Pt/AC catalyst showing limited leaching of bismuth.

Finally we also investigated the effect of the purity of glycerol, in order to assess the possibility to use directly raw glycerol as reactant, thus avoiding further expensive operation of purification. 1wt.%Au$_6$Pd$_4$ nanoparticles deposited on different supports were investigated in pure and raw glycerol. A general decrease in activity was observed when raw glycerol was used as the substrate. FT-IR results revealed the presence of traces of unsaturated fatty acids on the catalyst surface. These unsaturated compounds probably partially blocked the AuPd active sites, decreasing the activity. The effect of the nature of the glycerol was investigated on the durability of 1wt.% Au$_6$Pd$_4$/AC. A strong deactivation was observed in the presence of non-purified glycerol due to the agglomeration and leaching of the metal nanoparticles. On the contrary, the catalyst showed a good stability when purified glycerol was used.

References

[1] a) F. Baldiraghi, M. Di Stanislao, G. Faraci, C. Perego, T. Marker, C. Gosling, P. Kokayeff, T. Kalnes, R. Marinangeli, in *Sustainable Industrial Chemistry* (eds F. Cavani, G. Centi, S. Perathoner and F. Trifiró), 2009 Wiley-VCH Verlag GmbH & Co. KGaA, Weinheim, Germany. doi: 10.1002/9783527629114.ch8; b) K.T. Tcan, K.T. Lee, A.R. Mohamed,. *Bioresour. Technol*. 2010, 101(3), 965–969; c) Z. Yaakob, M. Mohammad, M. Alherbawi, Z. Alam, K. Sopian, *Renew. Sust. Energ. Rev*. 2013, 18, 184–193; d) M. Jerzykiewicz, I. Cwielag, W. Jerzykiewicz, *J. Chem. Technol. Biotechnol*. 2009, 84(8), 1196–1201; e) D.T. Johnson, K.A. Taconi, *Environ. Prog*. 2007, 26(4), 338–348

[2] a) D. Cespi, F. Passarini, G. Mastragostino, I. Vassura, S. Larocca, A. Iaconi, A. Chieregato, J.-L. Dubois and F. Cavani, *Green Chem.*, 2015, 17, 343–355; b) H. Pacini, A. Sanches-Pereira, M. Durleva, M. Kane and A. Bhutani, "The Emerging Biofuels Market: Regulatory, Trade and Development Perspectives", UNCTAD/DITC/TED/2013/8 United Nations Publication Copyright© United Nations, 2014.

[3] a) M. Pagliaro and M. Rossi, in The Future of Glycerol, 2nd edn (RSC Green Chemistry Book Series), 2010; b) R. Christoph, B. Schmidt, U. Steinberner, W. Dilla and R. Karinen, Glycerol., Ullmann's Encyclopedia of Industrial Chemistry, 2006 Wiley-VCH, Published Online: 15 April 2006, 10.1002/14356007.a12_477.pub2; c) W. J. A. Struyck, Glicerine-the global equation, inWorld Conference on Oleochemicals Into the 21st Century: Proceedings, The American Oil Chemists Society, 1991.

[4] a) C. H. Zhou et al., "Recent advances in catalytic conversion of glycerol," Catalysis reviews: science and engineering, vol. 55, pp. 369-453, 2013; b) F. Bauer and C. Hulteberg, *Biofuels, Bioproducts & Biorefining*, vol. 7, p. 43–51, 2013, c) M. Aresta, A. Dibenedetto, *J. Braz. Chem. Soc.*, 25 (12), 2014; d) B. Sels, E. D'Hondt, P. Jacobs in G. Centi, R. A. van Santen (eds.) "Catalysis for Renewables: From Feedstock to Energy Production", Chapter 11, 223-255, John Wiley & Sons, 2008, ISBN 3527621121, 9783527621125; e) "Future Climate Change." EPA. Environmental Protection Agency, n.d. Web. 17 Mar. 2013. <http://www.epa.gov/climatechange/science/future.html>

[5] a) S. Adhikari et al., *International Journal of Hydrogen Energy*, vol. 32, p. 2875 – 2880, 2007; b) E. L. Kunkes, R. R. Soares, D. A. Simonetti and J. A. Dumesic, *Applied Catalysis B: Environmental*, vol. 90, p. 693–698, 2009; c) V. Chiodo, S. Freni, A. Galvagno, N. Mondello and F. Frusteri, *Applied Catalysis A: General*, vol. 381, p. 1–7, 2010; d) A. Byrd, K. Pant and R. Gupta, *Fuel*, vol. 87, p. 2008, 2956–2960; e) B. Zhang, X. Tang, Y. Li, X. Y.D. and W. Shen, *International Journal of Hydrogen Energy*, vol. 32, p. 2007, 2367–2373.

[6] a) F. Jerome, Y. Pouilloux, J.Barrault, *Chemsuschem.*, 2008, 1(7), 586–613; b) A. Ramin, (2009) Flexible Glycerol Conversion Process. US Patent 2009054701A1; c) S. Zhu, Y. Zhu, S. Hao, H. Zheng, T. Mo, Y. Li, *Green Chem.* 2012, 14(9), 2607–2616; d) I. Furikado, T. Miyazawa, S. Koso, A. Shimao, K. Kunimori, K. Tomishige, Green Chem. 2007, 9(6), 582–588; e) I. Gandarias, P. L. Arias, J. Requies, M.B. Guemez, J.L.G. Fierro, *Appl. Catal., B Environ*. 2010, 97(1–2), 248–256.

[7] a) A. Behr, J. Eilting, K. Irawadi, J. Leschinski and F. Lindner, *Green Chemistry*, vol. 10, no. 1, pp. 13-30, 2008; b) M. Watanabe, T. Lida, Y. Aizawa, T. Aida, H. Inomata and Y. Lida, *Bioresource Technology*, vol. 98, p. 1285–1290, 2007; c) A. de Oliveira, S. Vasconcelos, J. R. de Sousa, F. de Sousa and Filho, *Chemical Engineering Journal*, vol. 168, p. 765–774, 2011; d) D. Cespi, F. Passarini, G. Mastragostino, I. Vassura, S. Larocca, A. Iaconi, A. Chieregato, J.-L. Duboise, F. Cavani, *Green Chem.*, 2015,17, 343-355.

[8] a) M. Dolores Soriano, P. Concepcion, J. Lopez Nieto, F. Cavani, S. Guidetti, C. Trevisanut, *Green Chemistry*, vol. 13, p. 2954–2962, 2011; b) A. Witsuthammakul and T. Sooknoi, *Applied Catalysis A: General,* Vols. 413-414, pp. 109-116, 2012.

[9] M. Guerrero-Perez and M. Banares, *Chemsuschem*, vol. 1, p. 511–513, 2008.

[10] a) V. Goncalves, B. Pinto, J. Silva and C. Mota, *Catalysis Today*, vol. 133–135, p. 673–677, 2008; b) P. Reddy, P. Sudarsanam, G. Raju and B. Reddy, *Catalysis Communications*, vol. 11, pp.

1224-1228, 2010; c) R. Luque, V. Budarin, J. Clark and D. Macquarrie, *Applied Catalysis B: Environmental*, vol. 82, p. 157–162, 2008; d) X. Liao, Y. Zhu, S. Wang and Y. Li, *Fuel Processing Technology*, vol. 90, pp. 988-993, 2009.

[11] a) A. M. Ruppert, J. D. Meeldijk, B. W. M. Kuipers, B. H. Erne and B. M. Weckhuysen, *Chemistry a European Journal*, vol. 14, p. 2016 – 202, 2008; b) M. Richter, Y. K. Krisnand, R. Eckelt and A. Martina, *Catalysis Communications*, vol. 9, p. 2112–2116, 2008.

[12] a) M. Di Serio, T. R. L. Casale, E. Santacesaria, *Energy Fuels*, vol. 24, pp. 4668-4672, 2010; b) J. Melero, G. Vicente, G. Morales, M. Paniagua, J. Moreno, R. Roldan, A. Ezquerro, C. Perez, *Applied Catalysis A: General*, vol. 346, pp. 44-51, 2008.

[13] a) G. Vicente, J.A. Melero, G. Morales, M. Paniagua, E. Martin, *Green Chem*. 2010, 12(5), 899–907; b) J. Deutsch, A. Martin, H. Lieske, *J. Catal*. 2007, 245(2), 428–435; c) S.B. Umbarkar, T.V. Kotbagi, A.V. Biradar, R. Pasricha, J. Chanale, M.K. Dongare, A.S. Mamede, C. Lancelot, E. Payen, *J. Mol. Catal. A: Chem*. 2009, 310(1–2), 150–158; d) V.R. Ruiz, A. Velty, L.L. Santos, A. Leyva-Perez, M.J. Sabater, S. Iborra, A. Corma, *J. Catal*. 2010, 271(2), 351–357; e) C.X.A. da Silva, V.L.C. Goncalves, C.J.A. Mota, *Green Chem*., 2009, 11(1), 38–41; f) B.L. Wegenhart, M.M. Abu-Omar, *Inorg. Chem*. 2010, 49(11), 4741–4743; g) C. Crotti, E. Farnetti, N. Guidolin, *Green Chem*. 2010, 12(12), 2225–2231; h) C.X.A. da Silva, C.J.A. Mota, *Biomass Bioener*. 2011, 35(8), 3547–3551.

[14] A. Dibenedetto, A. Angelini, M. Aresta, J. Ethiraj, C. Fragale and F. Nocito, *Tetrahedron*, vol. 67 , pp. 1308-1313, 2011.

[15] R. Bai, Y. Wang, S. Wang, F. Mei, T. Li and G. Li, *Fuel Processing Technology*, vol. 106, p. 2013, 209-214.

[16] M. Climent, A. Corma, P. De Frutos, S. Iborra, M. Noy, A. Velty and P. Concepcion, *Journal of Catalysis*, vol. 269, p. 140–149, 2010.

[17] J. Hu, J. Li, Y. Gu, Z. Guan, W. Mo, Y. Ni, T. Li and G. Li, *Applied Catalysis A: General*, vol. 386, p. 188–193, 2010.

[18] B. Bell, J. Briggs, R. Campbell, S. Chambers, P. Gaarenstroom, J. Hippler, B. Hook, K. Kearns, J. Kenney, W. Kruper, D. Schreck, C. Theriault and C. Wolfe, *Clean*, vol. 36, no. 8, pp. 657-661, 2008.

[19] a) H. Kimura et al., *Green Chemistry*, vol. 13, p. 1960–1979, 2011; b) A. Villa, N. Dimitratos, C. E. Chan-Thaw, C. Hammond, L. Prati, G. J. Hutchings, *Acc. Chem. Res*. 2015, 48, 1403−1412.

[20] Solvay Chemical Company, [Online]. Available: http://www.solvaychemicals.com/EN/Sustainability/Issues_Challenges/EPICEROL.aspx.

[21] H. Miya and M. Matsuda, Japan Patent Laid Open, 116415 (1977)

[22] a) T. Imanaka, H. Terasaki, A. Fujio and Y. Yokota, (Kao Corp. JP1992133500 (1992); b) T. Imanaka, H. Terasaki and A. Fujio, (Kao Corp.) JP1992149195 (1993).

[23] a) H. Kimura and K. Tsuto, *Appl. Catal., A*, 1993, 96, 217–228; b) H. Kimura and D. Keiichi, (Kao Corp.) JP1992-224983 (1992), US5274187 (1993), DE 4228487 A1; c) H. Kimura, *Appl. Catal., A*, 1993, 105, 147; d) H.Kimura,T. Imanaka,Y.Yokota, (KaoCorp.) JP199395253 (1994); e) H. Kimura, *Polym. Adv. Technol.*, 2001, 12, 69; f) H. Kimura, *J. Polym. Sci*., Part A: Polym. Chem., 1996, 34, 3615; g) H. Kimura, (Kao Corp.), JP1994315624, 1996, and JP1994253062, 1996; h) H. Kimura, *J. Polym. Sci., Part A: Polym. Chem.,* 1998, 36, 195; i) H. Kimura, (Kao Corp.) JP1994315623 (1996).

[24] a) R. Garcia, M. Besson and P. Gallezot, *Appl. Catal., A*, 1995, 127, 165–176; b) P. Fordham, M. Besson and P. Gallezot, *Appl. Catal., A*, 1995, 133, L179; c) P. Fordham, M. Besson and P. Gallezot, Catal. Lett., 1997, 46, 195–199; d) P. Gallezot, Catal. Today, 1997, 37, 405–418.

[25] L. Prati and M. Rossi, J. Catal., 1998, 176, 552–560.

[26] S. Carrettin, P. McMorn, P. Johnston, K. Griffin andG. J. Hutchings, Chem. Commun., 2002, 696-697

[27] T. Takei, T. Akita, I. Nakamura, T. Fujitani, M. Okumura, K. Okazaki, J. Huang, T. Ishida, M. Haruta Advances in Catalysis, 55, B.C. Gates, F.C. Jentoft ed., Elsevier, Chapter 1, 1-124 (2012)

[28] Conte, M.; Miyamura, H.; Kobayashi, S.; Chechik, V. J. Am. Chem. Soc. 2009, 131, 7189–7196.

[29] P. Fristrup, L. B. Johansen, C. H. Christensen, Chem. Commun., 2008, 2750–2752

[30] A.Abad, P. Concepcion, A. Corma, H. Garcia, *Angew. Chemie.*. **44**, 4066,(2005)

[31] A.Abad, A. Corma, H. Garcia, Chem. Eur. J. 2008, 14, 212 – 222

[32] a) Liu, Z. P.; Hu, P.; Alavi, A. J. Am. Chem. Soc. 2002, 124, 14770–14779; b) Wittstock, A.; Neumann, B.; Schaefer, A.; Dumbuya, K.; Kubel. C.; Biener, M. M.; Zielasek, V.; Steinruck, H. P.; Gottfried, J. M.; Biener, J.; Hamza, A.; Baumer, M. J. Phys. Chem. C 2009, 113, 5593–5600; c) Meyer, R.; Lemire, C.; Shaikhutdinov, S. K.; Freund, H. Gold Bull. 2004, 37, 72.

[33] a) B.N. Zope, D.D. Hibbitts, M. Neurock, R.J.Davis, Science (2010) 330, 74-8; b) M.S. Ide and R.J. Davis, *ACCOUNTS OF CHEMICAL RESEARCH*, Vol. **47**, No. 3, 825–833 (2014)

[34] a) C. Bianchi,; P. Canton,; N. Dimitratos,; F. Porta, L. Prati, *Catal. Today* 2005, 102, 203−212; b) N.; Dimitratos, C. Messi, F. Porta, L. Prati, A. Villa, *, J. Mol. Catal. A: Chem*. 2006, 256, 21−28; c) D. Wang, A. Villa, F. Porta, D. Su, L. Prati, *Chem. Commun*. 2006, 18, 1956−1958.; d) L. Prati, A. Villa, F. Porta, D. Wang, D.S. Su, *Catal. Today* 2007, 122, 386−390; e) A. Villa, C. Campione, L. Prati, *Catal. Lett*. 2007, 115, 133−136; f) D. Wang, A. Villa, F. Porta, L. Prati, D.S. Su, *J. Phys. Chem. C* 2008, 112, 8617−8622; g) N. Dimitratos, J. A. Lopez-Sanchez, G. J. Hutchings, *Top. Catal.* 2009, 52, 258−268; h) N. Dimitratos, J. A. Lopez-Sanchez,; J. M. Anthonykutty, G. Brett, A. F. Carley, R. C. Tiruvalam, A. A. Herzing, C. J. Kiely, D. W. Knight, G. J. Hutchings, *Phys. Chem. Chem. Phys*. 2009, 11, 4952−4961

[35] a) M. Besson, A. Blackburn, P. Gallezot, O. Kozynchenko, A. Pigamo, S. Tennison, Top. Catal., 2000, 13, 253; b) J. Gao, D. Liang, P. Chen, Z. Hou and X. Zheng, Catal. Lett., 2009, 130, 185–191; c) E. Auer, A Freund, J. Pietsch and T. Tacke, *Appl. Catal., A,* 1998, 173, 259–271; d) F. Porta, L. Prati, M. Rossi, S. Coluccia and G. Martra, *Catal. Today*, 2000, 61, 165–172.

[36] a) S. Demirel, K. Lehnert, M. Lucas and P. Claus, *Appl. Catal., B*, 2007, 70, 637; b) S. Demirel, P. Kern, M. Lucas and P. Claus, *Catal. Today*, 2007, 122, 292–300.

[37] J. Gao, D. Liang, P. Chen, Z. Hou and X. Zheng, *Catal. Lett*., 2009, 130, 185–191.

[38] D. Liang, J. Gao, J. Wang, P. Chen, Z. Hou and X. Zheng*, Catal. Commun*., 2009, 10, 1586.

[39] L. Prati, A .Villa, C.E. Chan-Thaw, R. Arrigo, D.Wang, D.S. Su, *Faraday Discuss.,* (2011), 152: 353-65.

[40] I. Sobczak, K. Jagodzinska and M. Ziolek, *Catal. Today*, 2010, 158,121–129.

[41] A. Villa, A. Gaiassi, I. Rossetti, C. L. Bianchi, K. van Benthem, G. M. Veith and L. Prati, *J. Catal*., 2010, 275, 108–116.

[42] A. Villa, G.M. Veith, D. Ferri, A. Weidenkaff, K.A. Perry, S. Campisi, L. Prati, *Catal. Sci.Tech*., 2013, 3, 394-9.

[43] N. Dimitratos,A. Villa, C. L. Bianchi, L. Prati and M. Makkee, *Appl. Catal. A*, 2006, 311, 185–192.

[44] F. Porta and L. Prati, *J. Catal*., 2004, 224, 397–403.

[45] D. Wang, A. Villa, D. Su, L. Prati and R. Schlog, *ChemCatChem*, 2013, vol. 5, 2717 – 2723.

[46] W.C.Ketchie,Y.-L. Fang, M. S.Wong,M.Muryama andR. J.Davis, *J. Catal*., 2007, 250, 94–101.

[47] S. Demirel-Guelen, M. Lucas and P. Claus, *Catal. Today*, 2005, 102–103, 166.

[48] A. Villa, C. E. Chan-Thaw, G. M. Veith, K. L. More, D. Ferri and L. Prati, *ChemCatChem*, 2011, 3, 1612.

[49] a) A. Tsuji, K. Tirumala, V. Rao, S. Nishimura, A. Takagaki and K. Ebitani, *ChemSusChem*, 2011, 4, 542; b) A. Takagaki, M. Nishimura, S. Nishimura, K. Ebitani, *Chem. Lett*. 2011, 40, 150-152.

[50] A. Villa, G.M. Veith and L. Prati, *Angew. Chem. Int. Ed*. 49 (2010) 4499-4502.

[51] G. L. Brett, Q. He, C. Hammond, P. J. Miedziak, N. Dimitratos, M. Sankar, A. A. Herzing, M. Conte, J. A. Lopez-Sanchez, C. J. Kiely, D. W. Knight, S. H. Taylor, and G. J. Hutchings*, Angew. Chem. Int. Ed*. 50 (2010) 10136.

[52] N. Dimitratos, A. Villa, D. Wang, F. Porta, D. Su and L. Prati, *Journal of Catalysis* 244 (2006) 113-121.

[53] a) C. Morterra, G. Meligrana, G. Cerrato, V. Solinas, E. Rombi, M. F. Sini, *Langmuir*, 2003, 19, 5344; b) C. Morterra, G. Cerrato and G. Meligrana, *Langmuir*, 2001, 17, 7053

[54] E.B. Wilson, Jr., *Physical Review*, 1934, 45, 706-714

[55] C.H. Kline, J. Turkhevich, *J. Chem. Phys*. 12 (1944) 300.

[56] D. Stošić, S. Bennici, J.-L. Couturier, J.-L. Dubois, A. Auroux, *Catal. Commun*., 2012, 17, 23.

[57] A. Zecchina, L. Marchese, S. Bordiga, C. Pazè, E. Gianotti, *J. Phys. Chem*., 1997, 101, 1012.

[58] J. Datka and K. Góra-Marek, *Catal. Today*, 2006, 114, 205–210.

[59] Rodrigues, E.G.; Pereira, M.F.R.; Delgado, J.J.; Chen, X.; Orfao, J.J.M., *Catal. Commun*. 2011, 16(1), 64–69

[60] Hirasawa, S.; Nakagawa, Y.; Tomishige, K., Cataly. Sci. Technol. 2012, 2(6), 1150–1152

[61] A. Villa, D. Wang, G. M. Veith, L. Prati, *J. Catal*. 292 (2012) 73.

[62] Skrzyńska, E.; Wondołowska-Grabowska, A.; Capron, M.; Dumeignil, F. *Appl. Catal. A* 2014, 482, 245– 257.

[63] Konaka, A.; Tago, T.; Yoshikawa, T.; Nakamura, A.; Masuda, T., *Appl. Catal. B* 2014, 146, 267–273.

[64] Wu, N.; Fu, L.; Su, M.; Aslam, M.; Chun Wong, K.; Dravid, V.P., *Nano Lett*. 2004, 4, 383–386.

[65] Nor Hidawati, E.; Mimi Sakinah, A.M., *Int. J. Chem. Environ. Eng*. 2011, 2, 309–313.

[66] a) Gil, S.; Marchena, M.; Sánchez-Silva, L.; Sánchez, P.; Romero, A.; Valverde, J.L., *Chem. Eng. J*. 2011, 178, 423–435; b) Gil, S.; Marchena, M.; María Fernández, C.; Sánchez-Silva, L.; Romero, A.; Valverde, J.L.,*Appl. Catal. A* 2013, 450, 189– 203.

3 *Operando ATR-IR study as a suitable tool to investigate the catalytic active site: The case of Benzyl alcohol oxidation*
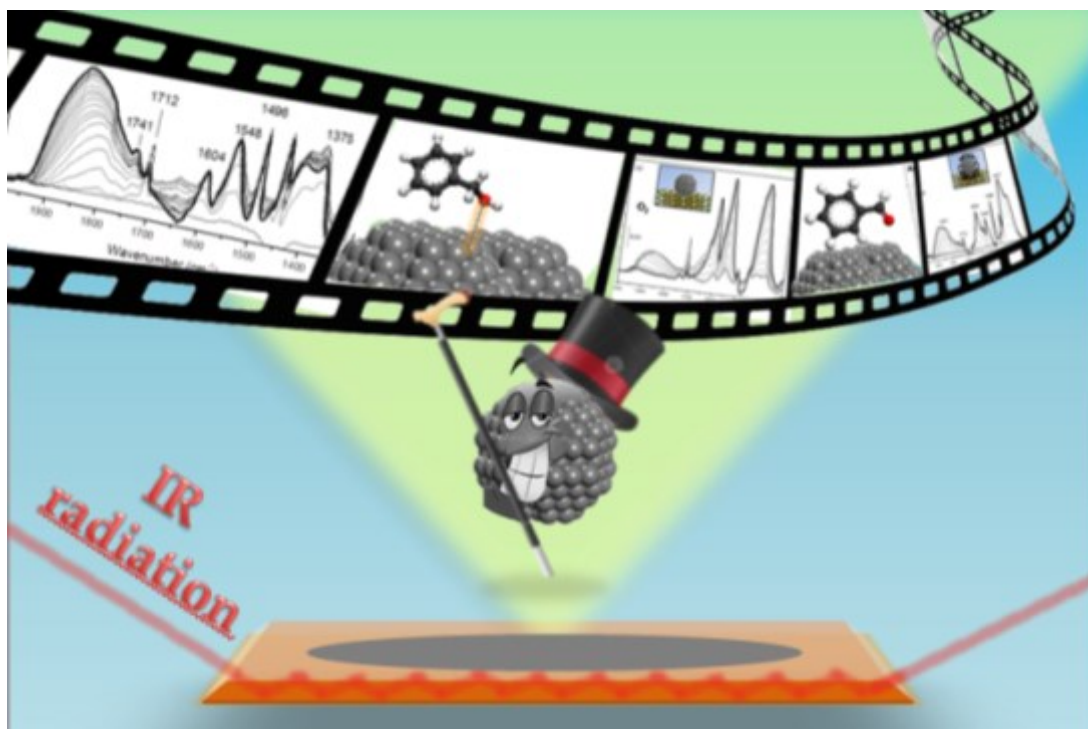
3.1 Attenuated Total Reflection Infrared Spectroscopy: an emerging tool for probing catalytic solid-liquid interfaces

"Catalysis is a science that cannot be understood without spectroscopy. Spectroscopy is the enabling tool for the knowledge-based design of catalysts."

Miguel A. Bañares (From Ref.[1])

From an industrial point of view the catalyst design consists in developing a catalytic system possessing some essential properties, such as activity, selectivity, high stability and regenerability. A high catalytic activity implies mild operating conditions (minimizing energy consumption); a high selectivity improves mass use, reducing environmentally noxious emissions. Durability and ease of regeneration assure a long catalyst life. Such a development process requires intensive and expensive testing and evaluations in order to establish empirical correlations between catalyst structural properties (catalyst composition, particle size and shape and pore dimensions) and catalytic efficiency.

The most common approach is the so-called Edisonian (trial-and-error) process [2]. Firstly the catalytic behaviour in terms of activity and selectivity is evaluated as a function of a set of experimental parameters (reaction temperature, reaction pressure, catalyst composition, class of support, etc.). In this phase the one variable at a time (OVAT) approach is usually used: only one parameter is progressively varied, while keeping all the other variables constant. Secondly the textural, morphological and surface properties of catalysts are characterized using different analytical tools.[3]

An example of this approach can be found in Chapter 2, where catalytic performances of bimetallic AuPt nanoparticles have been measured in base-free glycerol oxidation as a function of support nature, temperature, amount of promoter and purity of substrate; then the experimental results have been related to morphological and surface properties of catalysts as determined by different characterization techniques (FT-IR, XRD, XPS, TEM, EDS, Microcalorimetry).

Nevertheless, this kind of approach fails in providing all the essential elements for a rational design. Indeed any attempt for improving solid catalyst design should be based on the definition of the quantitative structure–activity relationships (QSARs), requiring insight into the reaction mechanism at molecular level and a detailed description of the active sites. For this purpose the main goal of catalyst characterization should be to provide atomic scale information about the exact structure of the catalytic surface (composition, lattice parameters, morphology, defects and steps, the exact position of promoter atoms).

However, regardless its initial structure, the catalyst is affected by its environment and therefore it will change under reaction conditions. Differences can be revealed for the same catalyst under different conditions. Indeed solid materials undergo physical and chemical modification under reaction conditions (temperature, pressure, pH, solvent, reactants) and active sites can be subjected to dramatic changes. In addition, usually characterization experiments are performed at room temperature (or liquid nitrogen or helium temperature) and in many cases under vacuum (ultra-high vacuum, UHV), thus resulting in an unbridgeable gap (see Chapter 1) between catalytic tests (high temperatures, high pressures) and characterizations (r.t. and UHV).

To circumvent this mismatch, characterization should be ideally carried out under realistic catalytic conditions or conditions close to operation conditions and, more preferably, with simultaneous activity/selectivity determination. This is the field of *in situ* and *operando* characterization. The former term derives from a Latin phrase and could be translate as "on site", "locally", the latter derives from the gerund of Latin verb *operare*, meaning operating or working. Both terms are often indiscriminately used. In fact the difference between *in situ* characterization and *operando* characterization have been debated during the past few years [4] without reaching an unanimous consensus.

The term *in situ* characterization and in particular *in situ* spectroscopy historically precedes the term *operando* and it is still much more common. Originally it was employed to describe experiments devoted to investigate structural properties of catalysts under reaction conditions. Rigorously, an ideal *in situ* experiment should be able to penetrate with a hypothetical probe inside an industrial reactor to disclose details of a chemical reaction (changes in active site structure, transition states, evolution of intermediates). At the same time, the information on the state of a catalyst at atomic scale (oxidation state and composition of the adsorbate layer) should be correlated with catalytic outcomes, such as activity, product distributions and selectivity in order to reveal structure-activity and structure-selectivity relationships. In other words, "It would have a very fine time resolution, enabling it to follow the temporal evolution of all spatial and compositional variables".[2] Borrowing a

very eloquent metaphor proposed by Weckhyusen [5] and exactly in line with recent social trends, the perfect in situ experiment should act as a photocamera filming the entire life cycle of a heterogeneous catalyst with the capability of zoom-in and zoom-out so as to focus on both the active sites at atomic scale and the macroscopic phenomena. Such an experiment is of course just a dream, however it is possible to approach the ideal experiment by combining complementary analytical tools and by simulating industrial conditions by a proper design of the reactor, which in this case is also the measure cell. Probably the most-remarkable progress in this field derived from the development of operando spectroscopy.

The term "*operando* spectroscopy" (or more generally "operando methodology") was introduced only recently to describe techniques which combine in situ spectroscopic characterization of a catalytic material during a reaction (in real time and under reaction conditions) with the simultaneous monitoring and measurement of the catalytic performances (activity/selectivity) in the same experiment, on the same sample and in an in situ cell fitted to a reaction-product analysis system. [6]

The combination of several operando measurements in a single experiment has been successfully proposed [7], moreover due to software and hardware progress in the last few years, the computational modelling is now able to match and rationalize results from in situ and operando studies. In any case, the accuracy and the validity of operando methodology depend on the observance of some requirements. First of all, the catalytic data (activity and selectivity) measured in the operando analysis should be consistent with those revealed in the conventional reactor. The second requirement concerns the match between the information that can be gained from the analysis and its relevance in the catalytic process. Thus, since in a heterogeneously catalysed reaction main phenomena occur at the surface, the characterization requires the investigation of an interface. Therefore a hypothetical characterization tool will be a valid candidate for operando methodology in so far as it is topically restricted, i.e. it is able to selectively probe just the region near to the interphase thereby minimising the contribution from the bulk (gas or liquid in contact to the catalyst surface). In contrast to solid-gas interfaces, probing catalytic solid-liquid interfaces is often challenging. From this point of view vibrational spectroscopy and in particular Attenuated Total Reflection Infrared Spectroscopy (ATR-IR) is a potential toool for fundamental investigations of these interfaces at work.[8]

In fact, vibrational spectroscopy is a non-invasive tool particularly sensitive to molecular structure, conformation and changes in the electronic density and therefore it provides detailed information about the nature of the interactions with the surface, the adsorption geometry and the reciprocal interactions between adsorbates. Attenuated Total Reflection Infrared Spectroscopy (ATR-IR) is particularly indicated for the investigation of solid-liquid interfaces. The surface-sensitivity of this technique is a consequence of the very short path length used. Principles of ATR-IR spectroscopy are illustrated in fig. 3.2.It is based on the attenuation of an evanescent electromagnetic field generated by multiple internal reflections of infrared radiation.[9]

When an IR radiation propagates through a transparent medium (characterized by a refractive index n_1) at an angle of incidence (θ) larger than the critical angle defined by Snell's Law (Equ. 3.1), total reflection occurs at the interface with a second material, optically less dense (i.e. characterized by a refractive index n_2, with $n_1 > n_2$).

$$\sin(\theta_c) = \frac{n_1}{n_2}$$
<div align="right">3.1</div>

An exponentially decaying evanescent electromagnetic field is generated at the interface between the two materials.

The intensity (E) of the electromagnetic field decays exponentially with the distance from the interface. The distance from the interface where the amplitude of the EM field drops to 1/e of its original value (E_0) is called penetration depth and depends on the wavelength of the incident radiation, on the angle of incidence and on the refractive indices of the materials in contact, according to equation 3.2

$$d_p = \frac{\frac{\lambda}{n_1}}{2\pi\sqrt{sin^2\theta - \left(\frac{n_2}{n_1}\right)^2}} = \frac{\lambda_1}{2\pi\sqrt{sin^2\theta - n_{21}^2}} \qquad 3.2$$

Generally **d_p** is on the order of 1µm.

The element with higher refractive index is called Internal Reflection Element (IRE) and it is typically a transparent crystal (Germanium, ZnSe and diamond are the most common). The geometry of IRE can be properly shaped so as to increase the effective pathlength of the reflected radiation (parallelepiped.shaped and trapezoidal are more frequently used), thus obtaining the multiple internal reflection (MIR) technique, in which several reflections take place inside the IRE (Figure 3.1).

Figure 3.1 Attenuated Total Reflection setup
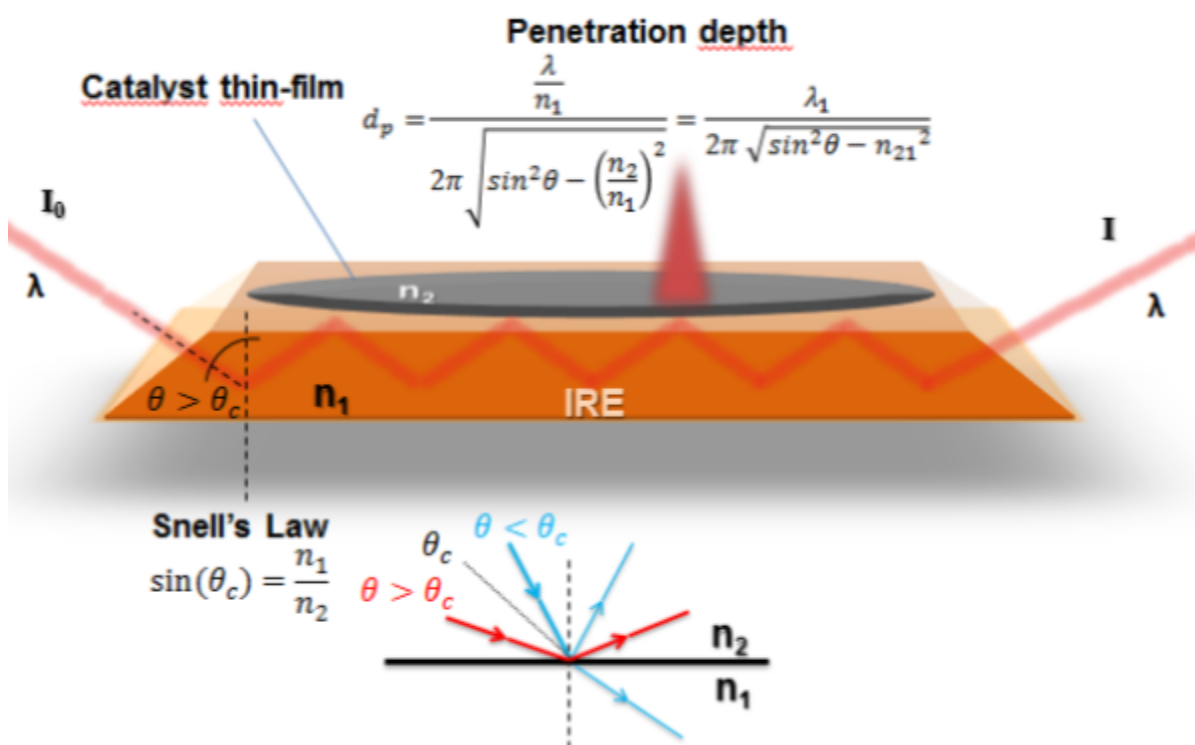
In a typical ATR-IR analysis the sample (catalyst powder) is deposited as thin-film on the IRE and located into an appropriate cell. During the experiment, the evanescent field penetrates into the sample (catalyst film surrounded by the liquid reaction medium) and is attenuated by it, thus resulting in the corresponding IR spectrum. The equation describing the penetration depth in this case is more complicated than Equ. 3.2 (valid only for a two-phase system) and it is not reported here. Another important parameter is the effective thickness (d_e), which represents the equivalent path length in an ideal Transmission IR experiment (TIRS) yielding the same absorption as in the ATR experiment (Equ. 3.3).

$$d_e = \frac{n_{21}E_0^2 d_p}{2cos\theta}$$

It is essential that the thickness of the layer is in the same order as the effective thickness (i.e. a few microns).

Excluded the invariable parameters imposed by the experimental setup (wavelength, the refractive index of the sample, the amplitude of the EM field), the effective thickness and hence the surface sensitivity can be tuned by properly selecting the material and the shape of the IRE.

The first application of the ATR-IR spectroscopy to study adsorption and reactions at the interface between solids and liquids was reported in 1986 [10] and it has been extensively used ever since with other spectroscopic techniques for performing operando experiments.

Several efforts were devoted to improving the design of in situ-ATR cell, starting from the horizontal ATR prototype invented by Messerschmidt [11]. Main configurations of commercial available ATR-IR accessories are shown in fig. 3.2. These systems can be heated up to ~200∘C and can resist up to 200 bar.[12]

Figure 3.2 Possible design for ATR-IR Cell (From Ref.[13])
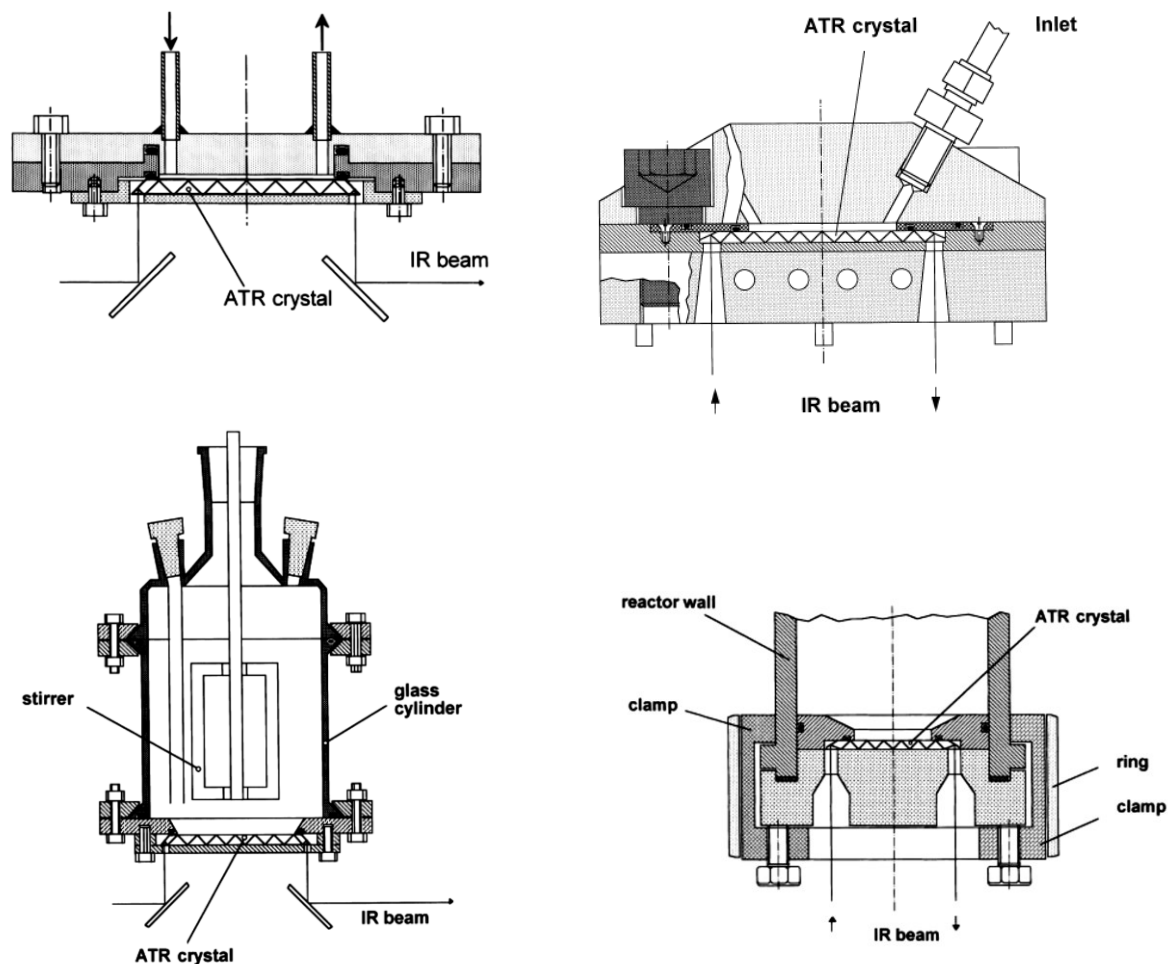
3.2 Benzyl alcohol oxidation

Benzyl alcohol is one of the most studied substrates for the selective aerobic oxidation [14]. The industrial relevance of benzyl alcohol oxidation is connected to the high commercial value of the corresponding products, benzaldehyde in primis, which is largely used in food and cosmetic industries as additive for artificial bitter-almond aroma. In addition, benzyl alcohol oxidation represents also a well-studied model reaction. Indeed the oxidation of benzyl alcohol proceeds smoothly on supported noble metal nanoparticles, because of the activating effect of the aromatic ring.

In many cases benzaldehyde is the main product, even if benzoic acid, toluene, benzyl benzoate and benzene are often observed as secondary products. [15]
Indeed, depending on the reaction conditions and on the presence of specific active sites, benzyl alcohol can undergo several reactions (Scheme 3.1, i-vii).

(i)   oxidative dehydrogenation to benzaldehyde,
(ii)   oxidation to benzoic acid
(iii)   formation of benzyl benzoate
(iv)   decarbonylation of benzaldehyde to benzene
(v)   disproportionation to equimolar toluene and benzoic acid
(vi)   dehydration to dibenzylether
(vii)   condensation (benzylation) to anthracene and stilbene (not shown)
(viii) reduction of benzyl alcohol by metal hydride

Scheme 3.1 Benzyl alcohol oxidation
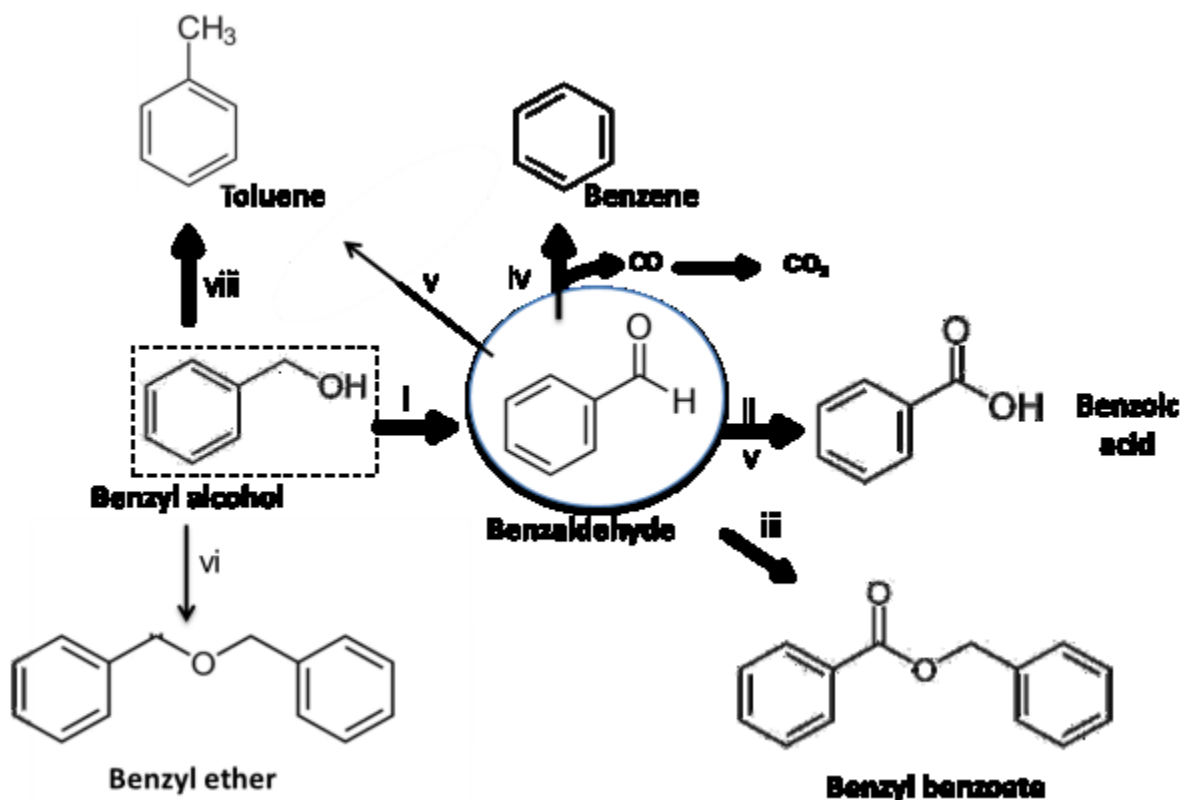
The transformation of benzyl alcohol to benzaldehyde is generally accepted to proceed according to a dehydrogenation mechanism via two elementary steps (Scheme 3.2).

In the first step benzyl alcohol adsorbs on catalyst surface and dissociates homolytically to produce an alkoxy intermediate. Computational and surface-science studies [16] have revealed that the dissociative adsorption onto the active site is surface oxygen assisted process, and recently theoretical modelling supported the possibility of an alternative hydroxyl-mediated pathway. [17]

The alkoxide subsequently undergoes β-H elimination to produce benzaldehyde [18]. The hydrogen abstraction from an alkoxy group is commonly accepted to be the rate-determining step. According to the literature, the hydrogen abstraction from the alkoxy intermediate is accomplished by an adjacent empty Pd site [19], even if the participation of surface hydroxyl or surface oxygen cannot be excluded.

Scheme 3.2 Dehydrogenation mechanism for benzaldehyde production
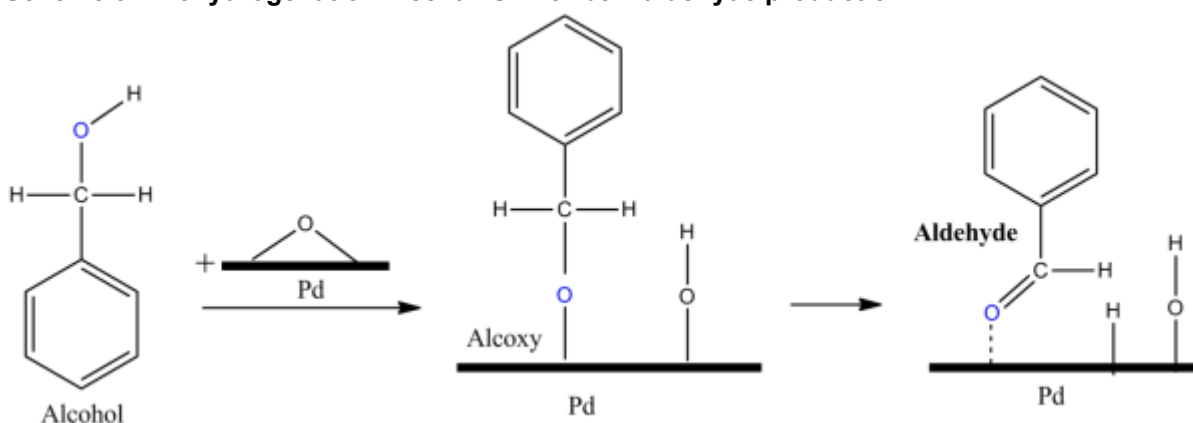
Benzyl alcohol dehydrogenation to benzaldehyde was found to be structure insensitive thus occurring at the same rate on all the exposed palladium sites. The mechanism for the conversion of benzyl alcohol to benzaldehyde has been supported by many kinetic, electrochemical, and other studies [20].

Otherwise, the mechanisms for other consecutive and side reactions, resulting in the formation of undesired by-products such as benzene, toluene, benzoic acid, and benzyl benzoate, have been debated for a long time. [21]

Benzoic acid has for a long time considered to be produced by benzaldehyde oxidation in the presence of oxygen. When benzyl alcohol oxidation is performed in a supercritical (SC) CO_2 medium[22], benzoic acid appeared only after the complete conversion of benzyl alcohol, suggesting that benzyl alcohol oxidation to benzaldehyde and subsequent oxidation to benzoic acid occur over the same active site. However, an alternative explanation can be found in the recent work of Sankar et al.[23] reporting about the inhibitor effect of benzyl alcohol towards benzaldehyde auto-oxidation to benzoic acid.

Recently alternative reaction pathway for benzoic acid formation have been proposed:

- hydration of benzaldehyde via a geminal diol, followed by a dehydrogenation: this hypothesis is supported by the evidence that benzoic acid is produced also under anaerobic conditions [24] (Scheme 3.3, a)
- the Cannizaro reaction of benzaldehyde to benzoic acid and benzyl alcohol in the presence of basic sites on the support [25] (Scheme 3.3, b).
- Formation from a dioxy or carbonyloxyl intermediate, generated by reaction of an alkoxy with a surface oxygen atom [26] (Scheme 3.3, c)

Scheme 3.3 Possible pathways for benzoic acid formation

a) Benzaldehyde hydration
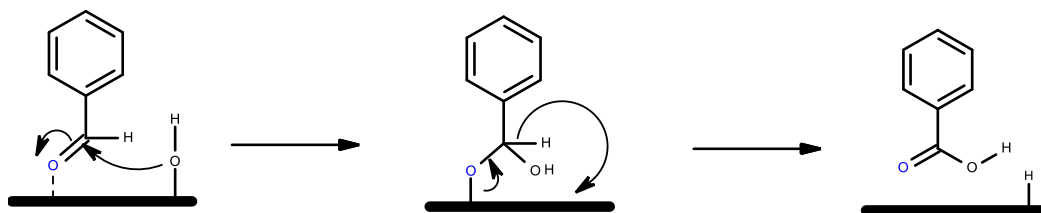
b) Cannizzaro reaction
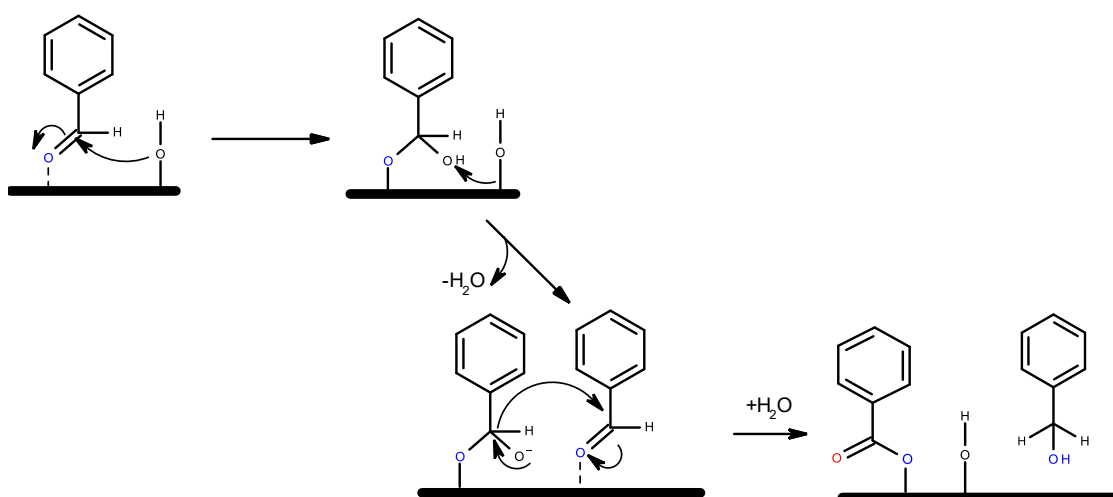
c) Via dioxy-intermediate
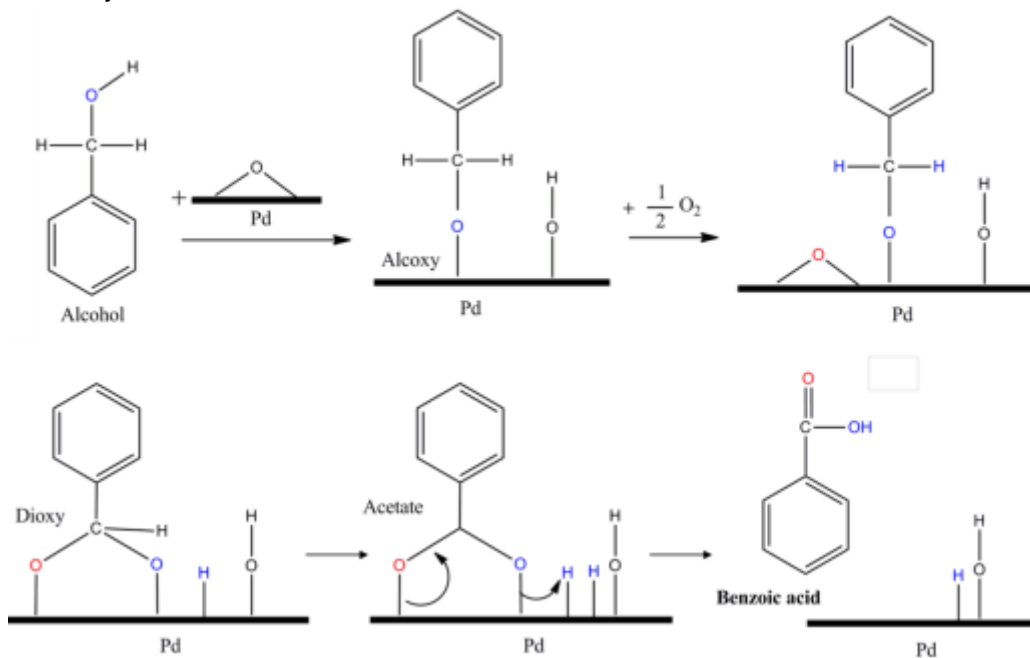
A carbonyloxyl intermediate has been proposed also as source for the production of benzyl benzoate. [26] (Scheme 3.4)

Scheme 3.4 Benzylbenzoate formation
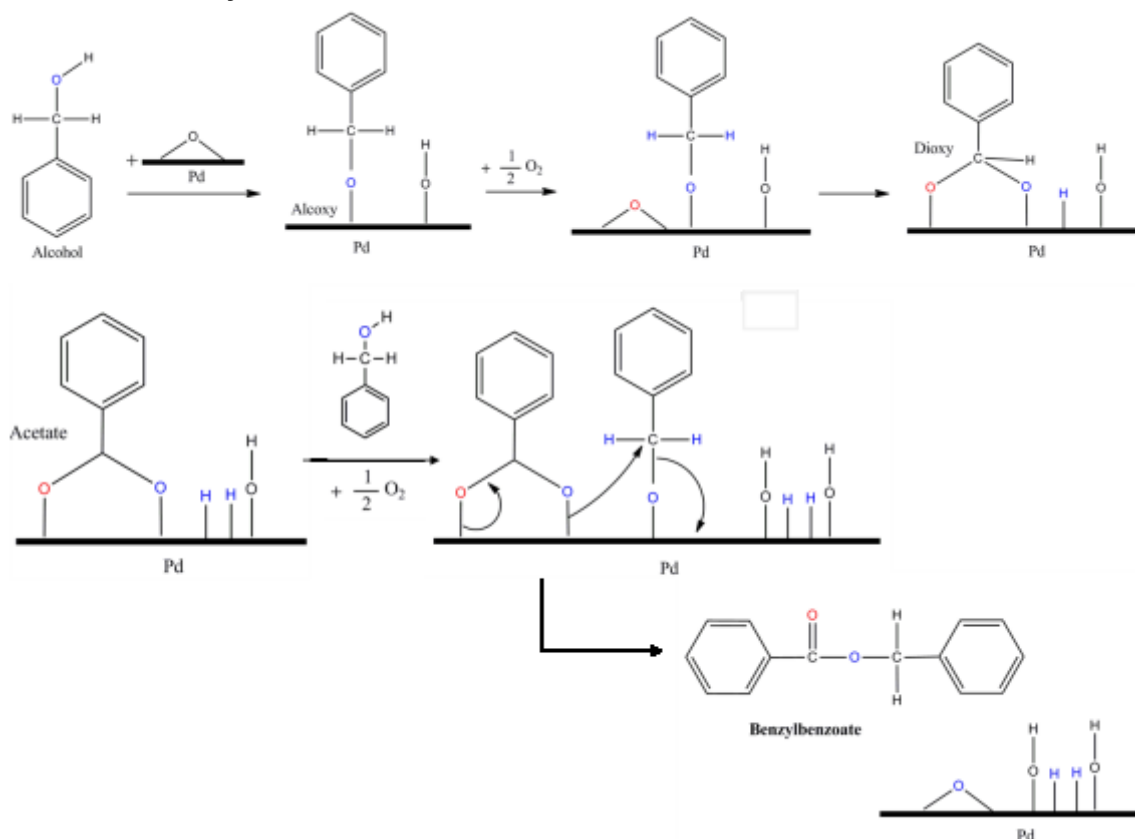
The mechanism of benzene formation via the decarbonylation of benzaldehyde during the liquid-phase oxidation of benzyl alcohol over a Pd/Al$_2$O$_3$ catalyst has been investigated by Keresszegi et al. [25] using in situ ATR-IR Spectroscopy. Monitoring the CO evolving on catalyst surface and exploiting the sensitivity of the C–O bond to the location of the CO molecule on the particle, they concluded that benzaldehyde decarbonylation occurs preferentially at the hollow sites distributed on the (111) terraces.

Two different reaction pathway has been proposed for toluene formation:

- the hydrogenolysis of benzyl alcohol by the hydride generated in the dehydrogenation of benzyl alcohol to benzaldehyde [21,b],
- the disproportionation reaction of benzyl alcohol to form an equimolar mixture of benzoic acid (or benzaldehyde) and toluene [27].

Recent kinetic studies [26] revealed a strong correlation between the kinetic profiles of the aldehyde and toluene. This evidence suggested a common origin for benzaldehyde and toluene. Toluene could originate from the same alkoxy intermediate as the aldehyde, reacting with surface hydride (Scheme 3.5).

Scheme 3.5 Toluene formation via-alkoxy

120
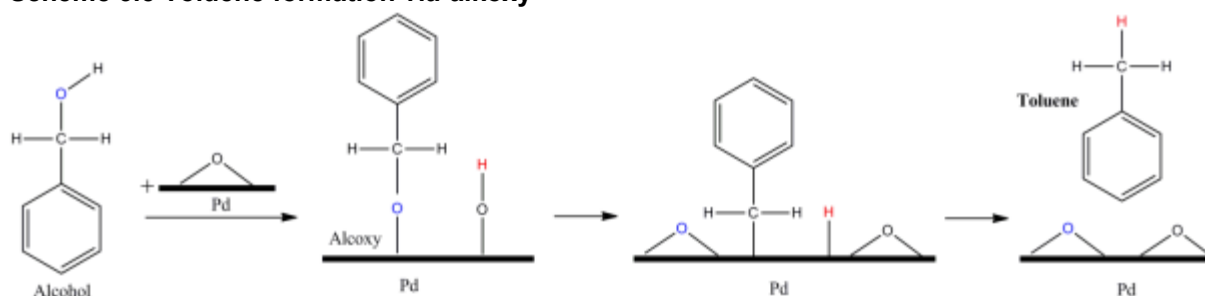
DFT calculations supported this hypothesis, by computing a higher activation energy for direct dissociation to produce an alkyl group compared to the barrier to produce an alkoxy one.[28] Furthermore, temperature-programmed desorption[29] (TPD) of benzyl alcohol and benzaldehyde from neat Pd(111) revealed the presence of toluene in the former case, whereas in the latter case no toluene was detected. This indicate that the alkyl formation occurred prior to benzaldehyde formation, thus confirming the previous interpretation. In the proposed mechanism, an additional surface oxygen is generated along with toluene production, while aldehyde production implies the consumption of a surface oxygen and the formation of water precursors. The overall reaction results therefore in the same stoichiometry as a "disproportionation" reaction.

Also the formation of benzyl ether could involve an alkoxy intermediate. Indeed ether can be obtained by combination of an alkyl group and an alkoxy group or by condensation of two alkoxy groups with the elimination of an oxygen atom or by nucleophilic attack of free benzyl alcohol on an adsorbed alkoxy or alkyl species (Scheme 3.6).

Scheme 3.6 Benzyl ether formation
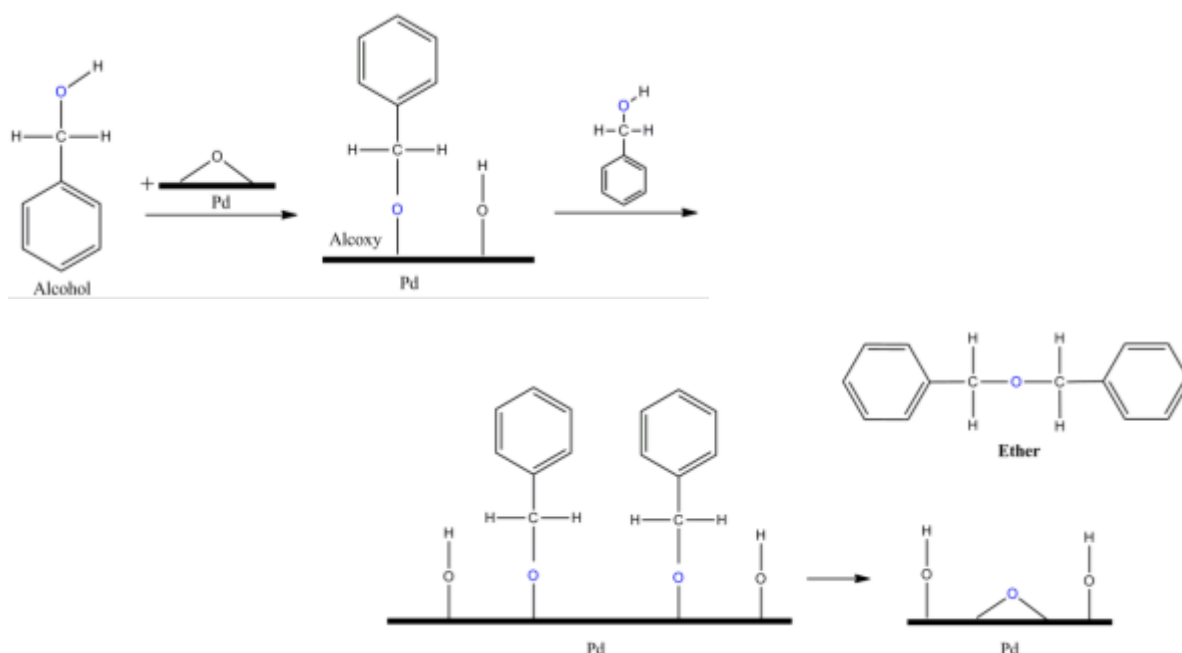
3.3 *In situ* Attenuated Total Reflectance FTIR Spectroscopy: insights on the bimetallic system behaviour in Benzyl Alcohol Oxidation

The peculiar catalytic behaviour of bimetallic systems has been extensively discussed in the previous chapters. In general it has been observed that alloyed Au-Pd nanoparticles showed enhanced catalytic activity and selectivity and also improved resistance to deactivation compared to the monometallic counterparts. [30] This phenomenon has been ascribed to synergistic effect and to isolated single Pd sites present in alloyed nanoparticles.[30a,31]

Recently ATR-FTIR Spectroscopy has been used by Nowicka et al.[32] to probe the interphase solid liquid during benzyl alcohol oxidation on bimetallic Au-Pd nanoparticles supported on TiO_2, MgO, ZnO, and carbon. Results from *operando* ATR-FTIR analysis in batch reactor were integrated with diffuse reflectance infrared Fourier transform spectroscopy (DRIFTS) and inelastic neutron scattering (INS) characterization. A contribution from the support was observed in terms of different selectivity: on MgO and ZnO only benzaldehyde, produced by the dehydrogenation of benzyl alcohol was revealed, whereas on the other supports toluene was detected among the products.

ATR-FTIR Spectroscopy has been also employed to investigate the deactivation of Pt based catalysts in alcohol oxidation [33]. By monitoring the species evolving and adsorbing on the catalyst surface, Ide et al. concluded that deactivation of Pt nanoparticles is a consequence of the presence of strongly adsorbed species and not of surface reconstruction phenomena or leaching.[33]

On the basis of these encouraging results, we decided to use ATR-IR spectroscopy to unravel events at the surface determining the catalytic performances of Au/TiO_2, Pd/TiO_2 and $AuPd/TiO_2$ in liquid-phase benzyl alcohol oxidation. For this purpose, results from batch catalytic tests were related to the information about the evolution of different surface species provided by ATR-FTIR spectroscopy.

Both monometallic (Au, Pd) and bimetallic (AuPd) catalysts were prepared by the sol immobilization technique using polyvinyl alcohol (PVA) as the protective agent. In particular, the bimetallic AuPd catalyst was prepared using the two-step procedure, consisting in the addition of palladium to pre-supported gold nanoparticles. This procedure has been reported in the literature to produce alloyed AuPd nanoparticles of a single composition and highly dispersed on the support.

Scanning transmission electron microscopy (STEM; Table 3.1) was used to measure the average particle sizes of TiO_2-supported Au, Pd, and AuPd.

Monometallic Au and Pd nanoparticles possess a similar particle diameter (3.7 and 3.5 nm, respectively), whereas the addition of Pd to the Au nanoparticles results in a slight increase of the average particle diameter (from 3.7 to 4.1 nm).

Table 3.1 Statistical median and standard deviation for the Pd, Au and AuPd (STEM)

Catalyst	Statistical median (nm)	Deviation standard (σ)
1 wt. % Pd/ TiO_2	3.7	0.9
1 wt. % Au/ TiO_2	3.5	0.7
1 wt. % Au_6-Pd_4/TiO_2	4.1	1.2

The composition and the structure of bimetallic nanoparticles was determined by Energy dispersive X-ray spectroscopy (EDS) and the correlated fast Fourier transforms (FFT) analysis.

Figure 3.3 a) Representative STEM image, b) PdAu loading [at%] in 10 random nanoparticles of AuPd/TiO2, c) high-resolution TEM image and d) the corresponding EDX spectrum of a AuPd particle with a Au/Pd composition of 7.4/2.6 wt%. e) A small particle (about 3 nm in size) showing multiply twinned structure. The twin boundaries in the images are indicated by straight lines. The FFTs of the two parts in the image of the small particle suggest additional twin boundaries, which are not directly visible.
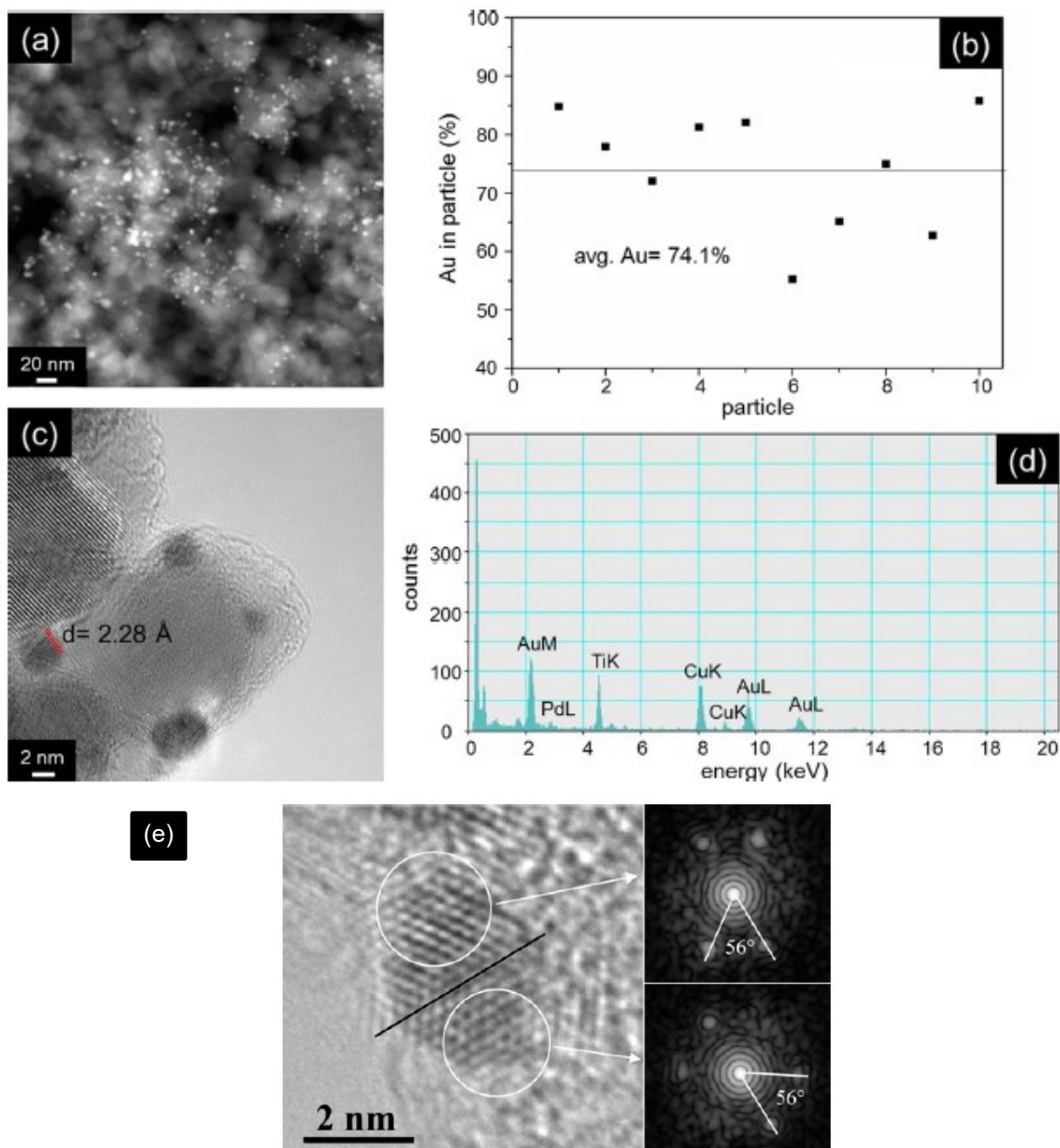
Energy dispersive X-ray spectroscopy (EDS) analysis of 10 randomly selected nanoparticles (Figure 3.3) suggested that they all contained both Pd and Au (Figure 3.3 d) with a Au/Pd ratio consistent with the nominal value (Au/Pd 7.3 : 2.7 wt%).

FFT is a useful mathematical tool for image processing. Using FFT it is possible to measure with high precision reciprocal lattice vectors and thus to obtain lattice parameters (d-spacing and angles). The maps from FFT analysis on a representative overview image of AuPd/TiO$_2$ is showed in figure 3.3. In this case a twin boundary is evident in the HRTEM image (Fig. 3.3, e) and the FFT analysis of both sides of the twin boundary revealed the presence of two sets of reflections.

The lattice spacing calculated from the FFT map has the value of about 2.29 Å, which is intermediate between the Pd (111) plane (2.26 Å) and the Au (111) plane (2.35 Å), which describes the alloy state. However, the angle between the two sets of (111) planes in either FFT map is about 56° instead of about 71°, typical value for an fcc single crystal. It has been demonstrated that this special value of the angle can be produced by two overlapped fcc lattices with a twin boundary in between. As a consequence, the particle possesses a multiply twinned structure with each twinned part being fcc structure and with more twin boundaries than just the one visible in the image. Moreover EDS analysis was performed in order to determine the composition and to verify the metal compositions in individual particles.

Carbon monoxide (CO) adsorption on Pd/TiO_2, $AuPd/TiO_2$, and Au/TiO_2 was then monitored in gas phase and liquid phase in order to characterize the surfaces and to investigate the effect of the liquid environment on the adsorption properties of the catalyst surfaces. CO is widely used as a probe molecule in the characterization of metal surfaces. Indeed monitoring by Infrared Spectroscopy CO adsorption on metals provides useful information about the sites present on the metal surface, due to the peculiar sensitivity of the $C-O$ bond vibration frequency to the oxidation state of the site, to its geometry and to its coordinative unsaturation degree. In particular the availability and the structure of binding sites are strictly related to the nanoparticle morphology and to the eventual presence of defects.

The traditional rationalization of CO chemisorption on metal surfaces invokes the donation-backdonation model.[34,35] This model describes the chemisorption bond in terms of donation of electrons from the CO 5σ orbital into empty d orbitals at the surface of the metal, and back-donation of d-electrons from the metal to the unoccupied $2\pi^*$ level of CO. These interaction results in the formation of two hybrid orbitals, which are both bonding with respect to the metal-CO (M-CO) bond, whereas are nonbonding and antibonding with respect to the intramolecular $C-O$ bond. In particular the increased occupation of the $2\pi^*$ state by backdonation results in a weakening of the $C-O$ bond. Therefore the CO bond weakens (and consequently ν_{C-O} decreases) as the metal–carbonyl bond strength increases.

Generally CO molecules can bond to sites according to three different adsorption geometries: μ_1 linearly adsorbed CO (CO_L), μ_2 bridge bonded CO (CO_B), and μ_3 hollow bonded CO surface species (CO_{B3}). Currently the assignment is well-established in the literature, confirmed by several experiments on single crystal or bulk powder, and supported by theoretical studies.[34] In general signals attributable to CO adsorbed on the noble metal particles appear in the spectral region below 2150 cm^{-1} (Figure 3.4). Since adsorbed CO experiences greater backdonation with a higher coordination number of the adsorption site, the M-CO bond strength is expected to increase in the order $CO_L < CO_B < CO_{B3}$ and consequently the vibrational frequencies for $C-O$ should decrease in the order $CO_L > CO_B > CO_{B3}$. Typically, the adsorption of CO on metallic Pd (Figure 3.4) results in signals associated with CO bound linearly (CO_L) above $\bar{\nu}$ =2000 cm^{-1}, and in a number of bands that can be divided qualitatively as follows: $\bar{\nu}$= 2000–1880 cm^{-1} for CO_B and $\bar{\nu}$=1880–1800 cm^{-1} for CO_{B3}).[34] The assignment of signals is complicated by the fact that CO adsorption is site dependent. The adsorption of CO (CO_L, CO_B, or CO_{B3}) on facets will give rise to signals at different frequencies from CO adsorbed in the same geometry on edges, steps, or defect sites. In particular coordination to facets produces higher-frequency signals than coordination to particles edges/steps. Indeed the electronic charge distribution at surface defects is generally higher than that for flat terraces (so-called Smoluchowski effect), thus resulting in a stronger M-CO interaction and a weaker $C-O$ bond. This can be used on a qualitative base to assess the morphology of the Pd nanoparticles using IR spectroscopy.

Figure 3.4 Typical CO adsorption geometries on metallic Pd and corresponding signals in IR region
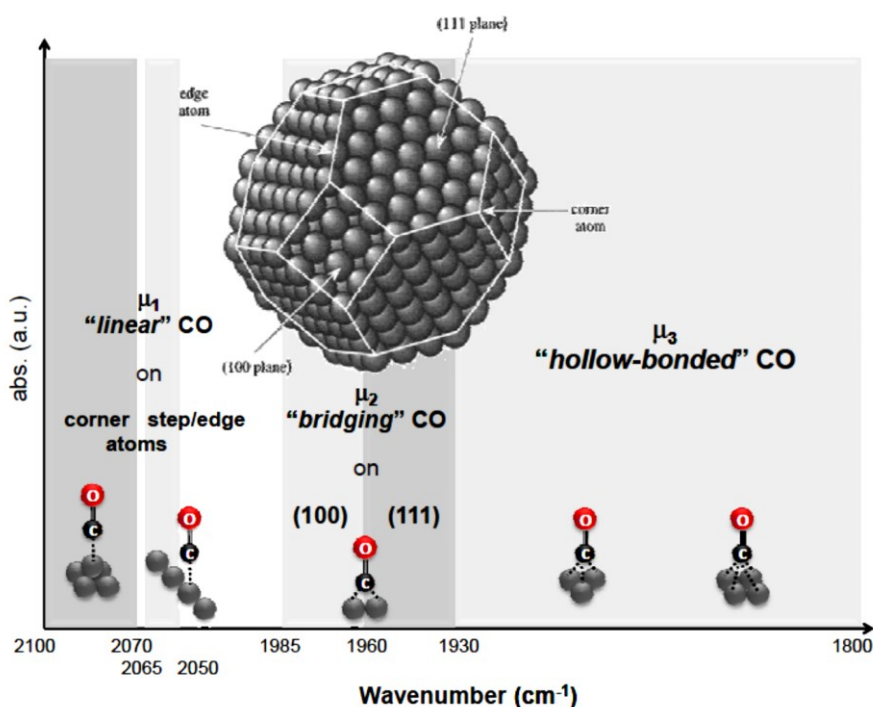
Moreover, by comparing the intensities of CO_L and CO_B signals[22] it is possible to qualitatively estimate the size of the Pd domains.[35] Indeed, according to Sachtler *et al.*[35,b], linear CO is more stable on the low coordination number palladium atoms at the edges and vertices, which are relatively more abundant in smaller crystallites, while bridged CO is preferred at higher coordination number atoms typical of facets. Therefore the fraction of CO in the bridging mode increases and that of the linear adsorption decreases with increasing Pd particle size.

The DRIFT spectra collected after 30 min adsorption under a flow of CO/He on the three catalysts and spectra recorded during desorption (He flow) are shown in Figure 3.5. The corresponding spectra The spectrum of CO adsorbed on Pd/TiO$_2$ exhibits signals at $\bar{v}$ =2097, 1981, and 1952 cm^{-1}, which according to the assignment reported above, can be attributed to CO_L and CO_B, respectively. The ratio between the intensity of CO_L and CO_B signals suggests that the Pd nanoparticles are relatively small.

The high energy of the CO_L signal (2097 cm^{-1}) is associated to CO coordination to corner atoms, whereas the shoulder at $\bar{v}$ = 2080 cm^{-1} can be ascribed to CO adsorption on edge sites.[34 a] The presence of signals overlapping with the ones of gas-phase CO ($\bar{v}$ = 2145 and 2130 cm^{-1}) can be related to CO adsorbed on Pd^{2+} cations [34 b], which can be generated at the surface of not perfectly capped or uncovered particles after interaction with air. Regarding signals due to CO_B, the band at $\bar{v}$ =1981 cm^{-1} can be assigned to CO coordinated to Pd(100) facets [36], whereas the signal at $\bar{v}$ =1952 cm^{-1} is attributed to coordination on edge/step sites. The unusual higher intensity of the latter compared to that of the high-energy CO_B species confirms the small sizes of Pd nanoparticles.

Information on the relative strength of the interaction can be obtained from the spectrum obtained during the subsequent desorption (under He flow).The signal intensity decreases

---

[22] Absorption coefficient of bridged and linear species have been determined in the literature and in particular resulted $\varepsilon(CO_B) > \varepsilon(CO_L)$[35,c]

generally after desorption. Additionally, a more defined structure within the CO_L signal is obtained, the shoulder at $\bar{v} = ..2070$ cm^{-1} (edge sites) being more pronounced after He flow.

The decrease in the intensity of CO_B signal at $\bar{v} = 1952$ cm^{-1} discloses more defined signals at $\bar{v} = 1980$ and 1900 cm^{-1}. Moreover the disappearance of the gas-phase CO bands makes more visible the signals of CO adsorbed on Pd^{2+} ($\bar{v} = 2145$ and 2130 cm^{-1}).

The large difference between the spectra corresponding to monometallic and bimetallic nanoparticles provides a qualitative picture of the modification of Pd nanoparticles by the presence of Au, thus confirming the formation of a AuPd alloy.

Looking at CO adsorption on bimetallic $AuPd/TiO_2$, it is immediately evident that the amount of adsorbed CO on $AuPd/TiO_2$ is lower than that on Pd/TiO_2 (Figure 3.5, b), indicating that the fraction of available metal atoms for adsorption is smaller. The absence of signals associated to Pd^{2+} species ($\bar{v} > 2100$ cm^{-1}) reveals a lower inclination to re-oxidation of surface Pd atoms in $AuPd/TiO_2$ probably due to the alloyed state. The presence of gold suppresses also the CO coordination to particle corners, as suggested by the absence of the CO_L signal at $\bar{v} = 2097$ cm^{-1}, previously observed on Pd/TiO_2. On the other hand a clear signal at $\bar{v} = 2079$ cm^{-1}, flanked by a shoulder on the low energy side, is now observed. This signal, present as shoulder of the major CO_L signal at $\bar{v} = 2097$ cm^{-1} in the case of Pd/TiO_2, is characteristic of CO adsorption on edge sites. The larger contribution of CO_L compared the CO_B signal ($\bar{v} = 1979$ cm-1) indicates the presence of small and less contiguous domains of Pd on the bimetallic AuPd particles compatible with the presence of isolated Pd centres. Although there is no evidence of CO adsorption on Au atoms, this cannot be ruled out completely given the complexity of the spectrum

The adsorption of CO on Au/TiO_2 is clearly different due to the nature of the metal (Figure 3.5 c). Initially a signal at $\bar{v} = 2128$ cm^{-1} appears and subsequently it undergoes redshift to $\bar{v} = 2106$ cm^{-1}, which is typical for CO adsorption in a linear geometry on coordinatively unsaturated Au atoms. Figure 3.5 (d) shows a time-resolved 2D-colour map of the 1750–2250 cm^{-1} region of the DRIFTS spectra to emphasize the temporal behaviour of infrared signals in this region (color gradient from red for high intensity to blue for low intensity). After 180 s. (3 min) on stream, this signal starts to transform into a signal that grows at $\bar{v} = 2075$ cm-1 (Figure 3.5 d). The isosbestic point at $\bar{v} = 2091$ cm^{-1} indicates that the species providing the initial signal at high frequency is converted into the species that provides the new signal, [37] originated from the reconstruction of Au nanoparticles under the high partial operative pressure or negatively charged $Au^{\delta-}$ carbonyl species arising from the interaction of adsorbed CO with functional groups (O-H and C=O groups of the PVA capping agent) present on the Au particles. A third signal appears as a shoulder at $\bar{v} = 2020$ cm^{-1} as this transformation occurs. The spectrum measured in He flow does not show any signals of adsorbed CO, since all of the signals do not resist desorption.

Figure 3.5 DRIFT spectra of adsorbed CO on a) Pd/TiO₂, b) AuPd/TiO₂, and c) Au/TiO₂. d) Color map of the time-resolved spectra recorded during CO adsorption on Au/TiO₂. Solid and dashed traces represent spectra recorded under CO/He and He flow, respectively. Spectra are offset for clarity.
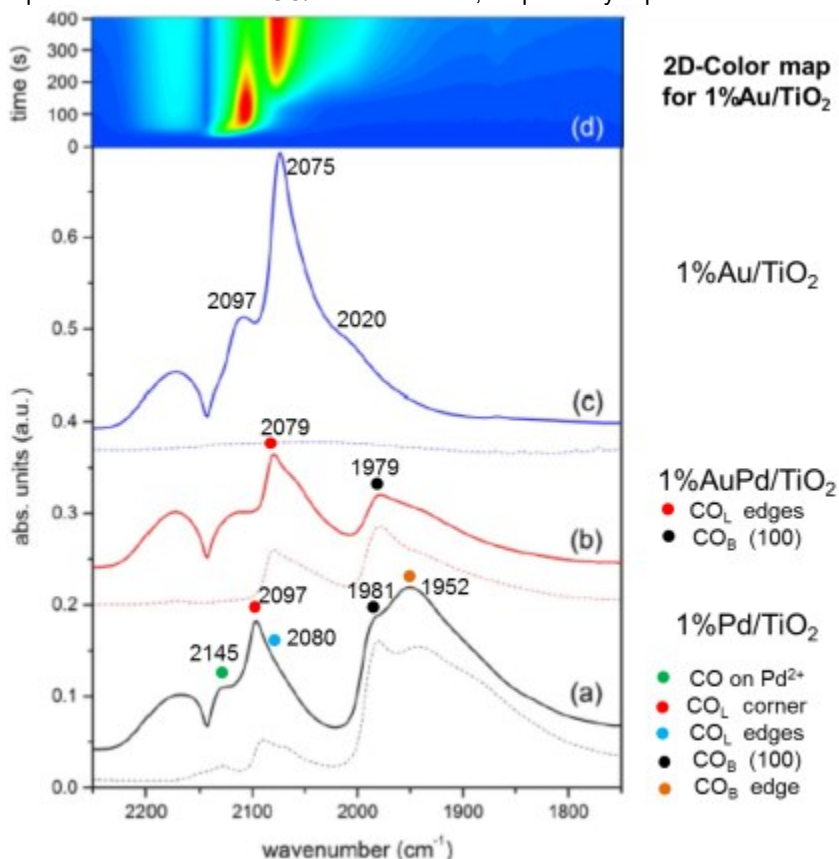
The catalytic activity of mono- and bimetallic catalysts has been evaluated in the liquid-phase oxidation of benzyl alcohol in a glass batch reactor, using cyclohexane as the solvent. Results are summarized in Table 3.2 and the corresponding reaction profiles are reported in Figure 3.6.

Table 3.2 Comparison of TiO₂-supported catalysts activities in benzyl alcohol oxidation

Catalyst[a]	Initial activity[b] $\left(\frac{conv.\,mol}{mol_{Pd}\,\cdot\,h}\right)$	Selectivity [c]			
		Toluene	Benzaldehyde	Benzoic acid	Benzyl benzoate
1 wt.% Au / TiO₂	14	-	80[d]	14[d]	3[d]
1 wt.% Pd/ TiO₂	532	10	84	1	3
1 wt.% Au₆Pd₄/ TiO₂	124	1	88	1	2

[a] Reaction conditions: alcohol/metal=500:1 molmol-1, 608C, pO2=2 bar, 1250 rpm.
[b] Mol of reactant converted per hour per mol of metal calculated after 15 min of reaction.
[c] Selectivity at 90% conversion. [d] Selectivity at 10% conversion.

Under the selected reaction conditions, Au/TiO₂ showed a very low initial activity (14 h⁻¹; Table 3.2) reaching a conversion of only 12% after 8 h (Figure 3.6). This results are in agreement with the behaviour reported in the literature for monometallic gold catalysts under neutral conditions.[38] Conversely, Pd/TiO₂ exhibited a good activity (532 h⁻¹) , attaining 89% conversion after 8 h (Figure 3.6). The addition of gold to Pd results in a decrease of the initial activity (124 h⁻¹; Table 3.2), but after an induction period (1.5 h) the activity of AuPd/TiO₂ (Figure 3.6) became similar and even superior to the Pd/TiO₂ one.

Figure 3.6 Reaction profiles of TiO$_2$-supported catalysts during benzyl alcohol oxidation
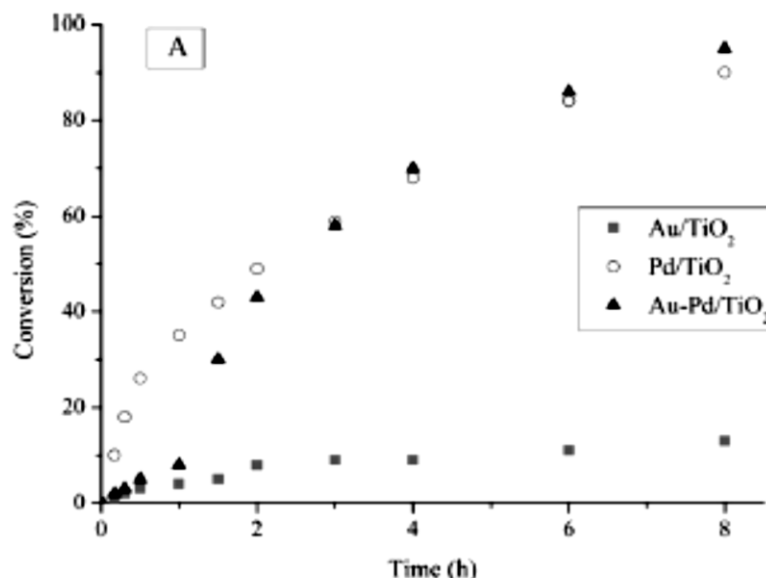
The presence of the induction period cannot be ascribed to the removal of the PVA layer, which initially could make the active sites less accessible. Indeed, if PVA was involved, the same effect should be present also in Pd/TiO$_2$ [39] assuming that PVA interacts equally with the surface in both cases. Therefore, the presence of an induction time could be connected to a different nature of the active site in the bimetallic system compared to that in the monometallic system. Note that the induction time is also present when recycled catalyst is used. This finding could be correlated with DRIFTS analysis that showed a different nature of active site betweem AuPd and Pd.

Concerning the selectivity, benzaldehyde was the main product with all the catalysts (80–88% selectivity). However, a different distribution of byproducts has been observed (Table 3.2 and Figure 3.7). Monometallic Pd favoured the formation of toluene (10% selectivity), linearly with the conversion (Figure 3.7 a). Conversely, according to earlier results,[15] toluene is not present among products in the case of bimetallic system, which in turn promoted the consecutive transformation of benzaldehyde to benzoic acid (Table 3.2 and Figure 3.7) similarly to the monometallic Au catalyst (Table 3.2).

Figure 3.7 The product distribution on a) Pd/TiO$_2$ and b) AuPd/TiO$_2$
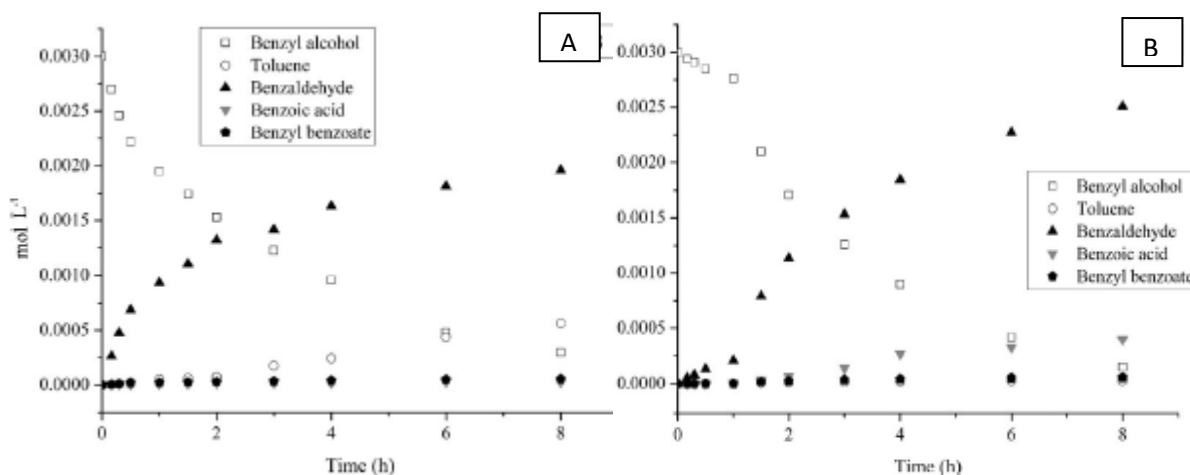
The durability of the most active catalysts (Pd/TiO$_2$ and AuPd/TiO$_2$) was verified by recycling tests, carried out by filtering the catalyst and adding a fresh solution of benzyl alcohol without any further treatment. Stability tests revealed the better durability of AuPd/TiO$_2$ compared to Pd/TiO$_2$ (Figure 3.8), the latter experiencing a drastic drop in the activity after the second run. This evidence confirms previous reports on the positive effect of bimetallic AuPd catalysts on the stability of catalysts supported on activated carbon.[15c] Inductively coupled plasma (ICP) analysis of the collected solution after six runs revealed a loss of <1 wt% metal in both cases. Therefore, we can exclude deactivation by metal leaching as the cause of the activity decrease in the case of Pd catalyst.

Figure 3.8 Stability tests
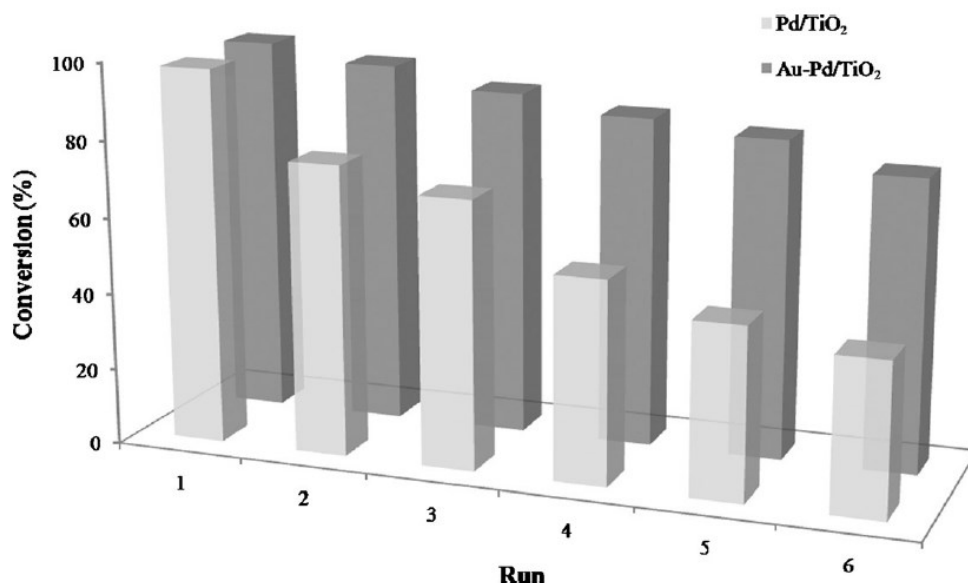
The morphology of metal nanoparticles after reaction was also investigated, by performing TEM analysis on used catalysts. TEM images revealed that after six runs Pd and AuPd NP morphology was unaltered and also particle size was similar to the fresh materials, thus excluding a contribution of particle aggregation.

The possible role of the adsorbed species on the catalyst surface was then investigated using *in situ* ATR-IR spectroscopy for monitoring the evolution of surface species during the oxidation of benzyl alcohol. Catalysts were deposited as particulate films on an trapezoidal ZnSe internal reflection element (IRE) mounted in a batch-reactor cell (Figure 3.9, left). The film was in contact with a cyclohexane solution of benzyl alcohol. The ATR-IR spectroscopy measurements were performed at reflux (time of reaction 1 h) with oxygen bubbling instead of pressurizing the reaction mixture as in the batch reactor study (where catalyst was dispersed as suspension in the reactant solution). This should be considered in directly comparing the two sets of data.

The time-resolved ATR-IR spectra (Figure 3.9, right) obtained for the three samples are very similar and differ only in the intensity of signals. Peak assignment can be performed according to the literature. [25] The signals that appeared at the early stages of the measurements at $\bar{v}$=1497 cm^{-1} and $\bar{v}$= 1397 cm^{-1} are characteristic of benzyl alcohol, most likely in the solution. A sharp signal at $\bar{v}$= 1712 cm^{-1} represents the benzaldehyde product dissolved in cyclohexane. By monitoring the increase in the intensity of this signal is possible to follow the progress of the catalytic reaction. The signals observed at $\bar{v}$ =1600 ($v_{C=C}$), 1531 (v_{COOas}), 1483 ($v_{C=C}$), 1452 ($v_{C=C}$), and 1417 cm^{-1} (v_{COOs}) belong to benzoate species, which appeared to be coordinated predominantly to TiO$_2$.[25]

Figure 3.9 Batch reactor cell (*left*); ATR-IR spectra (*right*) recorded during benzyl alcohol oxidation on a) Pd/TiO$_2$, b) AuPd/TiO$_2$, and c) Au/TiO$_2$. Spectra are offset for clarity. Vertical dashed lines indicate selected signals the kinetics of which is reported in Figure 3.11
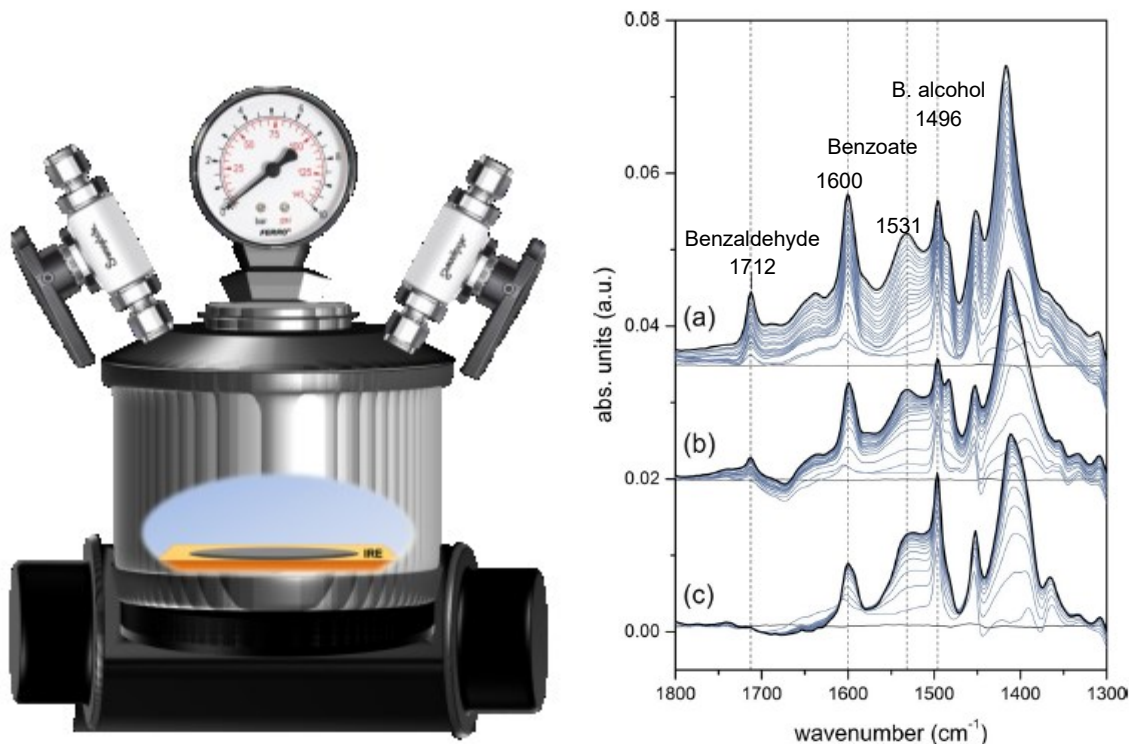
Indeed this assignment is supported by the spectra obtained upon the contact of a benzoic acid solution with TiO$_2$ and the corresponding metal-based catalysts (Figure 3.10). The signals exhibit shoulders that likely suggest different adsorption geometries. The most active Pd/TiO$_2$ catalyst exhibits the most intense benzoate signals.

Figure 3.10 ATR-IR spectra recorded for benzoic acid (0.005m solution in cyclohexane) adsorption on TiO$_2$, Pd/TiO$_2$, AuPd/TiO$_2$, and Au/TiO$_2$.
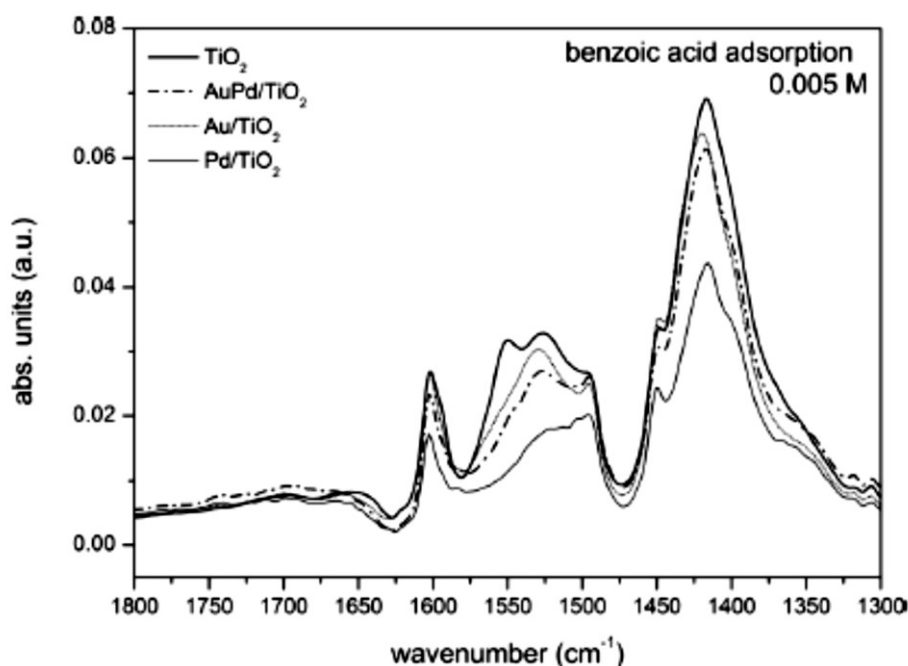
The temporal behavior of selected signals representative of benzaldehyde ($\bar{v}$=1712 cm^{-1}), benzoates ($\bar{v}$=1600 and 1531 cm^{-1}), and benzyl alcohol ($\bar{v}$=1496 cm-1) are shown in Figure 3.11, which demonstrates that the rate of accumulation of adsorbed benzoate species on the three catalysts is different.

A linear growth of the intensity with time has been detected on Pd/TiO$_2$, whereas on AuPd/TiO$_2$ and Au/TiO$_2$ benzoate signals remain constant after a rapid initial growth. A closer look at the spectra (Figure 3.9) reveals that also the ratio between the intensities of the benzoate signals at $\bar{v}$ = 1600 and 1531 cm^{-1} is not the same in the three cases. The ratio of the intensities of the bands at $\bar{v}$ =1600 and 1531 cm^{-1} (I_{1600}/I_{1531}) increases in the order Au<AuPd<Pd, whereas the increase of the signal at $\bar{v}$ =1600 cm^{-1} seems to be accompanied by that of the signal related to the symmetric stretch of the carboxylate group ($\bar{v}$ =1417 cm^{-1}). This observation suggests that the signals originate not only from the adsorption of benzoate species on the support, but an additional fraction of benzoate species is formed over the Pd-based catalysts, especially Pd/TiO$_2$, during the reaction. It is plausible to attribute this species to benzoates adsorbed specifically on Pd particles rather than on TiO$_2$. These species cannot be observed if benzoates are formed from benzoic acid adsorption in the control experiments shown in Figure 3.10.

The assessment of conversions in these experiments on the basis of IR signals is complicated by the overlap of the signals of the reactant and products (which include adsorbed species). The intensity of the signal of dissolved benzyl alcohol at $\bar{v}$ = 1496 cm-^{1} increases immediately after injection and after 15 min. reaches a constant intensity on the three catalysts. On Pd/TiO$_2$, this signal still tends to increase slightly, but probably it is an artefact deriving from the influence of the still increasing neighboring signal at $\bar{v}$ =1531 cm^{-1}, which stabilizes after 30 min on Au/TiO$_2$ and AuPd/TiO$_2$. Looking at the benzoate profiles, the different rates of benzoate formation on Au/TiO$_2$ and AuPd/TiO$_2$ compared with that on Pd/TiO$_2$ (Pd<AuPd<Au) match the selectivity obtained in the glass batch reactor study, despite the experimental differences. Moreover, the quantity of benzoic acid detected in solution has an opposite trend to the order detected by ATR-IR spectroscopy (Au<AuPd<Pd), suggesting that the negligible amount of benzoic acid obtained with Pd/TiO$_2$ compared to that with AuPd/TiO$_2$ and Au/TiO$_2$ can be ascribed to the preferential adsorption of these species on Pd. Previous experiments performed on Pd/Al$_2$O$_3$ evidenced that benzoic acid is formed in the early stage of the reaction and adsorbed strongly on the catalysts so that it remains undetectable in the effluent.[25] In the case of Pd/TiO$_2$ (Figure 3.7), the benzoic acid concentration in the liquid phase increased clearly only after 2 h. This induction time followed the trend of the signal of benzoates observed at the surface of the catalyst. Benzoate species accumulate initially on the catalyst surface until the saturation of some specific sites, whereas benzoates formed successively desorbed into the solution.

This behavior agrees with recent studies that showed that the formation of the AuPd bimetallic system alters the electronic structure of the metals, which potentially decreases the tendency for the formation of intermediates that are strongly adsorbed.[40] The higher rate of desorption of the products, in particular that of benzoate species, on AuPd/TiO$_2$ compared with Pd/TiO$_2$ could be a possible explanation for the lower durability of the Pd catalyst compared with the bimetallic AuPd system observed in the recycling tests.

Figure 3.11 Time response of selected ATR-IR signals observed during benzyl alcohol oxidation on Pd/TiO$_2$, AuPd/TiO$_2$, and Au/TiO$_2$: a) 1496 (benzyl alcohol), b) 1531 (benzoate), c) 1600 (benzoate), and d) 1712 cm^{-1}(benzaldehyde).
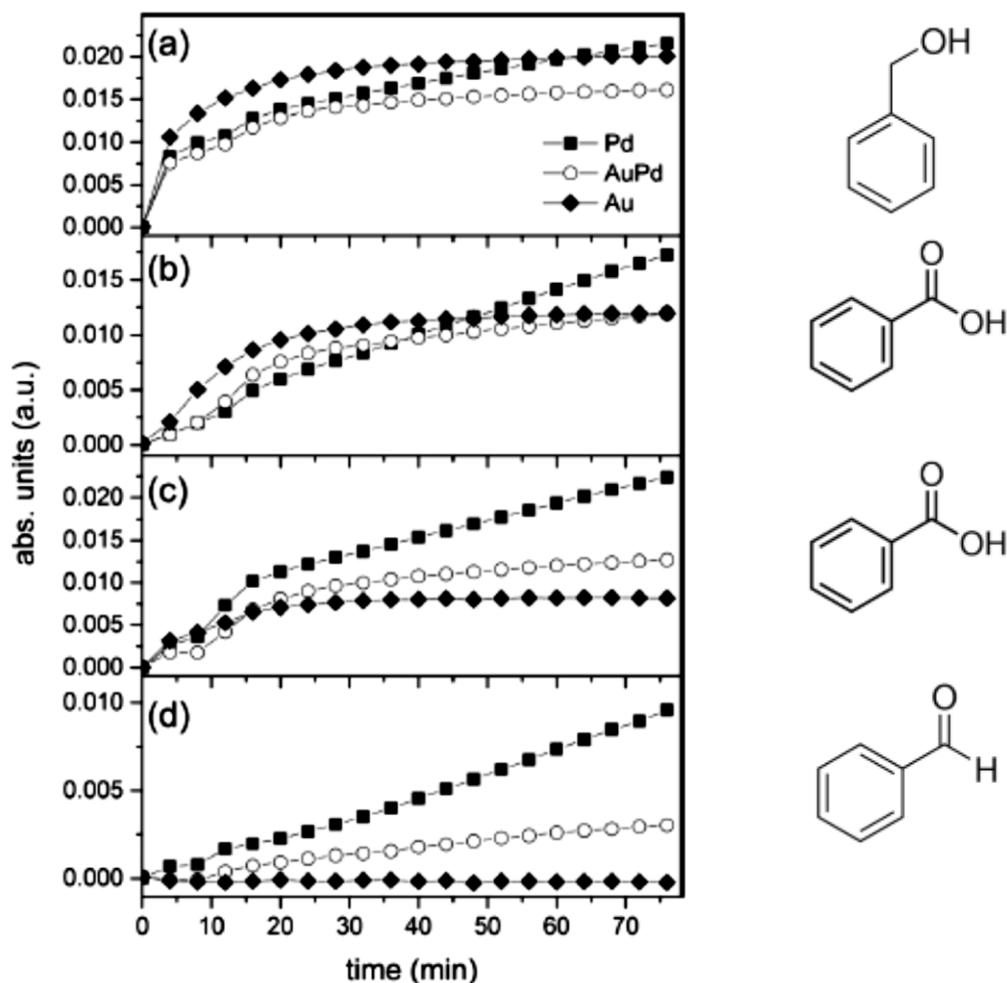
Batch reactor experiments revealed also differences in the selectivity to toluene. Specifically, the Pd catalyst promotes the formation of toluene (10%), while the presence of bimetallic AuPd nanoparticles suppressed the formation of toluene drastically, as reported in previous studies.[15] Looking at the product distribution for Pd catalyst (Figure 3.7), the formation of toluene rises with increasing conversion, whereas the formation of benzaldehyde shows the opposite trend. Unfortunately, ATR-IR spectroscopy is not a suitable technique for the direct detection of toluene because of the overlap of the vibrational modes of toluene with those of benzyl alcohol, benzaldehyde, and adsorbed benzoate species and because of the low toluene concentration. Therefore, we could not assess the presence of toluene directly from the *in situ* ATR-IR spectroscopy experiments and correlate it to the evolution of the observed species. Finally, no adsorbed CO derived from benzaldehyde decarbonylation was observed on all the samples, which reveals that this reaction is not favored on the catalysts prepared by sol immobilization in contrast to commercial Pd/Al$_2$O$_3$.[25] and this aspect will be examined in depth in the next section.

3.4 Selectivity control in Palladium catalysed benzyl alcohol oxidation through selective blocking of active sites

Among various catalyst preparation techniques, sol immobilization[41] possesses some undeniable advantages like the control of the metal particle size almost independently from the type of support and the improvement of catalyst resistance to deactivation compared to other classical methods (e.g. impregnation, deposition-precipitation).[42] The method is based on the pre-formation of metal nanoparticles and their subsequent immobilization on a support. The presence of a protecting agent (polymer, surfactant, polar molecule, etc.) is necessary to form stable metallic sols which do not undergo overgrowth or aggregation of metal nanoparticles. However the role of the capping agent in mediating catalyst activity and selectivity have been a matter of debate for a long time and is still not fully clarified. Generally, with comparable metal dispersion, catalysts derived from metallic sol immobilization typically present lower activity than catalysts with naked metal nanoparticles as for instance catalysts prepared by impregnation.[39] This effect was principally ascribed to the shielding effect of active sites due to the presence of protective agents.[41,42] However, recently, it was observed that the role of the protective agent is more complex. In fact, an electronic promoting effect was envisaged in PVP-protected Au NPs supported on SiO_2 used as catalyst in benzyl alcohol oxidation for some specific M/PVP ratio.[43] The beneficial effect of the protecting agent has been observed for supported Au, Pt and Pd NPs in different reactions, e.g. 1-epoxybutane formation from 1-epoxy-3-butene[44], cynnamaldehyde hydrogenation[45], furfural hydrogenation[45a] and alcohol oxidation[46]. Furthermore it has been observed that the presence of protecting agent molecules can induce a selectivity enhancement through the steric blocking of specific active sites, intramolecular interactions between reactant and capping agent and orientation effects.[39,45,47] It has been recently observed that PVA positively affects the selectivity of TiO_2-supported Au NPs in glycerol oxidation directing the adsorption of the reactant. [39] A comprehensive understanding of the role of protective agents on determining the catalytic performance requires the use of *in situ* techniques to investigate the catalyst surface under working conditions and to recognize structure and accessibility of active sites as well as interactions with adsorbates.[3] Attenuated total reflection infrared (ATR-IR) spectroscopy emerged as an ideal tool for this sort of studies, allowing to probe the solid-liquid interface between the catalyst surface and the reactant solution.[48] Recently, various works have appeared exploring reaction pathways at the surface of Pd[49], Pt[33] and alloy[50] catalysts using ATR-IR spectroscopy. Liquid phase benzyl alcohol oxidation is often selected as model reaction to unravel mechanistic aspects because of the rich reaction network involved in the oxidation of primary alcohols. In particular the aerobic liquid-phase benzyl alcohol oxidation over Pd/Al_2O_3 catalyst has been extensively explored using ATR-FTIR spectroscopy in order to identify the active sites responsible for different reaction pathways. For this reason we selected benzyl alcohol oxidation as the model reaction and 5%Pd/Al_2O_3 as catalytic reference. 5%Pd_{PVA}/Al_2O_3 was prepared by sol immobilisation, using poly(vinyl)alcohol as the stabilizing agent. The catalytic performances of protected Pd nanoparticles in the aerobic benzyl alcohol oxidation were compared to the ones of a commercial catalyst with the same composition, prepared by impregnation, without the use of protecting agent and thus possessing naked Pd nanoparticles.

The 5 wt% Pd_{PVA}/Al_2O_3 and the 5 wt% Pd/Al_2O_3 were characterized by transmission electron microscopy (TEM) and scanning transmission electron microscopy (STEM), revealing a

similar mean particle size and particle size distribution (Table 3.3) for naked and protected nanoparticles.

Table 3.3 Statistical mean particle size and standard deviation for Pd based catalysts

Catalyst	Mean size (nm)	Standard deviation
5 wt% Pd/γ - Al$_2$O$_3$	4.84	0.8
5 wt% Pd$_{PVA}$/γ - Al$_2$O$_3$	4.25	0.9

From high-resolution TEM (HRTEM) images very regularly-shaped Pd nanoparticles with similar morphology were detected in both cases. Moreover, looking at the HRTEM images for 5 wt% Pd$_{PVA}$/Al$_2$O$_3$ (figure 3.12), it is possible to clearly distinguish a thin carbon layer surrounding the Pd nanoparticle, thus confirming the presence of a PVA layer.

Figure 3.12 STEM images, HRTEM images and particle size distributions for the 5% Pd/Al$_2$O$_3$ catalysts (a-c) as-prepared, (d-f) calcined at 200ºC and (g-i) the commercial one.
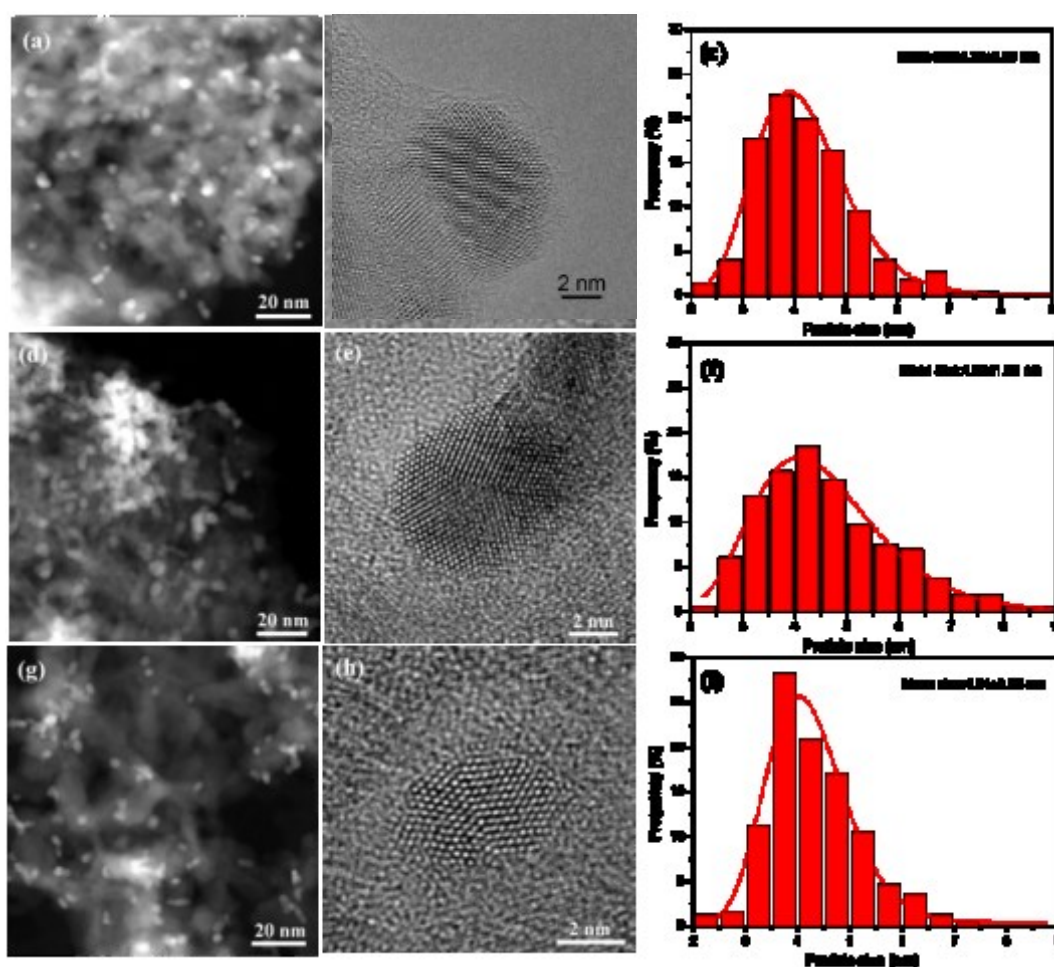
In order to assess eventual differences in the accessibility of active sites in protected and naked nanoparticles, Diffuse Reflectance Infrared Spectroscopy (DRIFTS) was used, monitoring the adsorption of CO as the probe molecule.

The diffuse reflectance infrared (DRIFT) spectra of CO ad-sorbed on 5 wt% Pd/Al_2O_3 obtained by impregnation and on 5 wt% Pd_{PVA}/Al_2O_3 obtained by PVA-sol deposition are reported in Fig.3.13 (a and b, respectively). Adsorbed CO on Pd/Al_2O_3 shows three main signals: a peak at 2095 cm^{-1} deriving from CO linearly bound to Pd particle corners (CO_L), a signal at 1980 cm^{-1} related to μ_2 bridge-bonded CO on Pd (100) facets and a signal at 1935 cm^{-1} which can be attributed to μ_2 bridge-bonded CO on (111) planes.[34] DRIFTS spectra of 5 wt% Pd_{PVA}/Al_2O_3 (Fig. 3.13 b) exhibit two main signals at 2098 cm^{-1} (CO_L) and in the region between 2050 and 1850 cm^{-1}. In this latter broad signal at least three components can be identified (1980, 1960, 1925 cm^{-1}). The main component is centered at 1960 cm^{-1} and is clearly absent on 5 wt% Pd/Al_2O_3. The overall higher intensity of the signals obtained on 5 wt% Pd/Al_2O_3 suggest that on average less Pd atoms are available for CO adsorption on 5 wt% Pd_{PVA}/Al_2O_3 at comparable particle size. This confirmed the shielding effect produced by PVA invoked to justify the lower catalytic activity normally observed for sol-derived catalyst compared with impregnated ones. Based on the similar morphology of the Pd particles obtained by TEM, we associate the presence of the additional signals in the spectral region of bridge-bonded CO to the effect of the PVA molecule present on the Pd NPs. Beside adsorption on naked Pd(100), we associate the signals at 1960 and 1925 to a perturbation acted by PVA on the Pd(100) and Pd(111) active sites. PVA, acting as electron-donor and affects CO π-backbonding, thus lowering the vibrational frequency.[51] On the other hand PVA does not perturb linear adsorption of CO (the signal of CO_L being at the same frequency , 2065 cm^{-1},for both catalysts).

Figure 3.13 DRIFT spectra of adsorbed CO on (a) 5 wt% Pd/Al$_2$O$_3$, (b) 5 wt% Pd$_{PVA}$/Al$_2$O$_3$ and (c) calcined 5 wt% Pd$_{PVA}$/Al$_2$O$_3$.
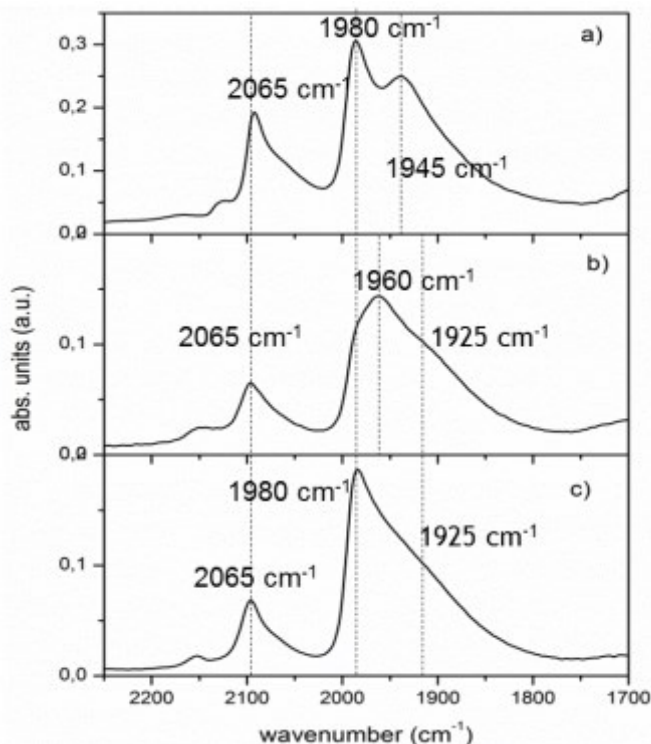
Pd$_{PVA}$/Al$_2$O$_3$ was then calcined at quite low temperature in order to maintain the metallic dispersion. Under these conditions only partial removal of PVA was obtained.

Our assignment is validated by the DRIFT spectrum of 5 wt% Pd$_{PVA}$/Al$_2$O$_3$ calcined at 200°C in air for 1h (Fig. 3.13 c). The TEM images confirm that the morphology of the Pd NPs remains intact, although an increase in particle sizes was observed. DRIFTS spectrum showed that the signal related to μ2 bridge-bonded CO on Pd (100) facets at 1960 cm^{-1} is completely restored at 1980 cm^{-1}, whereas the signal at 1925 related to a perturbation of the adsorption on Pd (111) is still evident. Therefore, we concluded that PVA coordinates and perturbs more strongly in the Pd(111) face sites.

In order to unravel the effect of the presence of the PVA on the catalytic performances, preliminary catalytic tests were carried out in a glass batch reactor

Reaction profiles, shown in Figure 3.14, evidenced a reduced activity of Pd$_{PVA}$/Al$_2$O$_3$ compared to the commercial catalyst, thus confirming the shielding effect of PVA.

Figure 3.14 Reaction profiles for benzyl alcohol oxidation over a) Pd/Al$_2$O$_3$ and b) Pd$_{PVA}$/Al$_2$O$_3$
Reaction conditions: alcohol/metal = 5000/1 mol/mol, 60 °C, pO2 = 2 bar, 1250 rpm., t = 2h
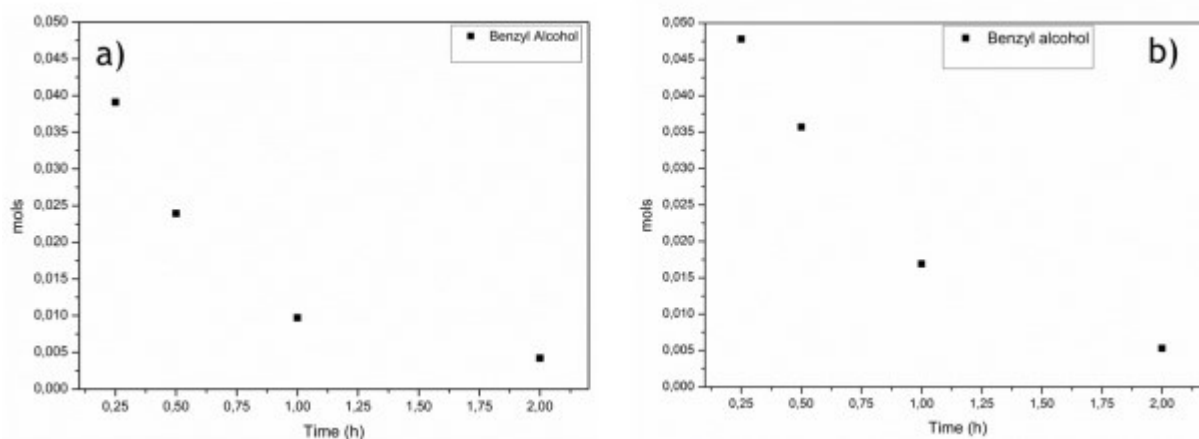
More surprisingly the selectivity is also affected by the presence of PVA (Table 3.4). In particular the presence of PVA has a beneficial effect, increasing the selectivity to benzaldehyde (S=84%), compared to naked nanoparticles (S = 75%).

Table 3.4 Selectivity at 90% conversion

Catalysts[a]	Selectivity[b]			
	Toluene	Benzaldehyde	Benzoic acid	Benzyl benzoate
5%Pd/Al$_2$O$_3$	2%	75%	12%	6%
5%Pd$_{PVA}$/Al$_2$O$_3$	9%	84%	6%	<1%

[a] Reaction conditions: alcohol/metal = 5000/1 mol/mol, 60 °C, pO$_2$ = 2 bar, 1250 rpm., t = 2h
[b] Selectivity at 90% conversion.

Considering the reaction pathway for benzyl alcohol oxidation described in section 3.2, the lower selectivity to benzaldehyde observed with unprotected Pd nanoparticles might be ascribed to the occurrence of one or more of the following reaction:

- Further oxidation to benzoic acid
- Disproportion to benzoic acid and benzyl alcohol
- Decarbonylation to benzene and CO

The lower selectivity to benzoic acid showed by PdPVA/Al2O3 with respect to Pd/Al2O3, let us exclude the first two possibilities. Therefore the lower selectivity to benzaldehyde of commercial catalysts should be attributed to benzaldehyde decarbonylation proceeding in a greater extent with unprotected nanoparticles. Unfortunately the products of this reaction, benzene and CO, are not detectable in our reaction and analytical conditions. Indeed CO is a gas and it is not present in the liquid reaction mixture, whereas the signal of benzene overlapped the signal of the solvent, cyclohexane, in the gas-chromatogram. Therefore we used ATR-FTIR Spectroscopy to follow the evolution of CO on the surface of Pd based catalysts.[25]

The flow-through cell mimicking a continuous-flow reactor configuration enables a better control of the reaction environment compared to a batch reactor cell where the products accumulate on the catalyst surface.[52] The catalyst layer deposited on the ZnSe crystal (Internal Reflection Element, IRE) was kept at 60°C while pumping benzyl alcohol in cyclohexane solution (0.02 M). The overall activity and selectivity have been evaluated by analysing the effluent through an Infrared Spectrophotometer connected online. (Fig.3.15)

Figure 3.15 Experimental set-up for Operando methodology
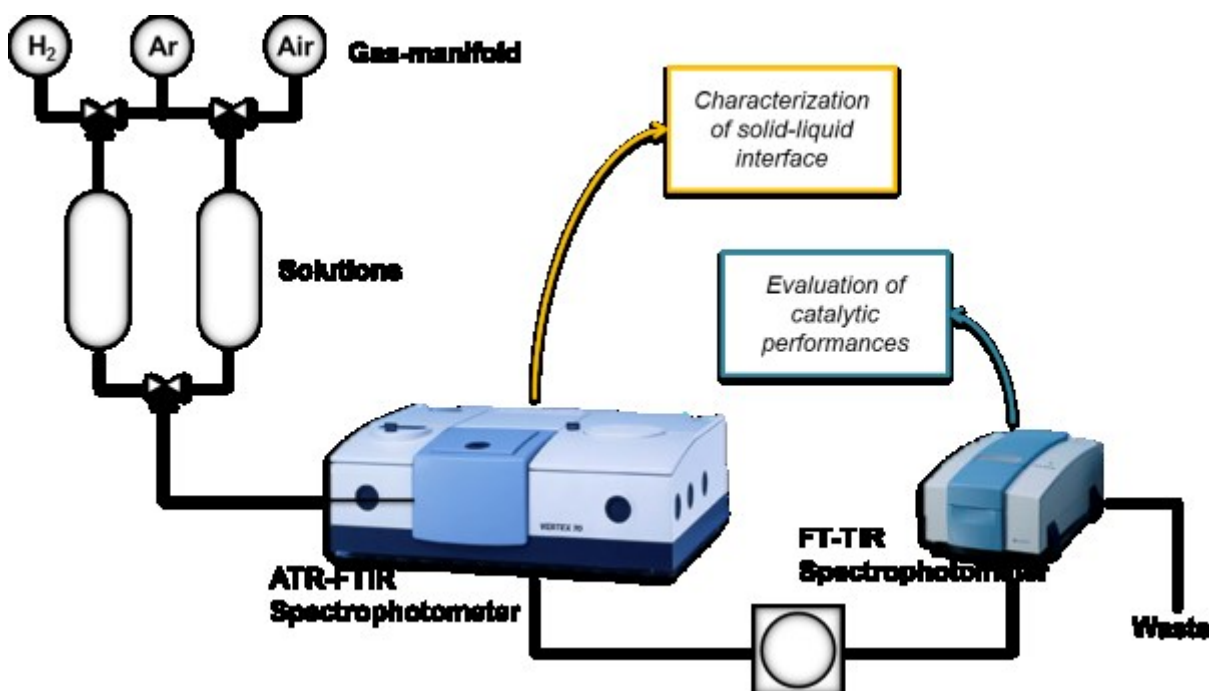
Both dehydrogenation (Ar) and oxidative conditions (O_2) were studied in order to separate the elementary steps of the oxidative dehydrogenation and to evidence eventual differences towards the production of CO for the two catalysts. ATR-IR spectra for benzyl alcohol oxidation under dehydrogenation conditions are shown in Fig.3.16. The region between 1370-1650 cm^{-1} is dominated by signals produced by benzoate species adsorbed on the catalyst surface.[25] The formation of benzoates also in the absence of oxygen has been previously reported in the literature and ascribed to Benzaldehyde formation in the proximity of the surface was monitored by the sharp band at 1712 cm^{-1} corresponding to the v(C=O) stretch mode of the carbonyl group of the aldehyde. The evolution of CO deriving from benzaldehyde decarbonylation is associated with the broad signal at 1806 cm^{-1} that shifts

with time on stream toward 1834 cm^{-1}.[25] Unfortunately toluene production via C-O bond hydrogenolysis of benzyl alcohol cannot be followed since the toluene signals are screened by the more intense ones of benzyl alcohol and benzoates.

Figure 3.16 Operando ATR-IR spectra of (a) 5 wt% Pd/Al2O3 and (b) 5 wt% Pd$_{PVA}$/Al2O3 in contact with a solution of benzyl alcohol under dehydrogenation conditions (Ar).
Dotted spectra are intermediate spectra taken at approximately similar times on stream. Conditions: $C_{alcohol}$ = 20 mM; 10 mg catalyst; cyclohexane solvent; 60°C; liquid flow rate = 0.6 mL/min.
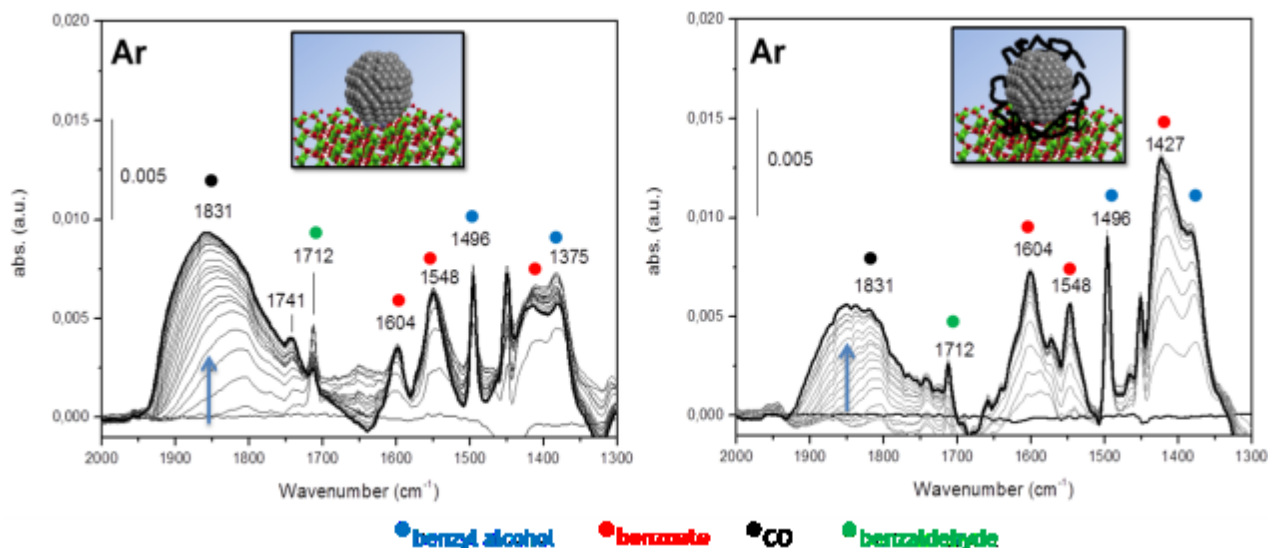
In the dehydrogenation segment (Fig. 3.16, a and b) benzaldehyde decarbonylation seems to take place to a lesser extent on 5 wt% Pd$_{PVA}$/Al$_2$O$_3$ compared to 5 wt% Pd/Al$_2$O$_3$ as it is obvious from the intensity and position of the CO signal. The difference can be better appreciated by analyzing the temporal response of the ν(C=O) signal of benzaldehyde in the ATR-IR spectra and in the transmission IR spectra obtained online at the exit of the cell (Fig.3.17).

Figure 3.17 shows that the amount of benzaldehyde that is formed in the catalyst layer monitored by the infrared radiation in the ATR mode is different in the two catalysts. In the case of 5 wt% Pd$_{PVA}$/Al$_2$O$_3$, benzaldehyde formation reaches a steady state approximately after ca. 15 min. On the contrary, benzaldehyde evolution on 5 wt% Pd/Al$_2$O$_3$ passes through a maximum before returning to the level observed for 5 wt% Pd$_{PVA}$/Al$_2$O$_3$. CO formation and coordination to Pd occurs parallel to benzaldehyde production. CO adsorption increases during the dehydrogenation phase. The rate of growth of the signal of adsorbed CO tightly follows the evolution profile of benzaldehyde, clearly indicating that decarbonylation occurs at the beginning of the reaction with 5 wt% Pd/Al$_2$O$_3$. The high amount of benzaldehyde obtained at the beginning of the reaction under dehydrogenation conditions for 5 wt% Pd/Al$_2$O$_3$ is confirmed by online infrared spectra of Fig. 3.17b.

Figure 3.17 Time response of selected (a) ATR-IR signals of benzaldehyde(1712 cm^{-1}), (b) FT-IR signals of benzaldehyde (1712 cm^{-1}) and (c) ATR-IR signals of adsorbed CO (1831 cm^{-1}) under dehydrogenation conditions (Ar).
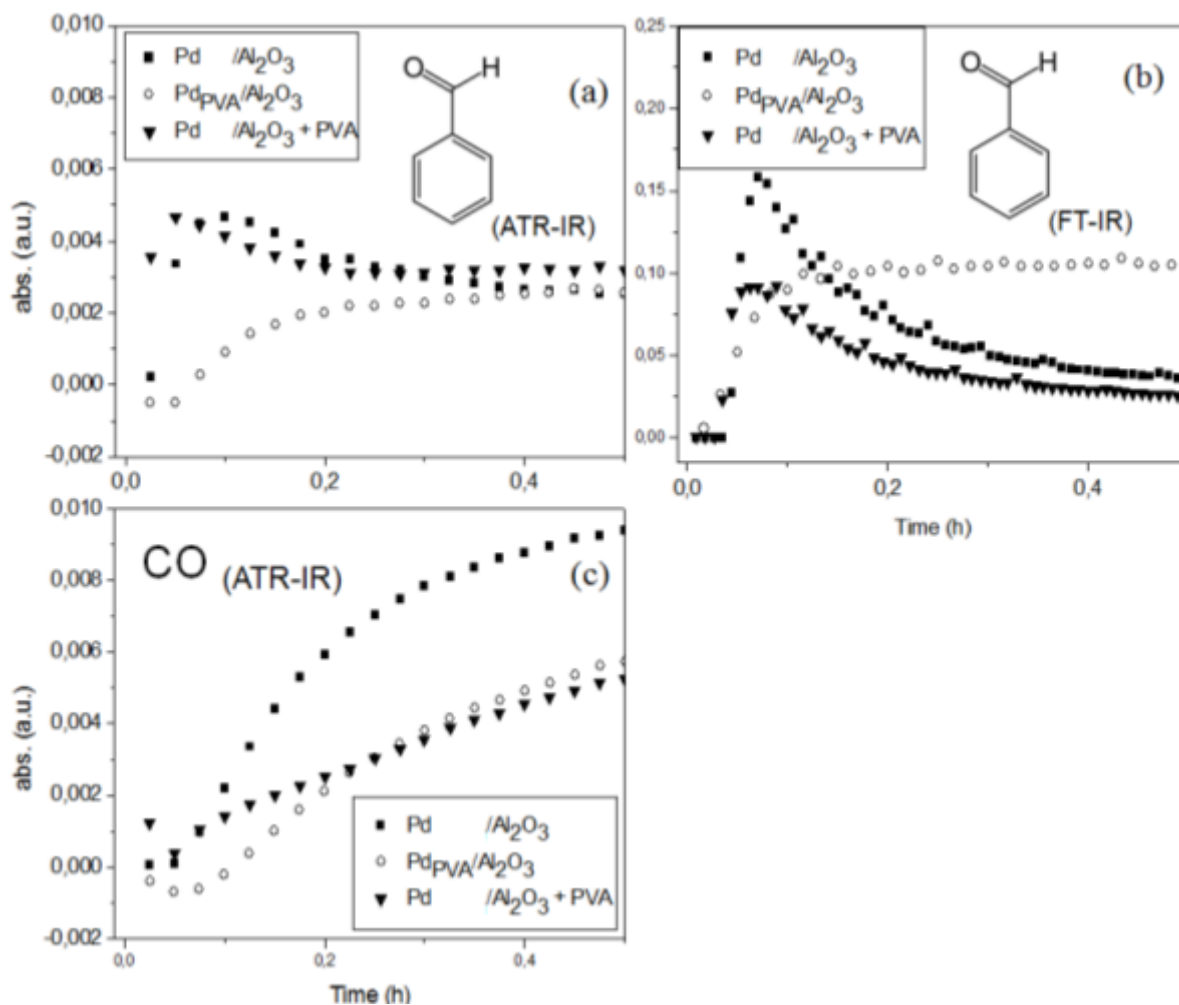
The discrepancy in the amount of benzaldehyde detected on the catalyst surface by ATR-IR spectroscopy in Fig. 3.17a and in solution by transmission spectroscopy in Fig. 3.17b is understandable remembering that ATR-IR spectroscopy monitors a thin layer of the catalyst (ca. 1-4 μm as a function of energy) that is identical in the two experiments. On the contrary, the online spectrometer at the exit of the cell measures the overall production of the catalyst layer on the IRE. Therefore, 5 wt% Pd$_{PVA}$/Al$_2$O$_3$ demonstrates higher benzaldehyde production than 5 wt% Pd/Al$_2$O$_3$ under dehydrogenation conditions. Despite the difficulty to accurately compare these infrared results with activity data from batch reactor measurements, spectroscopic data confirmed the higher selectivity toward benzaldehyde of Pd$_{PVA}$/Al$_2$O$_3$ than Pd/Al$_2$O$_3$ observed in tests performed in a conventional glass batch-reactor (Table 3.4) (S^{90} 84% and 75% respectively). Moreover ATR addressed the higher aldehyde production to a less decarbonylation process. As it has previously been demonstrated using ATR-IR spectroscopy that the occurrence of decarbonylation is strictly related to the presence of sites on Pd(111) faces, [25] the higher selectivity of Pd$_{PVA}$/Al$_2$O$_3$ can be attributed to the presence of PVA which selectively blocks part of the sites responsible for benzaldehyde decomposition. The interpretation that the residence time of benzaldehyde on the Pd(111) faces facilitates decarbonylation has been confirmed by recent TPD-HREELS experiments revealing the crucial role of the adsorption geometry of the aromatic moiety. The flat lying adsorption geometry adopted by benzyl alcohol molecules at low Pd(111) surface

coverage was shown to favour benzaldehyde decarbonylation.[53] Therefore the experimental results from DRIFTS and ATR-IR experiments pointed out that PVA molecules induce a selectivity control by influencing molecular adsorption orientation. In the proximity of PVA molecules anchored to Pd(111) faces, benzyl alcohol can likely adsorb with the ring away from the surface in a similar fashion to the Pd(100) faces where benzaldehyde is more likely formed and desorbed without decomposition.[25]

The selectivity improvement induced by the capping agent was also observed in the presence of molecular oxygen (Fig.3.18, a and b).

3.18 ATR-IR spectra of unprotected (a) and protected (b) Pd NPs supported on Al$_2$O$_3$ under oxidative conditions

ATR-IR spectra of a solution of benzyl alcohol under oxidative conditions on Pd/Al$_2$O$_3$ (a) and on Pd$_{PVA}$/Al$_2$O$_3$(b). Dotted spectra are intermediate spectra taken at approximately similar times on stream. Conditions: [alcohol] = 20 mM; 4 mg catalyst; cyclohexane solvent; 60 °C; liquid flow rate = 0.6 mL/min
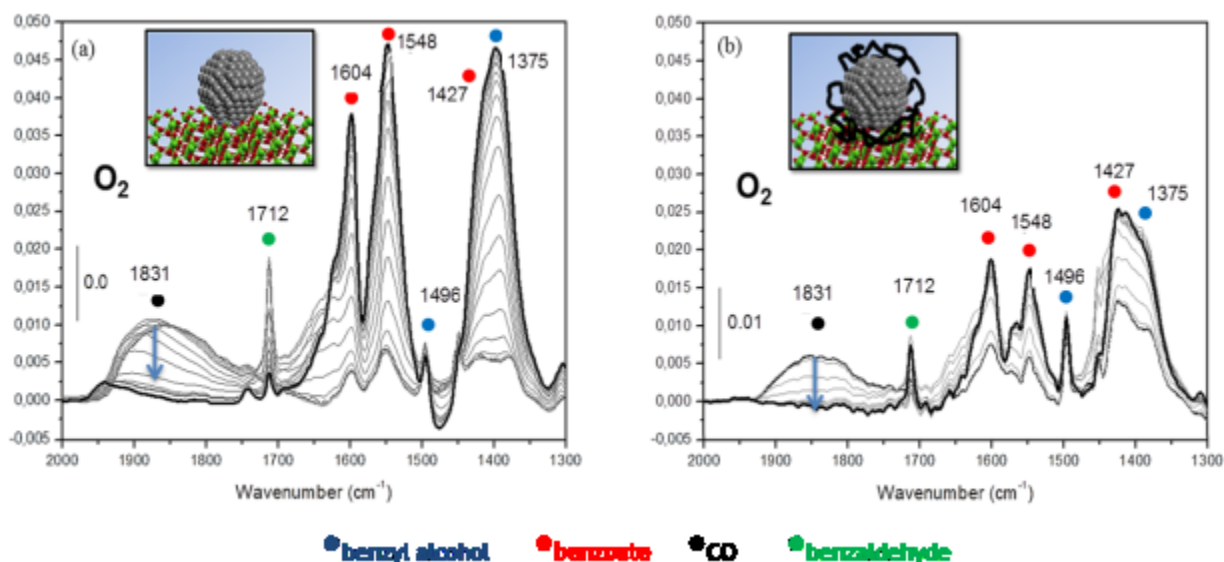
Under oxidative conditions an increase of benzoate signals on the catalyst surface was observed in both cases, while CO signal quickly disappeared as a consequence of the CO removal by oxygen. In agreement with the batch reactor data revealing higher selectivity to benzoic acid for 5 wt% Pd/Al$_2$O$_3$ (Table 3.4), a greater amount of adsorbed benzoate was detected in the case of 5 wt% Pd/Al$_2$O$_3$ compared to 5 wt% Pd$_{PVA}$/Al$_2$O$_3$. Furthermore, in the case of unprotected Pd NPs benzyl benzoate was detected by ATR-IR spectroscopy (Fig. 3.18 a, signal at 1741 cm^{-1}), whereas it is absent in protected Pd/Al$_2$O$_3$. It has been shown that benzyl benzoate formation by the dehydroesterification reaction between benzaldehyde and benzyl alcohol molecules adsorbed on adjacent sites is inhibited on Au/SiO$_2$ in the presence of polyvinylpyrrolidone (PVP),[15] as a consequence of site isolation induced by PVP. A similar effect could explain the lower fraction of benzyl benzoate in PVA-protected Pd NPs.

To further support our hypothesis that PVA is actively involved in addressing catalyst selectivity, PVA was adsorbed onto 5 wt% Pd/Al$_2$O$_3$ .The ATR-IR spectra and the catalytic behaviour monitored in the liquid phase (Fig. 3.18) showed however an intermediate behaviour between those obtained with Pd$_{PVA}$/ Al$_2$O$_3$ and Pd/ Al$_2$O$_3$. We then supposed that

in the latter case a non-selective adsorption of PVA occurred resulting simply in the decrease of the catalytic activity without differentiating the adsorption sites and selectivity.

3.5 Conclusions

By using *operando* spectroscopy it has been possible to investigate some critical points, concerning supported noble metal nanoparticles, still debated in the scientific community. In fact, monitoring by ATR-IR Spectroscopy the species evolving on catalytic solid-liquid interface allowed us to gain an insight into:

- the factors determining the improved durability of bimetallic catalysts and
- the role of the capping agent.

Regarding the first point, the catalytic performances of monometallic (Au and Pd) and bimetallic AuPd nanoparticles deposited on TiO_2 by sol immobilisation technique were investigated using *in situ* Attenuated total reflectance (ATR) IR spectroscopy in a batch-reactor cell. Experimental results provided a plausible explanation for the well-known improvement in durability observed with bimetallic catalysts. The presence of gold in AuPd bimetallic nanoparticles drastically limited the irreversible adsorption of products observed for Pd, by facilitating the desorption of the products, especially benzoate species and thus decreasing the extent of catalyst deactivation. The presence of gold affected also the selectivity. In particular the formation of toluene was suppressed in bimetallic catalysts probably because of the reduced amount of benzyl alcohol on the surface. Conversely, the transformation of benzaldehyde to benzoic acid was favoured.

Using *Operando* ATR-IR Spectroscopy it has been possible to gather deeper insight into the role of the PVA protective molecule in directing the selectivity of palladium catalyzed benzyl alcohol oxidation. In particular, a higher selectivity to benzaldehyde has been showed by 5wt% Pd_{PVA}/Al_2O_3 compared to 5 wt% Pd/Al_2O_3. Detailed catalyst characterization by TEM and DRIFTS revealed that, particle size and morphology being similar, the presence of PVA layer in protected Pd nanoparticles limits the accessibility of active sites thus reducing the catalytic activity. However, the presence of PVA has a beneficial effect on the selectivity, resulting in a lower degradation of benzaldehyde by decarbonylation, as a consequence of the selective blocking of Pd (111) faces. In conclusion, IR spectroscopy confirmed that the presence of PVA in catalysts prepared by metallic sol immobilization is not innocent neither from activity nor selectivity stand-points. The possibility to direct the selectivity in alcohol oxidation by a selective blocking of specific active site represents a potential tool and an additional advantage in using supported metal nanoparticles from colloidal synthesis as catalyst.

References

[1] G. Mestl, M. A. Bañares in J. A. Rodriguez, J. C. Hanson, P. J. Chupas (eds.), *In-situ Characterization of Heterogeneous Catalysts*, John Wiley & Sons, 2013, ISBN 1118355911, 9781118355916.

[2] J. F. Haw (ed.), *In Situ Spectroscopy in Heterogeneous Catalysis*, Wiley-VCH, Weinheim, 2002 –ISBN 3-527-30248-4.

[3] B. M. Weckhuysen, *Phys. Chem. Chem. Phys.*, 2003, 5, 4351–4360;

[4] a) B. M. Weckhuysen, Chem. Commun. 2002, 97; b) A. Brückner, Phys. Chem. Chem. Phys. 2003, 5, 4461; c) M. A. Banares, Catal. Today 2005, 100, 71; d) M. O. Guerrero-Perez, M. A. Banares, Catal. Today 2006, 113, 48.

[5] B.M. Weckhuysen, *Natl Sci Rev*, 2015, Vol. 2, No. 2

[6] M.A. Bañares, *Catal Today* 2005; 100, 71–7.

[7] U. Bentrup, *Chem Soc Rev* 2010; 39: 4718–30.

[8] a) D. Ferri, T. Bürgi, A. Baiker, J. Phys. Chem. B 105 (2001) 3187; b) D. Ferri, T. Bürgi, J. Am. Chem. Soc. 123 (2001) 12,074; c) D. Ferri, T. Bürgi, A. Baiker, J. Chem. Soc., Chem. Commun. (2001), 1172; d) N. Bonalumi, T. Bürgi, A. Baiker, J. Am. Chem. Soc. 125 (2003) 13,342; e) T. Bürgi, A. Baiker, J. Phys. Chem. B 106 (2002) 10,649; f) T. Bürgi, R. Wirz, A. Baiker, J. Phys. Chem. B 107 (2003) 6774.

[9] N.J. Harrick, Internal Reflection Spectroscopy, Interscience, New York, 1967.

[10] M.I. Tejedor-Tejedor, M.A. Anderson, Langmuir 2 (1986) 203

[11] Messerschmidt, US Patent 4 730 882.

[12] A. Savara, E. Weitz, *Annu. Rev. Phys. Chem.* 2014. 65:249–73.

[13] U. Wolf, R. Leiberich, J. Seeba, *Catalysis Today* 49 (1999) 411-418.

[14] a) C.P. Vinod, K. Wilson, A.F. Lee, *J. Chem. Technol. Biotechnol.*, (2011), 86,161–171; b) N.Dimitratos, J.A. Lopez-Sanchez, G.J. Hutchings, *Chem. Sci.*, (2012), 3, 20–44; c) C.D. Pina, E. Falletta, M. Rossi, Chem. Soc. Rev.,(2012) 41, 350–369; d) N. Dimitratos, J. A. Lopez-Sanchez, D. Morgan, A. Carley, L. Prat, G. J.Hutchings, *Catalysis today*, (2007),122(3), 317-324.

[15] a) T. Mallat, A. Baiker, *Chem. Rev.* 2004, 104, 3037–3058; b) F. Porta, L. Prati, *J. Catal.* 2004, 224, 397–403; c) A. Villa, D. Wang, P. Spontoni, R. Arrigo, D. Su, L. Prati, *Catal. Today*, 2010, 157, 89–93; d) Q. He, P. J. Miedziak, L. Kesavan, N. Dimitratos, M. Sankar, J. A. Lopez-Sanchez, M. M. Forde, J. K. Edwards, D. W. Knight, S. H. Taylor, C. J. Kiely, G. J. Hutchings, *Faraday Discuss.* 2013, 162, 365–378.

[16] a) J. A. Gates, L. L. Kesmodel, J. Catal. 1983, 83, 437– 445; b) S. W. Jorgensen, R. J. Madix, Surf. Sci. 1987, 183, 27–43; c) J. L. Davis, M. A. Barteau, Surf. Sci. 1988, 197, 123 –152; d) J. L. Davis, M. A. Barteau, Surf. Sci. 1992, 268, 11 –24.

[17] B. N. Zope, D. D. Hibbitts, M. Neurock, R. J. Davis, Science 2010, 330, 74–78.

[18] A. Abad, A. Corma, H. Garcìa, Chem. Eur. J., 2008, 14, 212–222.

[19] a) N. Kruse, M. Rebholz, V. Matolin, G. K. Chuah, J. H. Block, Surf. Sci. 1990, 238, L457 – L462; b) M. Rebholz, V. Matolin, R. Prins, N. Kruse, Surf. Sci. 1991, 251, 1117 –1122; c) J. Hoffmann, S. Schauermann, V. Johanek, J. Hartmann, J. Libuda, J. Catal. 2003, 213, 176 – 190.

[20] a) M.K. Weldon, C.M. Friend, Chem. Rev., (1996), 96, 1391–1412; b) J.W. Nicoletti, G.M. Whitesides, J. Phys. Chem., (1989), 93, 759–767.

[21] a) S.S. Hladyi, , M.K. Starchevsky, Y.A. Pazdersky, M.N. Vargaftik, I.I. Moiseev, *Mendeleev Commun.,* (2002), 12, 45–46; b) D.M. Meier, A.Urakawa, A. Baiker, *J. Phys. Chem. C,* (2009) 113, 21849–21855; c) M. Sankar, E. Nowicka, R. Tiruvalam, Q. He, S.H. Taylor, C.J. Kiely, D. Bethell, D.W. Knight, G.J. Hutchings, Chem. Eur. J., (2011), 17, 6524–6532.

[22] M., Caravati, J.-D., Grunwaldt, A. Baiker, *Phys. Chem. Chem. Phys.,* (2005), 7, 278–285.

[23] M. Sankar, E. Nowicka, E. Carter, D. M. Murphy, D. W. Knight, D. Bethell, G. J. Hutchings, Nature communications, (2014), 5.

[24] J.-I. Hojo, S. Yuasa, N.,Yamazoe, I. Mochida, T. Seiyama, *J. Catal.*, (1975), **36**, 93–98.

[25] C. Keresszegi, D. Ferri, T. Mallat, A. Baiker, J. Phys. Chem. B 2005, 109, 958–967.

[26] A. Savara, C. E. Chan-Thaw, I. Rossetti, A. Villa, L. Prati, *ChemCatChem,* 2014, 6, 3464 – 3473.

[27] M. Sankar, E. Nowicka, P.J. Miedziak, G.L. Brett, R.L. Jenkins, N. Dimitratos, S.H. Taylor, D.W. Knight, D. Bethell, G.J. Hutchings, *Faraday Discuss.*, **2010**, 145, 341-356

[28] C. J. Zhang, P. Hu, J. Chem. Phys. 2001, 115, 7182 – 7186.

[29] S. H. Pang, A. M. Roman, J. W. Medlin, J. Phys. Chem. C, 2012, 116, 13654 –13660.

[30] a) D. Wang, A. Villa, F. Porta, D. Su, L. Prati, Chem. Commun. 2006, 1956 –1958; b) D. I. Enache, J. K. Edwards, P. Landon, B. Solsona-Espriu, A. F. Carley, A. A. Herzing, M. Watanabe, C. J. Kiely, D. W. Knight, G. J. Hutchings, Science 2006, 311, 362–365; c) A. Villa, D. Wang, N. Dimitratos, D. Su, V. Trevisan, L. Prati, Catal. Today, 2010, 150, 8–15; d) W. Hou, N. A. Dehm, R. W. J. Scott, J. Catal. 2008, 253, 22–27.

[31] M. Chen, D. Kumar, C. W. Yi, D. W. Goodman, Science 2005, 310, 291 –293.

[32] E. Nowicka, J. P. Hofmann, S. F. Parker, M. Sankar, G. M. Lari, S. A. Kondrat, D. W. Knight, D. Bethell, B. M. Weckhuysen, G. J. Hutchings, Phys. Chem. Chem. Phys. 2013, 15, 12147– 12155.

[33] M. S. Ide, D. D. Falcone, R. J. Davis, J. Catal. 2014, 311, 295–305.

[34] a) A. R. Denton, N. W. Ashcroft, Phys. Rev. A 1991, 43, 3161–3164; b) T. Lear, R. Marshall, J. A. Lopez-Sanchez, S. D. Jackson, T. M. Klapçtke, M. Bumer, G. Rupprechter, H. J. Freund, D. Lennon, J. Chem. Phys. 2005,123, 174706–174713; c) D. Tessier, A. Rakai, F. Bozon-Verduraz, J. Chem. Soc. Faraday Trans. 1992,88, 741–749; d) N. Sheppard, C. De La Cruz, Catal. Today 2001, 70, 3–13; e) N. Sheppard, T. T. Nguyen in Advanced Infrared Raman Spectroscopy, Vol. 5 (Eds.: R. J. H. Clark, R. E. Hester), Heyden, London, 1978, pp. 67–148; f) C. De La Cruz, N. Sheppard, J. Mol. Struct. 1990, 224, 141–161; g) E. Ozensoy, D. W. Goodman, Phys. Chem. Chem. Phys. 2004, 6, 3765 –3778.

[35] a) G. Blyholder, *J. Phys. Chem*. 68 (1964) 2772; b) L. L. Shieu, Z. Karpinski, W. M. H Sachtler, *J. Phys. Chem*.,1989,93,4890; c) J. S. Bradley,* E. W. Hill, S. Behal, and C. Klein, B. Chaudret, A. Duteil, *Chem. Mater.* 1992,4, 1234-1239; d) M. A. Vannice, S. Y. Wang, J. Phys. Chem. 1981, 85, 2543–2546.

[36] F. Di Gregorio, L. Bisson, T. Armaroli, C. Verdon, L. Lemaitre, C. Thomazeau,Appl. Catal. A 2009, 352, 50–60.

[37] E. Roze, P. Gravejat, E. Quinet, J. L. Rousset, D. Bianchi, J. Phys. Chem. C, 2009, 113, 1037–1045.

[38] a) S. Carrettin, P. McMorn, P. Johnston, K. Griffin, C. J. Kiely, G. J. Hutchings, Phys. Chem. Chem. Phys. 2003, 5, 1329–1336; b) S. Demirel-Gìlen, M. Lucas, P. Claus, Catal. Today 2005, 102–103, 166 –172.

[39] A. Villa, D. Wang, G. M. Veith, F. Vindigni, L. Prati, Catal. Sci. Technol., 2013, 3, 3036–3041.

[40] M. B. Griffin, A. A. Rodriguez, M. M. Montemore, J. R. Monnier, C. T. Williams, J. W. Medlin, J. Catal. 2013, 307, 111–120.

[41] L. Prati and G. Martra, *Gold Bull*., **1999**, 32, 96.

[42] S. Coluccia, G. Martra, F. Porta, L. Prati, M. Rossi, *Catal. Today*, **2000**, 61, 165.

[43] K. Chen, H. Wu, Q. Hu, S. Chang, W. Huang, *Phys. Chem. Chem. Phys.*, **2013**, 15, 2273-- 2277

[44] S.T. Marshall, M. O'Brien, B. Oetter, A. Corpuz, R. M. Richards, D. K. Schwartz, J.W. Medlin, *Nature Material*, **2010**, 9, 853-858

[45] a) C. A. Schoenbaum, D. K. Schwartz, J. W. Medlin, *Acc. Chem. Res.*, **2014**, 47, 1438−1445; b) R. Zhong, K. Sun, Y. Hong, B. Xu, *ACS Catal.* **2014**, 4, 3982−3993; c) K. R. Kahsar, D. K. Schwartz, J. W. Medlin, *J. Am. Chem. Soc.*, **2014**, 136, 520−526

[46] a) B. Feng, Z. Hou, H. Yang, X. Wang,Y. Hu, H. Li, Y. Qiao, X. Zhao, Q. Huang, *Langmuir*, **2010**, 26(4), 2505–2513; b) A. Quintanilla, V.C.L. Butselaar-Orthlieb, C. Kwakernaak, W.G. Sloof, M.T. Kreutzer, F. Kapteijn, *Journal of Catalysis*, **2010**, 271, 104–114

[47] a) Z. Niu, Y. Li*, Chem. Mater*. **2014**, 26, 72−83; b) T. Mallat, A. Baiker, *Applied Catalysis A: General*, **2000**, 200, 3–22; c) G. Pieters, L. J. Prins, *New J. Chem.*, **2012**, 36, 1931–1939; d) W. Huang, Q. Hua, T. Cao, *Catal Lett*,**2014**, 144, :1355–1369; e) D. J. Gavia, Y.-S. Shon, *ChemCatChem*, **2015**, 7, 892 – 900.

[48] T. Bürgi, *CHIMIA*, **2003**, 57 (10), 623-627

[49] a) T. Bürgi, *Journal of Catalysis*, **2005**, 229(1), 55-63; b) D. Ferri, C. Mondelli, F. Krumeich, A. Baiker, *J. Phys. Chem. B*, **2006**, 110(46), 22982-22986; c) C. Mondelli, D. Ferri, J.Grunwaldt, F. Krumeich, S. Mangold, R. Psaro, A. Baiker, Journal of Catalysis, **2007**, 252, 77–87.

[50] A. Villa, D. Ferri, S. Campisi, C. E. Chan-Thaw, Y. Lu, O. Kröcher, L. Prati, ChemCatChem 2015, 7, 2534 – 2541

[51] N. A. Ray, R. P. Van Duyne, P. C. Stair, *J. Phys. Chem. C,* **2012**, 116, 7748−7756

[52] D. Ferri, A. Baiker, *Topics Catal*., **2009**, 52, 1323;

[53] R. M. Williams, J. W. Medlin, *Langmuir*, **2014**, 30, 4642−4653

4 *DFT modelling of Ethanol Aerobic Oxidation over Gold based Catalysts*

The relevance of computational modeling in heterogeneous catalyst design has been discussed in the introductive section (Chapter 1, Section 8).

An exhaustive catalytic process modelling should be able to provide and integrate detailed information regarding:

1. The electronic and structural changes which are directly involved in the reaction network
2. The dynamics of adsorbates and surface atoms at the interface
3. The kinetics for all steps of the catalytic cycle (physisorption, reaction and diffusion)
4. The fluid dynamics concerning heat and mass transfer inside the reactor
5. The deactivation phenomena affecting the catalyst-life over time.

Looking at the list reported above, it is self-evident that such a process modelling is a multiscale and multidisciplinary problem, which investigates events occurring in time-scale from 10^{-15} s for electronic transitions up to years for deactivation phenomena, and in a range of length scales that spans from 10^{-10} m (at atomic level) to 10^2 m (in industrial plants), and which involves various scientific disciplines, from physical chemistry to industrial engineering. It is therefore obvious that no just one rather many models have to be combined in order to obtain the information we need. Chemists usually focus on understanding structure and dynamics at atomic and/or microscopic scales.

At this level, the main goal of computational modelling is to identify the more energetically favored reaction paths, to calculate the elementary kinetics for each process, to unravel the influence of the local environment as well as of the particle size, shape, morphology, chemical composition and atomic configurations on the catalytic performances (activity, selectivity and lifetime). For this purpose, a full quantum-mechanical description of bond-breaking and bond-making events is provided by electronic structure method, and in particular by Density Functional Theory, which is the subject of this chapter.

The work presented in this chapter has been performed during my stay at Cardiff University – School of Chemistry in the research group of Dr. David J. Willock, in the frame of an Erasmus Placement Traineeship. The main aim of the collaboration with Dr. Willock is the application of DFT modelling to the study of mechanistic aspects in gold-based catalysts. In particular we are interested in disclosing not only the atomic scale structure of the active site, but also the influence of its close environment (the site coordination, the presence of additives like promoters or poisons, the role of the protecting agent, the addition of another metal forming an alloy, the role of the solvent and the relevance of metal-support interactions), to support with theoretical the experimental observations. Due to the brevity of the stay (3 months) at the moment just preliminary results on model systems have been obtained. However thanks to the kind support of Dr. D.J. Willock, who is providing me with remote access to the Cardiff HPC resources, further studies are ongoing.

4.1 Quantum mechanical methods and Density Functional Theory (DFT)

4.1.1 Electronic structure and Schrödinger equation

A wide range of properties, including relative energies, geometric structure, spectroscopic signatures and reactivity, is determined by the electronic structure of the system. The latter is definitively described by the exact position of all the atoms and their constituents (electrons and nuclei) and by the fundamental forces acting upon them. The final goal of quantum mechanical methods is to predict the electronic structure (the electronic states of the system and their energy levels) and related properties for an N-particle system. For this purpose, Schrödinger's equation, describing the state of the many body N-electron system and its corresponding energy, need to be solved. [1]

The time-independent Schrödinger equation is:

$$\hat{H}\Psi = E\Psi \tag{4.1}$$

where $\Psi(r)$ is the wavefunction (the square of the wavefunction Ψ^2 defines the probability distribution for the N-particle system), E is the energy of the N-particle system and $\hat{H}$ is the Hamiltonian, which is a mathematical operator including the kinetic energy ($\hat{T}$) and potential energy ($\hat{V}$) operators acting on the overall system wavefunction Ψ.

These operators can be written as:

$$\hat{T} = -\sum_{i=1}^{N} T_i = -\sum_{i=1}^{N} \frac{\hbar}{2m_1}\nabla_i^2 = -\sum_{i=1}^{N} \frac{\hbar}{2m_i}\left(\frac{\partial^2}{\partial x^2} + \frac{\partial^2}{\partial y^2} + \frac{\partial^2}{\partial z^2}\right) \tag{4.2}$$

$$\hat{V} = \sum_{i=1}^{N}\sum_{j>i}^{N} V_{ij} \tag{4.3}$$

where T_i is the kinetic energy of particle i and V_i and V_j represent the potential energy terms for electronic interactions between electron–electron, electron–nuclei and, nuclei–nuclei interactions.

Except rare cases, the solution of Schrödinger's equation for N-particle system is much complicated and therefore some simplifying approximations are necessary. The most common one is the Born–Oppenheimer approximation, assuming that it's possible to separate electronic from nuclear motions. Indeed, considering the heavier masses of nuclei compared to electrons, the motion of electrons occurs on a faster timescale compared to the nuclear one, thus allowing to factorize the wavefunction into its separate nuclear and electronic components. The electronic wavefunction can then be solved separately for a fixed set of nuclear positions (R) (4.4)

$$\hat{H} = -\sum_{i}^{n} \frac{\hbar}{2m_i}\nabla_i^2 - \sum_{i}^{n}\sum_{a}^{N} \frac{Z_a}{|r_i - R_a|}e^2 + \sum_{i}^{n}\sum_{j>i}^{n} \frac{1}{|r_i - r_j|}e^2 \qquad + \sum_{a}^{n}\sum_{b>a}^{n} \frac{Z_a Z_b}{|R_a - R_b|}e^2$$

$$\text{\textit{Kinetic} \quad \textit{Nuclear–Electron Attraction} \quad \textit{Electron–Electron Repulsion} \quad \textit{Nuclear–Nuclear Repulsion}}$$

Where r_i and R_a indicate the positions of electron i and atom a, Z_a is the atomic number of atom a, the number of electrons is defined as n and the number of nuclei as N. [1]

The solution of this equation can be obtained by quantum mechanical computational algorithms, which at the lowest level are based on a hierarchical structure composed by two loops: the inner loop requires the convergence of the electronic structure for a fixed set of atomic positions within a tolerance range defined by the user; the outer loop varies the atom positions so as to minimize the forces acting on each atom.

4.1.2 Quantum mechanical methods for Schrödinger equation solution

Quantum mechanical methods are useful for modeling all processes involving changes in the electronic structure (electron transfer processes, bond formation, bond breaking), however their predictions fail for system with more than 10^3 atoms.

The object of the calculation is a **structure**, which could be:
- A simple molecule (e.g. the reactants and products of the reaction)
- A macromolecule (e.g. the protecting agent in nanoparticles prepared by sol immobilization)
- A metal cluster (e.g. the active species of a catalyst)
- A bulk metal or metal oxide (the catalyst or the support)
- A complex system (catalytic surface with adsorbates, solution molecules and ions)

In order to describe the starting structure, the initial **atomic positions** have to be defined in terms of:
- Cartesian coordinates (x, y, z)
- Direct coordinates, or
- z-coordinates

The electronic structure can be mathematically described by an infinite number of basis functions. More practically, these functions can be relaxed to a finite number of **basis sets**. According to the quantum mechanical method, the property we want investigate and the required degree of accuracy, different functions can be selected as basis sets:
- Slater-type functions,
- Gaussian functions, and
- Plane waves

In addition to the atomic positions and to the basis functions, other variables have to be specified:
- The number of electrons, orbital occupations and the charge of the system
- The kind of calculation performed (a single point calculation, geometry optimization, a transition-state search, a molecular dynamics simulation),
- Operative instructions (the electronic and geometric convergence criterion, the density mixing scheme),
- The relative accuracy of the calculation (expanded basis sets, increased energy cutoffs, etc.)
- The information requested as output (orbitals, population analyses, density of states, frequencies, thermodynamic properties, etc.)

In general, quantum mechanical methods used to solve the Schrödinger equation can be classified as either semiempirical or ab initio, which in turn can be subdivided into wavefunction methods and density functional theory. The latter is the subject of this chapter and it will dealt separately in the next section.

As suggested by the name, semi-empirical methods combine quantum mechanical calculations with experimental data; in particular in semi-empirical methods electron–electron interactions are not calculated by solving multicenter integrals rather they are fitted in such a way as to produce results that best match with experimental data [2].

Ab initio is a latin term meaning "from the beginning" and refers to all computational methods don't introduce any experimental data in the calculations.

Ab initio wavefunction methods are based on the Hartree–Fock (HF) solution strategy, which avoids the direct solution of electron–electron interactions by replacing these interactions with a mean field approach. This approach neglects the reciprocal influence of electrons, which actually correlate their motion so as to avoid one another. Electron correlation is defined as the difference in the energy between the HF solution and the lowest possible energy for the particular basis set that is used. [3]

4.1.3 Density functional theory (DFT) and DFT+U approach

Density functional theory is an *ab initio* method, since it is derived from first principles without requiring any parametrization with experimental data. This theory originates from Hohenberg-Kohn theorem [4] and it can be considered as a result of theories by Thomas[5], Fermi[6] and Dirac[7] in which electron correlation was treated as a functional of the electron gas.

In fact, according to Hohenberg and Kohn[4], the ground-state energy for a system is a unique functional of its electron density:

$$E[n(r)] = F[n(r)] + \int n(r)V_{ext}(r)d^3r$$

(4.5)

Where the second term represents the external potential determined by the nuclear–electron attraction, while $F[n(\mathbf{r})]$ is an unknown functional, which can be partitioned into kinetic energy (T) for the motion of non-interacting electrons, potential energy (U) for and electron–electron repulsion (involving Coulomb forces as well as self-interactions), and exchange correlation (E_{XC}) which covers all other electron–electron interactions. Kohn and Sham equations provide the explicit form for $F[n(\mathbf{r})]$:

$$F[n(r)] = T[n(r)] + U[n(r)] + E_{XC}[n(r)]$$

(4.6)

$$F[n(r)] = T_s[n(r)] + \frac{e^2}{2}\iint \frac{n(r)n(r')}{|r-r'|}d^3rd^3r' + E_{xc}[n(r)]$$

(4.7)

Kohn and Sham demonstrated that the N-particle system could be rewritten as a set of n-electron problems that could be solved self-consistently way.[8] Indeed density of the system can be defined as the sum of squares of single particle wavefunctions $\Psi_i(\mathbf{r})$ (the Kohn–Sham orbitals):

$$n(r) = \sum_i |\Psi_i(r)|^2$$

(4.8)

And therefore $T_s[n(\mathbf{r})]$ can be rewritten:

$$T_s[n(r)] = -\frac{\hbar^2}{2m_e}\sum_i \Psi_i(r)\nabla^2\Psi_i(r)d^3r$$

(4.9)

Minimising the energy with respect to electron density, with a constant number of electrons, a set of equations are produced:

$$\left(-\frac{\hbar^2}{2m_e}\nabla^2 + V_{eff}(r)\right)\Psi_i(r) = \varepsilon_i\Psi_i(r)$$

(4.10)

the effective potential V_{eff} includes the external potential and the exchange correlation:

$$V_{eff} = V_{ext}(r) + e^2 \int \frac{n(r')}{|r - r'|} d^3r' + V_{xc}(r)$$

$$(4.11)$$

the exchange correlation potential corresponds to the derivative of the exchange correlation energy with respect to the density:

$$V_{xc}(r) = \frac{\delta E_{xc}}{\delta n(r)}$$

$$(4.12)$$

The N-electron Schrödinger equation is now reduced to n single-electron problems that take the following form:

$$\hat{H}_{KS}|\Psi_i\rangle = \varepsilon_i|\Psi_i\rangle$$

$$(4.13)$$

Unfortunately, the exchange correlation energy is not known and therefore approximations must be introduced in order to solve the electronic structure problem.

The most basic solution invokes the local density approximation (LDA) which assumes that exchange-correlation per electron can be assimilated to the exchange correlation per electron in a homogeneous electron gas with the same electron density at a specific point r :

$$E_{xc}^{LDA} = \int n(r)\varepsilon_{xc}(n(r)) d^3r$$

$$(4.14)$$

The local density approximation (LDA) is an oversimplification valid only in the regions where electron density varies slowly and for spherical charge distribution.[9] These limitations can be overpassed by introducing non-local gradient corrections ($\nabla(n(r))$) accounting for non-spherical electron density distributions.

In the General Gradient Approximation (GGA) [10] the exchange-correlation can be calculated as follows:

$$E_{xc}^{GGA} = \int n(r)\varepsilon_{xc}(n(r), \nabla n(r)) d^3r$$

$$(4.15)$$

As a consequence the exchange correlation energies are functionals of both the density and the gradient with respect to the density. The latter can be described by different functionals, such as PW91 (Perdew–Wang exchange functional)[11], PBE (Perdew–Burke–Ernzerhof)[12], RPBE (Revised PBE functional)[13] and BP86 (Becke[14] and Perdew[15] corrections).

More recently hybrid functionals, combining an exchange component derived from Hartree–Fock theory with the exchange-correlation calculated from LDA theory, were developed. An example is the B3LYP functional, which combines the Lee, Yang and Parr functional and the three-parameter model by Becke.[16]

The application of DFT to molecular system or few atom clusters requires the use of Gaussian or Slater basis sets. This approach (called cluster approach), however, fails in describing bulk solid-state systems (metals or metal oxides) and infinite surfaces, which are then more interesting from a catalytic point of view. For these systems a supercell approach and periodic basis functions, i.e. plane waves, are more suitable. [17]

The supercell is described by three lattice vectors defining a 3-D unit cell, which can be replicated infinitely along all three vectors using periodic boundary conditions, so as to mimic the solid state. In such an approach surfaces are obtained by truncating the bulk structure along the vector perpendicular to the surface and by replacing the metal atoms with a vacuum region. The single particle wavefunctions of Eq. 4.13 are then described by plane wave basis sets that obey Bloch's theorem. The basic wavefunction, according to Bloch's theorem contains a wave-like portion and a periodic cell portion. The wavefunction is

described by the summation of plane waves expanded so as to reproduce the same periodicity of the lattice. The choice of the cutoff energy determines the expansion of the wavefunction. Increasing the cutoff energy increases the accuracy.

The numerical integration for periodic solid-state systems is performed in the reciprocal space, described by the reciprocal lattice vector G. Observables (the energy, the density) are integrated over all k-points describing the first Brillouin zone. Optimal division of special k-points, accurately describing the electronic potential, has been provided by Chadi–Cohen[18] and Monkhorst–Pack[19] approaches. The required number of k-points in the irreducible Brillouin zone is dependent on the size of the cell.

The solution for the wavefunction close to the core of the nuclei is often too complicated, due to the strong interaction with the nuclei and the presence of significant oscillations. For this reason the detailed electronic structure of the core is neglected, by replacing the strong ionic potential and valence wavefunction with a weaker pseudopotential along with pseudo wavefunctions.

For the systems with highly localized electrons (belonging to *d* or *f* orbitals), the Hubbard-like term U and a term J have to be introduced for taking into account the on-site Coulomb interactions and the screened exchange, respectively.[20] This approach, called (DFT+U), has been formulated by Dudarev et al.[20] and it introduces a semi-empirical component in DFT, since U and J are selected to fit experimental data (e.g. band gap, lattice parameters).

4.1.4 Implementation of VASP

The Vienna ab initio Simulation Package (VASP) is a code developed by Professor J. Hafner and coworkers for computing an approximate solution to the Kohn-Sham equations within density functional theory (DFT).[21] This DFT scheme relies on plane wave basis sets to represent wave-functions and on a periodic system with projector augmented wave (PAW-PP) pseudopotentials to describe the interactions of valence electrons and ionic cores. The exchange and correlation energy is evaluated by using Generalised Gradient Approximation, (GGA) functionals with both the PBE (Perdew, Burke and Ernzerhof) and RPBE (Revised Perdew, Burke and Ernzerhof).

Running VASP simulations requires the definition of four files:

1. POSCAR: provides the crystallographic information (Bravais-lattice cell shape and size), and initial atom coordinates (position).
2. POTCAR: contains the pseudopotentials for each atom used
3. KPOINTS: integration grid over k-space;
4. INCAR: indicates algorithm choices for the update and motion of nuclei (IBRION) and sets parameters (e.g. the criteria for determining electronic and ionic convergence)

Once the required convergence has been reached, calculations are stopped and output files are generated. The main output files are:

1. OSZICAR: basic output, updated continually
2. OUTCAR: complete output (all information except coordinate history)
3. XDATCAR: coordinate history
4. CONTCAR: the atom coordinate in the optimized geometry

4.2 Mechanistic insights on Au-catalysed alcohol oxidation: state of the art

Gold catalyzed alcohol oxidation mechanism differs from the one of platinum group metals (PGMs) and it is still strongly debated. As a key feature, aerobic alcohol oxidation on gold catalysts requires the use of a base, which might be involved in the deprotonation of the alcohol. In fact the more accepted reaction network of gold catalysed oxidation[22] consists of three major steps (Scheme 4.1). The first step is the adsorption and deprotonation of the alcohol. The as-generated adsorbed alkoxide then undergoes the elimination of the hydride in beta position to form carbonyl compounds. The hydride removed from the alkoxide is chemisorbed on the gold surface. This second step of the oxidation, called β-elimination, is considered the rate determining step. The last step is represented by the re-oxidation of gold nanoparticle surface by O_2 to produce H_2O or H_2O_2. Such a mechanism has been supported by a considerable number of experimental evidences. The presence of Au-H species originated from β-elimination has been detected during alcohol oxidation on Au/CeO_2 by electron paramagnetic resonance spectroscopy (EPRS) and isotope labeling by Conte et al.[23] The formation of Au-H species could occur via transfer of either a hydrogen atom or hydride; the latter seems to be more probable, according to recent studies evaluating Hammet plots for the alcohol oxidation over Au/CeO_2.[24] In addition the support plays a crucial role in stabilizing and promoting the formation of Au-adduct. Prof. Corma and coworkers demonstrated that Au NPs supported on nanocrystalline cerium oxide are active for the oxidation of alcohols even in the absence of solvent and base.[25]

Scheme 4.1 Alcohol oxidation proposed mechanism on gold-based catalysts (Adapted from Ref.[22])
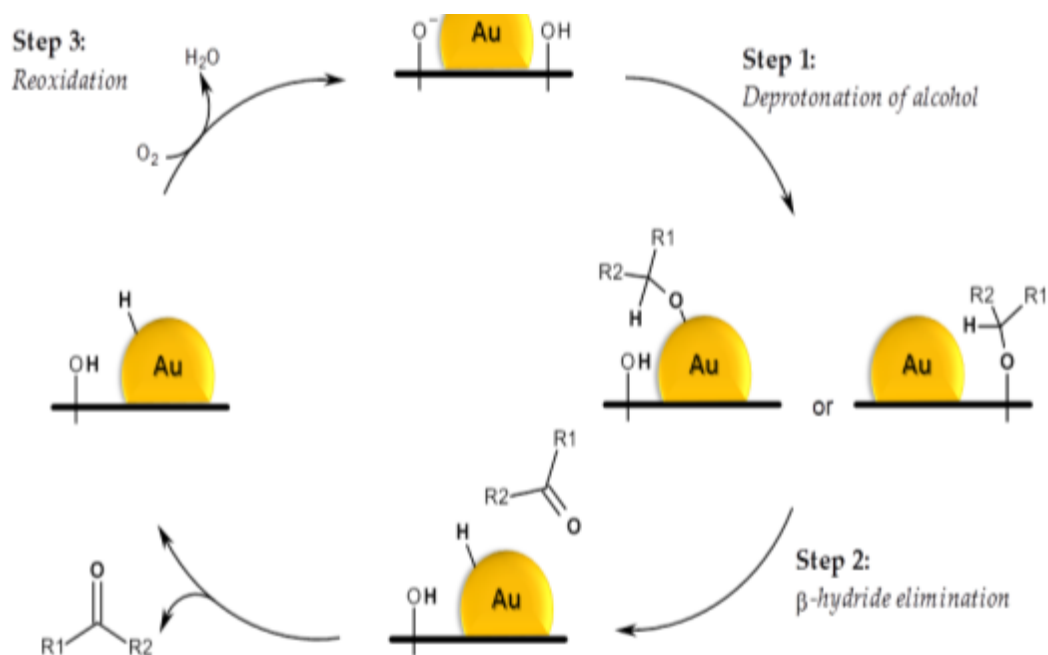
XPS analysis on Au/np-CeO_2 revealed the presence of Au^{3+} and Au^+, which can act as Lewis acid sites reacting with hydride. The intermediacy of positively charged species was confirmed by studying the influence of various electron donating/electron withdrawing substituents in the para-position on the reaction rate for benzyl alcohol oxidation.[26]
The role of oxygen is more controversial, in particular the mechanism for the dioxygen reduction on gold surface in the re-oxidation step is still elusive. Previous reports generally

showed that O_2 adsorption and dissociation is kinetically difficult on pure Au under ambient conditions,[27] which is disproved by the experimental observations endorsing the facile O_2 reduction over supported Au nanoparticles. A possible explanation for this apparent dichotomy refers to the presence of extremely low coordinated sites in nanosized gold, acting as preferential sites for the oxygen reduction. However these sites are present in low concentration after all, and therefore in this hypothesis the reoxidation (involving O_2 reduction) would be the rate-determining step. The O_2 reduction on Au therefore seems to be related to the peculiar reaction conditions of alcohol oxidation, including the presence of the interface, metal-support interactions, the cooperatiom of the base, and the possible presence of negatively charged Au particles. These aspects have been investigated by computational modelling. The role of water and hydroxyl groups in alcohol oxidation mechanism has been extensively studied by Davis et al.. by combining labelling experiments with $^{18}O_2$ and $H_2^{18}O$ with DFT calculations.[28] They demonstrated that oxygen atoms originating from hydroxide ions are incorporated into the alcohol during the oxidation reaction, instead of molecular oxygen. The presence of coadsorbed hydroxides on the Au(111) surface lowered the activation barrier for the deprotonation of ethanol to form the adsorbed ethoxide by an order of magnitude compared to a bare gold surface. Moreover co-adsorbed hydroxides can also promote the subsequent CH activation and H-elimination to produce an adsorbed aldehyde. According to the authors, the role of oxygen is to participate in the catalytic cycle not by dissociating to atomic oxygen, but by generating hydroxide ions via the interaction with water molecules or H chemisorbed on gold surface and the subsequent catalytic decomposition of peroxide intermediate. Similar conclusions were proposed by Prof. Mullins group for methanol[29], ethanol[30], 1-propanol[31] and, more recently, for allyl alcohol[32]. Pure Au surfaces with O ad-atoms and OH surface groups to facilitate H abstraction steps were investigated employing temperature-programmed desorption (TPD) technique and DFT simulations. In the case of ethanol oxidation, CO_2 was detected among reaction products at high oxygen coverages (i.e., greater than 1.0 ML). Carbon dioxide production by the γ-C-H bond and C-C bond cleavage might be attributed to the changed chemical state of atomic oxygen at different surface coverage (i.e., from chemisorbed surface oxygen at low coverage to an oxide phase at high coverage).

The influence of surface roughness on reactivity of Au by Prof. Corma Group[33], by investigating the classical three step ethanol oxidation mechanism (*i* adsorption-ethoxy formation; *ii* H$_\beta$-abstraction; *iii* reoxidation) on different gold surfaces and on Au$_{38}$ cluster (Figure 4.1, a). DFT calculations (Fig. 4.1 b) revealed a clear trend in the reactivity of the model surfaces: it increases with decreasing the Au coordination number. This means that not all active sites are equivalent and that real gold catalysts might have heterogeneous surfaces with Au atoms in different coordination state showing different reactivity towards alcohol dehydrogenation.

Finally also the molecular structure of the substrate can affect the reaction pathway. In particular a different dehydrogenation efficiency was observed for 2-cyclohexen-1-one versus cyclohexanone.[34] Indeed, 2-cyclohexen-1-one is more acidic than cyclohexanone, clearly due to the presence of allylic C – H bonds at C-4. Therefore, it is more prone to the selective attack by excess oxygen on the surface, leading to more efficient secondary transformations. In addition, the possibility to interact by van der Waals forces influences significantly the surface binding energy. [35]

Figure 4.1 Effect of surface roughness on the ethanol oxidation mechanism (From Ref.[33])
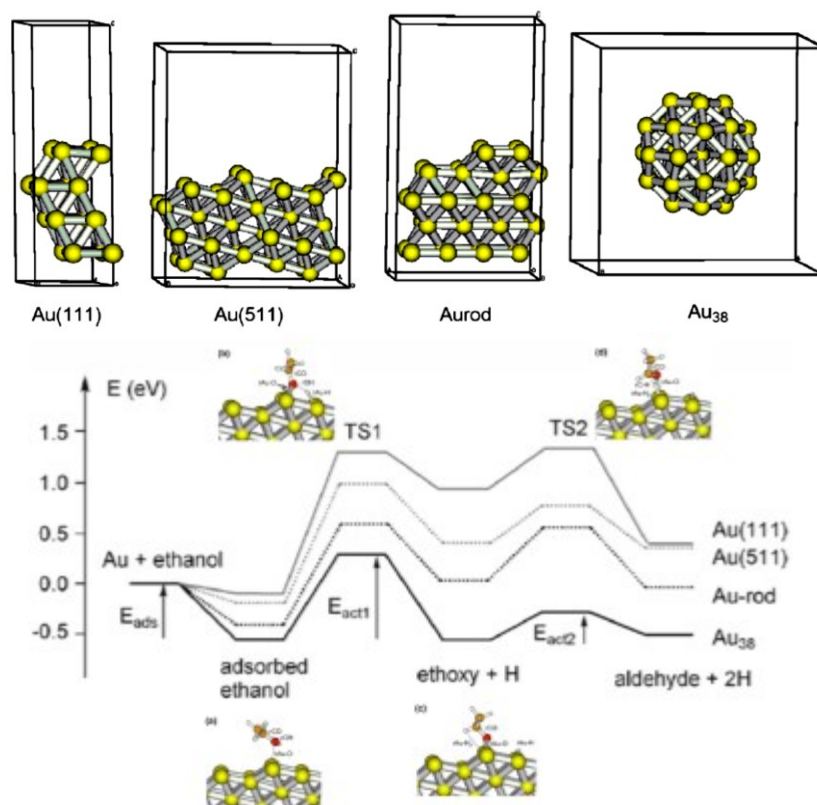
4.3 Preliminary results on DFT application to heterogeneous catalysis

As pointed in the introduction of the present chapter, herein just preliminary results on simple model systems will be presented. Au/TiO$_2$ was selected as model catalyst, since it has been already extensively explored from an experimental point of view. Few atoms gold clusters (Au$_{13}$ and Au$_{38}$) and TiO$_2$-Rutile have been chosen as representative for metal catalyst and support, respectively. Ethanol, a simple primary alcohol, was studied as substrate for alcohol oxidation.

4.3.1 Ethanol adsorption on model surfaces

The adsorption of the substrate on the catalytic surface is the first step in the catalytic cycle under kinetic regime (i.e. excluding the mass transfer phenomena, which are considered only under diffusional regime). Therefore, the adsorption of ethanol on various model surfaces has been investigated.

First of all, the geometry of ethanol as well as the geometries of isolated gold cluster and five layer TiO$_2$ slab were separately optimized. In order to study the interactions of the substrate with metal or metal oxide surface, the ethanol molecule and the slab were inserted in the same cell, locating the alcohol in the proximity of slab surface. The geometry of the as-obtained system was then optimized. After optimization, the binding energy (which can be considered as the adsorption energy) has been calculated by subtracting the energy of the fully-relaxed, isolated adsorbate and slab, from the total energy of the optimized system (adsorbate+slab).

$$E_{ads} = E_{slab+eth}^{tot} - E_{slab} - E_{eth}$$

156

For the gold nanoparticle two clusters have been considered: Au_{13} and Au_{38}. According to DFT simulations reported in the literature, in general small isolated clusters of bare gold (e.g. Au_4, Au_{12}) preferentially adopt a planar structure, whereas larger Au_n clusters (n > 13) assume 3D morphologies exposing (100)-like and (111)-like facets, thus introducing low-coordination edge and vertex. [36]

In both cases the structures were derived from the face-centered cubic (fcc) structure of bulk gold ($\alpha = \beta = \gamma = 90°$, a = b = c = 407.82 pm).

Au_{13} in its cuboctahedral symmetry is the smallest cluster with a bulk-like 12-fold coordinated central atom. Two symmetry axes, C_4 and C_3, six (100) faces, eight (111) faces and three different typologies of atoms (C = central, E = equatorial, and A = axial) are present in this structure. It should be specified that bare Au_{13} cluster is just a model and in the practice it can be obtained only as a ligand protected cluster. Actually for ligand-protected Au_{13} clusters an icosahedral structure (which possesses exclusively 20 triangular (111) faces) is preferred.

Cuboctahedral Au_{13} cluster structure, built using Accelrys Materials Studio software, has been centered within a 25 ^{x} 25 ^{x} 25 Å periodic box to ensure a vacuum gap of 15–20 Å around the cluster and then optimised using the VASP 5.2 code.[37] Exchange and correlation effects are considered within the generalized gradient approximation (GGA) using the Perdew–Burke–Ernzerhof (PBE) exchange–correlation (XC) functional, with the projector augmented-wave (PAW) method used to represent core states. A 1x1x1 k-point sampling grid is calculated using a Monkhorst-Pack scheme centred on the Γ-point. Geometry optimization has been performed setting the cut-off energy for the plane-wave basis to 500 eV, a residual force threshold of 0.015 eV Å^{-1} and using the conjugate-gradient algorithm. The convergence criterion for electronic relaxation was 10^{-4} eV.
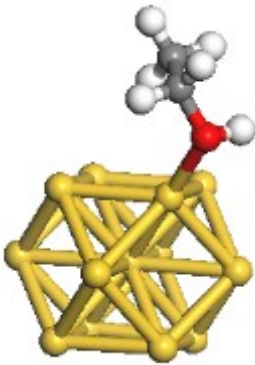
The optimized structure and corresponding atomic distances are reported in Fig.4.2. The obtained average values for nearest-neighbor distance, C-E and C-A distances (2,824Å, 2.868 Å and 2.874 Å, respectively) are longer compared to value reported in the literature (2.730, 2.725 and 2.764 Å, respectively).[38]

Figure 4.2 Cuboctahedral cluster Au_{13}: a) Symmetry axes C_4 and C_3, facets and labels of atoms (C = central, E = equatorial and A = axial); b) atom distances in optimized structure.
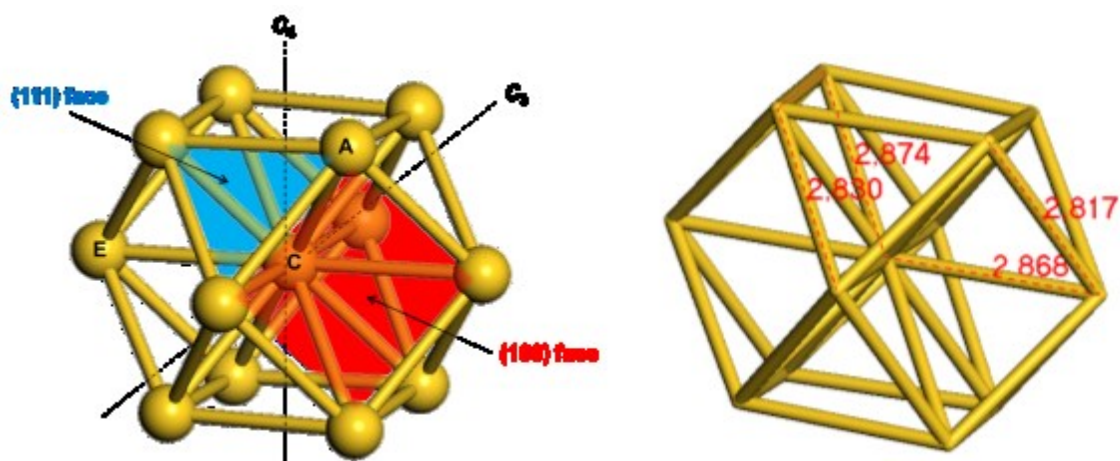
Various adsorbed configurations of Ethanol on Au13 cluster have been explored. For the bare Au_{13} cluster the most favourable adsorption geometry (the lowest adsorption energy) resulted in ethanol bound atop on axial gold atom. (Figure 4.3)

Figure 4.3 Ethanol adsorption on Au$_{13}$ cluster

E$_{ads}$ (eV)	- 0.480506
d $_{Au-O}$ (Å)	2.319
d $_{Au-Au\ 1-2}$ (Å)	2.862
d $_{Au-Au\ 1-3}$ (Å)	2.858
d $_{Au-Au\ 1-4}$ (Å)	2.851
d $_{Au-Au\ 1-5}$ (Å)	2.857
d $_{Au-Au\ 1-6}$ (Å)	2.673
d $_{C-O}$ (Å)	1,453
d $_{O-H}$ (Å)	0,975
Angle C − O − H	108.572

Au$_{38}$ has been described as an efficient catalyst for molecular oxygen dissociation by theoretical and experimental evidences. In the *fcc* symmetry Au$_{38}$ cluster is stable as truncated octahedron (with fcc symmetry). In this structure eight different adsorption sites are available. The most stable configuration (E= - 0.27 eV) was obtained with atop adsorption on gold atom labelled as 2 in Figure 4.4-a.

Figure 4.4 a) Au38 cluster in truncated octahedron symmetry; b) most stable configuration for ethanol adsorption on Au38 cluster.
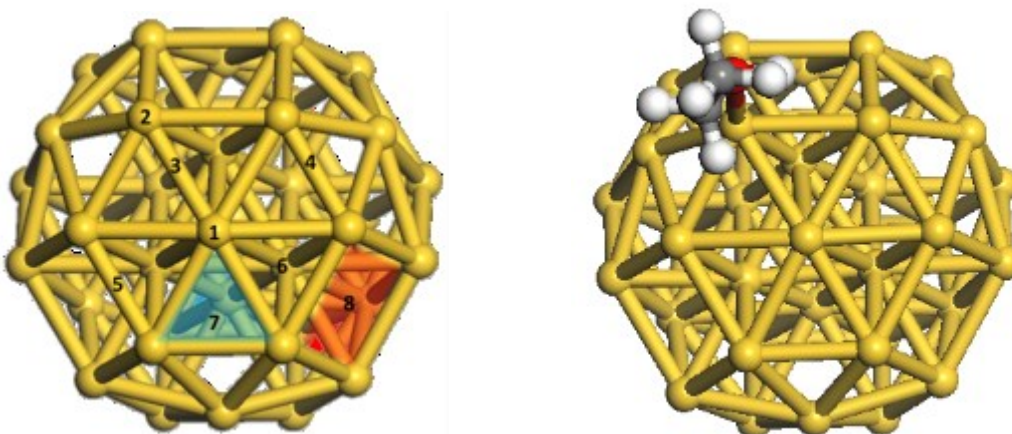
We also investigated the adsorption of ethanol on bare support, using TiO$_2$, as a reference. The rutile structure of TiO$_2$ has been selected, as it is the most stable phase. A (110) surface is generated and a five layer slab produced which is shown in figure 4.5. In this surface are 4 atoms with different coordination are present: 2 oxygen and 2 titanium. The oxygen atoms are in 2 coordinate bridging site and 3 coordinate on the surface, while the titanium atoms are 5 and 6 coordinate.

Figure 4.5 Representation of adsorption sites on TiO2-Rutile (110) surface
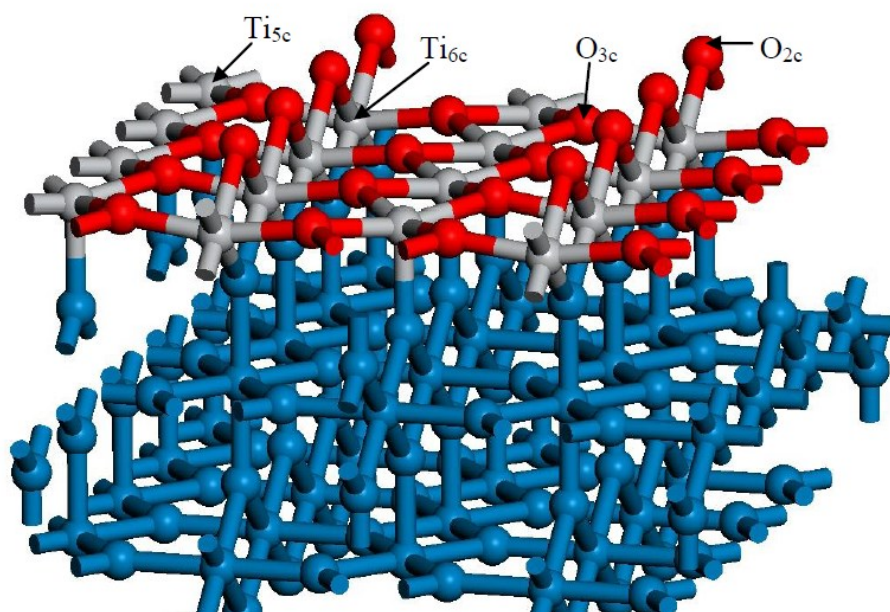
Calculations were performed in a cell (11.84 Å × 12.99 Å × 30.25 Å). Only the two top layer were allowed to relax during the optimization. The adsorption of ethanol on 3-coordinated oxygen atom of Titania surface resulted in a strong interaction (-1-19 eV), due to presence of 3-coordinated oxygen atom in the proximity of the adsorption site, which stabilize the adsorbate by H-bonding with the proton of ethanol hydroxyl group. (Figure 4.6)

Figure 4.6 Ethanol adsorption on TiO2 Rutile (110) surface

Ethanol adsorption	
E_{ads} **(eV)**	- 1.19783257
d_{Ti-O1} **(Å)**	2.139
$d_{C-O1\text{-}1}$ **(Å)**	1.463
$d_{H-O1\text{-}1}$ **(Å)**	1.017
d_{H1-Ob} **(Å)**	1.689
Angle $C_2 - O_2 - H_2$	112. 503
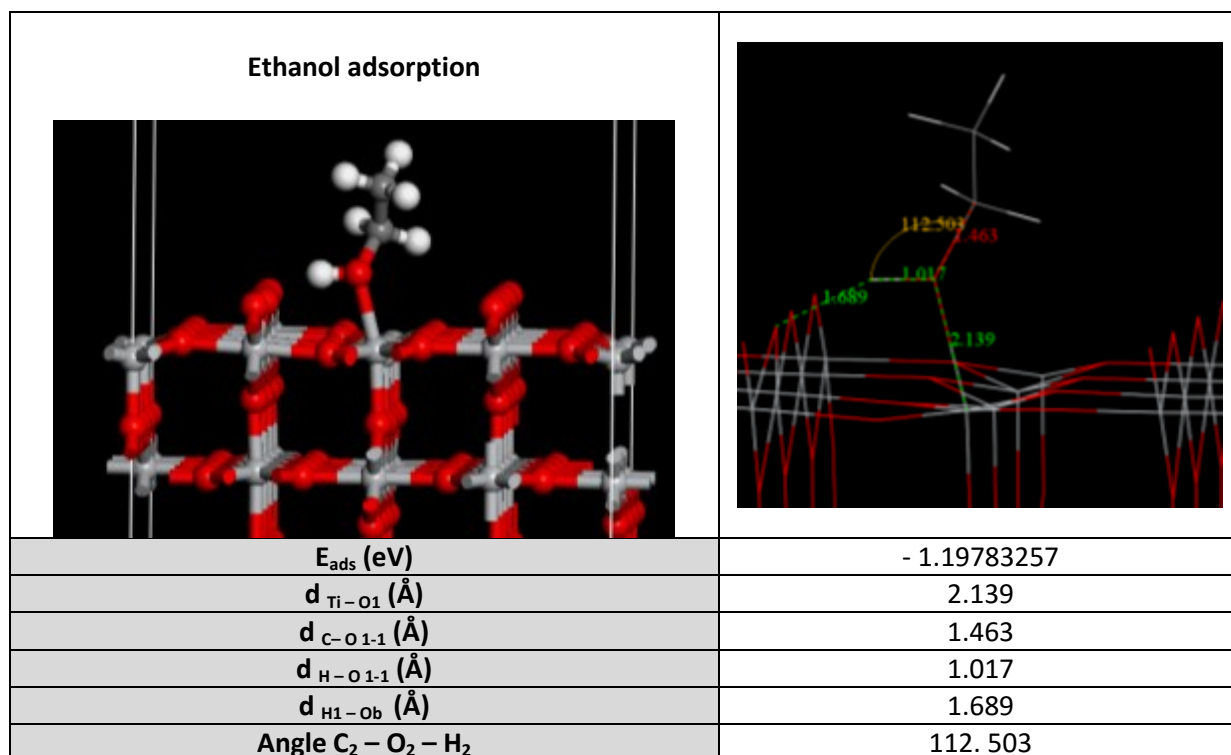
4.3.2 Ethanol oxidation on Au$_{13}$ and O-Au$_{13}$ clusters

In order to unravel the role of surface oxygen on the catalytic performances of gold-based catalysts, the oxidation of ethanol on Au-13 and on its oxygenated counterpart (O-Au13) was studied by DFT. O-Au13 cluster was obtained by adsorbing dioxygen with different orientation modes on the surface of Au$_{13}$ cluster. The most stable configuration was obtained in the case of dissociative chemisorption of molecular oxygen, resulting in two O-adatoms in 3-fold hollow sites (h-O) on adjacent (111) facets of the particle.

The classical three-step mechanism was considered, and in particular we focus only on the first two steps directly involving ethanol: i) ethanol adsorption and deprotonation and ii) β-hydride elimination (the third step is the re-oxidation, where only dioxygen and metal surface play an active role). Results obtained until now concern just the energy optimization of start points and end points and therefore they need to be soon completed, by calculating the transition state energy and consequently the kinetic barrier. In any case comparing the reaction pathway for ethanol oxidation on bare Au cluster and on the oxygenated one, it is evident that, as expected, the presence of oxygen on the metal surface positively affect the process, by promoting both proton abstraction (1st step) and β-hydride elimination. (Figure 4.7)

Figure 4.7 Ethanol oxidation on Au$_{13}$ and O-Au$_{13}$ clusters.
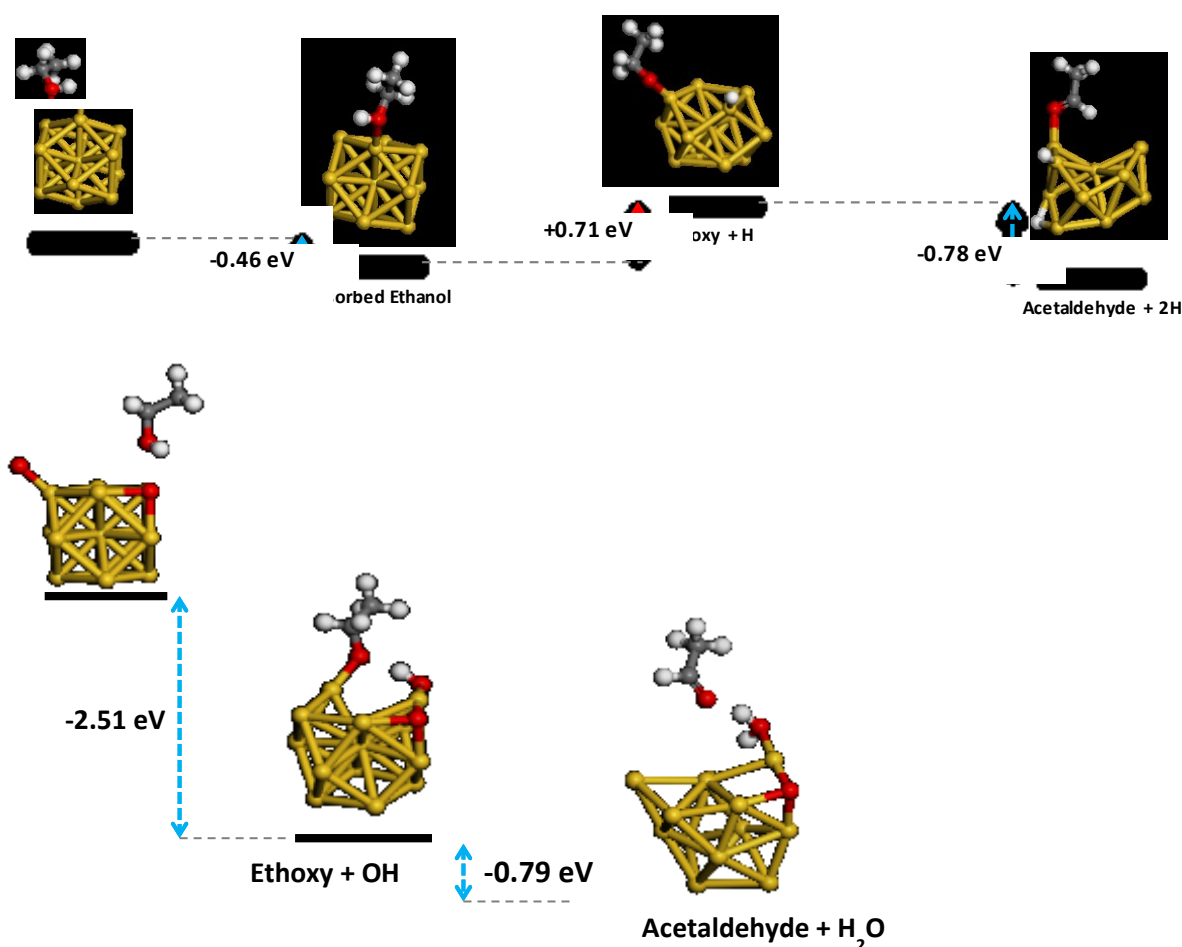
Interesting preliminary results on the role of surface oxygen encourage to extend the DFT study to more complex systems. In particular the next step will be the investigation of the presence of preferential adsorption sites created on the surface of a two layer Gold ribbon as a consequence of the strain induced by the mismatch with the support. A periodic slab model of the Au(111) surface was generated starting from the unit cell parameters. The as obtained gold ribbon has been located over the optimized structure of TiO_2 slab. Structure optimization revealed the formation of an evident surface roughness on gold ribbon . The next step will be the investigation of ethanol adsorption on the different sites created on the gold surface.

References

[1] a) F. Jensen, Introduction to Computational Chemistry, New York, Wiley (1999); b) A.R. Leach, Molecular Modeling: Principles and Applications, Pearson Education, Harlow (1996)

[2] a) M.C. Zerner, in *Reviews in Computational Chemistry,* K.B. Lipkowitz, D.B. Boyd (eds.), VCH , New York pp. 313–366 (1991); b) J.J.P. Stewart, in Reviews in *Computational Chemistry*, K.B. Lipkowitz, D.B. Boyd (eds.), VCH, New York. pp. 45–82 (1990)

[3] a) D.R. Hartree, *Proc. Cambridge Philos. Soc.* 24, 328 (1928); b) V.A. Fock, Phys. 15, 126 (1930)

[4] P. Hohenberg, W. Kohn, Phys. Rev. 136, B864 (1964)

[5] L.H. Thomas, Proc. Cambridge Philos. Soc. 23, 542 (1927)

[6] E.Z. Fermi, Z. Phys. 48, 73 (1928)

[7] P.A.M. Dirac, Proc. Cambridge Philos. Soc. 26, 376 (1930)

[8] W. Kohn, L. Sham, Phys. Rev. A, 140, 1133 (1965)

[9] T. Ziegler, Chem. Rev. 91, 651 (1991)

[10] R.G. Parr, W. Yang, Density Functional Theory of Atoms and Molecules, Oxford University Press, New York (1989)

[11] J.P. Perdew, J.A. Chevary, S.H. Vosko, K.A. Jackson, M.R. Pederson, D.J. Singh, C. Fiolhais, Phys. Rev. B46, 6671 (1992)

[12] J.P. Perdew, K. Burke, M. Ernzerhof, Phys. Rev. Lett. 77, 3865 (1996)

[13] B. Hammer, L.B. Hansen, J.K. Nørskov, Phys. Rev. B 59, 7413 (1999)

[14] A.D. Becke, Phys. Rev. B, 38, 3098 (1986)

[15] Perdew, Y. Wang, Phys. Rev., B33, 8800 (1986)

[16] A.D. Becke, Chem. Phys. 98, 5648 (1993)

[17] a) C. Stampfl, M.V. Ganduglia-Pirovano, K.R. Scheffler, M. Sc heffler, Surf. Sci. 500 (2001)

[18] D.J. Chadi, M.L. Cohen, Phys. Rev. B, 8, 5747 (1973)

[19] H.J. Monkorst, J.D. Pack, Phys. Rev. B, 13, 5188 (1976)

[20] S. L. Dudarev, G. A. Botton, S. Y. Savrasov, C. J. Humphreys, and A. P. Sutton, Physical Review B, 1998, 57, 1505–15

[21] G. Kresse and J. Hafner, Phys. Rev. B, 1994, 49, 14251–14269.

[22] T. Takei, T. Akita, I. Nakamura, T. Fujitani, M. Okumura, K. Okazaki, J. Huang, T. Ishida, M. Haruta Advances in Catalysis, 55, B.C. Gates, F.C. Jentoft ed., Elsevier, Chapter 1, 1-124 (2012)

[23] Conte, M.; Miyamura, H.; Kobayashi, S.; Chechik, V. J. Am. Chem. Soc. 2009, 131, 7189–7196.

[24] P. Fristrup, L. B. Johansen, C. H. Christensen, Chem. Commun., 2008, 2750–2752

[25] A.Abad, P. Concepcion, A. Corma, H. Garcia, *Angew. Chemie..* **44**, 4066,(2005)

[26] A.Abad, A. Corma, H. Garcia, Chem. Eur. J. 2008, 14, 212 – 222

[27] a) Liu, Z. P.; Hu, P.; Alavi, A. J. Am. Chem. Soc. 2002, 124, 14770–14779; b) Wittstock, A.; Neumann, B.; Schaefer, A.; Dumbuya, K.; Kubel. C.; Biener, M. M.; Zielasek, V.; Steinruck, H. P.; Gottfried, J. M.; Biener, J.; Hamza, A.; Baumer, M. J. Phys. Chem. C 2009, 113, 5593–5600; c) Meyer, R.; Lemire, C.; Shaikhutdinov, S. K.; Freund, H. Gold Bull. 2004, 37, 72.

[28] a) Bhushan N. Zope et al., Science **330**, 74 (2010); b) M.S. Ide and R.J. Davis, *ACCOUNTS OF CHEMICAL RESEARCH*, Vol. **47**, No. 3, 825–833 (2014)

[29] J. Gong, D. W. Flaherty, R. A. Ojifinni, J. M. White, and C. B. Mullins, J. Phys. Chem. C, 112, 5501-5509, (2008)

[30] J. Gong and C. B. Mullins, J. AM. CHEM. SOC., 130, 16458–16459 (2008)

[31] a) J. Gong, D. W. Flaherty, T. Yan, and C. B. Mullins, ChemPhysChem, 9, 2461 – 2466 (2008); b) M. Pan, J. Gong, G. Dong, and C. B. Mullins, ACCOUNTS OF CHEMICAL RESEARCH, 47, No. 3, 750–760 (2014)

[32] a) G.M. Mullen, L. Zhang, E.J. Evans , T. Yan, G. Henkelman and C.B. Mullins, JACS, 136, 6489, (2014); b) G.M. Mullen, L. Zhang, E.J. Evans , T. Yan, G. Henkelman and C.B. Mullins, PCCP, 17, 4730, (2015).

[33] A.Abad, A. Corma, and H. Garcia, *Chem. Eur. J.*, **14**, 212 – 222 (2008)

[34] M. Boronat, A. Corma, F. Illas, J. Radilla, T. Ródenas, M. J. Sabater, *Journal of Catalysis*, 278 50–58 (2011)

[35] X. Liu and C. M. Friend *, Langmuir*, **26** (21), 16552–16557, (2010)

[36] J. C. F. Rodríguez-Reyes, C. G. F. Siler, W. Liu, A. Tkatchenko, C. M. Friend, and R. J. Madix, *J. Am. Chem. Soc.*, **136**, 13333−13340 (2014)

[37] a) C. D. Zeinalipour-Yazdi, A. L. Cooksy and A. M. Efstathiou, Surf. Sci., 2008, 602, 1858; b) D. F. Mukhamedzyanova, N. K. Ratmanova, D. A. Pichugina and N. E. Kuz'menko, J. Phys. Chem. C, 2012, 116, 11507; c) A. A. Herzing, C. J. Kiely, A. F. Carley, P. Landon and G. J. Hutchings, Science, 2008, 321, 1331; d) M. S. Chen and D. W. Goodman, Science, 2004, 306, 252.

[38] a) G. Kresse and J. Furthmu¨ller, Phys. Rev. B: Condens. Matter Mater. Phys., 1996, 54, 11169; b) G. Kresse and J. Hafner, Phys. Rev. B: Condens. Matter Mater. Phys., 1993, 47, 558.

[39] A. Genest, S. Krüger, A. B. Gordienkoa, N. Rösch, Verlag der Zeitschrift für Naturforschung, Tübingen, 2004.

Part III

Experimental Section

5 *Materials and Methods*
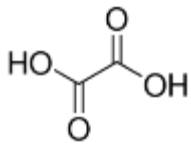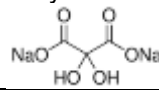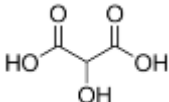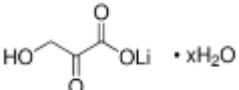
5.1 Experimental section - Chapter 2
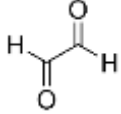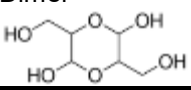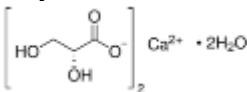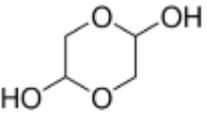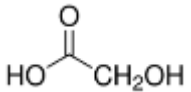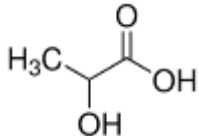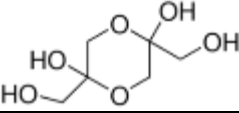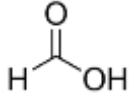
5.1.1 Materials
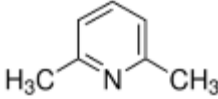
Catalyst preparation			
Material	**Origin**	**Properties**	**Safety information**
Metal precursors			
$NaAuCl_4 \cdot 2H_2O$	Sigma-Aldrich ®	Purity 99% MW 397,80 g mol^{-1}	GHS07 Warning Hazard statements H315-H319-H335 Precautionary statements P261-P305 + P351 + P338
K_2PtCl_4	Sigma-Aldrich ®	Purity 99% MW 415,09 g mol^{-1}	Danger GHS05, GHS06, GHS08 Hazard statements H301-H315-H317-H318-H334 Precautionary statements P261-P280-P301 + P310-P305 + P351 + P338-P342 + P311
Na_2PdCl_4	Sigma-Aldrich ®	Purity 99,995% MW 294,21 g mol^{-1}	-
$Bi(O)NO_3$	Sigma-Aldrich ®	Purity 99% MW 286,98 g mol^{-1}	Danger GHS03, GHS07 Hazard statements H272-H315-H319-H335 Precautionary statements P220-P261-P305 + P351 + P338
Protective agents			
Polyvinyl alcohol (PVA)	Sigma-Aldrich ®	form 87-89% hydrolized MW M_n ~13000-23000 falling ball 3.5-4.5 cP, 4 % in H_2O(20°C)(lit.)	-
Poly(ethylene glycol), reacted with Bisphenol A diglycidyl ether (PEG-BDE)	Sigma-Aldrich ®	Form flakes MW M_n ~15,000 Mp 62-64 °C(lit.)	-
Reducing agents			
Sodium borohydride ($NaBH_4$)	Sigma-Aldrich ®	Purity >96% MW 37,83 g mol^{-1} Mp >300°C anion traces chloride (Cl$^-$): ≤5000 mg/kg sulfate (SO_4^{2-}): ≤50 mg/kg cation traces Ca, Cd, Co, Cu, Fe, Ni, Pb, Zn: ≤50 mg/kg K: ≤1000 mg/kg	Danger GHS02, GHS05, GHS06 Hazard statements H260-H301 + H311-H314 Precautionary statements P223-P231 + P232-P280-P301 + P310-P370 + P378-P422
Gaseous hydrogen (H_2)	SIAD		-

Supports			
Sulfated-ZrO$_2$	Alfa-Aesar ®	SSA = 135 m^2 g^{-1} Total pore volume (N$_2$) 0.105 mL g^{-1} Xray diffraction: tetragonal ZrO$_2$, trace monoclinic ZrO$_2$. pH 3.3	GHS07 Warning Hazard statements H315-H319 Precautionary statements P280-P305+P351+P338- P362-P321-P332+P313- P337+P313
H-Mordenite	Degussa	SSA = 450 m^2/g; pH 4.2	Nd*
SiO$_2$	Alfa-Aesar ®	SSA = 242 m^2 g^{-1} Total pore volume (N$_2$) 1.23 mL g^{-1} Median pore diameter 116Å	nd
MCM-41	See 5.1.2.A	SSA = 980 m^2 g^{-1} pore volume 0.98 mL g^{-1} pore size 21-27 Å	Nd *
TiO$_2$	Aeroxide P25 – Evonik - Degussa®	SSA = 35-65 m^2 g^{-1} pH 7-8 Xray diffraction: Rutile:Anatase/ 85:15	Nd *
NiO	See 5.1.2.A	SSA = 210 m^2/g; pH 8.4	Nd *
MgO	Alfa-Aesar ®	SSA 38 m^2 g^{-1} pH	Nd *
Activated Carbon	Camel ® X40S	SSA = 900–1100 m^2 g^{-1} Pore Volume = 1.5 mL g^{-1} pH 9–10	Nd *
CNTs	Bayer ®	SSA = 288 m^2 g^{-1} average diameter:10 ± 2 nm	Nd *
CNFs	Pyrograph ® PR24-PS	SSA = 43 m^2 g^{-1} average diameter: 88 ± 30 nm	Nd *
N-CNFs	See 5.1.2.A		Nd *
Solvent			
Ultrapure Water	Milli-Q ® systems by Merck Millipore	Resistivity at 25 °C 18.2 MΩ•cm TOC ≤ 5 ppb	-
Additives			
Sulphuric acid H$_2$SO$_4$ 95%	VWR AnalaR NORMAPUR	MW 98.07 Density 1,84 kg/l	GHS05 Danger Hazard statements H314 H290 Precautionary statements P280 P301+P330+P331 P305+P351+P338 P309+P310
Commercial samples			
5% Pt/AC	Johnson Matthey 5R18	SSA = 950 m^2 g^{-1}	
1% Bi-5%Pt/AC	Johnson Matthey 5R160	SSA = 950 m^2 g^{-1}	

Catalytic tests			
Material	**Origin**	**Properties**	**Hazards**
Glycerol	Riedel-de-Häen® (Sigma-Aldrich®)	MW 92,09 g mol-1 Purity: 86-89% Density: 1.252 g/mL (25 °C)	-
Raw glycerol	Fatty acid methyl esters (FAMEs) and, therefore, the by-product, raw glycerol, were obtained by the homogeneous transesterification of rapeseed oil with methanol (MeOH:triglycerides = 6:1 mol/mol) and KOH (1% by weight) as the catalyst. This mixture was magnetically stirred for two hours at 40 °C. After the reaction, by simple decantation methyl esters are separated from the raw glycerol. The final methyl ester was obtained after removing the excess of alcohol under vacuum and a final filtration on silica powder.		
NaOH	Sigma-Aldrich ®	form beads MW 40.00 g mol-1 Purity >98%	GHS05 Danger Hazard statements H290-H314 Precautionary statements P280-P303 + P361 + P353-P304 + P340 + P310-P305 + P351 + P338
Ultrapure Water	Milli-Q ® systems by Merck Millipore	Resistivity at 25 °C 18.2 MΩ•cm TOC ≤ 5 ppb	-
Dioxygen	SIAD	99.99% pure	-
Standard for HPLC analysis			
Ortophosphoric acid H_3PO_4	Sigma-Aldrich®	Form crystalline MW 98.00 g mol^{-1} Purity >99.0%	GHS05 Danger Hazard statements H290-H314 Precautionary statements P280-P303 + P361 + P353-P304 + P340 + P310-P305 + P351 + P338
Oxalic acid	Sigma-Aldrich®	MW 90,03 Purity	Danger GHS05, GHS07 Hazard statements H302 + H312-H318 Precautionary statements P280-P305 + P351 + P338
Sodium mesoxalate monohydrate	Sigma-Aldrich®	MW 180,02 Purity > 98%	-
Tartronic acid	Sigma-Aldrich®	MW 120.06 Purity >97%	GHS07 Warning Hazard statements H315-H319-H335 Precautionary statements P261-P305 + P351 + P338
β-Hydroxypiruvic acid Lithium salt Hydrate	Sigma-Aldrich®	MW 109.99 +1mol aq. Purity ≥97.0% (calc. based on dry substance, NT)	GHS07 Warning Hazard statements H315-H319-H335 Precautionary statements P261-P305 + P351 + P338

Glyoxal solution 40 wt. % in H$_2$O	Sigma-Aldrich®	MW 58.04 Density 1.265 g/mL at 25 °C	⚠️ ☣️ Warning GHS07 GHS08 Hazard statements H315-H317-H319-H332-H341 Precautionary statements P280-P305 + P351 + P338
DL-Glyceraldehyde Dimer	Sigma-Aldrich®	MW 180.16 Purity >97%	-
D-Glyceric acid calcium salt dihydrate	Sigma-Aldrich®	MW 286.25 Purity 99%	-
Glycoladehyde dimer	Sigma-Aldrich®	MW 120.10 crystalline, mixture of stereoisomers. Melts between 80 and 90 °C depending on stereoisomeric composition	-
Glycolic acid	Sigma-Aldrich®	MW 76.05 Purity > 97%	☣️ ⚠️ Danger GHS05 GHS07 Hazard statements H314-H332 Precautionary statements P261-P280-P303 + P361 + P353-P304 + P340 + P310-P305 + P351 + P338
Lactic acid	Sigma-Aldrich®	MW 90.08	☣️ GHS05 Danger Hazard statements H315-H31 Precautionary statements P280-P305 + P351 + P338
1,3-Dihydroxyacetone dimer	Sigma-Aldrich®	MW 180.16 Purity 97%	⚠️ GHS07 Warning Hazard statements H315-H319-H335 Precautionary statements P261-P305 + P351 + P338
Formic acid	Sigma-Aldrich®	MW 46.03 Purity > 95%	🔥 ☣️ ☠️ Danger GHS02, GHS05, GHS06 Corrosive to the respiratory tract. Hazard statements H226-H302-H314-H331 Precautionary statements P210-P280-P303 + P361 + P353-P304 + P340 + P310-P305 + P351 + P338-P403 + P233

Catalyst characterization			
Material	**Origin**	**Properties**	**Hazards**
Infrared Spectroscopy and microcalorimetry			
2,6 – Dimethylpyridine H₃C – N – CH₃ (structure)	Sigma-Aldrich®	MW 107.15 Purity ≥99%	Warning GHS02, GHS07 Hazard statements H226-H302-H315-H319-H335 Precautionary statements P261-P305 + P351 + P338
Potassium Bromide KBr	Sigma-Aldrich®	MW 119.0 Purity FT-IR grade, ≥99%	GHS07 Warning Hazard statements H319 Precautionary statements P280-P305 + P351 + P338-P337 + P313

5.1.2 Methods and instruments

5.1.2.A Support preparation

Almost all materials used as supports are commercial sample, except MCM-41, NiO and N-CNFs, which have been prepared according to the procedures reported below.

<u>MCM-41</u>

The MCM-41 mesoporous framework was prepared by a sol–gel method at room temperature, by adopting the procedure described in ref. [1]. Typically, $C_{16}TABr$ (5.05 g, 0.014 mol, 98% from Sigma-Aldrich®) was dissolved in 100 ml of deionized water with constant stirring (400 r.p.m.).
Subsequently, aqueous ammonia solution (0.5 mol, 37 ml ammonia solution, NH_4OH, 25% NH_3, 99.99%, Merck) was added dropwise to the previous solution followed by the addition of 152 ml of ethyl absolute alcohol (C_2H_5OH, analytical grade product supplied by Alfa Aesar) as a co-solvent and finally by the addition of 10 ml of TEOS ($Si(OC_2H_5)_4$, 98% from Sigma-Aldrich®) as a silica source. The solution became turbid in one minute and then a bright white colloidal gel was formed. The solution was kept under constant stirring for 2 h and then aged at room temperature for 24 h. The resulting gel was filtered, washed with deionized water and dried at 363 K for 24 h.
The template was removed by heating the dried gel to 823 K (1 K min^{-1}) in a tube furnace for 8 h in pure N_2 flow. For complete removal of the template, the material was cooled to room temperature then flushed with pure O_2 and heated to 823 K (10 K min^{-1}) for 12 h.

<u>Nickel oxide (NiO)</u> [2]

$Ni(NO_3)_2 \cdot 6H_2O$ (0,030 g, from Sigma-Aldrich®, MW 290.79, Purity 99.999%) and urea (0,060 g., urea/Ni 10:1 mol/mol, from Sigma-Aldrich®, MW 60.06, Assay 98%) were added to 200 ml of MilliQ water under magnetic stirring($[Ni^{2+}]$ = 5*10^{-4}M). The solution was kept under stirring for 6h at 353 K (80°C). The $Ni(OH)_2$ was separated from the solution by filtration and washed several times. The powder was dried at 333 K (60°C) for 12h and then calcined at 300°C for 3h.

<u>N-containing CNFs</u> [3]

First, the supplied CNFs were treated with HNO_3 (Sigma-Aldrich) in order to create oxygenated functional groups that serve as reactive sites for nitrogen insertion. For this purpose, a suspension of CNFs in HNO_3 concentrate (20 g of CNF/L of HNO_3) was kept at 393 K for 2 h under continuous stirring, then rinsed with distilled water, and finally dried at 383 K for several hours. Through oxidation treatments, the removal of the accessible metal impurities occurs. Aminated samples were then obtained through thermal treatment of the pre-oxidized CNFs (10 g for each batch) with NH_3 in the temperature range 473-873 K for 4 h. Furthermore, amination at 473 K has been performed on oxidized CNF pretreated by annealing in He up to 973 K for 2 h to gain detailed information about the role of the oxygen functionalities on the surface of CNFs.

5.1.2.B Catalyst preparation

All the amount expressed in grams have been determined using an analytical balance Gibertini E42(weighing capacity: 100 g; detection limit : 0,0001 g).

<u>Bimetallic Au@Pt</u> (Figure 5.1)

$NaAuCl_4 \cdot 2H_2O$ (Au: 0.031 mmol) was dissolved in 60 mL of H_2O, and PVA (1%, wt%) was added (Au/PVA = 1:0.5 wt/wt). The yellow solution was stirred for 3 min, after which 0.1 M $NaBH_4$ (Au/$NaBH_4$ = 1:4 mol mol^{-1}) was added under vigorous magnetic stirring. The ruby red Au(0) sol was formed immediately. Within a few minutes of sol generation, the gold sol was immobilized by adding the support (acidified to pH 2 by sulphuric acid) under vigorous stirring. The amount of the support was calculated as having a gold loading of 0.60 wt%. After 2 h, the slurry was filtered and the catalyst washed thoroughly with distilled water (neutral mother liquors). The Au/support was dispersed in 40 mL of water, with K_2PtCl_4 (Pt: 0.021 mmol) and PVA solution (Pt/PVA = 1 : 0.5 wt/wt) added. H_2 was bubbled (50 mL min−1) under atmospheric pressure and room temperature for 2 h. After an additional 18 h, the slurry was filtered and the catalyst washed thoroughly with distilled water. ICP analyses were performed on the filtrate using a Jobin Yvon JV24 instrument to verify the metal loading on the support. The total metal loading was 1 wt%.

Figure 5.1 Sol immobilization two-step procedure
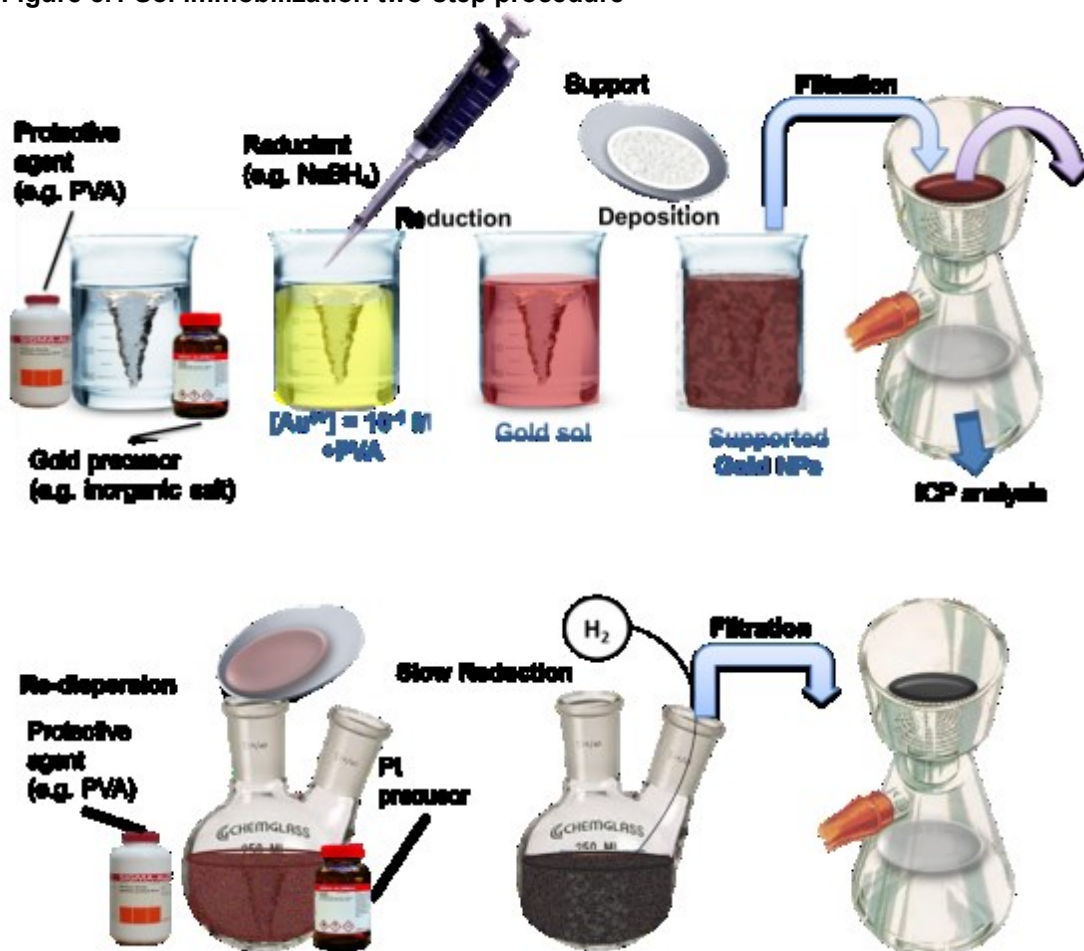
<u>Bimetallic Au@Pd</u>

NaAuCl$_4$ 2H$_2$O (0.072 mmol) was dissolved in 140 mL of H$_2$O, and PVA (2% w/w) was added (0.706 mL). The yellow solution was stirred for 3 minutes, and 0.1 M NaBH$_4$ (2.15 mL) was added under vigorous magnetic stirring. The ruby red Au(0) sol was immediately formed. A UV-visible spectrum of the gold sol was recorded to check the complete AuCl^{4-} reduction and the formation of the plasmon peak. Within a few minutes of sol generation, the gold sol (acidified until pH 2 by sulfuric acid) was immobilized by adding the support under vigorous stirring. The amount of support was calculated as having a final metal loading of 0.73 wt%. After 2 h, the slurry was filtered and the catalyst washed thoroughly with distilled water (neutral mother liquors). A check of Au loading was performed directly on the catalysts, confirming the quantitative adsorption of Au NPs of the sol. The Au/support was then dispersed in 140 mL of water; Na$_2$PdCl$_4$ (10 wt% in Pd solution) (0.0386 mL) and PVA (2% w/w) (0.225 mL) were added. H2 was bubbled (50 mL/min) under atmospheric pressure and room temperature for 2 h. The slurry was filtered and the catalyst washed thoroughly with distilled water. The total metal loading of 1 wt% and the Au-Pd molar ratio 6:4 was confirmed by ICP analyses for all of the catalysts. The catalysts were labeled as 1% Au$_6$Pd$_4$/AC, 1% Au$_6$Pd$_4$/N-CNFs, 1% Au$_6$Pd$_4$/CNTs, 1% Au$_6$Pd$_4$/CNFs and 1% Au$_6$Pd$_4$/TiO$_2$.

<u>Trimetallic Bi-Au-M/AC (M = Pt or Pd)</u> [4]

Bismuth was added to acidic H$_2$O (pH 1, H$_2$SO$_4$), a 10^{-2}M stock solution of BiO(NO$_3$) and a 2 wt% stock solution of PEG-BDE (polyethyleneglycol reacted with bisphenol diglycidyl ether) were added, under nitrogen and vigorous magnetic stirring. After 3 min, an alkaline NaBH$_4$solution (0.1 M, Bi/NaBH$_4$= 1, mol/mol) was added obtaining a brown sol. An UV–vis spectrum of the Bi sol was recorded, checking for complete reduction. After 1 min, 1 g of AuPt/AC (or AuPd/AC) was added as having the proper Bi loading (0.1 and 1 wt% for AuPt/AC and 0.1%for AuPd/AC) and the slurry was maintained under vigorous stirring for 0.5 h. The catalyst was then filtered, and washed thoroughly with distilled water (neutral mother liquors). The catalysts have been labeled as 0.1%Bi-AuPt/AC, 1%Bi-AuPt/AC and 0.1%Bi-AuPd/AC omitting that always the loading of AuM is 1 wt% and the atomic ratio Au/M is 6/4.

5.1.2.C Catalytic tests

<u>Preliminary glycerol purification</u> (valid only in the case of raw glycerol obtained by rapeseed oil)

To obtain a purified glycerol, the resulted glycerol solution was diluted in a ratio of 1/10 in order to reduce the fluid viscosity and used as obtained or further purified. In the latter case, H2SO4 was added in order to adjust the pH to 2 and to convert the soap into free fatty acid. The free fatty acid was removed by extraction with hexane. The obtained methanol-glycerol mixture was evaporated in a rotavapor in order to remove the methanol. The glycerol solution was then separated and treated with activated carbon in order to remove the free ions. The activated carbon was separated by filtration. Finally, the glycerol solution was diluted with water in order to obtain the desired concentration (0.3 M).

The presence of possible impurities was verified using high-performance liquid chromatography (HPLC) using a column (Alltech OA-10308, 300 mm ø 7.8 mm) with UV and refractive index (RI) detection or GC using an HP 7820A gas chromatograph equipped with a

capillary column (HP-5 30 m × 0.32 mm, 0.25 µm film, by Agilent Technologies)) and a TCD detector. GC-MS was used for the identification of the products.

<u>Catalytic tests</u>

Reactions were carried out in a glass reactor (30 mL) provided with an electronically controlled magnetic stirrer connected to a large reservoir (5000 mL) containing dioxygen at 3 atm. The dioxygen uptake was followed by the use of a mass flow controller (Readout&Control Electronics 0154 mass flow controller) connected to a PC through an A/D board, plotting a flow time diagram. 0.3 g. of glycerol were dissolved in 10 mL of water and mixed with the catalyst powder (final concentration of glycerol: 0.3 M, glycerol/metal = 500 mol mol^{-1} or 1000 mol mol^{-1}). Where indicated, 4 equivalents of NaOH were added.

The reactor was pressurized at 300 kPa of O_2 and thermostated at the appropriate temperature, by dunking in an oil-bath heated by Heidolph MR 3002 hot plate (maximum stirring rate: 1200 rpm; thermal power: 600W; maximum temperature: 300°C; dimension: 240 x 155 x 120 mm) with thermal control (Heidolph EKT 3001 thermocouple, -50°C ÷ 300°C). Once the required temperature (40, 50, 60, and 80 °C) was reached, the gas supply was switched to oxygen and the monitoring of the reaction started. The reaction was initiated by stirring.

<u>Recycling test</u>

Each run was carried out under the same conditions (0.3 M glycerol, glycerol/metal = 500 mol mol^{-1}, 300 kPa (3 atm) O_2, T = 313K/40°C - 353 K/80 °C, reaction time = 6-16 h). The catalyst was separated by centrifugation and recycled in the subsequent run after filtration without any further treatment.

<u>Product analysis</u>

The trend of the reaction and the distribution of product have been controlled by High Pressure Liquid Chromatography (HPLC) analyses.

Samples were removed periodically (after 15', 30', 60', 120', 180', 240',…from the start of reaction) and analyzed by high-performance chromatography (HPLC) Agilent 1220 LC system using a column (Alltech OA-10308, 300 mm × 7.8 mm, thermostated at 50°C) with an integrated UV detector (λ = 210 nm) and an online refractive index (RI) detector (Agilent 1260 infinity) in order to analyze the mixture of the samples. 1% H_3PO_4 solution was used as the eluent.

200 µl of solution (homogeneous sample) have been taken with a micropipette and diluted to 5ml with the eluent. The as-obtained solution has been filtered or centrifuged to remove traces of catalyst. The optimal concentration of the injected sample has been selected to be higher than the quantification limit (the lowest concentration that can be accurately determined), and lower than the linearity upper limit (where the linearity range is the range of concentrations over which the sensitivity of the detector is constant within a specified variation, usually ±5 percent). 40 µL solution has been injected in column and analysed at a flow of 0,400 ml/min.

The identification of the possible products was performed on the basis of retention times by comparison with the original samples. The quantification has been performed by peaks integration through Chem.Station for LC Systems software (Rev. B.04.03), using calibration curve method. The calibration curve is the plot of the recorded signal versus concentration.

For each product the corresponding three-point calibration curve has been constructed by injecting three aliquot of the standard solution at different and known analyte concentrations and measuring the peak area obtained.

The concentration range should always cover the concentration of the samples that must be analysed. Reporting in a graph area values as a function of the concentration a set of experimental points have been obtained. A line of best fit (regression line) is used to join the points of the curve obtained.

$$A = R_f\, C + i \tag{5.1}$$

The regression coefficient R^2, calculated using the residuals (error) of each data point, is a statistical measure for 'goodness of fit to a straight line. The intercept of the regression equation indicates systematic error. The slope (R_f) of the line represents the response factor that is the factor that relate the concentration and the area of peaks for the used detector (in our case, if it was possible, the response factors for both UV detector and refraction index has been considered).

From the concentration data it was possible to estimate glycerol conversion and product selectivity at different time. Conversion and selectivity were calculated on a carbon atom basis, *i.e.* considering the number of carbon atoms contained in the molecule.

In particular conversion of glycerol is calculated as ratio between converted mols, that is the differences between the initial moles and the residual moles of the substrate, and the initial concentration:

$$conv = \frac{converted\ mols}{initial\ mol} \times 100$$

The selectivity toward each product is express as the ratio between the mols of that product and the converted mols:

$$sel = \frac{product\ mols}{converted\ mols} \times 100$$

Another important parameter for kinetic studies is the activity, defined as :

$$\text{Activity} = \frac{conversion * initial\ substrate\ mols}{metal\ mols * time\ (h)}$$

The presence of glyceraldehyde was confirmed by NMR. ^{13}C NMR spectra were recorded on a Bruker AC 300 NMR spectroscope. The water signal was suppressed using a low power PRESAT pulse in order to minimize signal distortions. 200 µL of 0.3 M glyceraldehyde solution in H_2O were added to each sample (final volume 600 µL). The products were recognised by comparison with authentic samples.

5.1.2.D Characterization

ICP analysis

The actual metal content was checked by ICP analysis of the filtrate or alternatively directly on catalyst after burning off the carbon, on a Jobin Yvon JY24 (Figure 19). Metal leaching was checked by ICP on the reaction solution after the hot filtration of the catalyst.

FT-IR Spectroscopy for acidity measurements

FTIR spectra were taken on a Perkin-Elmer 2000 spectrometer (equipped with a MCT detector) with the samples in self-supporting pellets introduced in the cells allowing thermal treatments in controlled atmospheres and spectrum scanning at room temperature (r.t.) in vacuum or in the presence of probe gases. From each spectrum, the spectrum of the sample before the inlet of the probe was subtracted. The standard IR experiment of 2,6-DMP adsorption/desorption on the various samples, previously activated in vacuum at 393 K, was carried out as follows: (i) admission in the IR cell of an excess dose of 2,6-DMP vapor (~2 Torr) and equilibration at room temperature for 10 min; and (ii) evacuation of the IR cell at r.t. for 15 min.

FT-IR Spectroscopy on used catalysts

Fourier transform infrared (FT-IR) spectra were recorded with a JASCO FT/IR 410 spectrometer using a mercury cadmium telluride (MCT) detector. Spectra with 4 cm^{-1} resolution, 64 scans and a scan speed of 0.20 cm s^{-1} were recorded at room temperature using KRS5 thallium bromo-iodide windows in the range 4000–1000 cm^{-1}. The 1% Au_6Pd_4/TiO_2 used, which was filtered and dried after the reaction, was mixed with KBr to obtain a pellet (pressed at 10 MPa for 10 minutes).

Microcalorimetric analysis

Microcalorimetric measurements were run on Tian–Calvet heat flow calorimetric equipment (Setaram C80d). Each sample was pretreated in vacuum (10–5 Torr) at 393 K (for IR experiments) and then contacted with successive small doses of NH_3 vapour at 373 K. The first adsorption runs (primary isotherms) were stopped at a final equilibrium pressure of 35 Torr. The primary adsorption isotherms were followed by prolonged outgassing at the adsorption temperature and then by a second adsorption run up to the same final NH_3 pressure (secondary isotherms).Uptake differences between the primary and secondary isotherms are usually considered to monitor the occurrence and the extent of irreversible adsorption processes.

Transmission electron microscopy (TEM) and Energy Dispersive X-ray Spectroscopy (EDS)

Morphology and microstructures of the catalysts were characterized by transmission electron microscopy (TEM). Samples were prepared for TEM characterisation by dispersing the catalyst powder in high purity ethanol followed by sonication. A drop of this suspension was then evaporated on a holey carbon film supported by a 300 mesh copper TEM grid.

The samples were then subjected to bright field diffraction contrast imaging experiments in order to image the particles

A Philips CM200 FEG electron microscope, operating at 200 kV and equipped with EDX DX4 analyzer system and a FEI Titan 80-300 electron microscope (Figure), operating at 300 kV and equipped with EDX SUTW detector were used for TEM observation.

Alternatively a Jeol 2100 LaB$_6$ TEM operating at 200 kV was used. High resolution transmission microscopy (HRTEM) analysis was performed using a side entry Jeol JEM 3010 (300 kV) microscope equipped with a LaB$_6$ filament and fitted with a Link ISIS 200 detector for X-ray EDS analysis. All digital micrographs were acquired by an UltraScan 1000 camera and the images were processed by Gatan DigitalMicrograph. X-Ray powder diffraction data were obtained by using a Rigaku DMax diffractometer with Cu KR radiation operating at 40 keV and 40 mA, with a 0.05° divergence slit; the spectra were recorded in the range 1–8°.
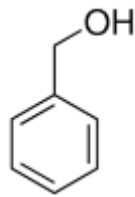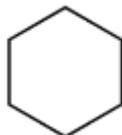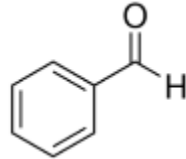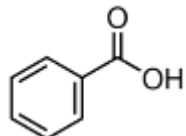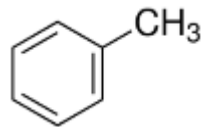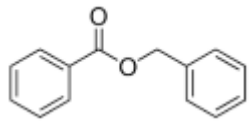
X-ray photoelectron spectroscopy (XPS)
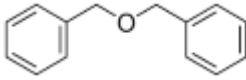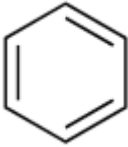
XPS measurements were performed in an M-Probe Instrument(SSI) equipped with a monochromatic Al K source (1486.6 eV) with a spot size of 200 mm 750 mm and a pass energy of 25 eV, providing a resolution for 0.74 eV. The accuracy of the reported binding energies (BE) can be estimated to be ±0.2 eV. The quantitative data were checked accurately and reproduced several times (at least 10 times for each sample). A curve fitting procedure of the experimental spectra was done.

5.2 Experimental section - Chapter 3

5.2.1 Materials

Catalyst preparation			
Material	**Origin**	**Properties**	**Safety information**
Metal precursors			
$NaAuCl_4 \cdot 2H_2O$	Sigma-Aldrich ®	Purity 99% MW 397,80 g mol^{-1}	GHS07 Warning Hazard statements H315-H319-H335 Precautionary statements P261-P305 + P351 + P338
Na_2PdCl_4	Sigma-Aldrich ®	Purity 99,995% MW 294,21 g mol^{-1}	
Protective agents			
Polyv11inyl alcohol (PVA)	Sigma-Aldrich ®	form 87-89% hydrolized MW M_n ~13000-23000 falling ball 3.5-4.5 cP, 4 % in H_2O(20°C)(lit.)	
Reducing agents			
Sodium borohydride $(NaBH_4)$	Sigma-Aldrich ®	Purity >96% MW 37,83 g mol^{-1} Mp >300°C anion traces chloride (Cl^-): ≤5000 mg/kg sulfate (SO_4^{2-}): ≤50 mg/kg cation traces Ca, Cd, Co, Cu, Fe, Ni, Pb, Zn: ≤50 mg/kg K: ≤1000 mg/kg	Danger GHS02, GHS05, GHS06 Hazard statements H260-H301 + H311-H314 Precautionary statements P223-P231 + P232-P280-P301 + P310-P370 + P378-P422
Gaseous hydrogen (H_2)	SIAD		
Supports			
TiO_2	Aeroxide P25 – Evonik - Degussa®	SSA = 35-65 m^2 g^{-1} pH 7-8 Xray diffraction: Rutile:Anatase/ 85:15	Nd *
γ-Al_2O_3	Sasol ® (Condea CHEMIE) ®	SSA = 110-220 m^2/g; pore volume 0.3-0.6 cm^3/g; the average radius 4-8 nm	Nd*
Solvent			
Ultrapure Water	Milli-Q ® systems by Merck Millipore	Resistivity at 25 °C 18.2 MΩ•cm TOC ≤ 5 ppb	
Additives			
Sulphuric acid H_2SO_4 95%	VWR AnalaR NORMAPUR	MW 98.07 Density 1,84 kg/l	GHS05 Danger Hazard statements H314 H290 Precautionary statements P280 P301+P330+P331 P305+P351+P338 P309+P310
Commercial samples			
5% Pd/Al_2O_3	Johnson Matthey 5R18	SSA = 150 m^2 g^{-1}	

Catalytic tests			
Material	**Origin**	**Properties**	**Hazards**
Benzyl alcohol — OH	Sigma-Aldrich®	MW 108.14 g mol-1 Purity: 99-100% Density: 1.045 g/mL (25 °C)	GHS07 Warning Hazard statements H302 + H332-H319 Precautionary statements P261-P301 + P312 + P330-P304 + P340 + P312-P305 + P351 + P338
Cyclohexane	Sigma-Aldrich ®	MW 84.16 g mol-1 Purity >99.5%	GHS02, GHS07, GHS08, GHS09 Danger Hazard statements H225-H304-H315-H336-H410 Precautionary statements P210-P261-P273-P301 + P310-P331-P501
Dioxygen	SIAD	99.99% pure	
Standard for HPLC analysis			
Benzaldehyde	Sigma-Aldrich®	MW 106.12 g mol-1 Purity >99.0%	GHS07 Warning Hazard statements H302
Benzoic acid	Sigma-Aldrich®	MW 122.12 g mol-1 Purity >99.5%	Danger GHS05, GHS07 Hazard statements H318-H335 Precautionary statements P261-P280-P305 + P351 + P338
Toluene	Sigma-Aldrich®	MW 92.14 g mol-1 Purity >99.7%	Danger GHS02, GHS07, GHS08 Hazard statements H225-H304-H315-H336-H361d-H373 Precautionary statements P210-P261-P281-P301 + P310-P331
Benzylbenzoate	Sigma-Aldrich®	MW 212.24 g mol-1 Purity >99.0%	Warning GHS07, GHS09 Hazard statements H302-H411 Precautionary statements P273

Benzylether	Sigma-Aldrich®	MW 198.26 g mol-1 Purity 98.0%	Warning GHS07, GHS09 Hazard statements H335-H410 Precautionary statements P273-P304 + P340 + P312-P391-P501
Benzene	Sigma-Aldrich®	MW 78.11 g mol-1 Purity >99.99%	Danger GHS02, GHS07, GHS08 Hazard statements H225-H304-H315-H319-H340-H350-H372-H412 Precautionary statements P201-P210-P273-P301 + P310-P308 + P313-P331
1.Octanol (internal standard) $CH_3(CH_2)_6CH_2OH$	Sigma-Aldrich®	MW 130.23 g mol-1 Purity 99.0%	GHS07 Warning Hazard statements H319-H412 Precautionary statements P273-P280-P305 + P351 + P338-P337 + P313

Catalyst characterization			
Material	**Origin**	**Properties**	**Hazards**
Diffuse Reflectance Infrared Fourier Transform Spectroscopy (DRIFTS)			
CO	PANGAS	5 vol.% CO/Ar	Danger GHS02, GHS06, GHS08 Hazard statements H220-H280-H331-H360D-H372 Precautionary statements P201-P210-P261-P311-P410 + P403
He	PANGAS	Ultrapure	
Attenuated Total Reflection Infrared Fourier Transform Spectroscopy (ATR-FTIRS)			
ZnSe	Crystran Ltd.	Trapezoidal crystal	Danger GHS06, GHS08, GHS09 Hazard statements H301 + H331-H373-H410 Precautionary statements P261-P273-P301 + P310-P311-P501
Ar	PANGAS	Ultrapure	

5.2.2 Methods and instruments

5.2.2.A Catalyst preparation

Au catalyst preparation

Solid $NaAuCl_4 \cdot 2H_2O$ (0.043 mmol) and PVA solution (1% w/w; Au/PVA 1:0,5, w/w) were added to H_2O (100 mL). After 3 min, $NaBH_4$ (Au/$NaBH_4$ 1:4 mol/mol) solution was added to the solution with vigorous magnetic stirring. A ruby-red Au^0 sol was formed immediately. The UV/Vis spectrum of the Au sol was recorded to check the complete reduction of $AuCl_4^-$ and the formation of the plasmon peak of Au^0 nanoparticles. Within a few minutes from its generation, the colloid (acidified at pH 2 by sulfuric acid) was immobilized by adding the support (TiO_2, Degussa P25) under vigorous stirring. The amount of support was calculated to obtain a final metal loading of 1 wt%. The catalysts were filtered, washed several times, dried at 80°C for 4 h.

Pd catalyst preparation

Solid Na_2PdCl_4 (Pd 0.043 mol for 1wt% loading and 0.215 mol for 5 wt. % loading) and 1% w/w PVA solution (Pd/PVA 1:0.5 w/w) were added to H_2O (100 mL). After 3 min, $NaBH_4$ (Pd/$NaBH_4$=1:8 mol/mol) solution was added to the yellow-brown solution with vigorous magnetic stirring. The brown Pd^0 sol was formed immediately. A UV/Vis spectrum of the Pd sol was recorded to check the complete reduction of $PdCl_4^{2-}$. Within few minutes from its generation, the colloid (acidified at pH 2 by sulfuric acid) was immobilized by adding the support (TiO_2 or Al_2O_3) under vigorous stirring. The amount of support was calculated to obtain the desired final metal loading (1 wt% or 5wt.%). The catalysts were filtered, washed several times, and dried at 80°C for 4 h.

Bimetallic AuPd catalysts

Bimetallic catalysts have been prepared following a procedure reported previously. After the preparation of 0.73 wt% Au/TiO_2 according to the procedure reported above, the material was dispersed in water (100 mL), and Na_2PdCl_4 (Pd 0.025 mol) and PVA solutions (1% w/w, Pd/PVA 1:0.5 w/w) were added. H_2 was bubbled (50 mL min^{-1}) under atmospheric pressure at RT. After 2 h, the slurry was filtered, and the catalyst was washed thoroughly with distilled water. ICP analysis was performed on the filtrate to verify the quantitative metal loading on the support. The final total metal loading was 1 wt% in all cases. For the bimetallic catalyst, the Au/Pd ratio was 7.3:2.7 wt% (6:4 mol/mol).

5.2.2.B Catalytic tests

The reactions were performed in a thermostated glass reactor (30 mL) provided with an electronically controlled magnetic stirrer connected to a large reservoir (5000 mL) that contained oxygen at 2 bar (SIAD, 99.99 %). The oxygen uptake was followed by a mass flow controller connected to a PC through an A/D board, which plotted a flow–time diagram. The oxidation experiments were performed in the presence of cyclohexane as the solvent and 0.3 M benzyl alcohol; substrate/metal=500 mol/mol for TiO_2 supported catalysts and 5000 for Al_2O_3-supported catalysts, 60°C, pO_2= 200 kPa/2 bar).

Product analysis

The periodic removal of samples from the reactor was performed. Mass recoveries were always 98±3% with this procedure. For the identification and analysis of the products, a GC HP 7820A gas chromatograph equipped with a capillary column (HP-5, 30 m, ø 0.32 mm, 0.25 mm film, Agilent Technologies) and thermal conductivity detector (TCD) was used.
During the analysis the GC column oven is set to run in the temperature program reported in figure 5.2.

Figure 5.2 Temperature program for GC analysis
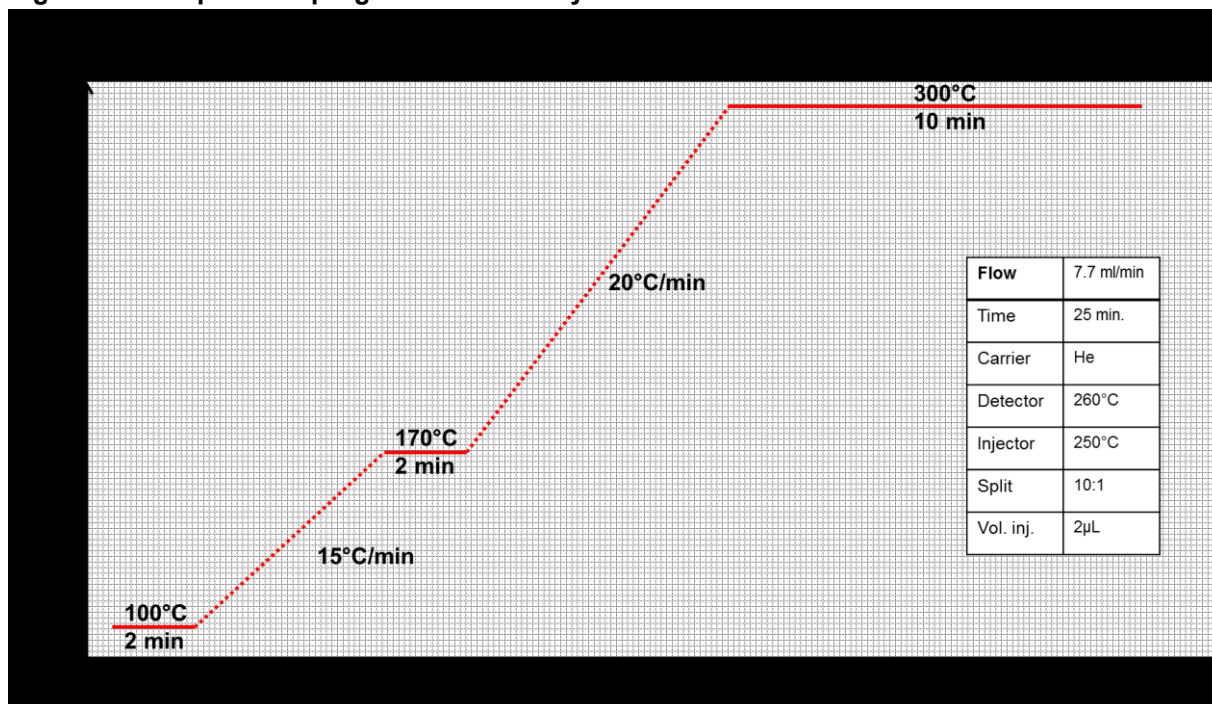
Quantification of the reaction products was performed by the internal standard method, using 1-octanol as internal standard. A constant amount of 1-octanol has been added to all samples. That same amount of the internal standard is also included in each of the calibration standards. For each compound a calibration curve has been drawn by reporting in a graph the ratio of the peak area of the analyte to the peak area of the internal standard as a function of the ratio of analyte concentration to internal standard concentration. As-obtained experimental points have been interpolated by a regression line. The slope of the line indicates the response factor, which is then used in the analyses for determining the concentration.

$$\frac{A_x}{A_{istd}} = RF \frac{C_x}{C_{istd}} \qquad \text{and} \qquad C_x = \frac{A_x}{A_{istd}} \frac{C_{istd}}{RF}$$

5.2.2.C Characterization

Transmission Electron Microscopy (TEM)

The morphology of the catalysts was observed by using a Jeol 2200FS transmission electron microscope equipped with a 200 kV field-emission gun and a high-angle annular dark field detector in STEM mode. The local composition was determined by EDX. The samples were prepared by evaporation of an alcohol suspension on a copper grid coated with a holey carbon film. The noble metal particle size distribution was obtained by measuring particles by using the software ImageJ.

CO adsorption

Diffuse reflectance infrared Fourier transform (DRIFT) spectra were collected with a Vertex 70V spectrometer (Bruker Optics) equipped with a liquid-nitrogen cooled MCT detector and a commercial mirror unit (Praying Mantis, Harrick). CO adsorption from the gas phase was followed at room temperature on as-received catalysts by admitting 50 mL/min of 5 vol.% CO/Ar subsequent to dehydration for 1 h at 120 °C in Ar and by accumulating spectra (first 100 scans, 14 s/spectrum; then 200 scans, ca. 180 s/spectrum; 4 cm^{-1} resolution) over 30 min. Adsorbed CO was then replaced by Ar in order to follow desorption under otherwise identical conditions. The powder samples (ca. 70 mg) were used without further dilution. Spectra were ratioed against a background spectrum recorded in Ar flow prior to admittance of CO. All spectra are presented in absorbance units and were corrected for contribution of atmospheric CO_2 and water where needed.

Operando characterization

a) ATR-IR Spectroscopy

A thin layer of 5 wt % Pd/Al$_2$O$_3$ catalysts deposited on an internal reflection element (IRE) was used to investigate the liquid-phase oxidation of benzyl alcohol.

An aqueous slurry of catalyst was allowed to evaporate on the ZnSe IRE (45°, 50 x 20 x 2 mm^3, Crystran) in a fume hood overnight. The deposited films were highly stable under the conditions applied.(Figure 5.3)

Figure 5.3 Catalyst film deposition on ZnSE IRE
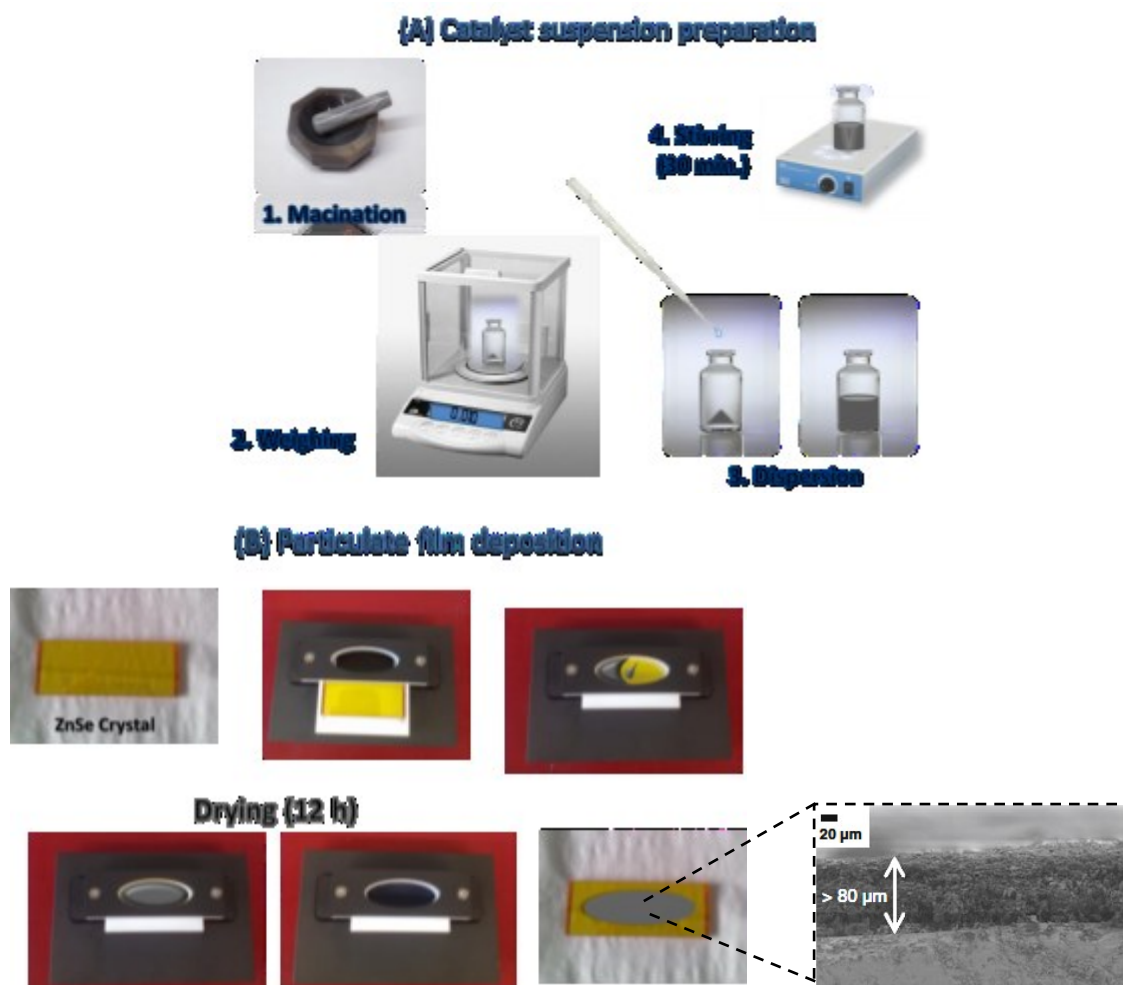
Batch-reactor cell

A homemade batch-reactor cell was used to monitor alcohol oxidation both on the surface of the catalyst and in solution using the ATR mode.

Figure 5.4 Homemade batch-reactor cell

Stirring was provided by using a conventional laboratory magnetic stirrer integrated in the base plate of the cell. The top of the cell was fitted with a stainless-steel cover with a circular aperture that allowed the insertion of a glass condenser (conical tapered ground joint, 19/26) for experiments under reflux. The ZnSe IRE coated with a powder film was placed on the horizontal heatable base of the cell.

After mounting the cell body and adding 20 mL of cyclohexane solvent, the temperature was increased to 60°C, and the system was left to equilibrate for 2 h under bubbling N_2 at reflux and stirring. Before the injection of benzyl alcohol (190 mL), a background IR spectrum of the catalyst was recorded at 60°C in cyclohexane. Then a series of consecutive ATR-IR spectra (200 scans, 4 min/spectrum, 4 cm^{-1} resolution) were collected to follow the reaction. After 5 min from the injection of benzyl alcohol, N_2 was replaced by O_2, and the system was allowed to react for 1 h.

Flow-through cell

For the ATR-IR measurement a home-built stainless steel flow-through cell serving as a continuous-flow reactor was mounted onto the ATR accessory (Specac) within the FT-IR spectrometer (Vertex 70V, Bruker Optics) equipped with an MCT detector cooled with liquid nitrogen.

Figure 5.5 Homemade stainless steel flow-through cell
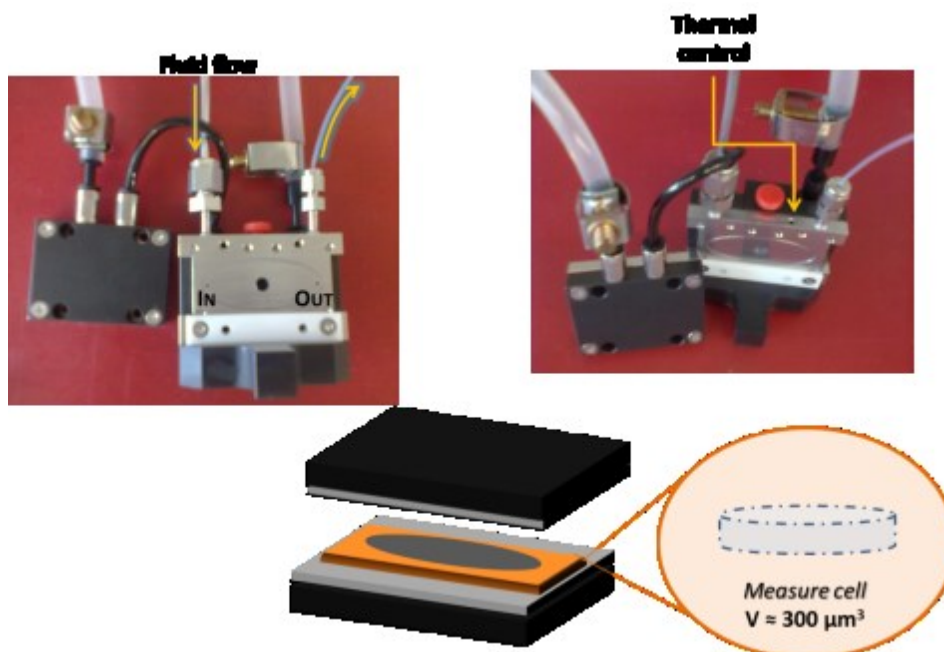
Spectra were recorded by averaging 100 scans at 4 cm^{-1} resolution. The cell was kept at 60°C throughout the measurements. Cyclohexane solvent and benzyl alcohol in cyclohexane (0.02 M) were flown over the catalyst layer at a rate of 0.6 mL min^{-1} by a peristaltic pump located after the cell.

Solutions were provided from two independent glass reservoirs. All transfer lines were of stainless steel.

In a general procedure, neat cyclohexane saturated with Ar was admitted to the cell until steady-state conditions were achieved (for 30 min). In the case of 5 wt % Pd/Al$_2$O$_3$ catalyst a pre-reduction was performed in situ by admitting H$_2$-saturated cyclohexane for 30 min. Then, the solution of the alcohol in Ar-saturated cyclohexane was admitted to the catalyst. After typically 40-50 min on stream, Ar was replaced by air for another 30-40 min. Finally, the catalyst was washed with Ar-saturated cyclohexane for about 30 min to monitor desorption of reactants and products. ATR-IR spectra were collected throughout the experiment and are presented in the form of A = -log(I/I$_0$). Where required, the spectra were corrected to compensate for the absorption of water vapor.

b) FT-IR Spectroscopy

The outlet of the ATR-IR in situ cell was connected to the inlet of the transmission infrared cell using 1/8" teflon tubing. Online measurements were triggered independently from the ATR-IR measurements. Typically, the online measurement was started few instants before benzyl alcohol solution admission.

Transmission infrared spectra were collected in the 4000–1000 cm^{-1} spectral range every 30 s (28 scans) at 4 cm^{-1} resolution with an Alpha spectrometer (Bruker Optics) equipped with a 1-mm flow-through liquid cell (CaF$_2$ windows).

5.3 Experimental section - Chapter 4

Computing facilities for this work were provided by ARCCA at Cardiff University, HPC Wales.

The Cardiff University Supercomputer, Raven, has been used.

The Raven system comprises of:

- Dedicated MPI Compute Node Partition with 128 dual-socket nodes (64* Bullx B510 blades), containing 2048 Intel Xeon (Sandy Bridge / E5-2670) 2.60GHz cores and 4GB memory per core
- 8 x SMP bullx B510 twin blades each with 2*Intel Sandy Bridge E5-2670 (2.60GHz), 8GB per core (128GB DDR3@1600MHz 8*16GB DIMMS), and 1*128GB SATA SSD
- Dedicated HTC Compute Node Partition with 72 dual-socket nodes, containing 864 Intel Xeon (Westmere / X5660) 2.80GHz cores and 4GB memory per core.
- Redundant Administration nodes
- 2 Front-end login nodes for users to access the cluster
- Infiniband (Connect2-X) 4x QDR/PCIe gen2 16x network infrastructure across the entire system (40Gbps HS/LL QDR, 1.2μsec latency)
- "Fabric A" is a QDR Infiniband for job traffic
- "Fabric B" is a 1Gbps network dedicated to cluster management traffic
- 50TB useable Lustre Cluster File System with:
  - 2 x Lustre MetaData Servers (MDS)
  - 2 x Lustre Object Storage Servers (OSS) nodes
- 100TB useable resiliant disk storage (SATA)
- 320TB Tape Storage
- Redundant NFS Storage Access Nodes

SSH Shell Client 3.2.9 was used as the terminal and file transfer client. It uses the Unix/ LINUX operating system.
DFT calculations were performed with the VASP plane-wave code with optimisation runs at the Perdew-Burke-Ernzerhof (PBE) functional level and a 400 eV planewave cut-off to define the basis set.

The coordinate files are in Accelrys ".car" format and were used to generate POSCAR files. An example of POSCAR file is reported in figure 5.6.

Figure 5.6 Example of POSCAR file

References

[1] K. M. S. Khalil, *J. Colloid Interface Sci*., 2007, 315, 562–568.

[2] A. Villa, C. E. Chan-Thaw, G. M. Veith, K. L. More, D. Ferri, L. Prati, *ChemCatChem,* 2011, 3, 1612.

[3] R. Arrigo, M. Haevecker, S. Wrabetz, R. Blume, M. Lerch, J. McGregor, E.P.J. Parrott, J.A. Zeitler, L.F. Gladden, A. Knop-Gericke, R. Schloegl, D. Su, *J. Am. Chem. Soc*. 2010, 132, 9616–9630.

[4] N. Dimitratos, A. Villa, D. Wang, F. Porta, D. Su, L. Prati, *J. Catal*. 244 (2006) 113.

Concluding remarks

The design of new heterogeneous catalysts to be integrated into emerging sustainable processes is one of the most important challenge for a complete integration between green chemistry and industrial chemistry.

Catalyst design requires an improved understanding of the chemistry on the surface, a clear disclosure of the mechanism of catalyzed processes and the ability to probe catalyst active sites under reaction conditions. This is possible if a knowledge-based approach is shaped around three pillars: 1) the controlled synthesis of nanomaterials; 2) theoretical modelling of materials that enable experimental results to be understood; and 3) ex situ and advanced in situ characterization under working conditions (operando methodology). All these aspects have been examined in my Ph.D. project, focused on the optimization of supported noble metal based catalysts for liquid-phase oxidation processes through a deep insight on their structure.

Two possible strategies for tailoring the selectivity in the base-free glycerol oxidation have been extensively investigated, by exploring the ability to orientate the reaction pathway towards the selective oxidation either of the primary alcohol function or the secondary alcohol function. The selective oxidation of the primary hydroxyl group in the glycerol molecule results in the production of glyceric acid. Supported AuPt bimetallic nanoparticles have been shown to be active and durable catalysts for the selective glycerol oxidation to glyceric acid under neutral conditions. In particular a high selectivity to glyceric acid has been reported using acidic support as H-mordenite. Starting from these considerations we studied more in the detail the effect of surface acidity, by comparing various metal oxides with different type, number and strength of acid sites. We observed that the acid/base properties, especially the strength of H-bonding, of these catalysts are the key factor in tuning the selectivity.

In the past years many efforts were devoted to switch the reaction pathway towards the oxidation of the secondary alcohol function, to maximize the yield of dihydroxyacetone, a high value-added product, currently produced by biotechnological route. Until now, best results in terms of DHA yield have been obtained using Bi-Pt/AC catalysts. However these systems suffer from quick deactivation due to metal leaching. For this reason we examined the possibility to improve the durability of BiPt based catalysts by properly tuning the metal composition. In particular trimetallic BiAuPt nanoparticles were supported on activated carbon and tested in base free glycerol oxidation. By comparing the catalytic performances of trimetallic AuPtBi NPs with the ones of bimetallic AuPt and BiPt NPs, we concluded that the addition of Bi promotes the oxidation of the secondary OH function leading to the production of dihydroxyacetone (DHA) as the main product. Furthermore the addition of gold enhances the catalyst stability by limiting the Bi leaching and thus resulting in a good selectivity to DHA even at high conversion(selectivity of 63% at 80% conversion). Moreover the amount of bismuth is important in selectively affecting the catalytic activity and selectivity.

Beside the metal composition and the surface properties of supports, also the preparation route can influence the catalytic performances of supported noble metal nanoparticles. From this point of view the sol immobilisation technique, in which a protective agent (such as polyvinylalcohol or polyvinylpyrrolidone) is used to stabilize metal nanoparticles, possesses advantages like the control of the metal particle size almost independently from the type of support and the improvement of catalyst resistance to deactivation compared to other

methods. On the other hand, with comparable metal dispersion, catalysts derived from metallic sol immobilization, typically present lower activity than catalysts with naked metal nanoparticles as for instance catalysts prepared by impregnation. Moreover also a different selectivity was often observed. Using operando ATR-IR spectroscopy we revealed that in the liquid phase benzyl alcohol oxidation PVA produces a selectivity enhancement to benzaldehyde limiting its decarbonylation. DRIFT experiments with CO as probe molecule allowed to relate this behavior to a specific blocking of Pd(111) facets which has been recognized to facilitate the decarbonylation process. The possibility to direct the selectivity in alcohol oxidation by a selective blocking of specific active site represents a potential tool and an additional advantage in using supported metal nanoparticles from colloidal synthesis as catalyst as the selectivity issue is one of the most important parameter for the industrial development of catalytic processes.

In an ideal knowledge-based approach experimental evidences should be supported by theoretical results. For this reason, the last part of my Ph.D. was devoted to the application of Density Functional Theory (DFT) modelling to the investigation of all those features previously investigated from an experimental point of view (metal composition, the role of support, the effect of protecting agent). Promising preliminary results revealed that the local structure and composition of active site play a crucial role in affecting the reaction mechanism of ethanol oxidation. In particular the presence of oxygen and defects strongly modify the reaction mechanism from an energetic point of view.

Concluding, the design of supported noble metal nanoparticle based catalysts can be optimized by using a novel approach, which takes into account and harmonizes all the different aspects involved in the process.

List of figures

List of tables

List of publications

Title: **AuPt alloy on TiO2, a selective and durable catalyst for the L-sorbose oxidation to 2-keto gulonic acid**
1 Author(s): C.E. Chan Thaw, et al.
Source: *ChemSusChem* (**2015**), *Accepted*.
Published on line:

Title: **Operando Attenuated Total Reflectance FTIR Spectroscopy: Studies on the Different Selectivity Observed in Benzyl Alcohol Oxidation**
2 Author(s): A. Villa, et al.
Source: *ChemCatChem, (2015), 7(16)*
Published on line: July 2015 DOI: DOI: 10.1002/cctc.201500432

Title: **AuRu/AC as an effective catalyst for hydrogenation reactions**
3 Author(s): A. Villa, et al.
Source: *Phys. Chem. Chem. Phys., 2015, Advance Article*
Published on line: 23 March 2015 DOI: *10.1039/C5CP00632E*

Title: *Selective Oxidation of Raw Glycerol Using Supported AuPd Nanoparticles*
4 Author(s): C.E. Chan Thaw, et al.
Source: *Catalysts* (**2015**), *5*, 131-144.
Published on line: 13 February 2015 DOI: 10.3390/catal5010131

Title: **Bismuth modified Au-Pt bimetallic catalysts for dihydroxyacetone production**
5 Author(s): Alberto Villa, et al.
Source: *Cat. Tod.*, (**2015**)
Published on line: 8 January 2015 DOI: 10.1016/j.cattod.2014.12.012

Title: **Tailoring the selectivity of glycerol oxidation by tuning the acid–base properties of Au catalysts**
6 Author(s): Alberto Villa, et al.
Source: *Catal. Sci. Technol*., (**2015**), Advance Article
Published on line: 17 October 2014 DOI: 10.1039/C4CY01246A

Title**: Fragrances by selective oxidation of long-chain alcohols**
7 Author(s): Alberto Villa, Carine E. Chan-Thaw, Marco Schiavoni, Sebastiano Campisi, Di Wang, Laura Prati
Source: *Chinese Journal of Catalysis* 35 (**2014**) 945-951
Published: 20 June 2014 DOI: 10.1016/S1872-2067(14)6010

Title: **Amino Alcohol Oxidation with Gold Catalysts: The Effect of Amino Groups**
8 Author(s): Villa, Alberto; et al.
Source: *Materials* Volume: 6 Issue: 7 (**2013**) Pages: 2777-2788
Published: JUL 2013 DOI: 10.3390/ma6072777

Title: **NiO as a peculiar support for metal nanoparticles in polyols oxidation**
Author(s): Villa, Alberto; et al.
9 Source: Catalysis Science & Technology Volume: 3 Issue: 2 (**2013**) Pages: 394-399
Published: 2013 DOI: 10.1039/c2cy20370g

Title: **Pd-modified Au on Carbon as an Effective and Durable Catalyst for the Direct Oxidation of HMF to 2,5-Furandicarboxylic Acid**
10 Author(s): Villa, Alberto; et al.
Source: *Chemsuschem* Volume: 6 Issue: 4 (**2013**) Pages: 609-612
Published: APR 2013 DOI: 10.1002/cssc.201200778

Acknowledgements